

Wind Engineering *for Natural Hazards*

*Modeling, Simulation, and Mitigation of
Windstorm Impact on Critical Infrastructure*

Fluids Dynamics Committee

Edited by

Aly Mousaad Aly, Ph.D.
Elena Dragomirescu, Ph.D.



ENGINEERING
MECHANICS
INSTITUTE

TRENDS IN ENGINEERING MECHANICS SPECIAL PUBLICATION NO. 3

Wind Engineering for Natural Hazards

MODELING, SIMULATION, AND MITIGATION
OF WINDSTORM IMPACT ON CRITICAL
INFRASTRUCTURE

Edited by
Aly Mousaad Aly, Ph.D.
Elena Dragomirescu, Ph.D.

Sponsored by
Fluid Dynamics Committee of the Engineering Mechanics Institute
of the American Society of Civil Engineers



Published by the American Society of Civil Engineers

@Seismicisolation

Library of Congress Cataloging-in-Publication Data

Names: EMI (Conference) (2016 : Nashville, Ten.), author. | Aly, Mousaad Aly, editor. | Dragomirescu, Elena, editor. | Engineering Mechanics Institute. Fluids Dynamics Committee, sponsoring body.

Title: Wind engineering for natural hazards modeling, simulation, and mitigation of windstorm impact on critical infrastructure / prepared by Fluids Dynamics Committee of the Engineering Mechanics Institute of the American Society of Civil Engineers ; edited by Aly Mousaad Aly, Ph.D., Elena Dragomirescu, Ph.D.

Description: Reston, Virginia : American Society of Civil Engineers, [2018] | Includes bibliographical references and index.

Identifiers: LCCN 2018030046 | ISBN 9780784415153 (soft cover : alk. paper) | ISBN 9780784481844 (pdf) | ISBN 9780784481851 (epub)

Subjects: LCSH: Wind resistant design—Congresses. | Wind-pressure—Congresses. | Winds—Simulation methods—Congresses.

Classification: LCC TA658.48 .E45 2016 | DDC 624.1/75-dc23

LC record available at <https://lccn.loc.gov/2018030046>

Published by American Society of Civil Engineers

1801 Alexander Bell Drive

Reston, Virginia 20191-4382

www.asce.org/bookstore | ascelibrary.org

Any statements expressed in these materials are those of the individual authors and do not necessarily represent the views of ASCE, which takes no responsibility for any statement made herein. No reference made in this publication to any specific method, product, process, or service constitutes or implies an endorsement, recommendation, or warranty thereof by ASCE. The materials are for general information only and do not represent a standard of ASCE, nor are they intended as a reference in purchase specifications, contracts, regulations, statutes, or any other legal document. ASCE makes no representation or warranty of any kind, whether express or implied, concerning the accuracy, completeness, suitability, or utility of any information, apparatus, product, or process discussed in this publication, and assumes no liability therefor. The information contained in these materials should not be used without first securing competent advice with respect to its suitability for any general or specific application. Anyone utilizing such information assumes all liability arising from such use, including but not limited to infringement of any patent or patents.

ASCE and American Society of Civil Engineers—Registered in U.S. Patent and Trademark Office.

Photocopies and permissions. Permission to photocopy or reproduce material from ASCE publications can be requested by sending an e-mail to permissions@asce.org or by locating a title in the ASCE Library (<http://ascelibrary.org>) and using the “Permissions” link.

Errata: Errata, if any, can be found at <https://doi.org/10.1061/9780784415151>.

Copyright © 2018 by the American Society of Civil Engineers.

All Rights Reserved.

ISBN 978-0-7844-1515-3 (print)

ISBN 978-0-7844-8184-4 (PDF)

ISBN 978-0-7844-8185-1 (ePub)

Manufactured in the United States of America.

Contents

Preface	v
1. Recent and Current Wind Engineering Research at the National Institute of Standards and Technology	1
Dat Duthinh, Jianghua Ke, Marc L. Levitan, Sejun Park, Long T. Phan, Adam L. Pintar, Liang Shi, Emil Simiu, and DongHun Yeo	
2. Investigation on a Generalized Intervention Cost Function to Examine Wind-Induced Damage on Tall Buildings.....	25
Luca Caracoglia	
3. Wind Response Control of Tall Buildings with Flexible Foundation using Tuned Mass Dampers	55
Said Elias and Vasant Matsagar	
4. Wind Loading on Tall Building Structures in Consideration of Performance-Based Design	79
U. Y. Jeong and K. Tarrant	
5. Interrogation of Relation between Design Load Level and Lifetime of Individual Building and Its Element	97
Yukio Tamura, Di Wu, and Qingshan Yang	
6. Simulating the Role of Axial Flow in Stay Cable Vibrations via a Perforated Wake Splitter Plate	111
Ran Wang, Shaohong Cheng, and David S-K. Ting	
7. Longitudinal Forces on Transmission Towers due to Non-Symmetric Downburst Ground Wire Loads	133
Amal Elawady and Ashraf El Damatty	
8. Effects of Chamber Shape on Simulation of Tornado-like Flow in a Laboratory	149
Fangping Yuan, Guirong Yan, Ryan Honerkamp, Kakkattukuzhy M. Isaac, and Ruoqiang Feng	
9. Computational versus Wind Tunnel Simulation of Atmospheric Boundary Layer Flow for Structural Engineering Applications....	169
DongHun Yeo and Liang Shi	

10. Application of Wind Fairings for Building Aerodynamic Optimization.....	193
Zhendong Xu and Jiming Xie	
11. Bottom Plate Slope Effects on Aerodynamic Behaviour of Hexagonal Cross-Section Bridge Deck	205
Md. Naimul Haque, Hiroshi Katsuchi, and Hitoshi Yamada	
Index.....	225

Preface

Although wind itself may not be visible to the human eye, its effect on the built environment can be seen readily, and the hazards that it brings are of tremendous impact, both on life and critical infrastructure. Climate change has increased the risks of wind hazards among other natural hazards, and understanding the often-encountered hurricanes, tornadoes, and other types of nonsynoptic winds and large-scale wind storms became crucial for realistically predicting the wind impact on the built environment.

Wind engineering is a multidisciplinary research area that lies at the intersection of different disciplines: fluid mechanics, structural dynamics, mathematics, atmospheric science, and computer science, among other technical areas. The physics involved in the processes of atmospheric boundary layer (ABL) and the interaction with the built environment are indispensable for the understanding of wind-induced loads and the response of the infrastructure. The tools employed in wind engineering include atmospheric modeling, boundary layer wind tunnels, computational fluid dynamics (CFD), and full-scale data collection, among others.

This publication addresses the challenge of modeling and understanding windstorms' impact on the built environment to mitigate natural hazard threats on high-rise buildings, long-span bridges, power transmission lines, and other critical infrastructure. It also addresses the complexity of simulating nonsynoptic and synoptic wind flows, owing to the need for high-resolution flow characteristics.

Several research topics in wind engineering are currently progressing at the National Institute of Standards and Technology (NIST). The contribution by Duthinh et al., "Recent and Current Wind Engineering Research at the National Institute of Standards and Technology," reviews previous and current NIST research projects aimed at improving standard provisions and advancing structural design practice for wind loads.

For high-rise buildings, it may be astute to design cladding and components using a shorter recurrence period wind load than that of the main force resisting system (structural frames). The paper by Tamura and Yang, "Interrogation of Relation between Design Load Level and Lifetime of Individual Building and Its Element," strongly recommends that the optimal design wind load level in Japan involve a group of buildings, rather than attempting to optimize the life-cycle cost (LCC) of individual buildings.

The simulation of the stochastic dynamics of high-rise buildings, under turbulent wind loads, is imperative for investigating the wind-induced damage of high-rise buildings. In the paper by Caracoglia, "Investigation on a Generalized Intervention Cost Function to Examine Wind-Induced Damage on Tall

Buildings,” the author takes into consideration the influence of the cross-wind modal response on the damage and the simultaneity of the structural response along the two directions of the investigated building model.

Moreover, high-rise buildings are susceptible to wind-induced loads; therefore, their design is frequently dominated by the wind governing loads. In the work by Jeong and Tarrant, “Wind Loading on Tall Building Structures in Consideration of Performance-based Design,” the authors show that the “heavy-headed, light-tailed” probabilistic distributions of wind speeds, as well as building aerodynamic characteristics, can generate high loads in service level winds, which diminishes the application of performance-based design (PBD) to tall building wind design.

Wind fairings, based on principles of wind-adaptable design (WAD), is a promising approach to optimize buildings’ aerodynamic properties. In their paper, “Application of Wind Fairings for Building Aerodynamic Optimization,” Xu and Xie achieve a reduction of about 20% in design wind loads by properly designed wind fairings adapted for buildings.

Multiple-tuned mass dampers (MTMDs) are effective devices for response control in high-rise buildings. The paper by Elias and Matsagar, “Wind Response Control of Tall Buildings with Flexible Foundation using Tuned Mass Dampers,” analyzes the response of high-rise buildings equipped by MTMDs, accounting for soil-structure interaction (SSI). The authors’ findings suggest that the type of soil may influence tuning parameters, and the MTMDs show better effectiveness, compared to the single-tuned mass dampers.

Secondary axial flow on inclined bridge stay cables contributes to the intensity of wind-induced vibrations. The work by Wang et al., “Simulating the Role of Axial Flow in Stay Cable Vibrations via a Perforated Wake Splitter Plate,” proposes a solid wake splitter plate for achieving a symmetric surface pressure distribution pattern and a weaker von Kármán vortex shedding strength, leading to reductions in the lift and drag forces, which may affect the wind-induced vibrations.

Long-span bridges may exhibit diverse aeroelastic phenomena, and the shape of the deck plays an important role in governing the aerodynamic stability. In the paper by Haque et al., “Bottom Plate Slope Effects on Aerodynamic Behaviour of Hexagonal Cross-Section Bridge Deck,” the authors carry out detailed numerical investigations on the bottom plate web slope effect on flow behavior of a hexagonal bridge deck, using a two-dimensional finite volume code with the RANS turbulence model, and they compare the results with those obtained from the study of a pentagonal shape.

Long-span slender structures, such as transmission lines, may be subjected to a unique load because of the spatial localization of the downburst, which is different from synoptic winds. In their paper, “Longitudinal Forces on Transmission Towers due to Non-Symmetric Downburst Ground Wire Loads,” Elawady and El Damatty develop a simplified approach to estimate downburst-induced forces for ground wires of transmission lines.

It can be challenging to capture the characteristics of the wind field during a tornado event, especially in the near ground region. In the paper by Yuan et al., “Effects of Chamber Shape on Simulation of Tornado-like Flow in a Laboratory,” the authors produce tornado-like vortices, employing three simulators with different geometric shapes, to systematically study and understand the violent tornadic wind field and its effect on civil engineering structures.

Computational wind engineering is a promising area of research that has received significant attention in recent years. The paper by Yeo and Shi, “Computational vs. Wind Tunnel Simulation of Atmospheric Boundary Layer Flow for Structural Engineering Applications,” presents atmospheric boundary layer computational simulation used to assess its suitability for structural wind engineering applications.

We hope that this book reveals the knowledge shown with the most recent advances and applications in wind/structural engineering and thus is of interest to numerous researchers looking to pursue further investigations leading to major improvements of design approaches, with the intent of creating more resilient and sustainable infrastructures. This is imperative per the current climate change and population growth.

Last, but not least, we would like to thank all the authors for their contributions, as well as the reviewers for their support and helpful critiques, which made this publication possible. Many thanks to Dr. Chaker, Dr. Hajj, Dr. Diplas, and members of the EMI Fluid Dynamics Committee for their collaboration.

Aly Mousaad Aly, Ph.D.
Louisiana State University, Baton Rouge, LA, USA

Elena Dragomirescu, Ph.D.
University of Ottawa, Ottawa, ON, Canada

This page intentionally left blank

Downloaded from ascelibrary.org by Iowa State University on 02/06/19. Copyright ASCE. For personal use only; all rights reserved.

CHAPTER 1

Recent and Current Wind Engineering Research at the National Institute of Standards and Technology

Dat Duthinh, M. ASCE*

Jianghua Ke*

Marc L. Levitan, A.M. ASCE*

Sejun Park*

Long T. Phan, M. ASCE*

Adam L. Pintar†

Liang Shi*

Emil Simiu, F. ASCE*

DongHun Yeo, M. ASCE*

Abstract: This paper briefly reviews recent and current National Institute of Standards and Technology (NIST) research aimed at improving standard provisions and advancing structural design practice for wind loads. The research covers: (i) New wind speed maps for the conterminous United States; (ii) Risk-consistent estimation of wind load factors for use with the wind tunnel procedure; (iii) Modern peaks-over-threshold approaches to estimation of peak wind effects; (iv) User-friendly procedures for the database-assisted design of rigid and flexible structures; (v) Novel approaches to codification of pressures on cladding and components; (vi) Modern modeling of synoptic storm planetary boundary layers and its implications for super-tall building design; (vii) Computational Wind Engineering (CWE); (viii) Tornado climatology and development of tornado-resistant design

*Ph.D., National Institute of Standards and Technology, Engineering Laboratory, Gaithersburg, MD 20899; email: {dat.duthinh, jianghua.ke, marc.levitan, sejun.park, long.phan, liang.shi, emil.simiу, donghun.yeo}@nist.gov

†Ph.D., National Institute of Standards and Technology, Information Technology Laboratory, Gaithersburg, MD 20899; email: adam.pintar@nist.gov

methodologies; (ix) Joint climatology of wind speeds, storm surge and waves heights, and estimates of their combined effects on structures.

Keywords: Cladding and components; computational wind engineering; database-assisted design; peaks over threshold; super-tall buildings; synoptic storms; storm surge; tornadoes; wind speed maps.

INTRODUCTION

“Wind engineering is an emerging technology and there is no consensus on certain aspects of current practice . . .” (SOM 2005). Much of the ongoing research reviewed herein was prompted by the NIST recommendation, following the Federal Building and Fire Investigation of the WTC Disaster and the SOM (2005) report, that “nationally accepted performance standards be developed for . . . estimating wind loads and their effects on . . . buildings for use in design . . .” (NIST 2011). That research led to the development of (i) new wind speed maps for the conterminous United States (Pintar et al. 2015), (ii) a simple methodology for determining wind load factors or design mean recurrence intervals (MRIs) of wind effects (Simiu et al. 2017b), (iii) peaks-over-threshold methods for estimating peak wind effects, demonstrated to significantly outperform methods currently in use (Duthinh et al. 2017), (iv) user-friendly procedures for the database-assisted design of rigid and flexible structures, which limit the contribution of the wind engineer to (a) participating in the preliminary design process, and (b) providing the requisite wind velocity and aerodynamic pressure time series data in formats fully open to effective scrutiny, while leaving the structural engineer in full control of the final design process, including the dynamic analyses and the determination of the global forces, the internal forces, and the peak demand-to-capacity indexes (Simiu and Yeo 2015), (v) novel, effective approaches to codification of pressures on cladding and components (Duthinh et al. 2015, 2017; Gierson et al. 2015, 2017), and (vi) a recent proposal for modifying ASCE 7-10 Standard provisions for the design of super-tall buildings by the wind tunnel procedure, determined on the basis of modern models of the planetary boundary layer to be severely unconservative (Simiu et al. 2017a). More recently, with the publications of the Technical Investigation (Kuligowski et al. 2014) of the May 22, 2011 Joplin, MO, Tornado, and the Measurement Science R&D Roadmap for Windstorm and Coastal Inundation Impact Reduction (NIST 2014), NIST added to its research agenda (vii) Computational Wind Engineering, with the objective of developing computational procedures capable of providing, in the not too distant future, a substitute for certain types of aerodynamic testing (Yeo and Chowdhury 2013), (viii) the development of tornado-resistant design methodologies, since (a) the tornado hazard has recently been estimated to be significantly higher than shown in current tornado wind speed maps, and (b) the US death toll in tornadoes is greater than in hurricanes and earthquakes combined (data available from 1950 to present) (Kuligowski et al. 2014, Phan et al. 2010, Phan and Simiu 2011), and (ix) the development of joint probabilities of hurricane wind speeds, storm surge, and waves and of approaches to the probabilistic estimation of their combined effects on coastal structures (Phan and Simiu 2011).

WIND SPEED MAPS FOR THE CONTIGUOUS UNITED STATES

NIST has recently led an effort to improve upon the ASCE 7-10 ([ASCE 2010](#)) wind speed maps for inclusion in the ASCE 7-16 Standard (to be released in early 2017). In the new maps, super-stations—which resulted in an artificially uniform spatial distribution of wind speeds over most of the contiguous United States—are no longer used, and risk-consistent maps are obtained using statistical spatial smoothing techniques to individual stations. Also, peaks-over-threshold (POT) models for individual stations are used in place of classical extreme value models applied to maximum yearly data. A summary of the procedure used for the contiguous US-areas not prone to hurricanes ([Pintar et al. 2015](#)) follows.

The available raw data are the time histories of peak wind gusts, mostly over 11 m/s at more than 1,000 stations. Winds were classified by storm type. Data from hurricanes and tornadoes were excluded, with all remaining data classified as either thunderstorm or non-thunderstorm. The data were checked for quality and were converted to speeds at 10 m height above ground over terrain with open exposure. No stations in service for less than 15 years were considered.

The procedure has two stages. In the first stage, the two-dimensional Poisson process described by [Smith \(1989\)](#), which is a POT model, was used to estimate all return speeds of interest for all stations deemed suitable. In the second stage, the return speeds were smoothed using local regression ([Cleveland and Devlin, 1988](#)) to produce the final maps.

An advantage of POT over classical models is the ability to leverage more data. Whereas classical extreme value models describe the probability distribution of the maximum value over, for example, one year, POT models describe the stochastic nature of all observations crossing some high threshold. As part of this work, an approach to choosing an optimal threshold based on the data was developed and employed.

Local regression is a well-established general purpose statistical approach to smoothing. In this particular setting, the return value at some location would depend on all stations within a neighborhood of that location. The closest stations are weighted most heavily. Neighborhoods are chosen dynamically to include a fixed proportion of the available stations. Thus, neighborhoods in the western United States are expanded in comparison to those in the east. Figure 1 depicts the map of non-hurricane wind speeds with a 50-year MRI. The points show station locations.

WIND LOAD FACTORS FOR USE IN THE WIND TUNNEL PROCEDURE

[SOM \(2004\)](#) notes that the ASCE 7 Standard is incomplete insofar as it provides no guidance on wind load factors appropriate for use with the Standard's wind tunnel procedure. The purpose of the NIST research on this topic is to contribute to such guidance. For example, design wind effects with a 50-year mean recurrence interval, the classical expression for the wind load factor γ as a

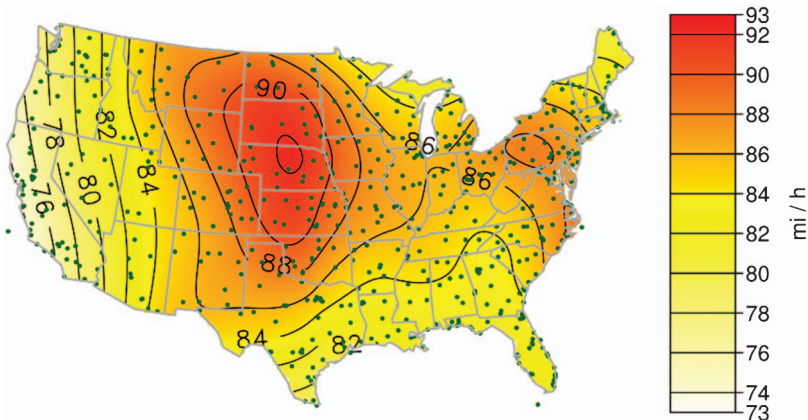


Figure 1. Map of non-hurricane wind speeds for a 50-year MRI

Source: [Pintar et al. \(2015\)](#).

function of the uncertainties in the micrometeorological, wind climatological, aerodynamics and dynamics elements that determine wind loads can be written as follows ([Ellingwood et al. 1980](#)):

$$\gamma(N = 50 \text{ yrs}) \equiv 1 + k \text{COV}[p_{pk}(N = 50 \text{ yrs})] \quad (1)$$

$$\begin{aligned} \text{COV}[p_{pk}(N)] \approx & \{\text{COV}^2(E_z) + \text{COV}^2(K_d) + \text{COV}^2[G(\theta_m)] \\ & + \text{COV}^2[C_{p,pk}(\theta_m)] + 4\text{COV}^2[V(N)]\}^{1/2} \end{aligned} \quad (2)$$

where p_{pk} is a peak wind effect (e.g., pressure, force, moment, deflection, acceleration), and the aerodynamic coefficient $C_{p,pk}(\theta_m)$ depends upon the area being considered, which can be as small as a roof tile or as large as an entire building. Once this dependence is taken into consideration, for rigid structures the gust response factor $G = 1$ and $\text{COV}(G) = 0$. COV is covariance, and $V(N)$ is the wind speed with an N -year MRI, estimated from samples of largest wind speeds regardless of wind direction θ ; θ_m is the direction for which the product $G(\theta) C_{p,pk}(\theta)$ is largest; E_z is a terrain exposure factor assumed for simplicity to be independent of direction; z denotes height above the surface; and K_d is a wind directionality reduction factor that takes into account the fact that the direction θ_m and the directions of the largest directional wind speeds typically do not coincide. The factor k in the first equation is based on calibration against past practice. According to [Ellingwood et al. \(1980\)](#), it is reasonable to assume $k \approx 2$, which, for rigid structures, typical uncertainties, and $N = 50$ years, yields $\gamma(50 \text{ yrs}) \approx 1.6$. The design peak wind effect is

$$p_{pk,des}(N = 50 \text{ yrs}) \approx \gamma(N = 50 \text{ yrs}) \bar{p}_{pk}(50 \text{ yrs}) \quad (3)$$

$$\bar{p}_{pk}(N) \approx a\bar{E}_z\bar{K}_d\bar{G}(\theta_m)\bar{C}_{p,pk}(\theta_m)\bar{V}^2(N) \quad (4)$$

where the overbar denotes mean. This straightforward approach allows practitioners to use appropriate wind load factors applicable when the uncertainties are different from those assumed in the ASCE 7 Standard. Illustrations of the approach are presented for a variety of cases of practical interest in Simiu et al. (2017b). The approach reflects the fact that the various uncertainties should not be accounted for in isolation. Rather, to achieve risk-consistent designs, they should be accounted for collectively, in terms of their joint effect on the design wind loading. In particular, specifying peak pressure coefficients with percentage points higher (e.g., 80%, as in ISO 4354 (2009) than those corresponding to their expected values (i.e., approximately 57%) would be an instance of double counting, since the variability of the peak pressure coefficients about their mean is already taken into account in the definition of the wind load factor [Eq. (3)]. To further clarify this point, in applications, design peak pressures are commonly estimated by substituting in Eq. (5) estimated values for the “true” values of the location and scale parameters μ and σ of the Extreme Value (EV) Type I distribution, for the probability $F_r = 0.78$ or 0.8 (as specified in ISO 4354 (2009), p. 22), rather than $F_r = 0.5704$ (expected value).

$$C_{p,pk}(\theta, T/n)_{Fr} = \mu + \sigma \ln r - \sigma \ln(-\ln F_r) \quad (5)$$

where the peak pressure coefficient $C_{p,pk}$ is a function of wind direction θ , the length of the pressure record T and the number of epochs n in which it is subdivided. F_r is the probability that the variate $C_{p,pk}(\theta, T/n)$ is not exceeded in r epochs, with $r \geq n$. Assuming that the EV Type I distribution is an appropriate model, the use of the probability $F_r = 0.8$ rather than $F_r = 0.5704$ would be inconsistent with the meaning of \bar{p}_{pk} as a *mean* value. The deviation from the mean is accounted for by Eqs. 1 and 2. It need not and should not be accounted for twice: once in Eqs. 1 and 2, and once by selecting a value for F_r greater than the mean. It could be argued that the use of the 0.78 or 0.8 value of F_r is consistent with storm durations in excess of one hour (e.g., three hours). Note, however, that if a storm duration longer than one hour was assumed, the expected peak corresponding to it should be estimated directly by using in Eq. 5 with a value of r consistent with that duration. Also, the assumption that the storm durations are longer than one hour would clearly violate the accepted design practice, which follows the convention of a storm duration of one hour (see, e.g., ASCE 7-10, Eq. 26.9-11; ASCE 7-10 Commentary, Figure C26.5-1).

The design wind effect is equal to the estimated expectation of the peak wind effect times a wind load factor. Simple calculations based on the expression for the load factor given in Simiu et al. (2017b) show that the load factor is not affected significantly by errors associated with the interpolations required in typical database-assisted design applications (see section on database-assisted design). However, if the available wind speed records are very short (5 years, say), the wind load factors

increase by amounts that can exceed 15%. If, as is done in the ASCE-7 Standard, the wind load factor is accounted for by using increased MRIs of the design wind effects, those MRIs must be commensurate with the estimated wind load factor. For example, for $N = 50$ years, the increased MRIs of the design wind effects may have to be longer than the 700-yr value specified in the ASCE 7 Standard.

ESTIMATION OF TIME SERIES PEAKS USING THE TWO-DIMENSIONAL POISSON PROCESS AS A PEAKS-OVER-THRESHOLD MODEL

As shown in the next section, the database-assisted design procedure makes use of time histories of pressures measured in the wind tunnel at large numbers of taps on the external surface of building models; wind effects on structural members consist of time series obtained via weighted summations of individual pressure time histories. The design process assures that, after the application of appropriate safety margins, the combined estimated peak wind effect and gravity load effect do not exceed the member capacity. Given the time series of a wind effect, it is therefore necessary to estimate the distribution of its peak corresponding to a specified storm duration (e.g., one hour). The preceding section showed that special attention needs to be paid to the mean and coefficient of variation of that distribution, and notes that the mean of the distribution, rather than the 80th percentile specified in the ISO 4354 (2009) Standard, should be used in calculations. The procedure for estimating peaks usually partitions the time series into $n = 16$ equal epochs (Gavanski et al. 2016). The respective n maximum values are then fitted to a EV Type I (Gumbel) distribution. A weakness of this approach is the arbitrary choice $n = 16$, since the estimates can depend significantly upon n . NIST has recently developed the following six-step approach, denoted POTMax, based on a peaks-over-threshold (POT) model consisting of a two-dimensional Poisson process described by Smith (1989).

(1) If a minimum is considered, as in Figure 2, reflect the measurements about zero to estimate the distribution of a maximum. (2) De-cluster the observations x by forming clusters and discarding all but the cluster maxima, thus obtaining the de-clustered data x_{dec} . (Clusters are observations between an up-crossing and the following down-crossing of the mean. De-clustering is required to meet the independence assumption on which the POT model is based). (3) Select the threshold u (dashed line in Figure 2). The threshold is selected by an optimization procedure described in Pintar et al. (2015). (4) Fit the POT model to the de-clustered and thresholded data ($x_{dec} > u$; dots in Figure 2) via maximum likelihood estimation. In structural engineering applications, one may conform to accepted practice by fixing the model's tail length parameter to zero (i.e., specifying the Gumbel distribution). (5) Estimate the distribution of the maximum via Monte Carlo simulation (MCS). (6) Quantify uncertainty in the estimated distribution via MCS.

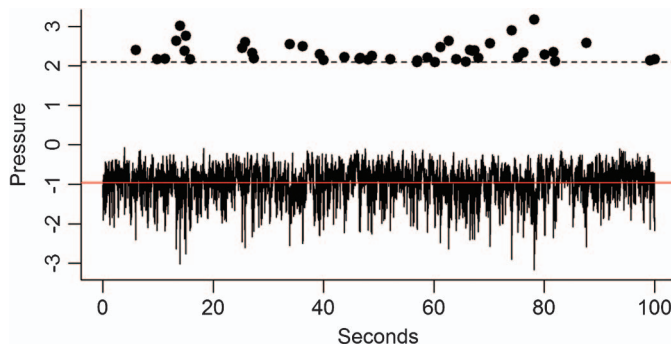


Figure 2. Time history of pressure measurements, and cluster maxima (with signs reversed)

Source: Duthinh et al. (2017).

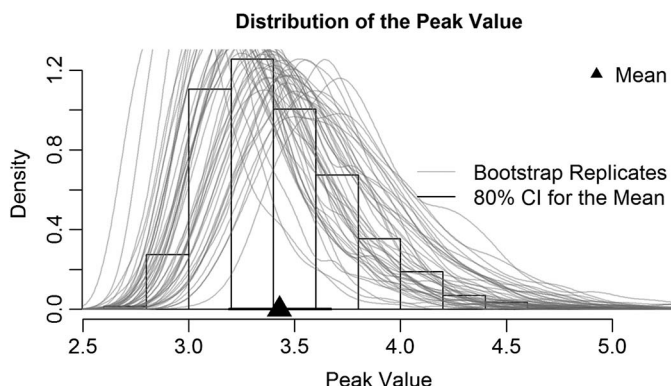


Figure 3. Results of running POTMax on the time history of Figure 2

Figure 3 shows the results of applying POTMax to the history in Figure 2. The histogram shows the estimated distribution for 200 seconds, twice the length of the original. The triangle indicates the mean of the distribution. The curves are bootstrap replicates of the estimated distribution of the maximum and illustrate the uncertainty in the estimated distribution of the peak. The line surrounding the triangle is an 80% confidence interval (CI) for the mean of the distribution.

DATABASE-ASSISTED DESIGN AND ITS APPLICATION IN STRUCTURAL ENGINEERING PRACTICE

Estimates of wind effects on buildings by database-assisted design (DAD) methods can be far more accurate than those based on the reductive information available in standards. An upgraded version of DAD was developed that streamlines the

wind and structural engineering components of the design process via the direct computation of demand-to-capacity Indexes (DCIs, i.e., left-hand sides of design interaction equations). The computation achieves the rigorous combination of imperfectly correlated time series of wind forces and effects, thus eliminating errors due to subjective estimates of combined effects. This approach is applicable to any rigid or flexible building (Simiu and Yeo 2015). It allows the structural engineer to control all phases of the design, including the dynamic analysis, and the computation of global and internal forces and of the requisite DCIs; the wind engineer participates in the preliminary design, and produces the requisite wind speed and aerodynamic data.

NIST's DAD work on rigid buildings has focused on simple buildings with gable roofs, portal frames, and bracing parallel to the ridge (Habte et al. 2017). Useful features of this work include (i) the capability to use the two largest building aerodynamics databases available worldwide, (ii) the use of large simulated extreme wind speed databases, (iii) a novel interpolation scheme that allows the design of buildings with dimensions not represented in the databases. One important limitation for any interpolation procedure is that the roof slopes being considered should not correspond to qualitatively different aerodynamic behaviors, which would be the case if one of the slopes is less than, while the other slope exceeded, approximately 22°, or if one of the slopes is less than, while the other slope exceeded 39° (Stathopoulos 2013, personal communication). For details, see Habte et al. 2017, (iv) an effective multiple-points-in-time algorithm for estimating peaks, (v) parameter-free methods for estimating DCIs with specified MRIs, and (vi) accounting for P-delta effects (Coffman et al. 2010, Habte et al. 2017). The results obtained confirm (i) the published results showing that the ASCE 7-10 envelope procedure can significantly underestimate wind effects, (ii) the mutual consistency of the two aerodynamic databases being used, and (iii) DAD's potential for practical use. Updated software is being developed for flexible structures, for which dynamic analyses are performed by the structural engineer using inputs based on actual member sizes as determined from wind speed and aerodynamic pressure data. For rigid buildings the software developed for the implementation of the procedure and a user's manual are available in NIST (2004) and in Habte et al. (2016), respectively.

Figure 4 shows the peak DCI associated with axial force and bending moment for a frame column as a function of wind speed and direction. Such plots, used in conjunction with the matrix of simulated peak directional wind speeds in a large number of storm events yield, via non-parametric statistics, DCIs with any design MRI. If, for any cross section, the DCI differs significantly from unity, the procedure is iterated until that cross section is sized appropriately.

Examples of interpolation results are shown in Figure 5. Note that, even if the results of the interpolations are in error by, say, 10% or even 15%, the consequent global errors in the design values are considerably smaller, as shown by the results on the estimation of wind load factors (Simiu et al. 2017b).

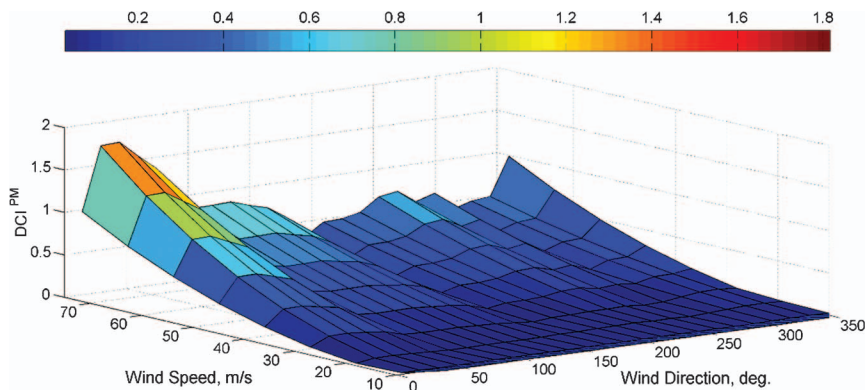


Figure 4. DCI plot as function of wind speed and direction

Source: [Habte et al. \(2016\)](#).

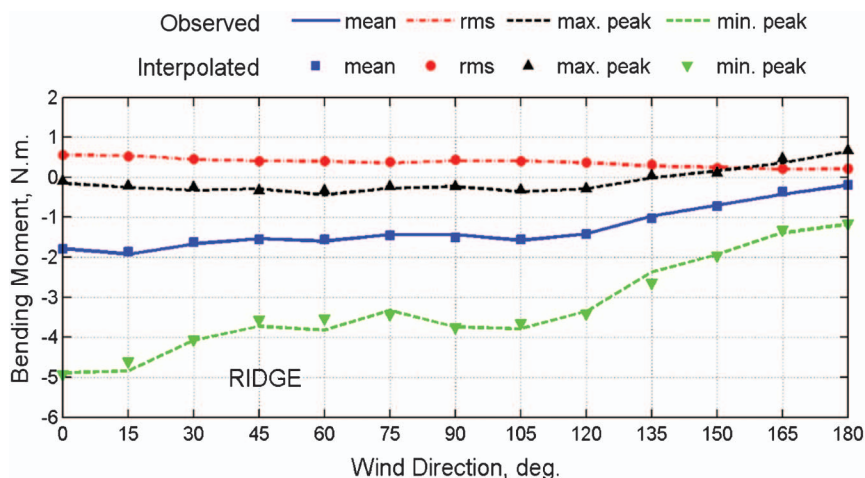


Figure 5. Measured and interpolated values of bending moment at ridge

Source: [Habte et al. \(2016\)](#).

CODIFICATION OF PRESSURES ON COMPONENTS AND CLADDING

Current ASCE 7-10 (2010) specifications of wind pressures on low-rise buildings are based on data that are in some cases thirty to forty years old. Advances in computer technology currently allow simultaneous recording of as many as hundreds of pressure taps. Also, wind tunnel test measurements are now available for many building geometries. The NIST/UWO database ([NIST 2004](#)) and the Tokyo Polytechnic University (TPU) database ([Tamura 2012](#)) are the most referenced databases.

Duthinh et al. (2015, 2017) establish a clear and reproducible methodology for using the NIST-UWO database, to calculate peaks of wind pressure over different size areas of building surfaces. This is an essential component to updating wind pressure coefficients for components and cladding and for eliminating deficiencies in the current wind load specifications.

The time series of the aerodynamic force is obtained by summing up the product of pressure time series measured in wind tunnel tests at adjoining pressure taps by their respective tributary areas or cells. Cell boundaries are straight lines equidistant to adjacent taps, but the taps are at the center of cells only in a regular grid. This summation is carried out for *all* combinations of tributary areas that make up rectangular areas, and is simplest when the grid of taps is regular. Special consideration must be given to the study zone edges and corners, which generally do not coincide with cell boundaries, and to the places where grids of different densities merge.

To limit the number of combinations for large zones of interest, and not to lose any data (as some of the cells along the long edges of roofs have an aspect ratio of 3.5), the aspect ratio of the rectangles formed by the aggregation of cells is limited not to exceed four. This aspect ratio covers many practical units of components and cladding, and allows consideration of long, narrow zones along the edges of roofs and walls. This choice also covers all “effective wind areas used to evaluate (GC_p)”, whose width, according to the Commentary of ASCE 7-10, “need not be taken as less than one-third of the length of the area. This increase in effective wind area has the effect of reducing the average wind pressure acting on the component.”

Note that there are two consecutive steps in the selection of the peak wind pressures for design purposes: selection of peaks over time, and selection of peaks over all wind directions. The selection of the peaks over all wind directions is inherent in the envelope method, as defined in the ASCE 7 Standard. Finally, the peaks corresponding to the most unfavorable combination of cells forming various areas are chosen for the development of design specifications.

An alternative method of area averaging of pressures measured by irregularly spaced taps was developed by Gierson et al. (2015, 2017). In this method, the assignment of tributary areas uses [Voronoi \(1908\)](#) diagrams, which in turn can be derived from [Delaunay \(1934\)](#) triangulation. Delaunay triangulation consists in connecting a set of taps by straight lines forming triangles that (1) do not overlap, (2) cover the entire interior space formed by the taps, and (3) do not have any taps within a triangle's circumcircle. A Voronoi diagram is created by drawing perpendicular bisectors to the previously generated lines. Regions formed by these bisectors contain one tap each, and bound the area that is closer to that tap than to any other tap. A [MATLAB \(2014\)](#) function used to automate this procedure is able to generate both Delaunay triangulation and Voronoi diagrams from an arbitrary set of Cartesian coordinates. In this application, the Cartesian coordinates are selected as pressure tap locations on a flattened representation of the building. This method provides a general, automated means to assign tributary areas to irregularly spaced taps.

Next in this alternative method, a grid consisting of identical rectangles is superposed on a flattened representation of the building enclosure. Grids of various size are placed at various offsets with respect to the pressure taps, and the wind tunnel pressure time series are area-averaged from their tributary areas into the corresponding grid areas using Boolean algebra. The two methods produce comparable results for the same data set (Figure 6 shows a limited comparison) and when applied to the UWO and the TPU databases respectively.

Results reported in Duthinh et al. (2015, 2017) and in Gierson et al. (2015, 2017) show significant underestimation of wind pressure coefficients by ASCE 7-10 (2010) for the roofs and walls of low-rise buildings. Possible reasons for the underestimation include the fact that wind tunnel tests from four or five decades ago used many fewer pressure taps than nowadays, and even fewer taps could be read simultaneously, given the technology available at the time. Future work includes the validation of these conclusions by alternative methods for the estimation of peaks (see section Estimation of non-Gaussian time series peaks using the two-dimensional Poisson process as a peaks-over-threshold model above). All buildings in the NIST-UWO database are being investigated, together with those in other publicly available databases such as the TPU. Only at the conclusion of the study can more definitive recommendations be made, including

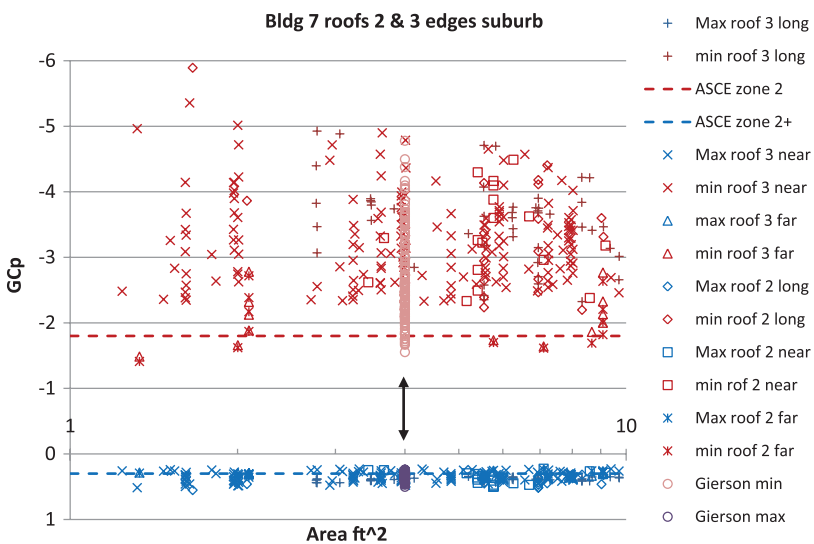


Figure 6. Pressure coefficients for UWO Bldg 7 [40 ft (12 m) wide, 62.5 ft (19 m) long, 40 ft high (12 m, eave height), roof slope of 1:12 (4.8°)] in suburban terrain exposure. The two halves of the gable roof are denoted as roofs 2 and 3.

The symbols correspond to various edge zones defined as zones 2 in ASCE 7-10 Fig. 30.4-2A. Gierson's results (circles pointed at by double arrows) are shown for 4 ft² for the case of no grid offset ($1 \text{ ft}^2 = 0.0929 \text{ m}^2$)

Source: Duthinh et al. (2017).

possibly changes in the number, size, shape and location of the various wind pressure zones, together with their associated pressure coefficients.

MODERN PLANETARY BOUNDARY LAYER MODELING AND ITS IMPLICATIONS FOR ASCE 7-10 PROVISIONS ON SUPER-TALL BUILDING DESIGN

In the ASCE 7-10 Standard (2010) the wind speeds in the Planetary Boundary Layer (PBL) are modeled by strictly empirical power laws developed mostly in the 1960s. In these models, wind speeds increase monotonically within the boundary layer up to the gradient height z_g (a term applied in the Standard to both cyclostrophic and geostrophic conditions), specified to be 200 to 250 m for water surface exposure, 300 to 350 m for open terrain exposure, and 400–450 m for suburban terrain exposure; for elevations $z \geq z_g$ the wind speed is assumed to be constant and equal to the gradient speed. However, in the 1990s and subsequent years, theory supported by PBL flow measurements and Computational Fluid Dynamics (CFD) Direct Numerical Simulation, established the role played by the free flow in determining the PBL characteristics and developed realistic PBL models that are significantly different from ASCE 7-10 models.

As shown by [Zilitinkevich and Esau \(2002\)](#) among others, neutrally stratified flows can be either of the “truly neutral” or the “conventionally neutral” type. “Truly neutral” flows are characterized by a Kazanski-Monin surface buoyancy flux parameter $\mu_b = 0$ and the number $\mu_N = N/|f| = 0$, where N is the Brunt-Väisälä frequency and f is the Coriolis parameter. [Zilitinkevich and Esau \(2002\)](#) note that “truly neutral flows are observed during short transition periods after sunset on a background of residual layers of convective origin,” “are often treated as irrelevant because of their transitional nature, and are usually excluded from data analysis;” “neutrally stratified PBLs are almost always ‘conventionally neutral,’ that is, neutral *and* developing against a background stable stratification; they have parameters $\mu_b = 0$, $\mu_N \neq 0$; typically, $50 < \mu_N < 300$. [Simiu et al. \(2016\)](#) showed that at mid-latitudes, for heights of up to a few kilometers, (i) the mean velocities $U(z)$ (parallel to the friction velocity) increase monotonically with height, (ii) the velocities $V(z)$ (normal to the friction velocity), and the veering angles, are negligibly small for buildings with height $h < 1$ km, and (iii) the mean wind profile can be described by the log law up to elevations that, for the strong wind speeds of interest in structural design, far exceed those indicated in ASCE 49-12 Standard (2012). For further details, see [Simiu et al. \(2017a, Figure 6\)](#).

Since PBL heights are considerably greater than the ASCE 7-10 gradient heights z_g , for $h > z_g$ the PBL model inherent in the Standard is not appropriate. To eliminate the possibility of unconservative designs, the Standard must explicitly provide for an exception to its definition of gradient heights by specifying that the increase of mean wind speeds with height for elevations $z > z_g$ be taken into

account for buildings with height $h > z_g$. For example, considering a building with height $h = 10$ m and 71.6 m \times 71.6 m in plan (Baker et al. 2000), it is assumed that the terrain exposure is suburban, with roughness length $z_0 = 0.3$ m; the natural frequency of vibration and the damping ratio in the fundamental mode are 0.1 Hz and 0.02 , respectively; and the mean hourly wind at 10 m above ground in open terrain is 35 m s $^{-1}$. The mean hourly wind speed at 10 m above ground over suburban terrain is then estimated to be $U(10\text{ m}) \approx 29$ m s $^{-1}$. According to the ASCE 7-10 (2010) Standard, the PBL height is $z_g = 366$ m, meaning that, for elevations $z > z_g = 366$ m $= 0.6h$, $U(z) \equiv U(0.6h)$ and the turbulence intensity vanishes. Calculations of along-wind response then yield a deflection at the top of the building $\delta(h) = 1.05$ m. On the other hand, if it is assumed that the contemporary PBL model is valid, the calculated peak deflection is $\delta(h) = 1.61$ m. The difference between the two results is due to the fact that in contemporary PBL modeling, mean speeds increase, and the flow is turbulent, up to $z > h = 610$ m $> z_g = 366$ m.

ASCE 7-10 (2010) Section 31.4.3 applied to buildings states: “Loads for the main wind force resisting system determined by wind tunnel testing shall be limited such that the overall principal loads in the x and y directions are not less than 80% of those that would be obtained from Part I of Chapter 27 . . . The overall principal load shall be based on the overturning moment for flexible buildings . . .” Since in the example above $h > z_g$, this means that, according to the Standard, the design overturning moment shall not be less than 80% of its calculated value corresponding to the deflection $\delta(h) = 1.05$ m, i.e., to the design overturning moment based on Table 26.9-1. However, this deflection would be an artifact of the unrealistic ASCE 7-10 specifications. In fact, since the PBL height exceeds the height $h = 610$ m, the intent of the ASCE 7-10 Section 31.4.3 would be satisfied if the overturning moment used in design was greater than 80% of the larger overturning moment consistent with a peak deflection $\delta(h) = 1.61$ m, rather than with the smaller value $\delta(h) = 1.05$ m obtained by using the low gradient height specified in ASCE 7-10 Table 26.9-1. We assumed that the tall building may be affected aerodynamically by neighboring structures (as was the case, for example, for the WTC twin towers or the Petronas towers in Kuala Lumpur).

COMPUTATIONAL WIND ENGINEERING

NIST is currently engaged in an effort to develop CFD algorithms for use in structural engineering. As part of that effort, the authors performed three-dimensional simulations of turbulent Atmospheric Boundary Layer (ABL) flows over open terrain and of flow past a square cylinder, and are assessing the quality of the simulated flows from a wind/structural engineer’s viewpoint.

Comparative study of subgrid-scale models in wall-bounded flow. Subgrid-scale (SGS) models are required in large-eddy simulations (LES) of turbulent

flows. We conducted a comparative study of different SGS models, including kEqn (k -equation eddy viscosity, Yoshizawa 1985), WALE (Wall-adapting local eddy-viscosity, Nicoud and Ducros 1999), Sigma (Nicoud et al. 2011) and CSGS (Constrained SGS, Chen et al. 2012) models to investigate their performance in wall-bounded flow. The flow considered in the study has the advantages of being well-documented and validated in the fluid dynamics literature and of being similar to atmospheric boundary layer flow near a wall. Wall-resolved LES simulations of channel flows were performed at Reynolds number $Re_\tau = 395$. The simulations showed that the sensitivity of the results to the SGS model is greatest in the buffer sublayer. From a benchmark DNS (Direct Numerical Simulation) result (Moser et al. 1999), it was found that the WALE and Sigma models perform better in profile that agrees with the DNS results to within about 5%. A remarkably close match is found in the viscous sublayer for all models. In the logarithmic sublayer and outer layer, all profiles the simulation of the fluctuations, while the CSGS model achieves the best mean velocity profile. The SGS dissipation influences strongly the velocity fluctuations but has little effect on the mean flow and the log-layer mismatch. As shown in Figure 7, all SGS models achieve a mean-velocity display the log-layer mismatch problem. However, in the buffer sublayer, where turbulence flow is the most intense, the simulated flows show the highest deviations from SGS models used in this study.

Large-eddy simulations of atmospheric boundary-layer (ABL) turbulence. We performed large-eddy simulations of model-scaled neutrally stratified ABL flows. The kEqn model was employed for the SGS motions, and a wall shear model (Schumann 1975) was applied on the ground. The mean streamwise velocity

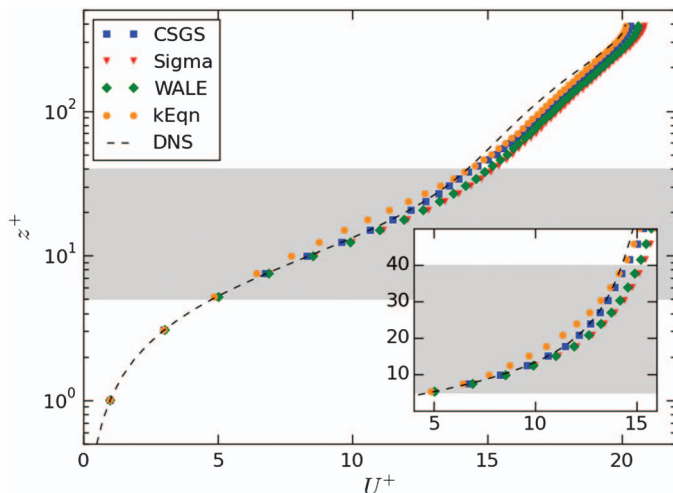


Figure 7. Profiles of the mean streamwise velocity in wall units ($U^+ = U/u_*$, $z^+ = zu_*/\nu$) for different models. Dashed line: DNS data. The shaded region is the buffer sublayer. The inset is a magnified plot of the buffer layer
Source: Shi (2017).

profile is approximately logarithmic, yet near the ground the log-layer mismatch persists. The second and third moments of the turbulence represent well the underlying physics. The SGS dissipation agrees well with the analytical counterpart from the theory. The spatial spectra follow well the $-5/3$ power law at large wavenumbers. The spatial coherences decay exponentially as functions of reduced frequencies. Except for a well-known problem of the log-layer mismatch (i.e., the mean velocity near the ground), the turbulence statistics can be simulated adequately by LES using simple SGS and wall models. Figure 8 shows that the simulation represents adequately convective ABL flow contributing to the vertical turbulent energy transport.

URANS and hybrid LES/RANS simulations of flow over a bluff-body.

Simulations of flow past a square cylinder were performed by using URANS (Unsteady Reynolds-Average Navier-Stokes) and Hybrid LES/RANS based IDDES (Improved Delayed Detach Eddy Simulation, [Shur et al. 2008](#)) and the Giesecking blending function ([Giesecking et al. 2011](#)) simulations to numerically investigate the velocity field around, and pressures distribution and forces over a square cylinder immersed in a uniform, smooth oncoming flow with Reynolds number $Re = 21400$ ([Ke and Yeo 2016](#)). The vortex shedding responses in terms of Strouhal number, the pressure distribution, the velocity profile and the velocity fluctuations obtained by numerical simulations were compared with experimental data ([Bearman and Obasaju 1982](#), [Lyn et al. 1995](#), [Nishimura and Taniike 2000](#), [Noda and Nakayama 2003](#)). Both URANS and IDDES simulations accurately predict the vortex shedding frequency and the velocity field upwind of the wake region. The study ([Ke and Yeo 2016](#)) shows that the finest spanwise

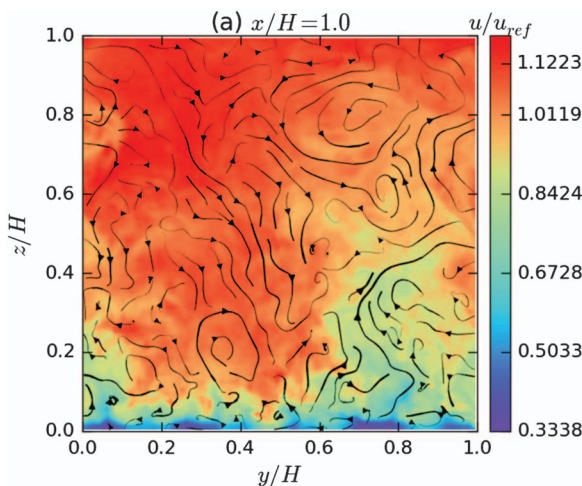


Figure 8. Contours of the normalized streamwise x -velocity in a vertical yz -cross section. The black lines are streamlines of (v, w) , with the line width coded by its magnitude

Source: [Shi and Yeo \(2017\)](#).

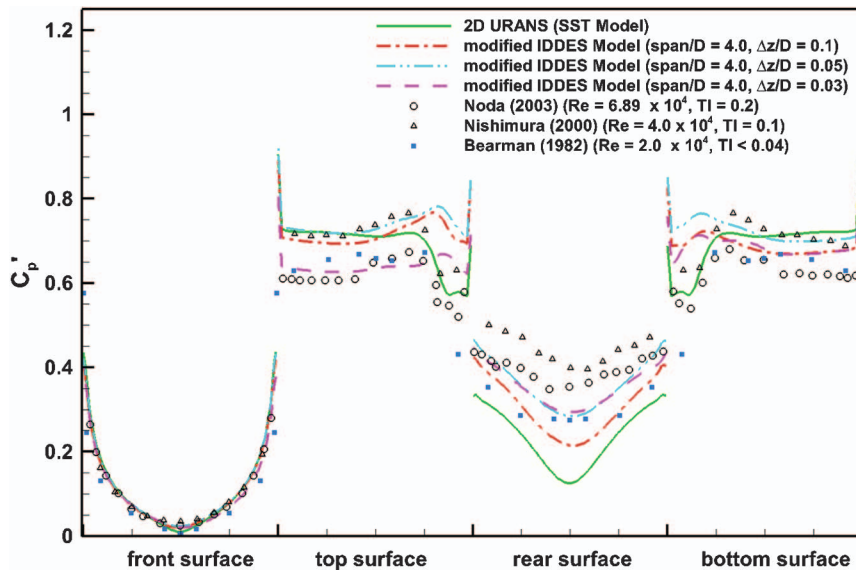


Figure 9. RMS pressure coefficients. Similar results were obtained for mean pressures

Source: Ke and Yeo (2016).

grids do not necessarily produce the most reliable results. Rather, if a spanwise cell spacing is appropriately chosen (e.g., $H/24$ in this study where H is the dimension of the square cross-section), the IDDES model reasonably predicts the wake region flow (in terms of pressure coefficient distribution, streamwise and cross-stream velocity profiles and *rms* (root mean square) velocity fluctuations), while URANS is less effective in predicting pressures on the rear surface near the wake (Figure 9).

TORNADO HAZARD MAPPING AND TORNADO-RESISTANT DESIGN

Even though the United States experiences more than 1,200 tornadoes annually, and tornadoes have caused more fatalities per year than hurricanes and earthquakes combined (since the beginning of official tornado record in 1950), building codes, standards and practices do not require conventional buildings to be designed for tornado hazards except for storm shelters¹, safe rooms², and the safety-related

¹Buildings, structures, or portions thereof, constructed in accordance with the ICC 500 Standard.

²A storm shelter specifically designed to meet FEMA safe room recommended criteria as provided in FEMA P-320 or P-FEMA 361.

structures, systems, and components³ of nuclear power plants. Based on findings from its technical investigation of the deadly 2011 tornado in Joplin, Missouri, NIST “recommends that nationally accepted performance-based standards for the tornado-resistant design of buildings and infrastructure be developed and adopted in model codes and local regulations to enhance the resiliency of communities to tornado hazards. The standards should encompass tornado hazard characterization, performance objectives, and evaluation tools” (Kuligowski et al. 2014). Toward that end, NIST is also working to develop a new generation of tornado hazard maps, which will underpin a planned national performance-based design standard for tornadoes (Phan et al. 2016).

A major challenge in developing accurate tornado hazard maps is understanding the limitations and biases in the tornado databases maintained by the National Weather Service (NWS), which go back to 1950. Changes over time in weather observing technology, communications technology, information technology, tornado science, NWS tornado rating and reporting practices, and many other factors complicate the analysis of the available tornado climate data. One element of this challenge is the so-called population bias, where tornadoes are under-reported in areas with smaller populations, where they are less likely to be observed or are classified as less intense than they really are. This is because observed damage to structures is the primary means for assigning tornado intensity ratings. Under-classification was documented for 51 Midwest super-cell tornadoes by Alexander (2010), who compared F (Fujita) or EF (Enhanced Fujita) ratings (a) assigned by the NWS based on observed damage, and (b) developed from mobile radar measurements (Figure 10). According to the measurements 82% were strong or violent tornadoes (EF2-EF5), whereas 69% of the same set of 51 tornadoes were rated and recorded by the NWS as weak (EF0-EF1).

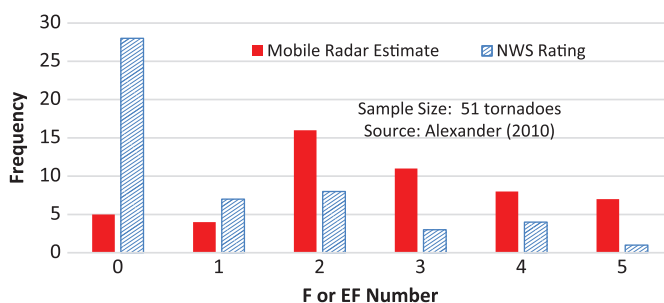


Figure 10. Comparison of F/Ef Tornado Ratings Estimated by Mobile Radar and Damage

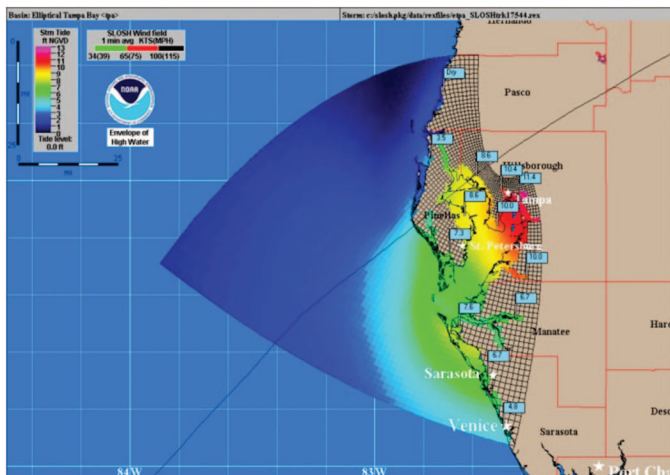
Source: [Alexander \(2010\)](#).

³As defined by U.S. Nuclear Regulatory Commission/Regulatory Guide 1.117, *Tornado Design Classification*.

Systematic empirical and modeling studies are currently underway to quantify the population bias. Preliminary results from a geospatial analysis of tornado data from 1995 to 2005 ([Phan et al. 2016](#)) indicate that in rural areas where the average building density is only a few buildings per square kilometer, which characterizes much of the most tornado-prone US including the Great Plains, Midwest, and Southeast, the observed rate of tornado occurrence may be as much as an order of magnitude smaller than in more densely populated areas. A complementary modeling study is also being conducted, where simulated tornadoes are passed over grids of different spacing, with each grid point representing the location of a hypothetical building or other damage indicator. Early results from this modeling approach are consistent with observations from the empirical study and from the mobile radar climatology ([Alexander 2010](#)), indicating that many tornadoes in rural areas have not been detected and included in the database, and many tornadoes in the database have been rated as less intense than they really were.

JOINT WIND, STORM SURGE, AND WAVES HAZARDS AND COMBINED EFFECTS

Hurricanes, which produce strong wind, storm surge, and waves, wreak havoc on the lives and infrastructure of coastal communities. Of these hurricane hazards, storm surge – a local rise in sea elevation – is perhaps the most devastating element. Storm surge depends on the tidal stage, barometric pressure, Coriolis effect, wind stress, and wave forcing, and is strongly influenced by the local topography and bathymetry. Thus, designing for the effects of the combined hurricane wind, storm surge, and wave hazards requires a multi-hazard approach that can account for their combined effects and the influence of local topography and bathymetry. NIST developed methodologies for (1) computing the joint probability of wind speeds and storm surge heights, with consideration of site specificity ([Phan et al. 2007, 2011](#)), and (2) integrating the Simulating Waves Nearshore (SWAN) third-generation wave model into the Sea, Lake, and Overland Surges from Hurricane (SLOSH) model ([Phan et al. 2010](#)). Briefly, the methodology for computing the joint probability of wind speeds and storm surge heights calls for (1) mass hydrodynamic simulations using SLOSH for the “basin” of interest (Figure 11 shows a typical SLOSH simulation); (2) the development of joint histograms of wind speeds and storm surge heights that result from the mass hydrodynamic simulations (Figure 12 shows the joint histogram of peak wind speed/storm surge height at the Port of Tampa); (3) the computation of the joint probability of wind speed/storm surge height exceedance from the joint histogram (Figure 13), and (4) the mean recurrence intervals of joint hurricane wind speed/storm surge events for the site of interest as the inverse of the bivariate joint annual probability of exceedance for the site.



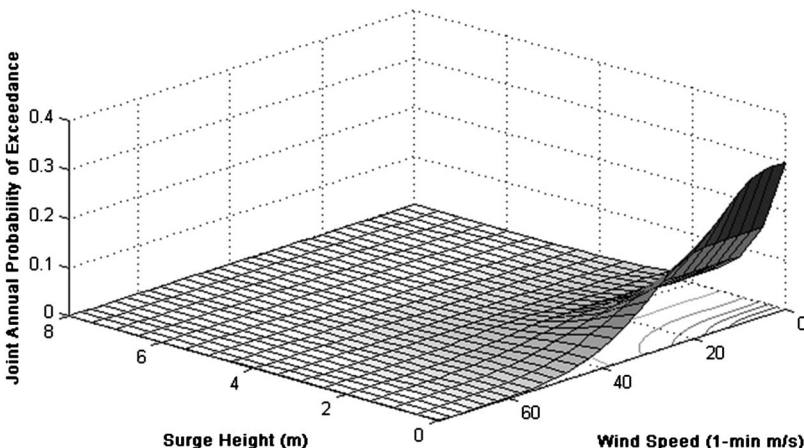


Figure 13. Joint probability of exceedance for the Port of Tampa site

Source: [Phan et al. \(2007\)](#).

1. Calculate the combined scalar effects σ_{ij} of the directional wind speeds v_{ij} and corresponding storm surges s_{ij} for all i, j with $i = 1, 2, \dots, n$, n = number of simulated hurricanes used in the calculations, $j = 1, 2, \dots, m$, and m is the number of wind speed directions considered (e.g., $m = 16$). The combined effect could be the maximum stress in a member under gravity, wind and storm surge, or the left-hand side of the interaction equation for members subjected to combined axial load and bending; or the aggregate loss of electrical power in a specified region due to damage to overhead power lines induced by wind and damage to underground cables caused by seepage of water following a storm surge and the consequent flooding.
2. Perform a probabilistic analysis of the univariate time series σ_i similar to the analysis applied to hurricane wind effects representing the maximum of the directional effects in each of a number n of simulated hurricanes (see [Phan and Simiu, 2011](#)). This analysis can yield effects σ_N corresponding to any specified mean recurrence interval N .
3. For a design to be acceptable σ_N must be less than the corresponding specified limit state associated with the mean recurrence interval N .

SUMMARY AND CONCLUSIONS

A brief review was presented of recent and current NIST research on wind effects on structures, aimed to improve and modernize current standard provisions and design practices, and achieve a more resilient built environment in regions subjected to significant wind loads. The review covered research on: the development of the

contiguous US wind maps included in the ASCE 7-16 Standard to replace earlier maps according to which the extreme wind climate is the same throughout most of the US territory; the development of wind load factors for use in the wind tunnel procedure, and the need to change the ISO 80% percentage point for the design peak pressure coefficients by a 57% percentage point; the estimation on non-Gaussian peaks using the peaks-over-threshold two-dimensional Poisson process; the codification of pressures on components and cladding; the development of Computational Wind Engineering algorithms aimed to achieve numerical tools for use in structural engineering practice within the next decade; progress in tornado hazard mapping and tornado resistant design; and joint wind, storm surge, and wave hazards and their combined effects on structures.

The recent and current wind engineering work summarized herein is part of an effort anticipated to be of the order of ten years, aimed at improving the resilience of the built environment in the United States through retrofitting and design practices and to achieve more economical as well as safer structures subjected to windstorms, including loads due to tornadoes, storm surge and waves. Tools being developed for this purpose include Computational Fluid Dynamics methods and Database-assisted Design. In addition to the research described here to better understand US tornado climatology, being conducted to support development of new tornado hazard maps and performance-based design methods and standards for tornado hazards, NIST is also working to improve future tornado data collection and climatology. In collaboration with NOAA, NIST is leading development of a new ASCE standard on tornado wind speed estimation. The standard will incorporate major improvements to the EF scale and address other damage-based methods for estimating wind speeds, including forensic engineering and treefall pattern analysis as well as methods using measurements during the tornado, including in situ (anemometry) and remotely sensed (radar) data.

References

- Alexander, C. 2010. "A mobile radar based climatology of Supercell Tornado structures and dynamics." Ph.D. dissertation, Univ. of Oklahoma.
- ASCE. 2010. *Minimum design loads for buildings and other structures*. ASCE/SEI 7-10. Reston, VA: ASCE.
- ASCE. 2012. *Wind tunnel testing of buildings and other structures*. ASCE 49-12. Reston, VA: ASCE.
- Baker, W., R. Sinn, I. Novak, and J. Viise. 2000. "Structural optimization of 2000-foot Tall 7 South Dearborn Building." In *Advanced technologies in structural engineering*. Reston, VA: ASCE.
- Bearman, P. W., and E. D. Obasaju. 1982. "An experimental study of pressure fluctuations on fixed and oscillating square-section cylinders." *J. Fluid Mech.* **119**: 297–321.
- Chen, S., Z. Xia, S. Pei, J. Wang, Y. Yang, Z. Xiao, and Y. Shi. 2012. "Reynolds-stress-constrained large-eddy simulation of wall-bounded turbulent flows." *J. Fluid Mech.* **703**: 1–28.
- Cleveland, W. S., and S. J. Devlin. 1988. "Locally weighted regression: An approach to regression analysis by local fitting." *J. Am. Stat. Assoc.* **83** (403): 596–610.

- Coffman, B. F., J. A. Main, D. Duthinh, and E. Simiu. 2010. "Wind effects on low-rise buildings: Database-assisted design vs. ASCE 7-05 standard estimates." *J. Struct. Eng.* **136** (6): 744–748.
- Delaunay, B. 1934. "On the empty sphere." In Vol. 6 of *Memory of Georges Voronoi: Bulletin of the USSR Academy of Sciences, section: Mathematics and natural sciences*, 793–800.
- Duthinh, D., J. A. Main, M. L. Gierson, and B. M. Phillips. 2017. "Analysis of wind pressure data on components and cladding of low-rise buildings." *ASCE-ASME J. Risk Uncertainty Eng. Syst. Part A Civil Eng.* **4** (1): 04017032.
- Duthinh, D., J. A. Main, and B. M. Phillips. 2015. "Methodology to analyze wind pressure data on components and cladding of low-rise buildings." National Institute of Standards and Technology Technical Note 1903, Gaithersburg, MD. <http://nvlpubs.nist.gov/nistpubs/TechnicalNotes/NIST.TN.1903.pdf>.
- Duthinh, D., A. L. Pintar, and E. Simiu. 2017. "Estimating peaks of stationary random processes: A peaks-over-threshold approach." *ASCE-ASME J. Risk Uncertainty Eng. Syst. Part A Civil Eng.* **3** (4): 04017028.
- Ellingwood, B., T. V. Galambos, J. G. MacGregor, and C. A. Cornell. 1980. *Development of a probability based load criterion for American National Standard A58*. NBS Special Publication 577. Washington, DC: National Bureau of Standards.
- Gavanski, E., K. R. Gurley, and G. A. Kopp. 2016. "Uncertainties in the estimation of local peak pressures on low-rise buildings by using the Gumbel distribution fitting approach." *J. Struct. Eng.* **142** (11): 04016106.
- Gierson, M. L., B. M. Phillips, and D. Duthinh. 2015. "Evaluation of ASCE 7-10 wind velocity pressure coefficients on the components and cladding of low-rise buildings using recent wind tunnel testing data." In *6th Int. Conf. on Advances in Experimental Structural Engineering*. Urbana, IL.
- Gierson, M. L., B. M. Phillips, D. Duthinh, and B. M. Ayyub. 2017. "Evaluation of wind pressure coefficients on low-rise building enclosures using modern wind tunnel data." *ASCE-ASME J. Risk Uncertainty Eng. Syst.* **3** (4): 04017010.
- Gieseking, D. A., J. I. Choi, J. R. Edwards, and H. A. Hassan. 2011. "Compressible-flow simulations using a new large-eddy simulation/reynolds-averaged Navier-Stokes Model." *AIAA J.* **49** (10): 2194–2209.
- Habte, F., A. G. Chowdhury, and S. Park. 2016. "The use of demand-to-capacity indexes for the iterative design of rigid structures for wind," NIST Technical Note 1908, NIST. <http://nvlpubs.nist.gov/nistpubs/TechnicalNotes/NIST.TN.1908.pdf>.
- Habte, F., A. G. Chowdhury, D. Yeo, and E. Simiu. 2017. "Design of rigid structures for wind using time series of demand-to-capacity indexes: Application to portal frames." *Eng. Struct.* **132**: 428–442.
- ISO. 2009. *Wind actions on structures*. ISO 4354. Geneva: ISO.
- Ke, J., and D. Yeo. 2016. "RANS and hybrid LES/RANS simulations of flow over a square cylinder." In *8th Int. Colloquium on Bluff Body Aerodynamic and Applications (BBA VIII)*. Boston, MA: Northeastern Univ.
- Kuligowski, E., F. Lombardo, L. Phan, M. Levitan, and D. Jorgensen. 2014. "Final report: National Institute of Standards and Technology (NIST) Technical investigation of the May 22, 2011, Tornado in Joplin, Missouri." NCSTAR 3, NIST, Gaithersburg, MD. Accessed April 09, 2016. <http://nvlpubs.nist.gov/nistpubs/NCSTAR/NIST.NCSTAR.3.pdf>.
- Lyn, D. A., S. Einav, W. Rodi, and J. H. Park. 1995. "A laser-Doppler velocimetry study of ensemble-averaged characteristics of the turbulent near wake of a square cylinder." *J. Fluid Mech.* **304**: 285–319.

- Main, J. A. 2011. "Special-purpose software: MATLAB functions for estimation of peaks from time series." www.itl.nist.gov/div898/winds/homepage.htm.
- MATLAB. 2014. *MATLAB documentation 2014b*. Natick, MA: Mathworks.
- Moser, R. D., J. Kim, and N. N. Mansour. 1999. "Direct numerical simulation of turbulent channel flow up to $Re_\tau = 590$." *Phys. Fluids* **11** (4): 943–945.
- Nicoud, F., and F. Ducros. 1999. "Subgrid-scale stress modelling based on the square of the velocity gradient tensor." *Flow Turbul. Combust.* **62** (3): 183–200.
- Nicoud, F., H. B. Toda, O. Cabrit, S. Bose, and J. Lee. 2011. "Using singular values to build a subgrid-scale model for large eddy simulations." *Phys. Fluids* **23** (8): 085106.
- Nishimura, H., and Y. Taniike. 2000. "Fluctuating wind forces on a stationary two-dimensional square prism," In *16th Wind Engineering Symp.*, 255–260, Tokyo.
- NIST. 2004. "Extreme winds and wind effects on structures," Accessed April 09, 2015. www.itl.nist.gov/div898/winds/homepage.htm.
- NIST. 2011. "Status of NIST's recommendations following the federal building and fire investigation of the world trade center disaster." Accessed August 28, 2017. <https://www.nist.gov/sites/default/files/documents/el/disasterstudies/wtc/WTCRecommendationsStatusTable.pdf>.
- NIST. 2014. "Measurement science R&D Roadmap for windstorm and coastal inundation impact reduction." NIST GCR 14-973-13. http://ws680.nist.gov/publication/get_pdf.cfm?pub_id=915541.
- Noda, H., and A. Nakayama. 2003. "Free-stream turbulence effects on the instantaneous pressure and forces on cylinders of rectangular cross section." *Exp. Fluids* **34** (3): 32–344.
- Phan, L., M. Faletra, M. Levitan, E. Kuligowski, and D. Jorgensen. 2016. "Progress on implementation of the Joplin Tornado recommendation." NIST, Gaithersburg, MD. https://www.nist.gov/sites/default/files/documents/el/disasterstudies/ncst/01_Progress-on-Implementation-of-the-Joplin-Tornado-Recommendations_May.pdf.
- Phan, L. T., and E. Simiu. 2011. "Estimation of risk for design of structures exposed to combined effects of hurricane wind speed and storm surge hazards." In *Applications of statistics and probability in civil engineering*, edited by M. H. Faber, J. Köhler, and K. Nishijima. London: Taylor & Francis Group.
- Phan, L. T., E. Simiu, M. A. McInerney, A. A. Taylor, and R. Glahn. 2007. *Methodology for development of design criteria for joint hurricane wind speed and storm surge events: Proof of concept*. NIST Technical note 1482. Gaithersburg, MD: NIST.
- Phan, L. T., D. Slinn, and S. Kline. 2010. *Introduction of wave set-up effects and mass flux to the sea, lake, and overland surges from hurricanes (SLOSH) model*. NISTIR 7689.
- Pintar, A. L., E. Simiu, F. T. Lombardo, and L. Levitan. 2015. "Maps of Non-hurricane Nontornadic Wind Speeds with Specified Mean Recurrence Intervals." NIST Special Publication 500-301. <http://nvlpubs.nist.gov/nistpubs/SpecialPublications/NIST.SP.500-301.pdf>.
- Schumann, U. 1975. "Subgrid scale model for finite difference simulations of turbulent flows in plane channels and annuli." *J. Comput. Phys.* **18** (4): 376–404.
- Shi, L. 2017. "A comparative study on subgrid scale models in channel flow." *J. Phys. Fluids*, in press.
- Shi, L., and D. Yeo. 2017. "Large eddy simulation of model scale turbulent atmospheric boundary layer flows." *J. Eng. Mech.* **143** (9): 06017011.
- Shur, M. L., P. Spalart, M. Strelets, and A. Travin. 2008. "A hybrid RANS-LES approach with delayed-DES and wall-modelled LES capabilities." *Int. J. Heat Fluid Flow* **29** (6): 1638–1649.
- Simiu, E. 2011. *Design of buildings for wind*. Hoboken, NJ: Wiley.

- Simiu, E., N. A. Heckert, and D. Yeo. 2017a. "Planetary boundary layer modeling and standard provisions for super-tall building design." *J. Struct. Eng.* **143** (8): 06017002.
- Simiu, E., A. L. Pintar, D. Duthinh, and D. Yeo. 2017b. "Wind load factors for use in the wind tunnel procedure." *ASCE-ASME J. Risk Uncertainty Eng. Syst. Part A: Civil Eng.* **3** (4): 04017007.
- Simiu, E., L. Shi, and D. Yeo. 2016. "Planetary boundary-layer modelling and tall building design." *Boundary Layer Meteorol.* **159** (1): 173–181.
- Simiu, E., and D. Yeo. 2015. "Advances in the design of high-rise structures by the wind tunnel procedure: Conceptual framework." *Wind Struct.* **21** (5): 489–503.
- Smith, R. L. 1989. "Extreme value analysis of environmental time series: An application to trend detection in ground-level ozone." *Stat. Sci.* **4** (4): 367–377.
- SOM (Skidmore Owings and Merrill LLP). 2004a. "Report on estimation of wind effects on the wtc towers, App. D." Accessed February 22, 2017. <http://wtc.nist.gov/NCSTAR1/NCSTAR1-2intex.htm>.
- SOM (Skidmore Owings and Merrill LLP). 2004b. "Report on estimation of wind effects on the wtc towers, App. D." Accessed February 22, 2017. <https://www.nist.gov/sites/default/files/documents/2017/05/09/WTCRecommendationsStatusTable.pdf>.
- Tamura, Y. 2012. "Aerodynamic database for low-rise buildings." Tokyo Polytechnic University. Accessed April 09, 2016. <http://wind.arch.t-kougei.ac.jp/system/eng/contents/code/tpu>.
- Voronoi, G. 1908. "New applications of continuous parameters to the theory of quadratic forms." *J. Pure Appl. Math.* **133**: 97–178.
- Yeo, D., and A. G. Chowdhury. 2013. "A simplified wind flow model for the estimation of aerodynamic effects on small structures." *J. Eng. Mech.* **139** (3): 367–375.
- Yoshizawa, A. 1985. "A statistically-derived subgrid-scale kinetic energy model for the large-eddy simulation of turbulent flows." *J. Phys. Soc. Jpn.* **54** (8): 2834–2839.
- Zilitinkevich, S. S., and I. Esau. 2002. "On integral measures of the neutral barotropic planetary boundary layer." *Boundary Layer Meteorol.* **104** (3): 371–379.

DISCLAIMERS

1. The policy of the NIST is to use the International System of Units (SI) in its technical communications. In this paper building codes and standards are referenced in both customary (as is the practice in US construction industry) and SI units.
2. Some commercial products are identified in this paper for traceability of results. This does not imply recommendation or endorsement by the NIST, nor does it imply that the identified products are necessarily the best available for the purpose.

CHAPTER 2

Investigation on a Generalized Intervention Cost Function to Examine Wind-Induced Damage on Tall Buildings

Luca Caracoglia, A.M. ASCE*

Abstract: This paper reviews and discusses some results on the simulation of the stochastic dynamics of a tall building, subjected to turbulent boundary layer wind loads. The stochastic model employs state augmentation. It includes a first zero-mean random variable (or state) representing either modeling simplifications or wind tunnel experimental errors, associated with the wind load estimation. A second zero-mean random variable is introduced to simulate the variability in the “intervention costs” needed to repair the wind-induced damage incurred by the building envelope. Two distinct scalar, generalized intervention cost functions are proposed: the first one depends on the squared value of the along-wind modal structural response; the second one also considers the influence of the cross-wind modal response on damage and the simultaneity of the response in the two directions. The model is recast into the formalism of stochastic differential equations. Parametric simulations examine the response of the CAARC (Commonwealth Advisory Aeronautical Research Council) benchmark building. The effect of static mean loads on the simulated damage and intervention cost simulations is also considered.

Keywords: Tall Buildings; Dynamic Response; Along-Wind Loading Uncertainty; Generalized Intervention Cost Model; Stochastic Differential Equations; Stochastic Linearization.

*Department of Civil and Environmental Engineering, Northeastern University, 400 SN, 360 Huntington Avenue, Boston, MA 02115-5000, USA; email: lucac@coe.neu.edu

INTRODUCTION

Renewed research interests, aiming at the implementation of rational methods for performance-based design of tall buildings against wind hazards, has been noted in the recent literature (Barbato et al. 2014; Barbato et al. 2013, Jain et al. 2001, Pozzuoli et al. 2013, Spence and Kareem 2014, Yeo and Simiu 2011). Additional review of the literature may also be found in Caracoglia (2016). Since many uncertainty sources are present, especially if examination of structural serviceability is considered, it is important to characterize the structural performance within a rigorous probabilistic setting.

This paper discusses the results of a study aiming at the analysis of tall building performance by directly incorporating information on wind loading uncertainty and intervention costs. Intervention costs can be described as the maintenance and repair costs needed due to damage caused by a high-speed boundary-layer wind event. The damage, observed in a tall building does not usually involve inelastic response of the main wind-force resisting system but it is often caused by exceedance of serviceability limit states (e.g., inter-story drift), which imply failures of non-structural elements on the building envelope. A turbulence-stationary boundary-layer wind model is used to simulate either a high-speed synoptic wind field or the fully developed stages of a hurricane wind (approximately).

The procedure for cost analysis is embedded into a time-domain reduced-order model of the building, which includes the fundamental along-wind and cross-wind lateral vibration modes. The model also simulates the generalized dynamic turbulent wind loads using quasi-steady theory. The cost model, examined in this study, is an extension of previous results (Caracoglia 2016), as it accounts for the combined effect of the along-wind and cross-wind dynamic response and includes the effect of the static wind load. The cost variable represents, in a cumulative and generalized form, the relative intervention cost normalized to the total construction cost of the structure (i.e., the value of the building). A power-law intervention cost equation utilizes, as the mechanism responsible for the generation of damage to non-structural elements, the dynamic lateral drift of the structure. One of the main features of the model is the simulation of the variability in the wind load estimation, for example generated from wind tunnel experimental errors, physical simplifications or wind load assumptions.

A stochastic differential equation system is obtained, which is solved by equivalent stochastic linearization. A series of numerical simulations are described and illustrated in this paper. The CAARC (Commonwealth Advisory Aeronautical Research Council) benchmark building is used as the prototype structure (Melbourne 1980). Stationary wind loads are investigated. The mean wind speed ranges from 20 m/s to 50 m/s, with the upper limit simulating a Category-2 or Category-3 hurricane wind according to the Saffir-Simpson scale (Simiu and Scanlan 1996). The present study relates either to an isolated tall building or a building in an urban setting that is not surrounded by other tall buildings; interference effects are

not considered. The various scenarios examine the role of wind loading intensity on the probability density function of the main system variables. Preliminary results of this study were recently presented by [Caracoglia \(2015\)](#).

BACKGROUND

Reduced-order model

The reduced-order model, used in the present simulations, is briefly introduced and described in this section. The model is derived from the standard approach for building aerodynamics in the frequency domain (e.g., [Piccardo and Solari 2000](#)). The main structural response is linear.

The CAARC building ([Melbourne 1980](#)) has a rectangular floor-plan of dimensions $D_x = 30.5$ m and $D_y = 45.7$ m and height $h = 183$ m. Figure 1 shows a schematic of the building geometry and wind loading. The mean wind direction and mean loading plane are orthogonal to the vertical face of width D_y . Figure 1a depicts the vertical elevation view and corresponds to the plane of the along-wind loads. A continuous formulation of the equations of motion is used. Quantities $x(z, t)$ and $y(z, t)$ depend on time t and coordinate z ; they model the horizontal dynamic displacements in the primary lateral motion planes.

The building mass is uniformly distributed along the height. For a symmetric floor-plan with equally-distributed mass the analysis of the dynamic response can be restricted to the degrees of freedom, corresponding to the motion in the two principal vertical planes of the building mentioned above. This is acceptable if torsional effects are secondary and the vibration results from a loading condition

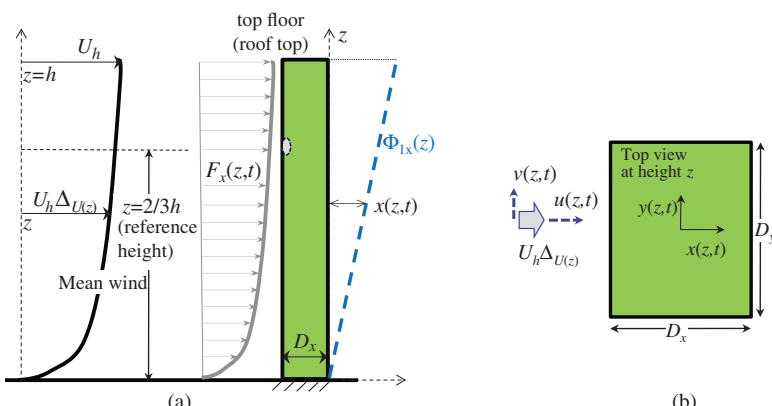


Figure 1. CAARC Benchmark building: (a) lateral elevation, and (b) cross sectional view at height z

Note: The reference height is selected in accordance with the theory indicated by the Equivalent Wind Spectrum Technique (e.g., [Piccardo and Solari 2000, Solari 1988](#)).

with mean wind direction perpendicular to one of the building faces (e.g., D_y in Figure 1b). Static wind loads and mean structural response will be considered in a later part of this study.

Dynamic vibration is modeled by modal expansion as $x(z, t) \approx \Phi_{1x}(z)D_x\xi_{1x}(t)$ and $y(z, t) \approx \Phi_{1y}(z)D_x\xi_{1y}(t)$, with ξ_{1x} and ξ_{1y} dimensionless generalized coordinates of the fundamental modes and $\Phi_{1x}(z)$ and $\Phi_{1y}(z)$ dimensionless mode shapes of the first lateral modes. The modes “1x” and “1y” are planar, with mode shape $\Phi_{1x}(z)$ in the “z-x” plane and $\Phi_{1y}(z)$ in the “z-y” plane. As an example, the motion in the lateral direction of the lateral mode 1x is illustrated in Figure 1a.

Stationary wind loads are based on boundary layer profile with mean speed $U(z)$, stationary turbulence components $u(z, t)$ and $v(z, t)$ (Figure 1b). The mean wind profile $U(z) = U_h\Delta_{U(z)}$ is normalized to U_h (the value at the roof top, $z = h$ in Figure 1a) and with $\Delta_{U(z)}$ a function describing the profile. The along-wind (direction “x” in Figure 1b) and cross-wind buffeting loads (direction “y” in Figure 1b) are separately considered. The static force coefficients per unit height of the CAARC building are constant along z and normalized with respect to D_x . For the along-wind load $F_x(z, t)$, shown in Figure 1a, they are: drag coefficient C_D and its derivative $dC_D/d\varphi$ with respect to wind incidence angle or angle of attack φ , evaluated at the mean static angle $\varphi_0 = 0$. For the cross-wind load $F_y(z, t)$, they are: transverse force coefficient C_L (“lift”) and its derivative $dC_L/d\varphi$, also evaluated at the same φ_0 .

Generalized forces and modal masses (M_{1x}, M_{1y}) of the generalized coordinates 1x and 1y can be found from the continuous formulation of the dynamic loads $F_x(z, t)$ and $F_y(z, t)$; for example, the generalized load 1x is $Q_{1x} = \int \Phi_{1x}(z)F_x(z, t)dz$, the generalized mass is $M_{1x} = \int \Phi_{1x}^2(z)m(z)dz$, with $m(z)$ being the building mass per unit height. Similar expressions can be obtained for the 1y quantities, $Q_{1y} = \int \Phi_{1y}(z)F_y(z, t)dz$, $M_{1y} = \int \Phi_{1y}^2(z)m(z)dz$. Details on the derivation may also be found in Caracoglia (2014). The dynamic response is expressed in terms of dimensionless time $s = tU_h/D_x$, reduced frequencies $K_{1x} = 2\pi n_{1x}D_x/U_h$ (mode 1x with natural frequency n_{1x} in Hz) and $K_{1y} = 2\pi n_{1y}D_x/U_h$ (mode 1y with frequency n_{1y}).

The generalized motion equations for 1x and 1y, in dimensionless form, are

$$\begin{aligned} \ddot{\xi}_{1x}'' + 2(\zeta_{1x} + H_{1x,1x}C_D)K_{1x}\dot{\xi}_{1x}' + H_{1x,1y}C_{L\hat{D}}K_{1y}\dot{\xi}_{1y}' + K_{1x}^2\xi_{1x} \\ = \rho D_x^2 h M_{1x}^{-1} \left[C_D \int_0^h \Delta_{U(z)} \hat{u}(z, s) \Phi_{1x}(z) h^{-1} dz \right] \end{aligned} \quad (1)$$

$$\begin{aligned} \ddot{\xi}_{1y}'' + (2\zeta_{1y} + H_{1y,1y}C_{D\hat{L}})K_{1y}\dot{\xi}_{1y}' + 2C_L H_{1y,1x} K_{1x}\dot{\xi}_{1x}' + K_{1y}^2\xi_{1y} \\ = \rho D_x^2 h M_{1y}^{-1} \left[C_L \int_0^h \Delta_{U(z)} \hat{u}(z, s) \Phi_{1y}(z) h^{-1} dz \right. \\ \left. + 0.5 C_{D\hat{L}} \int_0^h \Delta_{U(z)} \hat{v}(z, s) \Phi_{1y}(z) h^{-1} dz \right] \end{aligned} \quad (2)$$

In the previous equations, the apostrophe symbol designates the derivative with respect to dimensionless time s , $(\cdot)' = d(\cdot)/ds$. The air density is ρ . The buffeting loads on the right-hand side of Eqs. (1) and (2) depend on the longitudinal and transverse turbulence components at z (and time s), normalized as $\hat{u} = u/U_h$ and $\hat{v} = v/U_h$. The modal damping ratios are ζ_{1x} and ζ_{1y} . The aerodynamic static force coefficients are re-grouped in Eqs. (1) and (2) as follows:

$$C_{D\hat{L}} = (C_D + dC_L/d\varphi), \quad C_{L\hat{D}} = (dC_D/d\varphi - C_L) \quad (3a, 3b)$$

Coupling between modes $1x$ and $1y$ is induced by fluid-structure interaction; the coupling depends on reduced frequencies (K_{1x}, K_{1y}) modal masses (M_{1x}, M_{1y}), the coefficients in Eqs. (3a, b) and the following coupling terms:

$$H_{1x,1x} = \rho D_x^2 h / (2K_{1x}M_{1x}) \int_0^h \Delta_{U(z)} \Phi_{1x}^2(z) h^{-1} dz \quad (3c)$$

$$H_{1x,1y} = \rho D_x^2 h / (2K_{1y}M_{1x}) \int_0^h \Delta_{U(z)} \Phi_{1x}(z) \Phi_{1y}(z) h^{-1} dz \quad (3d)$$

$$H_{1y,1y} = \rho D_x^2 h / (2K_{1y}M_{1y}) \int_0^h \Delta_{U(z)} \Phi_{1y}^2(z) h^{-1} dz \quad (3e)$$

$$H_{1y,1x} = \rho D_x^2 h / (2K_{1x}M_{1y}) \int_0^h \Delta_{U(z)} \Phi_{1x}(z) \Phi_{1y}(z) h^{-1} dz \quad (3f)$$

The buffeting loads on the right-hand side of Eqs. (1) and (2) depend on $\hat{u} = u/U_h$ and $\hat{v} = v/U_h$ at various z . The aerodynamic loads, enclosed within square brackets in Eqs. (1) and (2), are subsequently simplified to separate dependence on coordinate z and time s . The partially correlated turbulence-induced forces are substituted by equivalent fully-correlated loads, acting on a reduced “projected area” of the lateral building surface and referred to an equivalent scalar turbulence term at a given height. This assumption, along with the selection of the equivalent or reference height ($z = 0.6h \approx 2/3h$ in Figure 1), is compatible with the theory specified by the Equivalent Wind Spectrum Technique (e.g., Piccardo and Solari 2000, Solari 1988). Lateral loads are represented in terms of a Modal Correlation Length (MCL) in the vertical direction, normalized with respect to h . Three MCLs are needed. The first one ($\Lambda_{1x,u}$) is the MCL of the $1x$ -mode generalized load related to u . This is

$$[\Lambda_{1x,u}]^2 \approx \int_0^h \int_0^h \Delta_{U(z_a)} \Delta_{U(z_b)} \Phi_{1x}(z_a) \Phi_{1x}(z_b) \times e^{-2c_{z,u} n_{1x} |z_a - z_b| U_h^{-1} (\Delta_{U(z_a)} + \Delta_{U(z_b)})^{-1}} h^{-2} dz_a dz_b \quad (4)$$

with $0 < \Lambda_{1x,u} \leq 1.0$ and $c_{z,u} = 10.0$ coherence decay coefficient (e.g., [Piccardo and Solari 2000](#), [Solari 1988](#)). Along with $\Lambda_{1x,w}$, $\Lambda_{1y,u}$ and $\Lambda_{1y,v}$ reference turbulence components are needed. They are calculated at $z = 0.6h \approx 2/3h$ since the objective is the estimation of generalized responses ξ_{1x} and ξ_{1y} . This procedure is compatible with theoretical developments by [Piccardo and Solari \(2000\)](#). The derivation of $\Lambda_{1x,u}$ in Eq. (4) and two other MCL terms, $\Lambda_{1y,u}$ and $\Lambda_{1y,v}$ ([Caracoglia 2014](#)), requires that the coefficients C_D , $C_{D\hat{L}}$ and $C_{L\hat{D}}$ are constant along the height. If the reference turbulence quantities are designated as $\hat{u}_{0.6h}(s) = \hat{u}(z=0.6, s)$ and $\hat{v}_{0.6h}(s) = \hat{v}(z=0.6, s)$, and all MCLs are considered, the previous equations become

$$\begin{aligned} \xi''_{1x} + 2(\zeta_{1x} + H_{1x,1x} C_D) K_{1x} \xi'_{1x} + K_{1y} H_{1x,1y} C_{L\hat{D}} \xi'_{1y} + K_{1x}^2 \xi_{1x} \\ = \rho D_x^2 h C_D M_{1x}^{-1} [\Lambda_{1x,u} + \lambda_u] \hat{u}_{0.6h}(s) \end{aligned} \quad (5)$$

$$\begin{aligned} \xi''_{1y} + (2\zeta_{1y} + H_{1y,1y} C_{D\hat{L}}) K_{1y} \xi'_{1y} + 2C_L H_{1y,1x} K_{1x} \xi'_{1x} + K_{1y}^2 \xi_{1y} \\ = \rho D_x^2 h M_{1y}^{-1} [C_L \Lambda_{1y,u} \hat{u}_{0.6h}(s) + 0.5 C_{D\hat{L}} \Lambda_{1y,v} \hat{v}_{0.6h}(s)] \end{aligned} \quad (6)$$

In Eq. (5) the effect of along-wind loading error is included. This effect is simulated and applied to the MCL of the 1x-mode generalized load. The generalized buffeting load in the along-wind direction in the absence of MCL error, $\rho D_x^2 h C_D M_{1x}^{-1} \Lambda_{1x,u} \hat{u}_{0.6h}(s)$, is replaced by an adjusted term, $\rho D_x^2 h C_D M_{1x}^{-1} [\Lambda_{1x,u} + \lambda_u] \hat{u}_{0.6h}(s)$. The deterministic (or mean) part of $\Lambda_{1x,u}$ is replaced by $[\Lambda_{1x,u} + \lambda_u]$, with λ_u being a zero-mean dimensionless random variable (MCL error) in accordance with the model proposed by [Caracoglia \(2014\)](#). The effect of the loading error is neglected in the cross-wind direction (1y mode) as a first approximation. This second error term effect is not included also because the largest total load (static plus dynamic), and consequently structural response, is observed on the principal lateral deformation plane corresponding to the 1x mode; this hypothesis is also based on the results of previous studies and is documented in [Caracoglia \(2014\)](#).

Dynamic equations are converted to Itô-type stochastic differential system to examine the effect of along-wind loading error as follows:

- $\hat{u}_{0.6h}$ and $\hat{v}_{0.6h}$ are represented as the outputs of two auto-regressive filters. These terms are written in accordance with Itô's differentiation rule as a function of a time-dependent scalar Wiener process $B(s)$ of unit-variance increments as: $d\hat{u}_{0.6h} = -G_{1u} \hat{u}_{0.6h} ds + \sqrt{2\pi} G_{2u} dB(s)$ and

- $d\hat{v}_{0.6h} = -G_{1v}\hat{v}_{0.6h}ds + \sqrt{2\pi}G_{2v}dB(s)$ (G_{1v} , G_{2v} , G_{1v} and G_{2v} are deterministic constants, found from turbulence power spectral densities);
- b) The random λ_u is also represented by a first-order auto-regressive model with a “flat spectrum”, $d\lambda_u = -\varepsilon_\lambda\lambda_u ds + \sqrt{2\pi(\sigma_{\lambda_u}\sqrt{\varepsilon_\lambda/\pi})}dB(s)$, with σ_{λ_u} = SD(λ_u) standard deviation of λ_u and $\varepsilon_\lambda \approx 10$ a “shape” parameter.

The intervention cost model Caracoglia (2014) is separately described in the next sub-section.

Basic intervention cost models

Most damage is usually observed on the façade of the structure and secondary non-structural elements. Consequently, the evaluation of the “failure” probability and the building performance against wind hazards should make use of indicators, the metric of which is suitable for serviceability analysis. The use of a generalized cost variable $\Gamma(s)$ is built on this idea and is considered herein. In a recent study Caracoglia (2014) describes the intervention cost variable in a dimensionless scalar form:

$$\Gamma(s) = \begin{cases} \Gamma_\tau \left(\frac{\xi_{1x}(s)}{\tau} \right)^2, & \text{if } |\xi_{1x}(s)| \geq \tau \\ \Gamma(s) = 0, & \text{if } |\xi_{1x}(s)| < \tau \end{cases} \quad (7)$$

The intervention cost $\Gamma(s)$ in Eq. (7) exclusively depends on the $1x$ generalized variable of the along-wind dynamic structural response. The proportionality between $\Gamma(s)$ and ξ_{1x} is quadratic; cost accumulation is restricted to dynamic vibration experienced by the structure beyond a pre-selected dimensionless vibration threshold τ . For this reason, the formula in Eq. (7) is designated as “quadratic” intervention cost equation.

The proportionality constant $0 \leq \Gamma_\tau \leq 1.0$ is a dimensionless marginal cost, (i.e., an initial cost incurred at incipient crossing of threshold τ). This constant can be interpreted as the ratio between marginal cost, in monetary units, and the structural construction cost of the structure ($\Gamma_\tau \rightarrow 1.0$ is the full replacement of the structure).

Generalizing Eq. (7), a second (new) intervention cost model is proposed in dimensionless form:

$$\Gamma(s) = \begin{cases} \frac{\Gamma_\tau}{\tau^\alpha} [\xi_{1x}^2(s) + \mu\xi_{1y}^2(s)]^{\alpha/2}, & \text{if } \delta_{dyn} \geq \tau \\ \Gamma(s) = 0, & \text{if } \delta_{dyn} < \tau \end{cases} \quad (8)$$

In this new model the modulus of the generalized dynamic lateral displacement is considered $\delta_{dyn} = \sqrt{\xi_{1x}^2(s) + \mu\xi_{1y}^2(s)}$; α is a real positive exponent. This equation is labeled as “power-law” intervention cost equation. It is remarked that

cost cannot be restricted to a basic value [i.e., $\alpha = 2$ and $\mu = 0$ in Eq. (8)], which coincide with Eq. (7)]. In this study a parametric analysis is carried out by varying the coefficient α and plausibly assuming values between 1.0 and 3.0. More studies are necessary to relate the damage function to monetary costs, for example by examining actual replacement, repair and other induced costs in a building with geometry and characteristics similar to the CAARC building. Some preliminary examples of this type of analysis are presented in the literature either for seismic design (Goulet et al. 2007) or, for example, considering the “ripple effects” associated with downtime or system outages (Pita and Mitrani-Reiser 2013).

In Eq. (8) the parameter μ is a Boolean constant equal to either 0 or 1. The case $\mu = 0$ only accounts for non-structural damage dominated by along-wind response. The case with $\mu = 1$ coincides with the vector combination of along-wind and cross-wind dynamic components. The static-load effect (i.e., the mean response) is considered in a subsequent section.

Figure 2a illustrates an example of normalized intervention cost function, corresponding to Eq. (7) and obtained using the following parameters: a marginal cost equal to $\Gamma_\tau = 0.30$ (30% of the construction cost) and minimum vibration threshold for damage $\tau = 0.03$ (i.e., with dynamic motion of $0.03D_x$ in the along-wind direction of generalized dynamic coordinate ξ_{1x}). Figure 2b replicates the same example for a power-law cost function in Eq. (8) with $\alpha = 2.5$. As evident from both plots, the intervention cost is equal to Γ_τ at $\xi_{1x} = \tau$. The variable $\Gamma(s)$ inherits the randomness from ξ_{1x} and ξ_{1y} . The threshold τ , used in Figure 2, approximately corresponds to a lateral sway of about $h/200$, a large lateral displacement (e.g., total along-wind displacements at wind speeds of 50 m/s for this building, Melbourne 1980). This type of damage is compatible with large inter-story drifts, likely to cause glass or window fall. It is not compatible with small damage such as window cracking or produced by

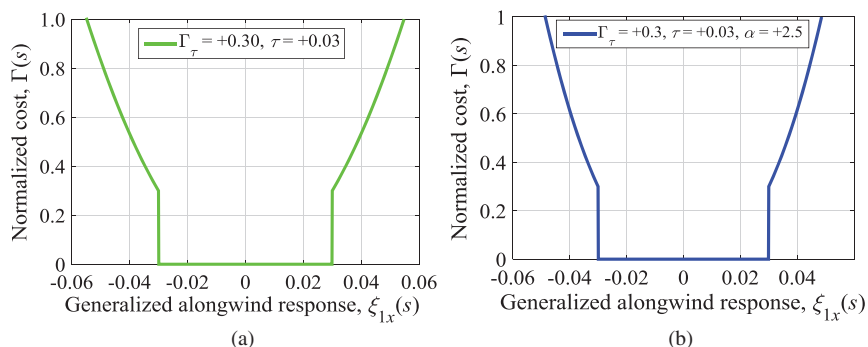


Figure 2. Normalized cost $\Gamma(s)$ vs. building's generalized dynamic response ξ_{1x} - examples ($s = tU_h/D_x$ dimensionless time variable): (a) Eq. (7) with $\Gamma_\tau = 0.30$ and $\tau = 0.03$, and (b) Eq. (8) with $\Gamma_\tau = 0.30$, $\tau = 0.03$, $\alpha = 2.5$, $\mu = 0$

wind-borne debris. This value of threshold τ is initially selected and employed in the next section when static load effects are ignored (basic model). A full parametric investigation, which includes τ values about one order of magnitude smaller, will be carried out in a later section with the extended model accounting for static load effects.

Stochastic differential system

Differentiation of either Eq. (7) or Eq. (8) with respect to time s , using Itô's differentiation rule (Grigoriu 2002), respectively leads to

$$d\Gamma(s) = \begin{cases} \{\Gamma_\tau/\tau^2(2\xi_{1x}\xi'_{1x} + \xi_{1x}^2) - \Gamma(s)\}ds + \sqrt{2\pi}(\sigma_\Gamma/\sqrt{\pi})dB(s), & \text{if } |\xi_{1x}| \geq \tau \\ 0, & \text{if } |\xi_{1x}| < \tau \end{cases} \quad (9)$$

$$d\Gamma(s) = \begin{cases} \left\{ \frac{\Gamma_\tau}{\tau^\alpha} (\xi_{1x}^2 + \mu\xi_{1y}^2)^{\alpha/2} [1 + \alpha(\xi_{1x}^2 + \mu\xi_{1y}^2)^{-1}(\xi_{1x}\xi'_{1x} + \mu\xi_{1y}\xi'_{1y})] \right\} ds \\ -\Gamma(s) \\ + \sqrt{2\pi}(\sigma_\Gamma/\sqrt{\pi})dB(s), & \text{if } \delta_{dyn} \geq \tau \\ 0, & \text{if } \delta_{dyn} < \tau \end{cases} \quad (10)$$

In the previous equations the randomization is carried out by introducing a “drift term” (Grigoriu 2002), in other words, the term enclosed within braces in the equations and depending on the differential time ds , and a “diffusion term” (Grigoriu 2002), which depends on the differential of the scalar Wiener process $dB(s)$. The drift terms are found from Eqs. (7) and (8).

Application of the Itô's rule to the second moment of Eq. (9) or Eq. (10), combined with the hypothesis of $|\xi_{1x}| > \tau$ at any time s , leads to $E[\Gamma^2(s)] = \sigma_\Gamma^2(E[]$ expectation). Therefore, σ_Γ in Eq. (9) or Eq. (10) is the standard deviation of the marginal intervention cost, which accounts for maintenance cost variability.

The stochastic differential equation is obtained by combining Eqs. (5) and (6) either with Eq. (9) or Eq. (10). If the generalized vector of the model of dimension $\tilde{n} = 8$ is $\mathbf{W}_\Gamma = [\xi_{1x}, \xi_{1y}, \dot{\xi}_{1x}, \dot{\xi}_{1y}, \hat{u}_{0.6h}, \hat{v}_{0.6h}, \Gamma(s), \lambda_u]^T$, the final equation becomes

$$d\mathbf{W}_\Gamma = \mathbf{a}_\Gamma(\mathbf{W}_\Gamma)ds + \sqrt{2\pi}\mathbf{d}_\Gamma dB(s) \quad (11)$$

The diffusion vector is linear and equal to $\mathbf{d}_\Gamma = [0^{1 \times 4}, G_{2u}, G_{2v}, \sigma_\Gamma/\sqrt{\pi}, \sigma_{\lambda_u}\sqrt{\varepsilon_\lambda/\pi}]^T$ (the “ T ” superscript symbol designates transpose operation).

The nonlinear drift function \mathbf{a}_Γ is

$$\mathbf{a}_\Gamma(\mathbf{W}_\Gamma) = \begin{cases} W_{\Gamma,3} \\ W_{\Gamma,4} \\ \left\{ -2K_{1x}(\zeta_{1x} + H_{1x,1x}C_D)W_{\Gamma,3} - K_{1y}H_{1x,1y}C_{L\hat{D}}W_{\Gamma,4} \right. \\ \left. - K_{1x}^2W_{\Gamma,1} + \rho D_x^2 h C_D M_{1x}^{-1}(\Lambda_{1x,u} + W_{\Gamma,8})W_{\Gamma,5} \right\} \\ \left\{ -[2\zeta_{1y} + H_{1y,1y}C_{D\hat{L}}]K_{1y}W_{\Gamma,4} - 2C_L H_{1y,1x}K_{1x}W_{\Gamma,3} \right. \\ \left. - K_{1y}^2W_{\Gamma,2} + \rho D_x^2 h M_{1y}^{-1}[C_L \Lambda_{1y,u} W_{\Gamma,5} + 0.5C_{D\hat{L}}\Lambda_{1y,v} W_{\Gamma,6}] \right\} \\ -G_{1u}W_{\Gamma,5} \\ -G_{1v}W_{\Gamma,6} \\ -W_{\Gamma,7} + \Delta_{NL}^{(\Gamma)}(s) \\ -\varepsilon_\lambda W_{\Gamma,8} \end{cases} \quad (12)$$

In Eq. (12) the function $\Delta_{NL}^{(\Gamma)}(s)$ is found either from Eq. (9) or Eq. (10), depending on the specific case and noting that $W_{\Gamma,1} = \xi_{1x}(s)$, $W_{\Gamma,7} = \Gamma(s)$ and $W_{\Gamma,8} = \lambda_u$. With the quadratic cost model [Eq. (9)], it is

$$\Delta_{NL}^{(\Gamma)}(s) = \begin{cases} (2W_{\Gamma,1}W_{\Gamma,3} + W_{\Gamma,1}^2)\Gamma/\tau^2, & \text{if } |W_{\Gamma,1}| \geq \tau \\ 0, & \text{if } |W_{\Gamma,1}| < \tau \end{cases} \quad (13)$$

With the power-law cost model [Eq. (10)], it is

$$\Delta_{NL}^{(\Gamma)}(s) = \begin{cases} \Gamma/\tau^\alpha \left(W_{\Gamma,1}^2 + \mu W_{\Gamma,2}^2 \right)^{\alpha/2} \left[1 + \alpha \left(W_{\Gamma,1}^2 + \mu W_{\Gamma,2}^2 \right)^{-1} \right], & \text{if } \sqrt{W_{\Gamma,1}^2 + \mu W_{\Gamma,2}^2} \geq \tau \\ 0, & \text{if } \sqrt{W_{\Gamma,1}^2 + \mu W_{\Gamma,2}^2} < \tau \end{cases} \quad (14)$$

The stochastic system in Eq. (11) is numerically solved by stochastic linearization at steady state (as $s \rightarrow \infty$) to obtain the Probability Density Function (PDF) of the vector \mathbf{W}_Γ .

Solution by stochastic linearization

Stochastic linearization is a method for approximate solution of nonlinear stochastic differential equations (Caughey 1963, Elishakoff and Cai 1993,

Spanos 1981). The method replaces the nonlinear system (Eq. 10) by an equivalent linear system of equations:

$$d\mathbf{W}_\Gamma(s) = \tilde{\mathbf{A}}\mathbf{W}_\Gamma(s)ds + \sqrt{2\pi}\mathbf{d}_\Gamma dB(s) \quad (15)$$

The matrix $\tilde{\mathbf{A}}$ depends on the mean wind speed at roof top (U_h) apart from other variables. In Eq. (15) the joint-PDF $p(\mathbf{w}_\Gamma)$ can be determined without directly solving this equation, which otherwise requires the use of the Fokker-Planck Equation (Grigoriu 2002). The nonlinear function $\mathbf{a}_\Gamma(\mathbf{W}_\Gamma)$ is split into a strictly linear part and a nonlinear term $\mathbf{a}_{NL}(\mathbf{W}_\Gamma)$: $\mathbf{a}(\mathbf{W}_\Gamma) = \mathbf{A}\mathbf{W}_\Gamma + \mathbf{a}_{NL}(\mathbf{W}_\Gamma)$. The matrix \mathbf{A} coincides with the system and model in the absence of both along-wind load error ($\lambda_u = 0$ identically) and damage ($\Gamma(s) = 0$ identically).

The equivalent system in Eq. (15) is found by minimizing the mean-square error e_{MS} between the true response and the approximated one (Lin and Cai 1995). If $\tilde{\mathbf{W}}_\Gamma$ designates the approximate vector computed by equivalent linearization, the minimization leads to a system of algebraic equations, in which each scalar term i, j with $i = 1, \dots, \tilde{n}$ and $j = 1, \dots, \tilde{n}$ is found as suggested in Lin and Cai (1995):

$$E[a_{NL,i}(\tilde{\mathbf{W}}_\Gamma)\tilde{W}_{\Gamma,j}] = \sum_{k=1}^{\tilde{n}} (\tilde{A}_{i,k} - A_{i,k}) E[\tilde{W}_{\Gamma,k}\tilde{W}_{\Gamma,j}] \quad (16)$$

If the linear matrices are partitioned as rectangular matrices $\mathbf{A} = [\mathbf{A}^{(U)}, \mathbf{A}^{(L)}]^T$, $\tilde{\mathbf{A}} = [\tilde{\mathbf{A}}^{(U)}, \tilde{\mathbf{A}}^{(L)}]^T$ with the upper (U) matrix and the lower partition (L) and since vector $\mathbf{a}_{NL}(\tilde{\mathbf{W}}_\Gamma) = [\mathbf{0}^{(1 \times 2)}, \mathbf{a}_{NL}^{(L)}(\tilde{\mathbf{W}}_\Gamma)]^T$ only affects these lower partitions, the solution of the lower partition of Eq. (15) is exclusively needed. The unknown matrix $\tilde{\mathbf{A}}^{(L)}$ is found from Eq. (16) and the implicit equation $\tilde{\mathbf{A}}^{(L)} = \mathbf{A}^{(L)} + \Psi^{(E)}\tilde{\Sigma}^{-1}$, where $\Psi^{(E)}$ comes from $E[a_{NL,i}(\tilde{\mathbf{W}}_\Gamma)\tilde{W}_{\Gamma,j}] = \Psi_{ij}^{(E)}$ and $\tilde{\Sigma}_\Gamma$ is the variance/covariance matrix of the approximate solution vector. Since both $\tilde{\mathbf{A}}^{(L)}$ and $\tilde{\Sigma}_\Gamma$ are unknown and $\Psi_{ij}^{(E)}$ terms require knowledge of the joint PDF of $\tilde{\mathbf{W}}_\Gamma$, the minimization is iteratively solved (Lin and Cai 1995). Once the minimization problem is solved (Caracoglia 2014), matrix $\tilde{\mathbf{A}}$ is found.

Finally, the multi-variable joint PDF $p(\mathbf{w}_\Gamma)$ can be approximately inferred from matrix $\tilde{\mathbf{A}}$ as a Gaussian random vector [as suggested by several authors (Caughey 1963; Spanos 1981)]:

$$p(\mathbf{w}_\Gamma) \approx [(2\pi)^{\tilde{n}} \det(\tilde{\Sigma}_\Gamma)]^{-1/2} \exp[-0.5(\mathbf{w}_\Gamma)^T \tilde{\Sigma}_\Gamma^{-1}(\mathbf{w}_\Gamma)] \quad (17)$$

The covariance matrix $\tilde{\Sigma}_\Gamma$ in Eq. (17) is calculated via Lyapunov matrix equation $\tilde{\mathbf{A}}\tilde{\Sigma}_\Gamma + \tilde{\Sigma}_\Gamma\tilde{\mathbf{A}} + 2\pi\mathbf{d}\mathbf{d}^T = 0$ (Martens et al. 2012). Equation (17) also implies that $E[\mathbf{W}_\Gamma] = \mathbf{0}$, i.e., the mean load and response do not affect the damage; this assumption will be relaxed in the next section. The solution procedure also ignores the contribution of higher moments and does not employ more sophisticated linearization techniques to overcome this issue (Naess 1995, Ricciardi 2007). It is only approximate for highly nonlinear systems.

EXTENDED FORMULATION EXAMINING STATIC WIND LOAD EFFECTS ON DAMAGE AND POWER-LAW MODEL INTERVENTION COST

Intervention cost and stochastic models

Since the effect of the static wind loads is often important as it causes a time-independent permanent effect on the structure (lateral static displacements), it is plausible to consider that damage accumulation may also depend on the effect of the static load, namely the static deformation of the building (Figure 1). As a result, a modified stochastic model is studied in this section.

First, the total response must be decomposed into static or mean components, $x(z)^{(m)}$ and $y(z)^{(m)}$, and the corresponding dynamic time-dependent zero-mean vibrations along the two principal bending planes of the building, $x(z, t)$ and $y(z, t)$. If modal expansion is employed, with truncation to the first fundamental modes Φ_{1x} and Φ_{1y} , as before, the two responses become $x(z)^{(m)} + x(z, t) \approx \Phi_{1x}(z) D_x[\xi_{1x}^{(m)} + \xi_{1x}(t)]$ and $y(z)^{(m)} + y(z, t) \approx \Phi_{1y}(z) D_y[\xi_{1y}^{(m)} + \xi_{1y}(t)]$ with $\xi_{1x}^{(m)}$ and $\xi_{1y}^{(m)}$ being the corresponding mean generalized coordinates. Consequently, modal superposition may be applied using a modified definition of generalized forces $Q_{1x} = \int \Phi_{1x}(z)[F_x^{(m)}(z) + F_x(z, t)] dz$ and $Q_{1y} = \int \Phi_{1y}(z)[F_y^{(m)}(z) + F_y(z, t)] dz$, which separately accounts for the static loads $F_x^{(m)}(z)$ and $F_y^{(m)}(z)$ computed at initial wind incidence angle $\varphi_0 = 0$. This decomposition leads to the same dynamic equations as before [Eqs. (1-2)] as a function of dimensionless time $s = tU_h/D_x$ dynamic generalized coordinates ξ_{1x} and ξ_{1y} . However, two generalized time-independent static displacements are also found:

$$\xi_{1x}^{(m)} = 0.5\rho C_D D_x^2 h K_{1x}^{-2} M_{1x}^{-1} \left[\int_0^h \Delta_{U(z)}^2 \Phi_{1x}(z) h^{-1} dz \right] \quad (18)$$

$$\xi_{1y}^{(m)} = 0.5\rho C_L D_x^2 h K_{1y}^{-2} M_{1y}^{-1} \left[\int_0^h \Delta_{U(z)}^2 \Phi_{1y}(z) h^{-1} dz \right] \quad (19)$$

In the previous equations the notation of the variables refers to the dimensionless generalized frequencies, K_{1x} and K_{1y} , and modal masses, M_{1x} and M_{1y} . The intervention cost power-law model in Eq. (8) is exclusively used in this section and in the derivation below. Following the same steps as in the previous section, Eq. (8) must be modified to account for the influence of the static load effect as follows:

$$\Gamma(s) = \begin{cases} \frac{\Gamma_\tau}{\tau^\alpha} \left[\left(\xi_{1x}(s) + \xi_{1x}^{(m)} \right)^2 + \mu \left(\xi_{1y}(s) + \xi_{1y}^{(m)} \right)^2 \right]^{\alpha/2}, & \text{if } \delta_{tot} \geq \tau \\ \Gamma(s) = 0, & \text{if } \delta_{tot} < \tau \end{cases} \quad (20)$$

In the previous expression, the quantity $\delta_{tot} = \sqrt{(\xi_{1x}(s) + \xi_{1x}^{(m)})^2 + \mu(\xi_{1y}(s) + \xi_{1y}^{(m)})^2}$ designates the modulus of the total lateral displacement in generalized modal coordinates at dimensionless time s . The stochastic form of Eq. (20) becomes

$$\begin{aligned} d\Gamma(s) &= \left\{ \begin{array}{l} \left\{ \frac{\Gamma_\tau}{\tau^\alpha} \left[\left(\xi_{1x} + \xi_{1x}^{(m)} \right)^2 + \mu \left(\xi_{1y} + \xi_{1y}^{(m)} \right)^2 \right]^{\alpha/2} \right\} \\ \left\{ 1 + \alpha \left[\left(\xi_{1x} + \xi_{1x}^{(m)} \right)^2 + \mu \left(\xi_{1y} + \xi_{1y}^{(m)} \right)^2 \right]^{-1} \left[\left(\xi_{1x} + \xi_{1x}^{(m)} \right) \xi'_{1x} \right. \right. \\ \left. \left. + \mu \left(\xi_{1y} + \xi_{1y}^{(m)} \right) \xi'_{1y} \right] \right\} \end{array} \right\} ds \\ &= \begin{cases} -\Gamma(s), & \text{if } \delta_{tot} \geq \tau \\ +\sqrt{2\pi}(\sigma_\Gamma/\sqrt{\pi})dB(s), & \text{if } \delta_{tot} < \tau \\ 0, & \text{else} \end{cases} \quad (21) \end{aligned}$$

The stochastic differential system can still be resolved since the mean response can be separated from the total response in the dynamic equations. It is now convenient to recast Eq. (11), which is a dynamic stochastic equation, in terms of the “centered” random state variable $\mathbf{W}_\Gamma^{(c)} = \mathbf{W}_\Gamma - \mathbf{w}_\Gamma^{(m)}$ with $E[\mathbf{W}_\Gamma] = \mathbf{w}_\Gamma^{(m)}$. The system can be rewritten as

$$d\left[\mathbf{W}_\Gamma - \mathbf{w}_\Gamma^{(m)}\right] = d\mathbf{W}_\Gamma^{(c)} = \mathbf{a}_\Gamma(\mathbf{W}_\Gamma^{(c)}, \mathbf{w}_\Gamma^{(m)}) ds + \sqrt{2\pi} \mathbf{d}_\Gamma dB(s) \quad (22)$$

with $\mathbf{d}_\Gamma = [0^{4 \times 1}, G_{2u}, G_{2v}, \sigma_\Gamma / \sqrt{\pi}, \sigma_{\lambda_u} \sqrt{\varepsilon_\lambda / \pi}]^T$ the same as before. Under the assumption that no damage is observed under mean static load effects, the mean vector is $E[\mathbf{W}_\Gamma] = \mathbf{w}_\Gamma^{(m)} = [\xi_{1x}^{(m)}, \xi_{1y}^{(m)}, 0]^T$ i.e., no longer identically zero owing to the contribution of the first two terms. Inspection of Eq. (22) reveals that the structure of the nonlinear vector function \mathbf{a}_Γ is the same as in Eq. (11) provided that the time-dependent vector \mathbf{W}_Γ is replaced by the centered one $\mathbf{W}_\Gamma^{(c)}$ and the non-linear scalar cost function $\Delta_{NL}^{(\Gamma)}(s)$ [originally presented in Eq. (14)] is modified as described below. Damage threshold crossing, in the extended formulation, also depends on $\mathbf{w}_\Gamma^{(m)}$. The new expression for $\Delta_{NL}^{(\Gamma)}(s)$ is

$$\Delta_N^{(\Gamma)}(s) = \begin{cases} \frac{\Gamma_\tau}{\tau^\alpha} \left[\left(W_{\Gamma,1}^{(c)} + w_1^{(m)} \right)^2 + \mu \left(W_{\Gamma,2}^{(c)} + w_2^{(m)} \right)^2 \right]^{\alpha/2} & \text{if } \delta_{tot} \geq \tau \\ 0, & \text{if } \delta_{tot} < \tau. \end{cases}$$

Solution by stochastic linearization

Application of the stochastic linearization to Eq. (22), using a_{Γ} as in Eq. (11) and replacing the second to the last equation with Eq. (23), leads to the following approximate solution:

$$d\mathbf{W}_\Gamma^{(c)}(s) = \tilde{\mathbf{A}}^{(\text{SLE})} \mathbf{W}_\Gamma^{(c)}(s) ds + \sqrt{2\pi} \mathbf{d}dB(s) \quad (24)$$

The previous expression depends on a modified linearized matrix $\tilde{\mathbf{A}}^{(\text{SLE})}$, compared to Eq. (15), because of Eq. (23) and the static load effect (SLE). After the matrix $\tilde{\mathbf{A}}^{(\text{SLE})}$ is found, the new expression of the joint PDF with $\mathbf{w}_\Gamma = \mathbf{w}_\Gamma^{(c)} + \mathbf{w}_\Gamma^{(m)}$ is:

$$p(\mathbf{w}_\Gamma) \approx \left[(2\pi)^n \det(\tilde{\Sigma}_\Gamma^{(\text{SLE})}) \right]^{-1/2} \exp[-0.5 (\mathbf{w}_\Gamma - \mathbf{w}_\Gamma^{(m)})^T (\tilde{\Sigma}_\Gamma^{(\text{SLE})})^{-1} (\mathbf{w}_\Gamma - \mathbf{w}_\Gamma^{(m)})] \quad (25)$$

The covariance matrix $\tilde{\Sigma}_\Gamma^{(\text{SLE})}$ is found from $\tilde{\mathbf{A}}^{(\text{SLE})} \tilde{\Sigma}_\Gamma^{(\text{SLE})} + \tilde{\Sigma}_\Gamma^{(\text{SLE})} \tilde{\mathbf{A}}^{(\text{SLE})} + 2\pi \mathbf{d} \mathbf{d}^T = 0$.

BRIEF DESCRIPTION OF THE SIMULATED CAARC BUILDING

Dynamic response of the CAARC building is analyzed by reproducing most features of the wind tunnel experiments, described in [Melbourne \(1980\)](#). The main parameters used in the model are summarized in Table 1. Schematics may be found in Figure 1.

The velocity deficit with respect to the roof top, $\Delta_{U(z)}$, is modeled by logarithmic law with roughness length 0.5 m, approximately corresponding to

Table 1. CAARC Building Model: (a) Main Structural, and (b) Wind Load Parameters

(a) Variable [units]	Value assigned	(b) Variable [units]	Value assigned
D_x [m]	30.5	ρ [kg/m ³]	1.25
D_y [m]	45.7	C_D	1.0
$m(z) = m$ [kg/m]	220800	C_L	-0.1
n_{1x} [Hz]	0.20	$dC_D/d\phi$	-1.1
n_{1y} [Hz]	0.22	$dC_L/d\phi$	-2.2
$\Phi_{1x}(z)$	(z/h)	I_u	0.14
$\Phi_{1y}(z)$	(z/h)	I_v	0.10
ζ_{1x} [.]	0.01	$c_{z,u}$	10.0
ζ_{1y} [.]	0.01	$c_{z,v}$	0.667 $c_{z,u}$
		G_{1u}	$0.29 < G_{1u} < 0.35^{(\dagger)}$
		G_{2u}	$0.08 < G_{2u} < 0.12^{(\dagger)}$
		G_{1v}	$0.29 < G_{1v} < 0.35^{(\dagger)}$
		G_{2v}	$0.06 < G_{2v} < 0.09^{(\dagger)}$

Note: ^(†)dependent on U_h ([Caracoglia 2014](#)).

the profile prescribed by [Melbourne \(1980\)](#). Normalized power spectral densities of turbulence at $z = 0.6h$, $\hat{u}_{0.6h}$ and $\hat{v}_{0.6h}$, are derived for both directions from the Harris spectrum ([Melbourne 1980](#)). The deterministic constants G_{1u} , G_{2u} , G_{1v} and G_{2v} of the auto-regressive turbulence model are calculated by setting a constant value to the turbulence intensities for $\hat{u}_{0.6h}$ (along-wind, I_u) and for $\hat{v}_{0.6h}$ (cross-wind, I_v). An example of the actual calculations may be found in [Caracoglia \(2014\)](#). Validation and verification of the procedure in the absence of wind load error ($\lambda_u = 0$ identically) is discussed in [Caracoglia \(2014\)](#) and is not reported herein.

BASIC COST MODEL WITHOUT STATIC LOAD EFFECT: NUMERICAL RESULTS

Cost probability results predicted by quadratic cost equation

In this first example, the normalized cost $\Gamma(s)$ of the first model in Eq. (7) (Figure 2a) is used to study the effects of MCL error on the dynamic response of the CAARC building. In this first example the following properties of $\Gamma(s)$ are used: marginal intervention cost $\Gamma_\tau = 0.30$ and minimum vibration threshold $\tau = 0.03$ ($0.03D_x$ in dimensional units). The diffusion term [cost variability in Eq. (8)] is set to $\sigma_\Gamma = 0.01$.

The MCL error is random, zero mean with standard deviation $\sigma_{\lambda u} = 0.25\Lambda_{1x,u}$. The shape parameter of the MCL error term λ_u is $e_\lambda = 10$. The reference value of the MCL is velocity-dependent and it is equal to $\Lambda_{1x,u} = 0.17$ at $U_h = 20$ m/s and $\Lambda_{1x,u} = 0.25$ at $U_h = 50$. Figure 3 shows an example of the numerical results, obtained by stochastic linearization; the figure illustrates the joint-PDF function between ξ_{1x} (roof-top vibration in generalized coordinates) and intervention cost Γ predicted by Eq. (5), $p(\xi_{1x}, \Gamma)$.

The PDF functions are centered at the origin, as expected, since effect of the static load is neglected at this stage of the investigation. The surfaces are shown as a function of the reference mean wind speed U_h . The vertical scale used in the graphs is different to highlight quantitative differences among various distributions. The parameters of the intervention cost function, Γ_τ and τ , are taken from Figure 2a. The joint-PDF surfaces are plotted for $\Gamma > 0$ only since the indication of a negative Γ , suggested by the model results, must be carefully interpreted. In fact, since the solution by stochastic linearization is nearly Gaussian as a first approximation, negative values of the cost variable Γ are possible but physically dubious.

The effect of a variation in the mean speed produces a non-negligible effect on the distributions, also visible in the figures, especially in terms of covariance. Quantitatively, the cross-correlation coefficient between ξ_{1x} and Γ is highly dependent on the mean wind speed by progressively decreasing with an increment of U_h , from 0.24 in Figure 3a to 0.12 in Figure 3c and to 0.09 Figure 3d in the example.

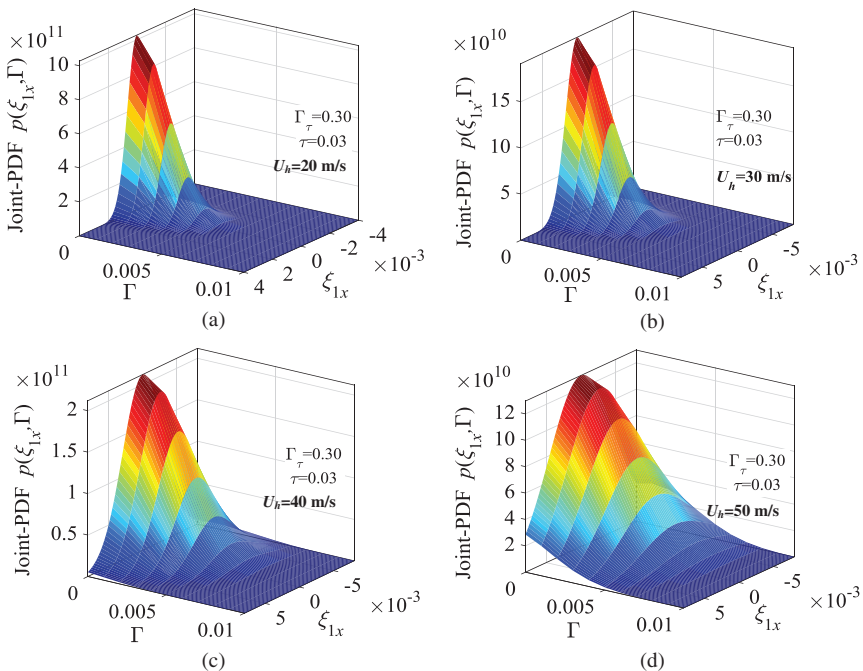


Figure 3. Joint PDF of the along-wind dynamic generalized response ξ_{1x} and intervention cost Γ [Eq. (7)] for the CAARC building with $\Gamma_\tau = 0.30$, $\tau = 0.03$ and $\sigma_{\lambda u} = 0.25\Lambda_{1x,u}$: (a) $U_h = 20$ m/s, (b) $U_h = 30$ m/s, (c) $U_h = 40$ m/s, and (d) $U_h = 50$ m/s

In contrast, a variation in the parameters of the cost model, Γ_τ and τ , tend to produce a less visible effect on the shape of $p(\xi_{1x}, \Gamma)$, which is substantially preserved in the simulations; this fact is believed to be influenced by the structure of Eq. (16), which is employed to generate the joint PDF of the dynamic response.

The plots in Figure 3 suggest that the shapes of the PDF surfaces are qualitatively similar. However, wider probability distributions are observable as U_h is incremented. The relative variations in the standard deviations of the generalized response ξ_{1x} between $U_h = 20$ m/s and $U_h = 50$ m/s, is about seven times if the MCL error is incorporated. The linearized solution generally indicates a somehow limited influence of the MCL error on the response characteristics. As a result, the shapes of the PDF functions are substantially preserved with the increase of U_h . In the figures a dynamic response amplitude $\xi_{1x} = 5E-3$ corresponds to about 0.15 m. Some dependence of the numerical results on the standard deviation of the MCL error $\sigma_{\lambda u}$ was noted; results are not discussed herein but they are available in Caracoglia (2014). Discussion on the joint probability between the along-wind and crosswind generalized responses, ξ_{1x} and ξ_{1y} , will be addressed in a subsequent section.

Cost probability results predicted by the power-law cost equation

The normalized cost, illustrated in Figure 2b, is employed in this section to study the effects of MCL error on the dynamic response of the CAARC building. In this second example the power-law equation is employed [Eq. (8)]; the following properties are initially considered: $\Gamma_\tau = 0.30$, $\tau = 0.03$ (as in the previous section) and power-law exponent $\alpha = 2.5$. The value $\alpha = 2.5$ is initially proposed to examine the situation, in which the damage-related cost function is a nonlinear function of the generalized lateral displacement beyond the threshold $\tau = 0.03$ (i.e., not proportional to the modulus of the top-floor displacement). In other words, damage is considered as a non-proportional function in order to investigate any potential influence of this non-linearity on the (approximated) PDF surface. As also explained in an earlier section, quantification of α should possibly consider the examination of actual repair and maintenance costs of non-structural elements in building structures. Other values of α will be considered in a subsequent section of this paper.

The diffusion term, describing the cost variability, is set to $\sigma_\Gamma = 0.01$. The MCL error is again simulated as a zero-mean variable with standard deviation $\sigma_{\lambda_u} = 0.25\Lambda_{1x,u}$. Figure 2b, illustrates the corresponding example of power-law intervention cost equation using the second model in Eq. (8) as a function of the generalized building response ξ_{1x} . The quantity $\Gamma(s)$ is calculated for marginal intervention cost $\Gamma_\tau = 0.30$ (30% of the construction cost) and minimum vibration threshold $\tau = 0.03$ ($0.03D_x$ in dimensional units). This case is similar to the example investigated in the previous section.

The first simulation example is illustrated in Figure 4; it is based on minimum vibration threshold for non-structural damage exclusively linked to along-wind vibration [$\mu = 0$ in Eq. (8)]. The figure presents the joint PDF plots $p(\xi_{1x}, \Gamma)$ for selected cases of U_h .

The shape of the linearized PDF $p(\xi_{1x}, \Gamma)$ in Figure 4 is quantitatively similar to the plots in Figure 3, suggesting that the linearization method tends to produce

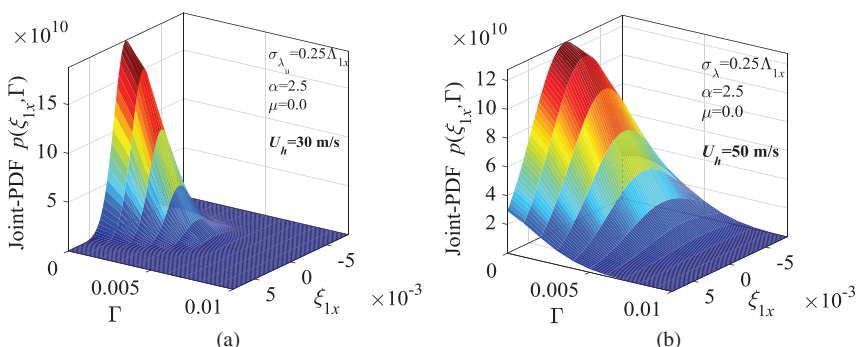


Figure 4. Joint PDF of the along-wind dynamic generalized response ξ_{1x} and power-law intervention cost Γ [Eq. (8)] for the CAARC building with $\alpha = 2.5$, $\mu = 0$, $\Gamma_\tau = 0.30$, $\tau = 0.03$ and $\sigma_{\lambda_u} = 0.25\Lambda_{1x,u}$ at selected U_h : (a) $U_h = 30$ m/s, and (b) $U_h = 50$ m/s

similar results even with qualitatively different cost functions. The cross-correlation coefficient between ξ_{1x} and Γ is variable between approximately 0.20 at $U_h = 30$ m/s and 0.09 at $U_h = 50$ m/s, very similar to the case shown in Figure 3. Inspection of Eq. (8) reveals that the cost function depends on two additional factors (α and μ). It seems, however, that the influence of these two factors on the output standard deviation of the cost function, suggested by the equivalent model of the cost function, is limited. This small difference (qualitatively small) may also be linked to the minimum threshold selected for damage to occur ($\tau = 0.03$); the value of τ is in fact relatively large in comparison with the mean wind speed. Furthermore, since $\mu = 0$ is used, the model ignores the influence of the cross-wind vibration on the damage. It is consequently believed that the combination of these three aspects contributes to the possibly partial influence on the PDF surfaces. In addition, variability in the cost function is essentially controlled by the σ_Γ term (i.e., an equivalent standard deviation), which is constant in this preliminary parametric investigation. Supplementary studies and additional examination have been considered. The results will be presented in the next sub-section.

The effect of the crosswind vibration on the cost and the corresponding probability density function is presented in Figure 5 [$\mu = 1.0$ in Eq. (8)] at selected wind speeds U_h to be compared with the corresponding panels shown in Figure 4. The figures are qualitatively similar to the previous case, indicating that the predictions by stochastic linearization are marginally affected by the choice of the cost function. The examination of the PDF curves tends to confirm the previous observation that the results are mainly influenced by the choice of $\sigma_\Gamma = 0.01$, the standard deviation of the marginal intervention cost, accounting for the variability in the structural maintenance costs.

Figure 6 examines the joint PDF function of the building generalized dynamic response in terms of coordinates ξ_{1x} (along-wind) and ξ_{1y} (crosswind). Two cases are investigated: $U_h = 30$ m/s (Figure 6a) and $U_h = 50$ m/s (Figure 6b). It is worth

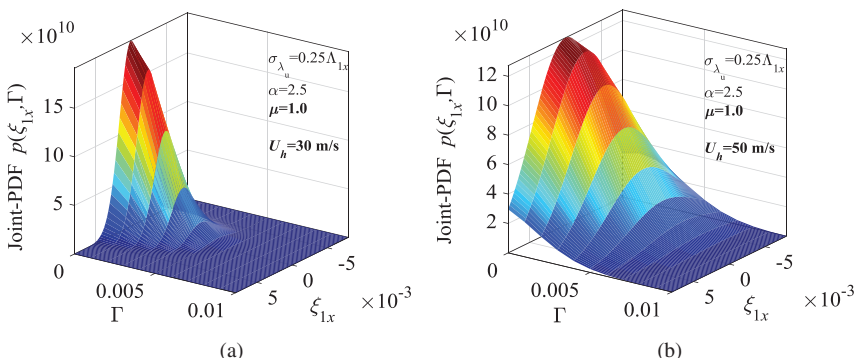


Figure 5. Joint PDF of the along-wind dynamic generalized response ξ_{1x} and power-law intervention cost Γ [Eq. (8)] for the CAARC building with $\alpha = 2.5$, $\mu = 1$, $\Gamma_\tau = 0.30$, $\tau = 0.03$ and $\sigma_{\lambda_u} = 0.25\Lambda_{1x,u}$ at selected U_h : (a) $U_h = 30$ m/s, and (b) $U_h = 50$ m/s

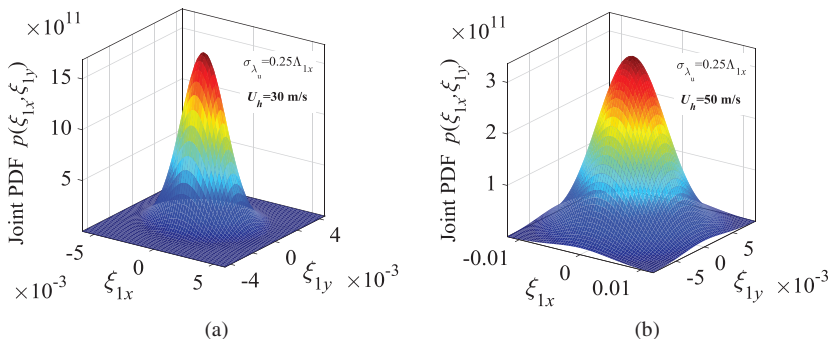


Figure 6. Joint PDF of the dynamic along-wind (ξ_{1x}) and cross-wind (ξ_{1y}) response for the CAARC building with $\alpha = 2.5$, $\mu = 1$, $\Gamma_\tau = 0.30$, $\tau = 0.03$ and $\sigma_{\lambda u} = 0.25\Lambda_{1x,u}$ at selected U_h : (a) $U_h = 30 \text{ m/s}$, and (b) $U_h = 50 \text{ m/s}$

noting that the scales of the axes are different to highlight the variations in the random variables. Even though the cost function depends on both ξ_{1x} and ξ_{1y} , further examination reveals that it does not produce a direct effect on the probability $p(\xi_{1x}, \xi_{1y})$. In fact, similar surface curves (not shown for the sake of brevity in the previous section) have been found.

The maximum value in the PDF graphs of Figure 6 is not the same. This value depends on the integration constant of the probability density function [the scalar quantity depending on the determinant of the covariance matrix Eq. (17)]. This scalar quantity must obey the physical property that the volume, under the joint PDF surface, is one. Once the multi-variable integration constant is determined, the two-variable joint PDF is determined by numerical integration of the full PDF. As the mean wind speed (U_h) increases, the standard deviation (and covariance matrix in general) of the dynamic displacements increases because of the increment in the buffeting loads. Therefore, the integration constant of the multi-variable joint PDF curves (and consequently the two-variable joint PDF) must change accordingly to satisfy the above-described physical property. This aspect is noticeable, for example, from the comparison between Figure 6b and Figure 6a.

Furthermore, the relative increment in the standard deviation (root-mean-square, RMS) value of ξ_{1x} between Figure 6a and Figure 6b is 3 to 1. The variability in the dynamic crosswind response ξ_{1y} is about 30% smaller than the anticipated variability in ξ_{1x} ; this remark is associated with the fact that the model for the dynamic building response in the 1y generalized coordinate neglects the wake effect induced by vortex shedding and tends to under-estimate the experimental results described by Melbourne (1980) for the same range of reduced wind velocities. This aspect has already been observed in a previous study (Caracoglia 2014); nevertheless, this approximation is acceptable in the context of the analysis of the cost model.

One of the advantages of the proposed simulation method is also evident from Figure 6. It would be possible to infer probabilities of exceedance for specific

displacement amplitudes or, in other words, the peak dynamic response as the vector summation between the two components (Chen and Huang 2009) by inspection of the surfaces, for example as described in Cui and Caracoglia (2015). The numerical method described in this study is advantageous since it directly accounts for the partial correlation between along-wind and cross-wind dynamic response. As an example, the correlation coefficient between ξ_{1x} and ξ_{1y} is equal to -0.11 in Figure 6a, confirming the dependency between the two modal response quantities.

Influence of a variation in the power-law cost model parameters, α and τ

A parametric investigation is conducted to examine the dependency of the PDF results on the parameters of the power-law intervention cost model in Eq. (7). The selection of the parameters α and τ has also been inspired by previous studies and the results presented in the previous section. The marginal intervention cost variable is taken as a constant ($\Gamma_\tau = 0.30$) since it is a linear proportionality term that alters the probability results (i.e., the scale) without influencing the shape (i.e., the dispersion) of the probability functions. Therefore, the supplementary simulations consider simultaneous variations of α and τ , with $\alpha = \{1.5, 3.0\}$ and $\tau = \{0.03, 0.05\}$. The range of τ values is based on previous exploratory studies (Caracoglia 2014) on the same building, whereas the values of α are selected to be above and below the non-proportional case with $\alpha = 2.0$, which also corresponds to the simplified cost model.

This choice is believed to be sufficient for exploring an adequate range of the parameter space; additional values of τ will be considered in a subsequent section of this paper. The dynamic response of the CAARC building at the reference mean wind speed $U_h = 50$ m/s (maximum wind speed) and for MCL error with $\sigma_{\lambda u} = 0.25\Lambda_{1x,u}$ under various combinations of α and τ , is computed. The other parameters of the cost model equation are taken as $\mu = 1$ (i.e., accounting for the simultaneous effect of along-wind and cross-wind dynamic response on the damage; the diffusion term), describing the cost variability in Eq. (8), is set to $\sigma_\Gamma = 0.01$ in this section. The PDF surfaces are not presented for the sake of brevity. The main results are quantitatively summarized in Table 2; neither an increment of damage threshold τ nor a variation in the power-law exponent produces a perceptible effect on the $p(\xi_{1x}, \Gamma)$ curves.

The analysis of the results tends to suggest a limited variability of the joint-PDF function, approximated by stochastic linearization. The differences among the three cases cannot qualitatively be discerned: the variation in the correlation coefficient between ξ_{1x} and Γ , as reported in Table 1 is not visible up to the second significant digit.

Influence of cost variability (σ_Γ) in the power-law cost model

A supplementary parametric study is carried out to examine the role of the diffusion term on the joint PDF functions. The study only considers the effect of a

Table 2. Correlation Coefficient $\rho_{\xi_{1x}, \Gamma}$ for the CAARC Building at $U_h = 50 \text{ m/s}$, with Loading Error $\sigma_{\lambda_u} = 0.25\Lambda_{1x,u}$ Intervention-cost Standard Deviation $\sigma_\Gamma = 0.01$ and with $\mu = 1$, $\Gamma_\tau = 0.30$

Minimum damage threshold, τ	Power law exponent, α	Correlation coefficient, $\rho_{\xi_{1x}, \Gamma}$
0.03	1.5	0.091
0.03	3.0	0.091
0.05	1.5	0.091

variation in the diffusion parameter σ_Γ applied to the power-law intervention cost equation [Eq. (8)]. The diffusion term, describing the cost variability and set to $\sigma_\Gamma = 0.01$ in the previous sections, is presently altered. Two additional values are explored in this section: $\sigma_\Gamma = 0.025$ and $\sigma_\Gamma = 0.05$. This proposition corresponds to 2.5 times and 5.0 times larger cost variability. It must be noted that the coefficient σ_Γ can be related to a physical measure of variability in the anticipated structural maintenance costs. For example, a small value of σ_Γ can be associated with a system in which the exceedance of the threshold τ for damage to occur leads to a “well defined” structural damage scenario, for example repair needed in selected areas of the façade. On the contrary, a large value of σ_Γ can be employed to simulate a less predictable damage scenario, for example distributed on large portions of the façade.

A higher cost variability (i.e., a larger σ_Γ) can result in a non-negligible increment of the randomness in the function Γ in Eq. (8). This remark is confirmed by the analysis of the numerical simulation results, used to derive the joint PDF $p(\xi_{1x}, \Gamma)$ between the intervention cost variable Γ and the generalized dynamic along-wind response ξ_{1x} in Figure 7. This figure illustrates the $p(\xi_{1x}, \Gamma)$ function, obtained for the CAARC building under stationary wind loads with mean wind speed $U_h = 50 \text{ m/s}$ and zero-mean MCL error λ_u with standard deviation $\sigma_{\lambda_u} = 0.25\Lambda_{1x,u}$.

The intervention cost equation in Figure 7 simulates the scenario, in which the damage is computed by considering the instantaneous vector summation between along-wind and cross-wind dynamic response [$\mu = 1$ in Eq. (8)]. The cost analysis is based on the following additional parameters: $\alpha = 2.5$ (power-law exponent), $\Gamma_\tau = 0.30$ (marginal intervention cost at first damage crossing) and $\tau = 0.03$ (damage threshold). The figure presents the two probability surfaces determined with $\sigma_\Gamma = 0.025$ (Figure 7a) and $\sigma_\Gamma = 0.050$ (Figure 7b). For comparison purposes, the same damage scenario simulation can be found in Figure 5a with $\sigma_\Gamma = 0.010$. For adequate interpretation of the results, it must be noted that the scale of the horizontal axes is not the same between Figure 5 and Figure 7 (smaller in Figure 7). Examination of Figure 7 reveals that the shape of the $p(\xi_{1x}, \Gamma)$ surfaces tends to be determined by the increment of σ_Γ . The doubling in the standard deviation of the equivalent system between Figure 7a and Figure 7b is adequately captured by stochastic linearization. In the probability surfaces the “interaction”

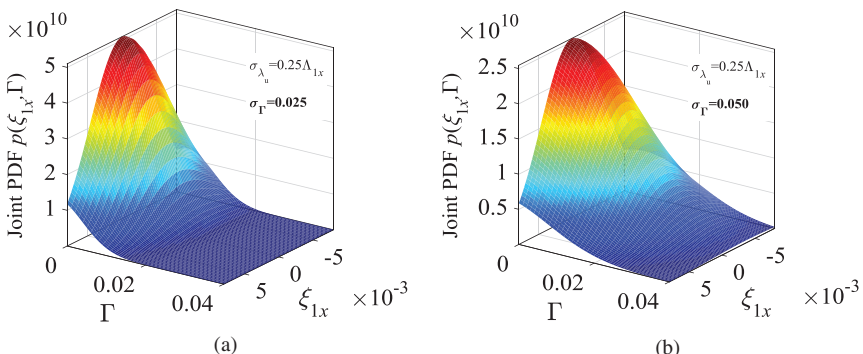


Figure 7. Joint PDF $p(\xi_{1x}, \Gamma)$ at mean wind speed $U_h = 50$ m/s and MCL error with $\sigma_{\lambda_u} = 0.25\Lambda_{1x,u}$ as a function of the cost standard deviation σ_Γ [Eq. (8)] (other cost model parameters are: $a = 2.5$, $\mu = 1$, $\Gamma_\tau = 0.30$, $\tau = 0.03$): (a) $\sigma_\Gamma = 0.025$, and (b) $\sigma_\Gamma = 0.050$

(not the correlation) between the cost variable Γ and the generalized along-wind dynamic response ξ_{1x} is almost imperceptible beyond $\Gamma > 0.02$ and $|\xi_{1x}| > 0.005$. On the contrary, this effect is more visible and no longer negligible for the same range of values in Figure 7b. As expected, amplification of cost variability, simulated through the variable σ_Γ , produces a progressive widening of the probability surfaces. It must be noted that large values in the joint PDF functions are locally expected because of the numerical integration procedure, used for the reduction of the multi-variable PDF to a two-variable surface. The random variables of the vector \mathbf{W} are centered since the effect of the mean load is zero (assumption re-examined in more detail in the next section). Therefore, the joint PDF surfaces are approximately symmetrical due to the stochastic linearization. High local values in the joint PDF surfaces are possible since distributions are still relatively narrow and despite the “widening” of the surfaces, induced by the increment of σ_Γ .

Additional inspection of the numerical results in Figure 7 reveals that, even though the curve $p(\xi_{1x}, \Gamma)$ is influenced by the variation of σ_Γ , the influence on the actual correlation coefficient between ξ_{1x} and Γ ($\rho_{\xi_{1x}, \Gamma}$) is not very significant. This remark suggests that the proposed cost relationship most likely acts as an exogenous variable, which is marginally coupled with the dynamical system model. It is also believed that this perhaps limited importance may be influenced by the solution method. In other words, the stochastic linearization may not be fully efficient in detecting small variations of probability and statistical properties, induced by the nonlinearity in Eq. (8). Alternative solution methods, not discussed in this study but available in Caracoglia (2016) may be considered to identify these features.

Examination of the cost alone (or the cost variability) may be of interest to the user. In order to evaluate the cost from the PDF surfaces shown in this figure (and similar figures in previous sections) the marginal PDF needs to be computed; this task can be accomplished by numerical integration of the PDF surface $p(\xi_{1x}, \Gamma)$ along the ξ_{1x} direction.

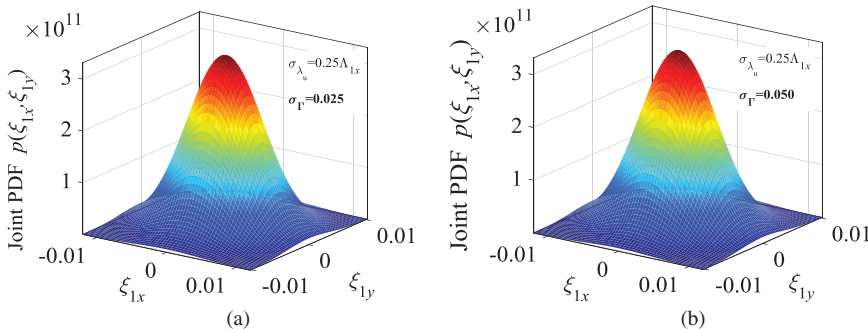


Figure 8. Joint PDF $p(\xi_{1x}, \xi_{1y})$ at mean wind speed $U_h = 50$ m/s and MCL error with $\sigma_{\lambda u} = 0.25\Lambda_{1x,u}$ as a function of the cost standard deviation σ_Γ [Eq. (8)] (other cost model parameters are: $\alpha = 2.5$, $\mu = 1$, $\Gamma_\tau = 0.30$, $\tau = 0.03$): (a) $\sigma_\Gamma = 0.025$, and (b) $\sigma_\Gamma = 0.050$

Figure 8 depicts the joint PDF $p(\xi_{1x}, \xi_{1y})$ at mean wind speed $U_h = 50$ m/s and MCL error with $\sigma_{\lambda u} = 0.25\Lambda_{1x,u}$. It accounts for an increment in the cost variability through σ_Γ , by varying it from $\sigma_\Gamma = 0.025$ to $\sigma_\Gamma = 0.050$. This figure is obtained under the same above-described assumptions on wind speed, lateral load and cost analysis model in Figure 7. Moreover, it corresponds to the surface plot between the two dynamic random vibration quantities, ξ_{1x} and ξ_{1y} , in Figure 6b with smaller σ_Γ . The two scenarios with increasing σ_Γ qualitatively produce the same $p(\xi_{1x}, \xi_{1y})$ surface. Additional inspection of the covariance matrix used by Eq. (16) indicates that the same standard deviations of the marginal PDF of either ξ_{1x} or ξ_{1y} , taken individually, is found in both cases shown in Figure 8a and Figure 8b: the correlation coefficient between ξ_{1x} or ξ_{1y} is equal to -0.103 in both cases.

This last observation tends to confirm the previous remark on the exogenous nature of the variable Γ , exhibited by the numerical model.

EXTENDED COST MODEL WITH STATIC LOAD EFFECT: NUMERICAL RESULTS

In this section the model described in Eqs. (18–23) is examined and applied to the study of the CAARC building once again. The parametric investigation is restricted to a sub-set of representative cases, selected among the results emerged from the preceding studies, presented in the previous sections. The wind load error variability (MCL) is taken as $\sigma_{\lambda u} = 0.25\Lambda_{1x,u}$. In the new analyses, the power-law cost model with the following constant parameters, is considered: exponent $\alpha = 2.5$, marginal intervention cost $\Gamma_\tau = 0.30$; the other parameters, namely the cost standard deviation σ_Γ and the minimum damage/vibration threshold τ , have been varied instead as follows: $\sigma_\Gamma = \{0.10, 0.25\}$ and minimum threshold $\tau = \{0.004, 0.006, 0.300\}$. The three τ values are respectively located between a small (equal to $0.4\%D_x = 0.12$ m) and a moderately large ($3\%D_x = 0.91$ m) roof-top displacement

in the full-scale structure. The core simulations are also carried out at two reference wind speeds, $U_h = \{30\text{m/s}, 50\text{m/s}\}$. The main results are illustrated in Figure 9 and Figure 10. All the numerical cases are summarized in Table 3.

The static mead load effect, simulated through the constant vector $\mathbf{w}_\Gamma^{(m)}$ in Eq. (22) of the extended formulation, is needed to compute and update the magnitude of the random generalized lateral displacement δ_{tot} (i.e., physically the displacement of the roof top normalized with respect to D_x). It must be recalled that δ_{tot} is based on the modal truncation considering shapes Φ_{1x} and Φ_{1y} only [i.e., given by $\xi_{1x}^{(m)}$ (along-wind) and $\xi_{1y}^{(m)}$ (cross-wind)]. Given the specific building geometry and initial mean-wind incidence angle orthogonal to the vertical face with horizontal dimension D_y (Figure 1), it is concluded that $\xi_{1y}^{(m)} \approx 0$. In contrast, preliminary evaluation of $\xi_{1x}^{(m)}$ is carried out before the stochastic simulations.

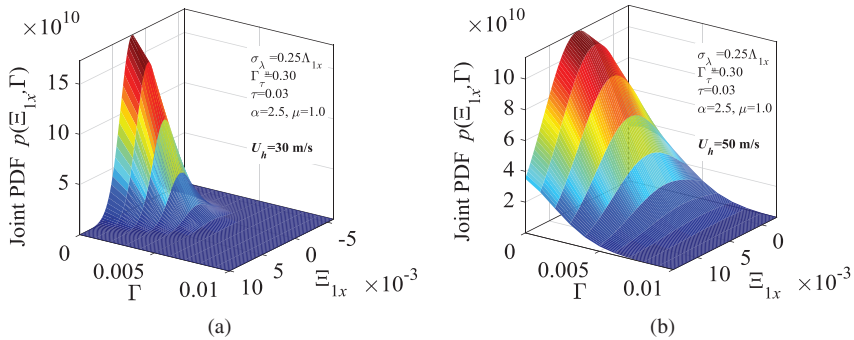


Figure 9. Influence of the generalized static response on the joint PDF $p(\Xi_{1x}, \Gamma)$ at selected wind speeds (model parameters are: MCL error with $\sigma_{\lambda u} = 0.25\Lambda_{1x,u}$; power-law cost model with $\alpha = 2.5$, $\mu = 1$, $\Gamma_\tau = 0.30$, $\tau = 0.03$, $\sigma_\Gamma = 0.01$): (a) $U_h = 30 \text{ m/s}$, and (b) $U_h = 50 \text{ m/s}$

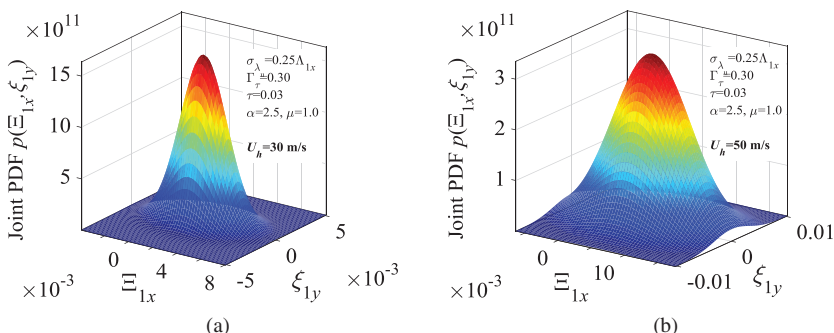


Figure 10. Influence of the generalized static response on the joint PDF $p(\Xi_{1x}, \xi_{1y})$ at selected wind speeds (model parameters are: MCL error with $\sigma_{\lambda u} = 0.25\Lambda_{1x,u}$; power-law cost model with $\alpha = 2.5$, $\mu = 1$, $\Gamma_\tau = 0.30$, $\tau = 0.03$, $\sigma_\Gamma = 0.01$): (a) $U_h = 30 \text{ m/s}$, and (b) $U_h = 50 \text{ m/s}$

Table 3. Influence of the Static Wind Load Effect on the Correlation Coefficient $\rho_{\xi_{1x}, \Gamma}$ at selected U_h and for Several Non-structural Damage and Cost Cases for the CAARC Building

Wind speed, U_h [m/s]	Generalized along-wind static response, $\xi_{1x}^{(m)}$	Cost standard deviation, σ_Γ	Min. damage threshold, τ	Correlation coefficient, $\rho_{\xi_{1x}, \Gamma}$
30	0.0020	0.10	0.004	0.1678
		0.10	0.030	0.1576
		0.25	0.030	0.1577
50	0.0057	0.10	0.004	0.1625
		0.10	0.006	0.1053
		0.10	0.030	0.0843
		0.25	0.030	0.0847

(Other model parameters are: MCL loading error with $\sigma_{\lambda u} = 0.25\Lambda_{1x,ui}$; power-law cost model with exponent $\alpha = 2.5$, $\mu = 1$, marginal cost $\Gamma_t = 0.30$)

In this section the total response in the along-wind direction, cumulating static and quasi-static effects, is labeled as $\Xi_{1x} = \xi_{1x}^{(m)} + \xi_{1x}$.

The values of the along-wind generalized static displacement, predicted by the model, vary between 0.0020 at $U_h = 30$ m/s and 0.0057 at $U_h = 50$ m/s, approximately corresponding to 0.06 m and 0.18 m at full scale. These values are compatible with the predictions by [Melbourne \(1980\)](#), respectively around 0.0039 and 0.0110 in dimensionless units; some differences are noticeable. They are possibly related to the selection of the force coefficients, in particular C_D , and the boundary layer wind profile. A better match of the mean response, against the experimental results discussed by [Melbourne \(1980\)](#), may be achieved if a larger value of C_D is used. Refer, for example, to simulation results by Cui and [Caracoglia \(2015\)](#). In any case, the present results are acceptable in the context of this investigation and compatible with previous validations of the model in [Caracoglia \(2014\)](#).

The probability surfaces, predicted by the model and illustrated in Figure 9 and Figure 10, are substantially in line with the anticipations. In comparison with the basic formulation, which neglects the effect of the static wind load, the qualitative appearance of the $p(\Xi_{1x}, \Gamma)$ in Figure 9 at $U_h = 30$ m/s and $U_h = 50$ m/s is similar to Figure 3b and Figure 3d, respectively. Even though the variability (i.e., the standard deviation) of the surface plots is dominated by the effect of $\sigma_\Gamma = 0.01$, which is the same in both models, the extended formulation exhibits some variations in the cross-correlation between ξ_{1x} and Γ , $\rho_{\xi_{1x}, \Gamma}$, if the case with $\sigma_\Gamma = 0.01$ is examined (Table 3).

For example, the cross-correlation reduces slightly for both $U_h = 50$ m/s (from 0.09 in Figure 3d to 0.08 in Figure 9b) and $U_h = 30$ m/s (from 0.170 in Figure 3d to 0.158 in Figure 9b). As expected, the PDF surfaces are no longer

centered at the origin in both Figure 9 and Figure 10 because $\xi_{1x}^{(m)} \neq 0$. This influence is clearly more noticeable at a higher wind speed, for example in Figure 10b, with the surface plot exhibiting a shift towards the positive side along the Ξ_{1x} axis. The cross-correlation between along-wind and cross-wind responses is also affected, moving from -0.11 at $U_h = 30$ m/s to -0.09 at $U_h = 50$ m/s. These values are, however, the same as the ones presented in Figure 3 and corresponding investigations. As expected, nonlinearity in the cost model does not have an indirect impact on the probability of the response. Nevertheless, there is a non-negligible influence on the joint probability between Ξ_{1x} and Γ as shown in Table 3 especially at very large wind speeds $U_h = 50$ m/s.

Furthermore, the simultaneous reduction of the non-structural damage threshold τ at $U_h = 50$ m/s (with $\tau = 0.004$ slightly smaller than the generalized along-wind static response) and reduction of cost standard deviation ($\sigma_\Gamma = 0.10$) are responsible for an increment in the correlation between the cost and the response. This trend is expected as the occurrence of damage becomes more frequent if τ is reduced and, therefore, the dependency between the cause [i.e., through the combination of $(\xi_{1x}^{(m)} + \xi_{1x})$ and ξ_{1y}] and effect is more relevant.

On the contrary, there is a clearer influence of the non-structural damage threshold τ on the joint PDF of probability distribution $p(\xi_{1x}, \Gamma)$. This aspect is discernible from the inspection of the table. As the minimum vibration and non-structural damage threshold slightly increases from $\tau = 0.004(\tau < \xi_{1x}^{(m)})$ to $\tau = 0.006(\tau > \xi_{1x}^{(m)})$ the correlation coefficient decreases from 16% to about 10%, suggesting that the role of $\xi_{1x}^{(m)}$ may not be neglected when the magnitudes of τ and the $\xi_{1x}^{(m)}$ coincide. With a larger value of $\tau = 0.030$, the correlation tends to increase again but becomes almost coincident with the values observed with the basic model formulation; an imperceptible difference is noted between $p_{\xi_{1x}, \Gamma} \approx 0.08$ in Table 3 and $p_{\xi_{1x}, \Gamma} \approx 0.09$ found in the previous sections. In this last case, the role of the “resonant component” of the wind-induced response possibly tends to dominate and controls the occurrence of non-structural damage. The partial correlation is an effect of the nonlinear relationships expressed in Eq. (14) or Eq. (23) and the choice of the non-structural damage model (Figure 2).

The previous remarks on intervention cost, cost variability and their evaluation are based on the use of the dimensionless variable Γ_τ , which is a marginal (or initial) intervention cost normalized to the construction cost of the building structure. The use of a dimensionless variable Γ_τ is preferable because it allows generalization of the model. This type of models may be used, for example, for comparison purposes between design options or structural configurations. This choice is compatible with recent studies on the examination of the intervention costs for structural dynamic analysis of tall buildings. Furthermore, even though monetary data are not provided explicitly, it would still be possible for a user to ascertain monetary costs because Γ_τ can be linked to actual monetary quantities. For instance, the value Γ_τ can readily be altered if more information about the structural costs is available.

All the previous observations must be, however, clearly interpreted in the context of the stochastic linearization, which unavoidably alters the exact solution

of Eqs. (11) and (22). Inspection of the residuals, associated with the minimization process needed by the stochastic algorithm (refer, e.g., to the numerical procedure described in Caracoglia 2014), indicates that, when τ is large and the likelihood of damage is smaller, the residuals decrease (by almost one order of magnitude) as opposed to the case with $\tau = 0.004$ and more frequent exceedance of the damage threshold. It is possibly suggested that accuracy of the linearized solution may become dubious with these special cases, in comparison with a more rigorous nonlinear solution of the stochastic equations and probability at steady-state (Kloeden et al. 1994, Soize 1988). This aspect requires careful consideration that is beyond the scope of this investigation.

CONCLUSIONS

This paper presented the results of a research activity devoted to the examination of parametric uncertainty propagation through aeroelastic systems, in particular tall flexible buildings, subjected to high wind loads. The study context is linked to the field of performance-based wind engineering. The study, described in this paper, is an extension to a series of recent investigations on the use of stochastic calculus and reduced-order models to examine the propagation of experimental or modeling uncertainty in the lateral along-wind and cross-wind loads on the response of the CAARC building. A generalized random variable is used to simulate the intervention costs, associated with wind-induced damage. In this paper, the original equation of the intervention cost model was critically revised and examined in detail by means of parametric investigations.

The main contributions of this study are: (i) derivation of a new generalized intervention cost model, which accounts for both along-wind and cross-wind dynamic response in its basic form along with the static wind load effects in its extended form; (ii) parametric investigation on the joint probability $p(\xi_{1x}, \xi_{1y})$ of the generalized dynamic building response (coincident with along-wind and cross-wind roof-top displacements in the two principal directions) and on the joint probability between the random intervention cost variable and the generalized along-wind building response $p(\xi_{1x}, \Gamma)$; (iii) identification of the main factor (coefficient σ_Γ) contributing to variations in the $p(\xi_{1x}, \Gamma)$; and (iv) influence of the static wind load and mean structural response on the non-structural damage and the probabilities of the intervention costs. Based on the applications of each model and the results of the investigations, the use of the extended intervention cost model, combined with the power-law cost function [Eq. (20) and Eq. (21)], is recommended. The cost equation is in fact more general and its parameters can suitably be altered to simulate a potential wider range of scenarios and building configurations. In addition, it more correctly accounts for the dependency of damage and intervention cost on the mean load effect.

Current studies are directed toward the extension and implementation of this approach to non-stationary winds, such as thunderstorms, starting from the formulations presented in recent investigations (Le and Caracoglia 2015). Future

studies should also consider the use of alternative methodologies for the solution of the stochastic differential problem; re-examination of the stochastic linearization for highly nonlinear reduced-order models is possibly needed. Finally, wind-induced non-structural failures are also very common on the envelope of low-rise buildings. The present model could potentially be adapted to examine this category of buildings, even though some modifications are necessary. Contrary to tall buildings, the response does not involve dynamic amplification effects (the main aspect examined in this study). The model should possibly be revised in such cases to more accurately account for quasi-static load effects.

ACKNOWLEDGMENTS

This work was supported in part by the National Science Foundation (NSF) of the United States, CAREER Award CMMI-0844977 in 2009–2014. The author would also like to acknowledge the support of NSF Award CMMI-1434880 in 2014–2018; the study, described in this document, is a preliminary investigation for the implementation of computer-based methods to study damage and repair costs due to non-stationary wind loads on tall buildings. Any opinions, findings and conclusions or recommendations are those of the author and do not necessarily reflect the views of the sponsoring agency.

References

- Barbato, M., A. Palmeri, and F. Petrini. 2014. “Special issue on performance-based engineering.” *Eng. Struct.* **78**: 1–2.
- Barbato, M., F. Petrini, V. U. Unnikrishnan, and M. Ciampoli. 2013. “Performance-based hurricane engineering (PBHE) framework.” *Struct. Saf.* **45**: 24–35.
- Caracoglia, L. 2014. “A stochastic model for examining along-wind loading uncertainty and intervention costs due to wind-induced damage on tall buildings.” *Eng. Struct.* **78**: 121–132.
- Caracoglia, L. 2015. “Investigating the quantification of intervention costs due to wind-induced damage on tall buildings.” In *14th Int. Conf. on Wind Engineering (ICWE14)*. Porto Alegre, Brazil: Federal Univ. of Rio Grande do Sul.
- Caracoglia, L. 2016. “Comparison of reduced-order models to analyze the dynamics of a tall building under the effects of along-wind loading variability.” *ASCE-ASME J. Risk Uncertainty Eng. Syst. Part A Civil Eng.* **2** (2): C4015002.
- Caughey, T. K. 1963. “Equivalent linearization techniques.” *J. Acoust. Soc. Am.* **35** (11): 1706–1711.
- Chen, X., and G. Huang. 2009. “Evaluation of peak resultant response for wind-excited tall buildings.” *Eng. Struct.* **31** (4): 858–868.
- Cui, W., and L. Caracoglia. 2015. “Simulation and analysis of intervention costs due to wind-induced damage on tall buildings.” *Eng. Struct.* **87**: 183–197.
- Elishakoff, I., and G. Q. Cai. 1993. “Approximate solution for nonlinear random vibration problems by partial stochastic linearization.” *Prob. Eng. Mech.* **8** (3–4): 233–237.

- Goulet, C. A., C. B. Haselton, J. Mitrani-Reiser, J. L. Beck, G. G. Deierlein, K. A. Porter, and J. P. Stewart. 2007. "Evaluation of the seismic performance of a code-conforming reinforced-concrete frame building - From seismic hazard to collapse safety and economic losses." *Earthquake Eng. Struct. Dyn.* **36** (13): 1973–1997.
- Grigoriu, M. 2002. *Stochastic calculus: Applications in science and engineering*. Boston, MA: Birkhäuser.
- Jain, A., M. Srinivasan, and G. C. Hart. 2001. "Performance based design extreme wind loads on a tall building." *Struct. Des. Tall Build.* **10** (1): 9–26.
- Kloeden, P. E., E. Platen, and H. Schurz. 1994. *Numerical solution of stochastic differential equations through computer experiments*. Berlin: Springer.
- Le, T.-H., and L. Caracoglia. 2015. "Reduced-order Wavelet-Galerkin solution for the coupled, nonlinear stochastic response of slender buildings in transient winds." *J. Sound Vib.* **344**: 179–208.
- Lin, Y. K., and G. Q. Cai. 1995. *Probabilistic structural dynamics*. New York: McGraw-Hill.
- Martens, W., U. Von Wagner, and V. Mehrmann. 2012. "Calculation of high-dimensional probability density functions of stochastically excited nonlinear mechanical systems." *Nonlinear Dyn.* **67** (3): 2089–2099.
- Melbourne, W. H. 1980. "Comparison of measurements on the CAARC standard tall building model in simulated model wind flows." *J. Wind Eng. Ind. Aerodyn.* **6** (1–2): 73–88.
- Naess, A. 1995. "Prediction of extreme response of nonlinear structures by extended stochastic linearization." *Prob. Eng. Mech.* **10** (3): 153–160.
- Piccardo, G., and G. Solari. 2000. "3D wind-excited response of slender structures: Closed-form solution." *J. Struct. Eng.* **126** (8): 936–943.
- Pita, G., and J. Mitrani-Reiser. 2013. "Modeling hurricane-induced building downtime." In *2th Americas Conf. on Wind Engineering (12ACWE), American Association for Wind Engineering (AAWE)*. CD-ROM: Seattle, WA.
- Pozzuoli, C., G. Bartoli, U. Peil, and M. Clobes. 2013. "Serviceability wind risk assessment of tall buildings including aeroelastic effects." *J. Wind Eng. Ind. Aerodyn.* **123**: 325–338.
- Ricciardi, G. 2007. "A non-Gaussian stochastic linearization method." *Prob. Eng. Mech.* **22** (1): 1–11.
- Simiu, E., and R. H. Scanlan. 1996. *Wind effects on structures*, 3rd ed. New York: Wiley.
- Soize, C. 1988. "Steady-state solution of Fokker-Planck equation in higher dimension." *Prob. Eng. Mech.* **3** (4): 196–206.
- Solari, G. 1988. "Equivalent wind-spectrum technique: Theory and applications." *J. Struct. Eng.* **114** (6): 1303–1323.
- Spanos, P. D. 1981. "Stochastic linearization in structural dynamics." *Appl. Mech. Rev.* **34** (1): 1–8.
- Spence, S. M. J., and A. Kareem. 2014. "Performance-based design and optimization of uncertain wind-excited dynamic building systems." *Eng. Struct.* **78**: 133–144.
- Yeo, D., and E. Simiu. 2011. "High-rise reinforced concrete structures: Database-assisted design for wind." *J. Struct. Eng.* **137** (11): 1340–1349.

This page intentionally left blank

CHAPTER 3

Wind Response Control of Tall Buildings with Flexible Foundation using Tuned Mass Dampers

Said Elias^{*}
Vasant Matsagar[†]

Abstract: Wind response control of tall buildings on flexible foundation using multiple tuned mass dampers (MTMDs) is studied. The MTMDs are installed at the top of the reinforced concrete (RC) buildings duly considering soil-structure interaction (SSI). The rigid circular foundation and the surrounding soil are modeled by considering frequency independent constants for the springs and dashpots. The time domain wind analysis based on Newmark's method of average acceleration is employed for the non-classically damped system. The performance of the MTMDs is compared with the case of single tuned mass damper (STMD). The displacement and acceleration response at the top of the building under the along-wind and across-wind forces are computed to study the effectiveness in installing the STMD and MTMDs. It is concluded that the soil type does affect the design parameters of the STMD and MTMDs, and wind response of the building on the flexible foundation. Furthermore, the MTMDs are found to be more effective than the STMD.

Keywords: Multiple tuned mass dampers (MTMDs); Soil-structure interaction (SSI); Tall buildings; TMD; Wind forces.

*Research Assistant at the Multi-Hazard Protective Structures (MHPS) Laboratory, Department of Civil Engineering, Indian Institute of Technology (IIT) Delhi, New Delhi - 110 016, India; email: eliasraimi959@gmail.com

†Associate Professor and Faculty Laboratory-in-Charge of the Multi-Hazard Protective Structures (MHPS) Laboratory, Department of Civil Engineering, Indian Institute of Technology (IIT) Delhi, New Delhi - 110 016, India; email: matsagar@civil.iitd.ac.in

INTRODUCTION

Vibrations experienced by the tall buildings under the wind action occur in the along-wind and in the across-wind directions. Along-wind vibrations consist of background and resonant components. The background is the quasi-static part which replicates the stochastic and broad-band nature of the incoming flow, while the dynamic contribution due to resonance to turbulence is the characteristics of the resonant component. [Davenport \(1962\)](#) developed gust response concept, which is the basis for the contemporary design wind load models, to account for along-wind vibrations. In the low frequency range, wind spectrum has significant energy contained and the structural frequencies coincide with the high frequency content of the wind excitation. Resonant component of the gust becomes significant, otherwise background vibrations predominate. The across-wind vibration is caused mainly by vortices generated in the building's wake. The vibration is not so large for the low-rise buildings having aspect ratio less than five. However, as per the Indian standard (IS) 875 - Part 3 (1987), a building is considered wind-sensitive if its aspect ratio is greater than five; and, the static analysis is no more recommended in such case. In the high-rise buildings with increased aspect ratio (generally above six), a vortex with a strong period is uniformly generated in the transverse direction, and the across-wind forces tend to increase. However, with increasing building height, the natural frequency decreases and it approaches the vortex shedding frequency. As a result, resonance components increase and the dynamic responses of the building become large. In general, responses to the across-wind vibration depending on wind speed increase more rapidly than the responses to the along-wind vibration. Therefore, it is recommended to consider both the along-wind and across-wind cases for the design of the wind-sensitive tall buildings. Further, the philosophy for the analysis of a structure under wind and earthquake are different. The vibration control of buildings with tuned mass damper (TMD) under wind and earthquake is well-established. Conventionally, the TMDs have been employed with fairly good results in the tall structures for suppressing dynamic response.

[Kareem \(1983\)](#) discussed the serviceability of buildings and various means of limiting the objectionable levels of motion, wherein the TMD was shown useful for mitigating objectionable levels of motion in the tall buildings. [Hadi and Arfiadi \(1998\)](#) used genetic algorithms (GAs) to optimize the parameters of the TMD under seismic excitations. Recently, [Elias and Matsagar \(2015\)](#) reported a detailed parametric study on the effectiveness of the TMDs in earthquake and wind response control in buildings. It is well-understood that two sources of excitation exist for dynamic response control of the tall building with the TMD. The first source is the TMD mass and second is the interactive force between the TMD and the tall building. In general, for wind excitation case, the force applied on the TMD is basically caused by interactive force. However, in case of the earthquake excitation, the force applied on the TMD is caused by both the sources. In addition, a TMD designed for earthquake may not be effective for the wind-sensitive tall buildings, which mandates multi-hazard analysis and design.

Effectiveness of a single TMD (STMD) may be reduced as a result of small offset in the frequency tuning; and larger detuning, in fact, amplifies the vibration response instead of reducing it. Therefore, the concept of multiple tuned mass dampers (MTMDs) attracted the attention of researchers and structural engineers. [Xu and Igusa \(1992\)](#) examined vibration control capabilities of the MTMDs with the frequencies distributed over a wide bandwidth. They concluded that the MTMDs are more effective and robust than the STMD for the same mass ratio. [Kareem and Kline \(1995\)](#) showed the effective performance of the MTMDs under random wind forces. Later, many researchers such as [Li \(2000, 2002\)](#); [Bakre and Jangid \(2004\)](#), and [Han and Li \(2008\)](#) optimized the parameters of the MTMDs and reported their improved performance. [Patil and Jangid \(2011\)](#) used optimum MTMDs to control the wind response of the benchmark building and showed their effectiveness. Distributed multiple tuned mass dampers (d-MTMDs) are most effective to control the across-wind vibration of 76-storey benchmark building, as shown by [Elias and Matsagar \(2014a and 2014b\)](#).

Generally, in wind engineering the research work related to structures with the TMDs considering the soil-structure interaction (SSI) is rather limited. [Liu et al. \(2008\)](#) found that the TMDs were more effective in suppressing structural oscillations for the higher soil stiffness and the SSI is required to be accounted for accurate predictions with low soil stiffness. All the aforementioned studies considered only one-direction of the wind forces. [Aly et al. \(2011\)](#) compared the response control in the tall buildings subjected to multi-directional wind forces. The study indicated that less guidance is available in the codes for estimation of the critical cross-wind forces. [Aly \(2014a, 2014b\)](#) proposed the robust vibration control of the tall structures subjected to multi-directional wind forces. These studies showed that controller schemes need to be robust while there is uncertainty in the parameters of the structures. Therefore, it will be interesting to study the performance of the TMDs in the along-wind and across-wind dynamic response control of tall building, while duly taking into account the SSI effects. In this study, the MTMDs are installed at the top of the building while subjected to both the along-wind and across-wind forces. The effectiveness of the MTMDs in wind response control of the building is compared with the STMD.

MATHEMATICAL MODELING

A 76-storey benchmark building proposed by [Yang et al. \(2004\)](#), and used for assessing structural control performance by several researchers, is adopted in this study. The authors could not find any study that takes in to account both the along-wind and across-wind forces applied on the 76-storey benchmark building. It is seemingly due to the fact that the aspect ratio of the building, i.e. height to width ratio is 7.3, which makes it more dominated under the across-wind forces. Also, the effects of the SSI on the dynamic response control of the 76-storey benchmark building have been ignored. In view of this, in order to check the

performance of the STMD and MTMDs, the effects of the SSI are included in this study, along with considering both components of the wind forces applied. The along-wind and across-wind forces need not be applied simultaneously because there is no correlation between them as per Aly and Abburu (2015). Figure 1(a) shows the three dimensional (3D) model of the 76-storey benchmark building and definition of the wind forces and directions. Figure 1(b) shows the elevation of the benchmark building with all the MTMDs installed at the top floor, and mathematic model of the benchmark building included with the SSI is shown in Figure 1(c). Figure 1(a–c) also shows N degree of freedom (DOF) building with n DOF TMDs, and two DOF due to consideration of the SSI effects. Mass and moment of inertia for each DOF of the building are indicated as M_i and I_i , and those of the foundation are shown as M_0 and I_0 , respectively. The stiffness and

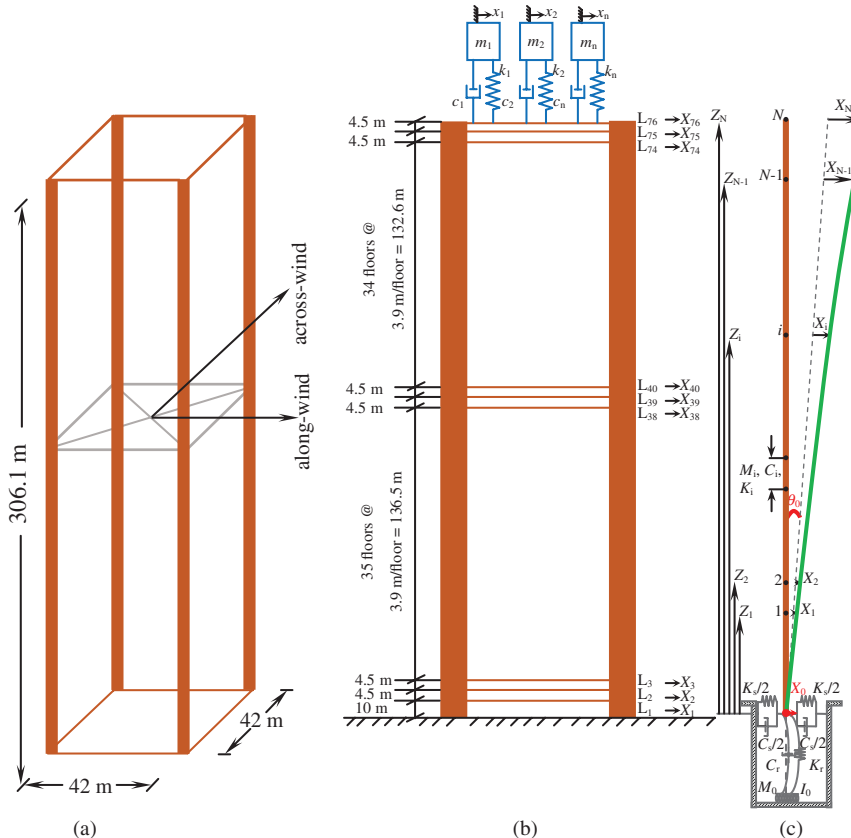


Figure 1. (a) Three dimensional (3D) model of the 76-storey benchmark building, (b) the benchmark building installed with MTMDs all at top floor, and (c) mathematic model of the benchmark building included with the SSI

damping between the DOFs are shown as K_i and C_i , respectively. The mass, stiffness, and damping of the TMDs are respectively denoted as m_i , k_i , and c_i . The stiffness of the swaying and rocking springs are represented as K_s and K_r , and the damping in the corresponding dashpots are indicated as C_s and C_r , respectively. The governing equations of motion for the wind-excited benchmark building duly considering the SSI effect, installed with the STMD and all MTMDs at the top floor are obtained by ensuring equilibrium of the forces at the location of each degree of freedom as follows:

$$[M_s]\{\ddot{x}_s\} + [C_s]\{\dot{x}_s\} + [K_s]\{x_s\} = \{F_t\} \quad (1)$$

where $[M_s]$, $[C_s]$, and $[K_s]$ are the mass, damping, and stiffness matrices of the building, respectively of order $(N+n+2) \times (N+n+2)$. Here, N indicates DOF for the building and n indicates DOF for the STMD and MTMDs. Additionally, $\{F_t\}$ is the wind load column vector of order $(N+n+2)$. The wind load is considered acting on all the N DOF of the building, however, not on the TMDs and the soil DOFs are of course independent of the direct wind load application. Further, $\{x_s\} = \{X_1, X_2, \dots, X_{N-1}, X_N, x_1, \dots, x_n, X_0, \theta_0\}^T$, $\{\dot{x}_s\}$, and $\{\ddot{x}_s\}$ are the unknown relative nodal displacement, velocity, and acceleration vectors, respectively for the building, TMDs, and soil DOFs. In Eq. (1) only the DOFs in one direction are considered when the building is subjected to the across-wind forces. Subsequently, the building is subjected to the along-wind forces separately, which has exactly the same DOF because of the symmetrical shape of the building.

Due to the symmetrical shape of the building the natural frequencies in both the mutually perpendicular lateral directions are the same, and the first five natural frequencies of the uncontrolled (NC) building are 0.1600, 0.7651, 1.9921, 3.7899, and 6.3945 Hz. Elias and Matsagar (2014a, 2014b) defined the $[M_s]$, $[C_s]$, and $[K_s]$ matrices for the building rigid foundation. However, the mass, damping, and stiffness matrices for the building where the SSI effects are included are as given following:

$$[M_s] = \begin{bmatrix} [M_N]_{N \times N} & [0]_{N \times n} & [M_N]_{N \times 1} & [M_N Z_N]_{N \times 1} \\ [0]_{n \times N} & [m_n]_{n \times n} & [m_n]_{n \times 1} & [m_n Z_n]_{n \times 1} \\ [M_N]_{1 \times N} & [m_n]_{1 \times n} & M_0 + M_t + m_t & \sum_{i=1}^N M_i Z_i + \sum_{i=1}^n m_i Z_i \\ [M_N Z_N]_{1 \times N} & [m_n Z_n]_{1 \times n} & \sum_{i=1}^N M_i Z_i + \sum_{i=1}^n m_i Z_i & I_0 + \sum_{i=1}^N I_i + M_i Z_i^2 + \sum_{i=1}^n m_i Z_i^2 \end{bmatrix} \quad (2)$$

$$[C_s] = \begin{bmatrix} [C_N]_{N \times N} + [c_n]_{N \times N} & -[c_n]_{N \times n} & [0]_{(N+n) \times 1} & [0]_{(N+n) \times 1} \\ -[c_n]_{n \times N} & [c_n]_{n \times n} & 0 & 0 \\ [0]_{1 \times (N+n)} & 0 & C_s & 0 \\ [0]_{1 \times (N+n)} & 0 & 0 & C_r \end{bmatrix} \quad (3)$$

$$[K_s] = \begin{bmatrix} [K_N]_{N \times N} + [k_n]_{N \times N} & -[k_n]_{N \times n} & [0]_{(N+n) \times 1} & [0]_{(N+n) \times 1} \\ -[k_n]_{n \times N} & [k_n]_{n \times n} & 0 & 0 \\ [0]_{1 \times (N+n)} & 0 & K_s & 0 \\ [0]_{1 \times (N+n)} & 0 & 0 & K_r \end{bmatrix} \quad (4)$$

where Z_i ($i = 1$ to N) is the height of the N^{th} DOF of the building; $[M_N]_{N \times N}$, $[C_N]_{N \times N}$, and $[K_N]_{N \times N}$ are the mass, damping, and stiffness matrices of the building; $[m_n]_{n \times n}$, $[c_n]_{n \times n}$, and $[k_n]_{n \times n}$ indicate the mass, damping, and stiffness matrices of the TMDs; $m_t = \sum_{i=1}^{i=n} m_i$ is the total mass of the TMDs; and $M_t = \sum_{i=1}^{i=N} M_i$ is the total mass of the building. The TMDs are modeled by assuming that the mass is equally divided among them (i.e., $m_i = \frac{m_t}{n}$). Natural frequencies of the MTMDs are uniformly distributed around their average frequencies. The natural frequency of each TMD (ω_i) is calculated by

$$\omega_i = \omega_T \left[1 + \left(i - \frac{n+1}{2} \right) \frac{\beta}{n-1} \right] \quad i = 1 \text{ to } n \quad (5)$$

and

$$\omega_T = \sum_i^n \frac{\omega_i}{n} \quad (6)$$

$$\beta = \frac{\omega_n - \omega_1}{\omega_T} \quad (7)$$

where ω_T is the average frequency of the MTMDs and β is the non-dimensional frequency bandwidth of the MTMDs systems. The stiffness (k_i) is used for adjusting frequency of each TMD unit such that

$$k_i = m_i \omega_i^2 \quad i = 1 \text{ to } n \quad (8)$$

The damping ratio ($\zeta_d = \zeta_1 = \zeta_2 = \dots = \zeta_n$) of the TMDs is kept the same and the damping coefficients (c_i) of the TMDs are calculated as follows:

$$c_i = 2\zeta_d m_i \omega_i \quad i = 1 \text{ to } n \quad (9)$$

Tuning frequency ratio (f) of the STMD and MTMDs system is expressed as

$$f = \frac{\omega_T}{\Omega_N} \quad (10)$$

where Ω_N is the natural frequency of the main building. The same procedure (Equations 5 through 10) used for calculation of the MTMDs parameters.

The STMD is always placed at topmost DOF of the building and tuned to the fundamental frequency of the building.

Wind force simulation

The along-wind forces are simulated from the power spectral density function (PSDF) of the longitudinal wind velocity fluctuations defined by [Kaimal et al. \(1972\)](#), [Simiu \(1974\)](#), [Simiu and Scanlan \(1996\)](#), which is given as

$$S_{rr}(H, \omega_f) = \frac{1}{2} \frac{200}{2\pi} u_*^2 \frac{H}{U(H)} \frac{1}{\left[1 + 50 \frac{\omega_f H}{2\pi U(H)}\right]^5} \quad (11)$$

where H is the height of the structure whereas ω_f , u_* , and $U(H)$ are respectively the circular frequency (rad/s), friction velocity, and the mean wind speed at height H .

Time histories are generated based on the discrete frequency function with the fast Fourier transform (FFT) given by [Wittig and Sinha \(1975\)](#) along the height of the structure. Discrete time series can be simulated using the following model:

$$y_p(r\Delta t) = \frac{1}{R} \sum_{k_f=0}^R Y_p(k_f \Delta f_f) \exp\left(j \frac{2\pi k_f r}{R}\right) \quad (12)$$

where $Y_p(k_f \Delta f_f)$ are complex random numbers; and to obtain it, a set of completely independent Gaussian random numbers are generated. Further, R is the total number of points used for the simulation, k_f is the running random frequencies, and r indicates the integers from 0 to R . The Gaussian random numbers are generated based on the following equation:

$$\varepsilon_{ik} = \xi_{ik} + j\eta_{ik} \quad (13)$$

where $E[\xi_{ik}] = E[\eta_{ik}] = 0$ and $E[\xi_{ik}^2] = E[\eta_{ik}^2] = 0.5$, and E is the expectation operator. Then, the complex random numbers may be expressed as

$$Y_p(k_f \Delta f_f) = \sum_i^p H_{pi}(k_f \Delta f_f) \varepsilon_{ik} \times \sqrt{2f_{fc}R} \quad (14)$$

where $H_{pi}(k_f \Delta f_f)$ is the lower triangular matrix from Cholesky decomposition of one-sided power spectral density function $S(f_f)$, and f_{fc} is the Nyquist frequency. Further, the size of the Cholesky matrix may assume, $p = 1$ to l , which is taken here as, $l = 200$.

[Kwon and Kareem \(2006\)](#) have made available an online wind simulation tool based on the abovementioned theory, which has been used in the present work. The fluctuating wind force at each elevation is calculated as

$$F_i(t) = \rho C_D A [U_i + u_i(t)]^2 \quad (15)$$

where $F_i(t)$, $\rho = 1.2 \text{ kg/m}^3$, $C_D = 1$, $A_i = D_i \times H_i$, U_i , $u_i(t)$, D , and H are respectively the fluctuating wind force, air density, drag coefficient, tributary area, mean wind speed, fluctuating wind speed, width, and height. Simulation of wind velocity $u_i(t)$ from the specified wind spectrum is carried out using the online program prepared by Kwon and Kareem (2006). The wind force time histories are calculated at time interval, $\Delta t = 1/(2f_{fc})$.

The across-wind forces are taken from the wind tunnel tests conducted at the University of Sydney, given by Samali et al. (2004a, 2004b) and the time histories of the across-wind loads are available at the website SSTL (2002). Figure 2 shows the calculated power spectral density function (PSDF) of the along-wind and across-wind forces as applied through the height on different mass along the DOFs of the building for the parameters defined in the numerical study.

NUMERICAL STUDY

The wind response of the 76-storey benchmark building controlled using the single tuned mass damper (STMD) and multiple tuned mass dampers (MTMDs) is investigated under the deterministic along-wind and across-wind forces. In this study, the effect of considering different soil types is also investigated to evaluate the performances of the STMD and MTMDs. The shear wave velocity (V_s) of 1200 m/sec, 500 m/sec, 300 m/sec, and 100 m/sec are considered for rock (rigid foundation), dense soil, medium soil, and soft soil, respectively. Also, the shear modulus (G), density (ρ), Poisson's ratio (ν) and other parameters used for the soil in the SSI study are provided in Table 1. Note that the rigid foundation condition corresponds to ignoring the flexibility of the foundation soil (i.e., no SSI).

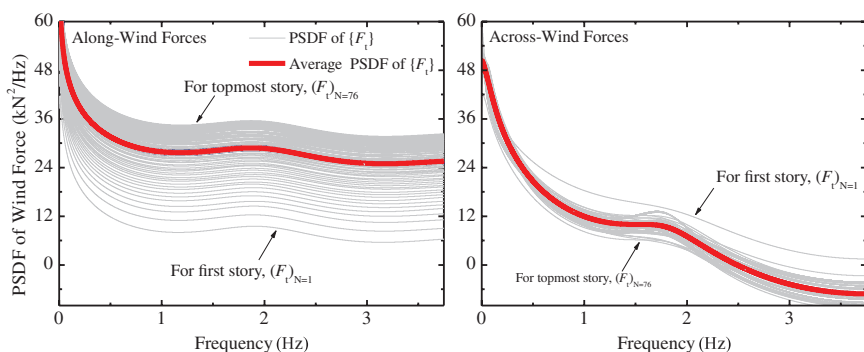


Figure 2. PSDF of the along-wind and across wind forces applied at different floor levels

Table 1. Dynamic Properties of Different Types of Soil

Properties of Soil	Type of Soil		
	Dense	Medium	Soft
Shear Modulus, G (10^7 N/m)	60	17	1.8
Poisson's Ratio, ν	0.25	0.30	0.35
Soil Density, ρ (kg/m ³)	2000	1900	1600
Shear Wave Velocity, V_s (m/s)	500	300	100
Translational Stiffness of Soil Medium, K_s (10^{11} N/m)	1.03	0.25	0.06
Rocking Stiffness of Soil Medium, K_r (10^{14} N/m)	1.62	0.417	0.01
Translational Damping Coefficient, C_s (10^{10} N · s/m)	5.37	0.26	0.04
Rocking Damping Coefficient, C_r (10^{12} N · s/m)	2.19	1.12	0.18

Because objective of the present study does not include optimizing parameters of the STMD and MTMDs, the optimized parameters suggested by Patil and Jangid (2011) are adopted herein. Thereby, with the optimized TMD parameters chosen, their performance evaluation becomes meaningful. Patil and Jangid (2011) compared the performance of the optimum STMD and MTMDs installed on the top of the same benchmark building; however, the effects of the SSI were ignored. Hence, the total mass of the STMD is considered to be 1,500 ton, which leads to a mass ratio of 0.01 with respect to the total mass of the building. The parameters for optimum STMD and MTMDs are provided in Table 2. The mean wind velocity at the top of the building is assumed to be 47.25 m/sec for calculating the along-wind as well across-wind forces.

Table 2. Design Parameters for the STMD and MTMDs in the Building

Scheme	TMDs	Frequency, ω_i (rad/sec)	Mass, m_i (ton)	Stiffness, k_i (kN/m)	Damping, c_i (kN · sec/m)
STMD	TMD-1	0.987	1500 (1% of M_t)	1461.5	89
MTMDs	TMD-1	0.839	300	211	15
	TMD-2	0.913	300	250	16
	TMD-3	0.987	300	292	18
	TMD-4	1.061	300	338	19
	TMD-5	1.135	300	387	20

Comparison of uncontrolled and controlled responses

A comparison of the dynamic responses of the uncontrolled (NC) and controlled building installed with the STMD and MTMDs is made. Figures 3 and 4 show the PSDF of the acceleration response at the top of the building while subjected to the along-wind and across-wind forces for the cases: NC, STMD, and MTMDs. The shifting of the fundamental frequency on account of installing the TMDs is apparent in the PSDF.

The PSDF of the topmost floor acceleration indicates the fact that, by installing the STMD and MTMDs, energy contained in the modal responses is reduced in both the STMD and MTMDs. From the total modal energy dissipated in the NC case, significant amount of energy is dissipated by the MTMDs, hence modal energy in case of the STMD is significantly lower especially in case of the dense and medium soil. In addition, the effect of soil type is seen to be lesser for the NC case under the along-wind and across-wind forces. However, it is seen that the SSI affects the performance of the STMD and MTMDs significantly. In case of the STMD, the modal response has been controlled near the mode which is tuned. Nevertheless, the MTMDs have shown better performance as compared to those obtained by the STMD. Therefore, it is concluded that installing optimal MTMDs significantly reduce the dynamic response of the wind-excited tall building under both along-wind and across-wind forces. In addition, the MTMDs are not sensitive to the de-tuning caused due to the soil types.

Effectiveness of the STMD and MTMDs

In this section, the effectiveness of the response control with the STMD and MTMDs considering the SSI is presented. The peak and root mean square (RMS) of the acceleration and displacement at different floors are calculated, to evaluate the performance of the STMD and MTMDs while SSI is included. In Figures 5 through 8 (Tables A1 through A4 in Appendix) the RMS and peak responses of

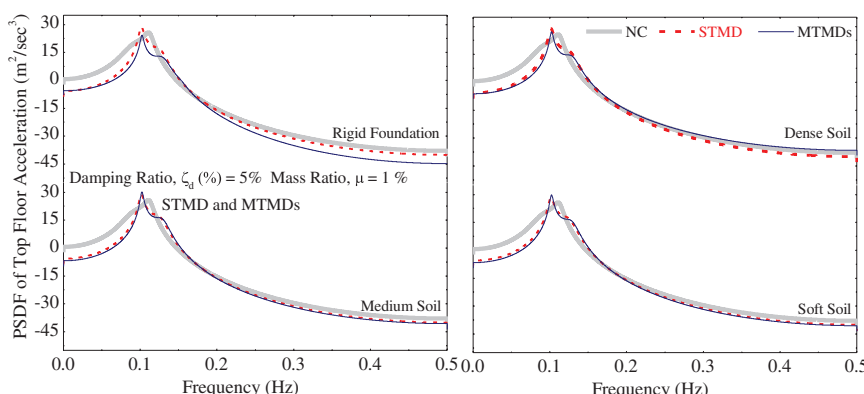


Figure 3. PSDF of the acceleration at the topmost floor of the building under along-wind loads for the cases of the STMD and MTMDs

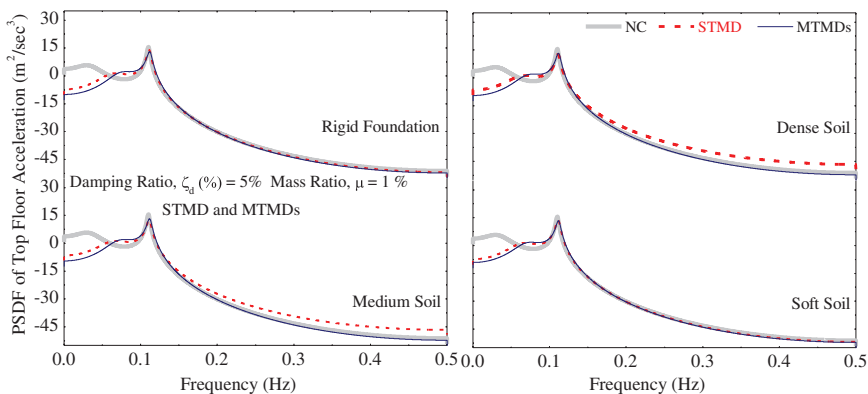


Figure 4. PSDF of the acceleration at topmost floor of the building under across-wind loads for the cases of the STMD and MTMDs

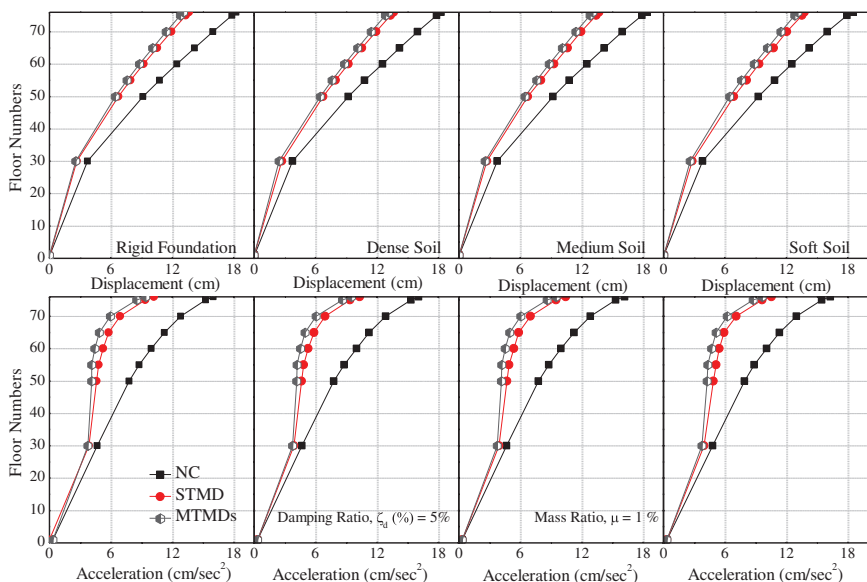


Figure 5. RMS responses of different floors of the building under along-wind forces when SSI is considered

the building under along-wind and across-wind forces for the cases: NC, STMD, and MTMDs are shown.

Figure 5 shows the RMS responses of the building installed with/without the STMD and MTMDs when subjected to the along-wind forces. It is observed that the RMS acceleration and displacement at the lower floors increased from the case of the building with rigid foundation to the building with flexible foundation

(i.e., effect of different soil types). However, the results show that the increases in the RMS responses are marginal for the floors at higher levels. Around 50% increase in the responses are observed for the floors at lower levels; however, the value is quite less for the floors at higher levels.

The importance of the critical damping is vital in reduction of the dynamic response in the tall and flexible structures. The optimal STMD and MTMDs are shown to be effective in response control of the high-rise building. The RMS displacement at lower floors is reduced by around 27% and 31%, respectively, for the STMD and MTMDs. Also, the RMS displacement at floors at higher levels is decreased by around 25% and 28%, respectively, for the STMD and MTMDs. The SSI effect is more pronounced on the design parameters of the STMD as compared to the MTMDs. The effectiveness of the STMD has degraded by around 3% with inclusion of the SSI; however, the MTMDs have shown more robustness with different soil types (i.e., flexibility of the foundation). Further, the RMS acceleration at lower floors is reduced by around 18% and 20%, respectively, for the STMD and MTMDs. Also, the RMS acceleration at floors at higher levels is decreased by around 47% and 55%, respectively, for the STMD and MTMDs. Similar to that of the displacement response, the effect of the SSI is more pronounced on the design parameters of the STMD as compared to the MTMDs. The effectiveness of the STMD has degraded by around 4% with inclusion of the SSI; however, the MTMDs have shown more robustness with different soil types. In Figure 6, similar trend can be observed for the peak responses of the building for different cases

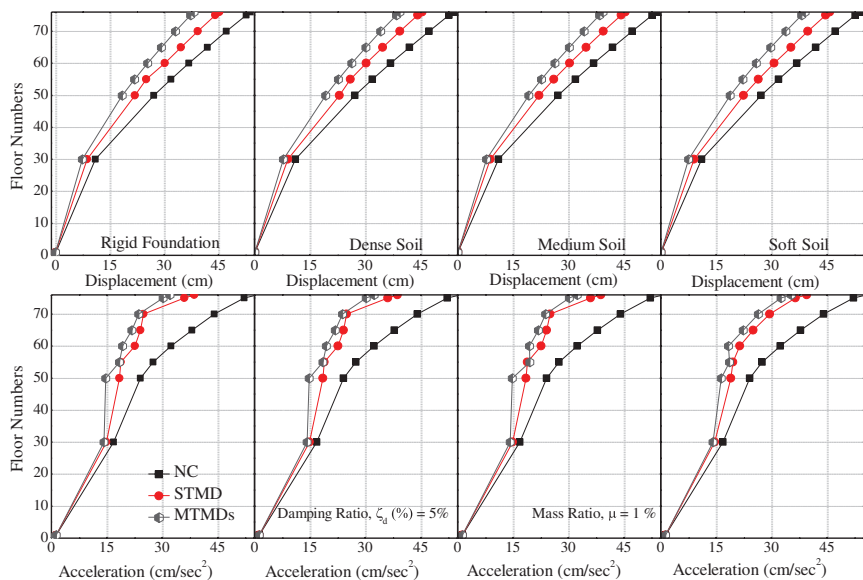


Figure 6. Peak responses of different floors of the building under long-wind forces when SSI is considered

investigated under the along-wind forces. Therefore, it is concluded that the lower floors of the tall buildings might be more sensitive to the along-wind forces if the SSI is included. However, the SSI effect for the floors at higher level can be ignored in case of the NC. Both the controller schemes have significantly reduced the dynamic responses of the building under the along-wind forces. However, it is recommended not to ignore the SSI effect while designing the controller schemes. Figure 7 shows the RMS responses of the building subjected to the across-wind forces for the cases: NC, STMD, and MTMDs. It is seen that the SSI affects the responses of the uncontrolled building by 25%, which is quite high. It indicates that the SSI effects must not be ignored. The STMD and MTMDs have shown their effectiveness in the RMS response reduction of the high-rise building subjected to the across-wind forces. The RMS displacement is reduced by around 28% and 32%, and the RMS acceleration is reduced by around 47% and 57% respectively for the STMD and MTMDs. In Figure 8, it is observed that the peak displacement in the NC case has increased by 27%, and the peak acceleration has increased by 20% with consideration of the SSI effect. The peak displacement is reduced by around 22% and 22%, and the peak acceleration is reduced by around 35% and 44% respectively for the STMD and MTMDs. Therefore, it is concluded that under the across-wind forces the effect of the SSI must not be ignored. Further, the MTMDs are better controllers as compared to the STMD for dynamic response control of the tall buildings under wind loads.

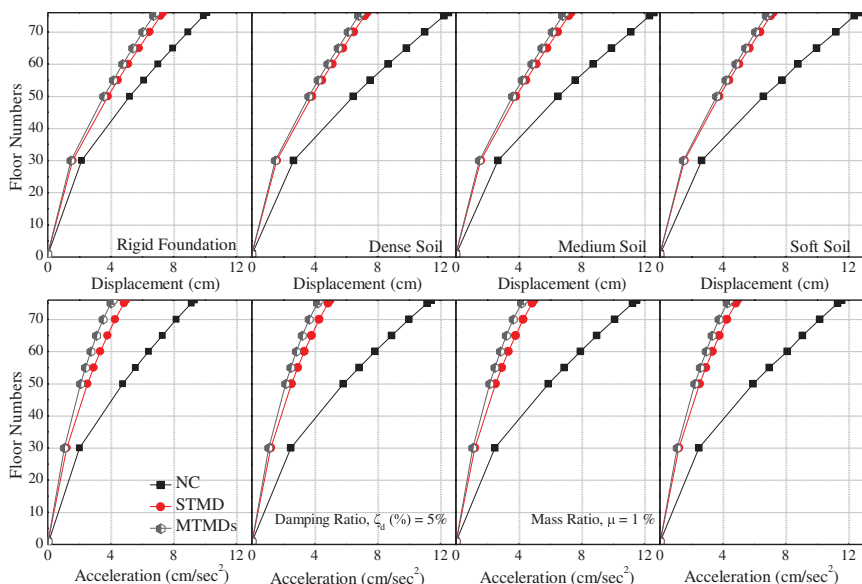


Figure 7. RMS responses of different floors of the building under across-wind forces when SSI is considered

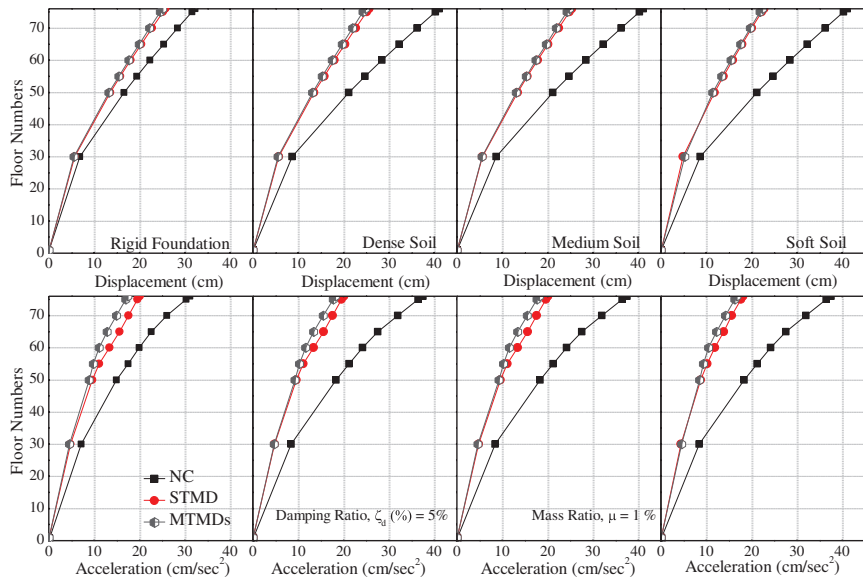


Figure 8. Peak responses of different floors of the building under across-wind forces when SSI is considered

CONCLUSIONS

Wind response control of tall building installed with single tuned mass damper (STMD) and multiple tuned mass dampers (MTMDs) is presented. The effect of the soil-structure-interaction (SSI) is incorporated to evaluate the performance of the STMD and MTMDs under the along-wind and across-wind forces. The following conclusions are drawn from the trends of the results shown in the present study.

1. The dynamic response of the wind-excited tall building under both the along-wind and across-wind forces can be significantly reduced by installing the optimal MTMDs. Notably, the MTMDs are less sensitive to the de-tuning caused due to the soil flexibility.
2. The lower floors of the tall buildings might be more sensitive to the along-wind forces if the SSI is included. However, the SSI effect for the floors at higher level can be ignored in case of the uncontrolled (NC) structure.
3. Both the controller schemes, STMD and MTMDs have significantly reduced the dynamic responses of the building under the along-wind and across-wind forces.
4. It is recommended not to ignore the SSI effect while designing the controller schemes.
5. The MTMDs are better controllers as compared to the STMD for dynamic response control of the tall buildings under wind loads.

References

- Aly, A. M. 2014a. "Proposed robust tuned mass damper for response mitigation in buildings exposed to multi-directional wind." *Struct. Des. Tall Spec. Build.* **23** (9): 664–691.
- Aly, A. M. 2014b. "Vibration control of high-rise buildings for wind: A robust passive and active tuned mass damper." *Smart Struct. Syst.* **13** (3): 473–500.
- Aly, A. M., and S. Abburu. 2015. "On the design of high-rise buildings for multi-hazard: Fundamental differences between wind and earthquake demand." *Shock Vib.* 148681.
- Aly, A. M., A. Zasso, and F. Resta. 2011. "Dynamics and control of high-rise buildings under multi-directional wind loads." *Smart Mater. Res.* 549621.
- Bakre, S. V., and R. S. Jangid. 2004. "Optimum multiple tuned mass dampers for base excited damped main system." *Int. J. Struct. Stab. Dyn.* **4** (4): 527–542.
- BIS (Bureau of Indian Standards). 1987. *Code of practice for design loads (other than earthquake) for buildings and structures part 3 wind loads.* IS 875 - Part 3, New Delhi, India: BIS.
- Davenport, A. G. 1962. "The response of slender line-like structures to a gusty wind." *Proc. Soc. Civ. Eng.* **23**: 389–408.
- Elias, S., and V. Matsagar. 2014a. "Distributed multiple tuned mass dampers for wind vibration response control of high-rise building." *J. Eng.*
- Elias, S., and V. Matsagar. 2014b. "Wind response control of a 76-storey benchmark building installed with distributed multiple tuned mass dampers." *J. Wind Eng.* **11** (2): 37–49.
- Elias, S., and V. Matsagar. 2015. "Optimum tuned mass damper for wind and earthquake response control of high-rise building." In Vol. 2 of *Advances in structural engineering*. New Delhi, India: Springer.
- Hadi, N. S., and Y. Arifiadi. 1998. "Optimum design of absorber for MDOF structures." *J. Struct. Eng., Am. Soc. Civ. Eng.* **124** (11): 1272–1280.
- Han, B., and C. Li. 2008. "Characteristics of linearly distributed parameter-based multiple-tuned mass dampers." *Struct. Control Health Monit.* **15** (6): 839–856.
- Kaimal, J. C., J. C. Wyngaard, Y. Izumi, and O. R. Cote. 1972. "Spectral characteristics of surface-layer turbulence." *J. R. Meteorol. Soc.* **98** (417): 563–589.
- Kareem, A. 1983. "Mitigation of wind induced motion of tall buildings." *J. Wind Eng. Ind. Aerodyn.* **11** (1–3): 273–284.
- Kareem, A., and S. Kline. 1995. "Performance of multiple tuned mass dampers under random loading." *J. Struct. Eng.* **121** (2): 348–361.
- Kwon, D., and A. Kareem. 2006. "NatHaz on-line wind simulator (NOWS): Simulation of Gaussian multivariate wind fields." NatHaz Modeling Laboratory Report, University of Notre Dame, Indiana (IN), USA, <http://windsim.ce.nd.edu>.
- Li, C. 2000. "Performance of multiple tuned mass dampers for attenuating undesirable oscillations of structures under the ground acceleration." *Earthquake Eng. Struct. Dyn.* **29** (9): 1405–1421.
- Li, C. 2002. "Optimum multiple tuned mass dampers for structures under the ground acceleration based on DDMF and ADMF." *Earthquake Eng. Struct. Dyn.* **31** (4): 897–919.
- Liu, M.-Y., W.-L. Chiang, J.-H. Hwang, and C.-R. Chub. 2008. "Wind-induced vibration of high-rise building with tuned mass damper including soil-structure interaction." *J. Wind Eng. Ind. Aerodyn.* **96** (6–7): 1092–1102.
- Patil, V. B., and R. S. Jangid. 2011. "Optimum multiple tuned mass dampers for the wind excited benchmark building." *J. Civil Eng. Manage.* **17** (4): 540–557.

- Samali, B., K. C. S. Kwok, G. S. Wood, and J. N. Yang. 2004a. "Wind tunnel tests for wind-excited benchmark building." *J. Eng. Mech.* **130** (4): 447–450.
- Samali, B., E. Mayol, K. C. S. Kwok, A. Mack, and P. Hitchcock. 2004b. "Vibration control of the wind-excited 76-storey benchmark building by liquid column vibration absorber." *J. Eng. Mech.* **130** (4): 478–485.
- Simiu, E. 1974. "Wind spectra and dynamic along wind response." *J. Struct. Div.* **100** (9): 1897–1910.
- Simiu, E., and R. H. Scanlan. 1996. *Wind effects on structures*. 3rd ed. New York: Wiley.
- SSTL (Smart Structures Technology Laboratory). 2002. "Structural control, benchmark comparisons." Accessed January 28, 2018. <http://sstl.cee.illinois.edu/benchmarks/index.html>.
- Wittig, L. E., and A. K. Sinha. 1975. "Simulation of multi correlated random processes using the FFT algorithm." *J. Acoust. Soc. Am.* **58** (3): 630–634.
- Xu, K., and T. Igusa. 1992. "Dynamic characteristics of multiple substructures with closely spaced frequencies." *Earthquake Eng. Struct. Dyn.* **21** (12): 1059–1070.
- Yang, J. N., A. K. Agrawal, B. Samali, and J. C. Wu. 2004. "Benchmark problem for response control of wind-excited tall buildings." *J. Eng. Mech.* **130** (4): 437–446.

APPENDIX

Tables A1 through A4 show the peak dynamic response; wherein, the values in the brackets indicate increase in the responses when the sign is positive, or it indicate reduction in the response when the sign is negative.

Table A1. RMS Responses of Different Floors of the Building under Along-wind Forces when SSI is Considered

Floor No.	Rigid Foundation			Dense Soil			Medium Soil			Soft Soil		
	Displacement (cm)	Acceleration (cm/sec ²)										
1	0.02 (0)	0.34 (0)	0.03 (+50)	0.34 (0)	0.03 (+50)	0.34 (0)	0.03 (+50)	0.34 (0)	0.03 (+50)	0.34 (0)	0.03 (+50)	0.34 (0)
30	3.71 (0)	4.67 (0)	3.75 (+1)	4.66 (0)	3.76 (+1)	4.68 (0)	3.83 (+3)	4.79 (+3)	3.83 (+3)	4.79 (+3)	3.83 (+3)	4.79 (+3)
50	9.15 (0)	7.80 (0)	9.19 (0)	7.79 (0)	9.20 (+1)	7.78 (0)	9.28 (+1)	7.91 (+1)	9.28 (+1)	7.91 (+1)	9.28 (+1)	7.91 (+1)
55	10.76 (0)	8.78 (0)	10.78 (0)	8.80 (0)	10.80 (0)	8.79 (0)	10.85 (+1)	8.85 (+1)	10.85 (+1)	8.85 (+1)	10.85 (+1)	8.85 (+1)
60	12.44 (0)	9.96 (0)	12.55 (+1)	10.00 (0)	12.52 (+1)	9.99 (0)	12.55 (+1)	10.09 (+1)	12.55 (+1)	10.09 (+1)	12.55 (+1)	10.09 (+1)
65	14.19 (0)	11.23 (0)	14.21 (0)	11.25 (0)	14.22 (0)	11.26 (0)	14.26 (0)	11.33 (0)	14.26 (0)	11.33 (0)	14.26 (0)	11.33 (0)
70	15.97 (0)	12.82 (0)	15.98 (0)	12.85 (0)	15.97 (0)	12.85 (0)	16.00 (0)	12.99 (0)	16.00 (0)	12.99 (0)	16.00 (0)	12.99 (0)
75	17.83 (0)	15.27 (0)	17.85 (0)	15.32 (0)	17.91 (0)	15.33 (0)	17.95 (+1)	15.48 (+1)	17.95 (+1)	15.48 (+1)	17.95 (+1)	15.48 (+1)
76	18.24 (0)	16.02 (0)	18.28 (0)	16.07 (0)	18.41 (+1)	16.21 (+1)	18.55 (+2)	16.32 (+2)	18.55 (+2)	16.32 (+2)	18.55 (+2)	16.32 (+2)
STMD												
Floor No.	Rigid Foundation			Dense Soil			Medium Soil			Soft Soil		
	Displacement (cm)	Acceleration (cm/sec ²)										
1	0.02 (0)	0.00 (+100)	0.00 (-100)	0.34 (0)	0.03 (+50)	0.34 (0)	0.03 (+50)	0.34 (0)	0.03 (+50)	0.34 (0)	0.03 (+50)	0.34 (0)
30	2.69 (-27)	3.85 (-18)	2.71 (-27)	3.88 (-17)	2.75 (-26)	3.91 (-16)	2.81 (-24)	3.95 (-15)	2.81 (-24)	3.95 (-15)	2.81 (-24)	3.95 (-15)
50	6.72 (-27)	4.61 (-41)	6.73 (-26)	4.64 (-41)	6.75 (-26)	4.71 (-40)	6.88 (-25)	4.89 (-37)	6.88 (-25)	4.89 (-37)	6.88 (-25)	4.89 (-37)
55	7.93 (-26)	4.80 (-45)	7.94 (-26)	4.85 (-45)	8.01 (-26)	4.92 (-44)	8.12 (-25)	5.15 (-41)	8.12 (-25)	5.15 (-41)	8.12 (-25)	5.15 (-41)
60	9.20 (-26)	5.24 (-47)	9.21 (-26)	5.28 (-47)	9.29 (-25)	5.37 (-46)	9.33 (-25)	5.45 (-45)	9.33 (-25)	5.45 (-45)	9.33 (-25)	5.45 (-45)
65	10.53 (-26)	5.80 (-48)	10.54 (-26)	5.85 (-48)	10.62 (-25)	5.85 (-48)	10.75 (-24)	5.93 (-47)	10.75 (-24)	5.93 (-47)	10.75 (-24)	5.93 (-47)
70	11.90 (-25)	6.90 (-46)	11.92 (-25)	6.93 (-46)	11.95 (-25)	7.01 (-45)	12.05 (-25)	7.12 (-44)	12.05 (-25)	7.12 (-44)	12.05 (-25)	7.12 (-44)

(Continued)

Table A1. RMS Responses of Different Floors of the Building under Along-wind Forces when SSI is Considered (Continued)

STMD	Rigid Foundation			Dense Soil			Medium Soil			Soft Soil		
	Floor No.	Displacement (cm)	Acceleration (cm/sec ²)	Displacement (cm/sec ²)								
75	13.32 (-25)	9.39 (-39)	13.34 (-25)	9.36 (-39)	13.42 (-25)	9.50 (-38)	13.55 (-24)	9.65 (-37)				
76	13.63 (-25)	10.23 (-36)	13.65 (-25)	10.31 (-36)	13.72 (-25)	10.45 (-35)	13.78 (-24)	10.56 (-34)				
MTMDS	Rigid Foundation			Dense Soil			Medium Soil			Soft Soil		
	Floor No.	Displacement (cm)	Acceleration (cm/sec ²)	Displacement (cm/sec ²)								
1	0.00 (-100)	0.34 (0)	0.00 (-100)	0.34 (0)	0.02 (0)	0.34 (0)	0.02 (0)	0.34 (0)	0.02 (0)	0.34 (0)	0.02 (0)	0.34 (0)
30	2.57 (-31)	3.75 (-20)	2.43 (-35)	3.76 (-19)	2.58 (-30)	3.76 (-19)	2.59 (-30)	3.77 (-19)				
50	6.43 (-30)	4.12 (-47)	6.45 (-30)	4.17 (-47)	6.45 (-30)	4.17 (-47)	6.47 (-29)	4.26 (-45)				
55	7.59 (-29)	4.14 (-53)	7.61 (-29)	4.21 (-52)	7.61 (-29)	4.21 (-52)	7.63 (-29)	4.34 (-51)				
60	8.81 (-29)	4.45 (-55)	8.84 (-29)	4.54 (-54)	8.84 (-29)	4.54 (-54)	8.86 (-29)	4.70 (-53)				
65	10.10 (-29)	4.87 (-57)	10.12 (-29)	4.97 (-56)	10.12 (-29)	4.97 (-56)	10.14 (-29)	5.15 (-54)				
70	11.41 (-29)	5.94 (-54)	11.44 (-28)	6.05 (-53)	11.44 (-28)	6.05 (-53)	11.46 (-28)	6.22 (-51)				
75	12.78 (-28)	8.54 (-44)	12.81 (-28)	8.63 (-43)	12.81 (-28)	8.64 (-43)	12.83 (-28)	8.77 (-43)				
76	13.09 (-28)	9.42 (-41)	13.12 (-28)	9.51 (-41)	13.11 (-28)	9.51 (-41)	13.14 (-28)	9.64 (-40)				

Table A2. Peak Responses of Different Floors of the Building under Along-wind Forces when SSI is Considered

Floor No.	Rigid Foundation			Dense Soil			Medium Soil			Soft Soil		
	Displacement (cm)	Acceleration (cm/sec ²)										
1	0.09 (0)	1.32 (0)	0.08 (-11)	1.31 (-1)	0.08 (-11)	1.31 (-1)	0.08 (-11)	1.31 (-1)	0.08 (-11)	1.31 (-1)	0.08 (-11)	1.31 (-1)
30	11.08 (0)	16.80 (0)	11.11 (0)	16.85 (0)	11.08 (0)	16.85 (0)	11.08 (0)	16.85 (0)	11.08 (0)	16.85 (0)	11.08 (0)	16.85 (0)
50	27.19 (0)	24.09 (0)	27.18 (0)	24.08 (0)	27.18 (0)	24.08 (0)	27.18 (0)	24.08 (0)	27.18 (0)	24.08 (0)	27.18 (0)	24.08 (0)
55	31.93 (0)	27.51 (0)	31.95 (0)	27.46 (0)	31.93 (0)	27.46 (0)	31.93 (0)	27.46 (0)	31.93 (0)	27.46 (0)	31.93 (0)	27.46 (0)
60	36.88 (0)	32.40 (0)	36.89 (0)	32.37 (0)	36.87 (0)	32.37 (0)	36.87 (0)	32.37 (0)	36.87 (0)	32.37 (0)	36.87 (0)	32.37 (0)
65	42.01 (0)	38.02 (0)	42.00 (0)	37.87 (0)	42.00 (0)	37.87 (0)	42.00 (0)	37.87 (0)	42.00 (0)	37.87 (0)	42.00 (0)	37.87 (0)
70	47.25 (0)	44.13 (0)	47.24 (0)	44.08 (0)	47.24 (0)	44.08 (0)	47.24 (0)	44.08 (0)	47.24 (0)	44.08 (0)	47.24 (0)	44.08 (0)
75	52.68 (0)	52.21 (0)	52.67 (0)	52.20 (0)	52.67 (0)	52.20 (0)	52.67 (0)	52.20 (0)	52.67 (0)	52.20 (0)	52.67 (0)	52.20 (0)
76	53.90 (0)	55.81 (0)	53.88 (0)	55.83 (0)	53.88 (0)	55.83 (0)	53.88 (0)	55.83 (0)	53.88 (0)	55.83 (0)	53.88 (0)	55.81 (0)
Floor No.	Rigid Foundation			Dense Soil			Medium Soil			Soft Soil		
	Displacement (cm)	Acceleration (cm/sec ²)										
1	0.07 (-22)	1.29 (-2)	0.08 (-11)	1.30 (-2)	0.07 (-22)	1.29 (-2)	0.07 (-22)	1.29 (-2)	0.07 (-22)	1.29 (-2)	0.07 (-22)	1.29 (-2)
30	8.80 (-21)	14.91 (-11)	8.99 (-19)	14.89 (-11)	8.82 (-20)	14.88 (-11)	8.82 (-20)	14.88 (-11)	9.06 (-18)	14.63 (-13)	9.06 (-18)	14.63 (-13)
50	21.96 (-19)	18.45 (-23)	22.98 (-15)	18.48 (-23)	22.01 (-19)	18.52 (-23)	22.01 (-19)	18.52 (-23)	22.41 (-18)	18.99 (-21)	22.41 (-18)	18.99 (-21)
55	25.14 (-21)	18.83 (-32)	25.97 (-19)	18.85 (-31)	26.02 (-19)	18.92 (-31)	26.02 (-19)	18.92 (-31)	26.44 (-17)	19.50 (-29)	26.44 (-17)	19.50 (-29)
60	30.23 (-18)	22.59 (-30)	30.28 (-18)	22.65 (-30)	30.31 (-18)	22.59 (-30)	30.31 (-18)	22.59 (-30)	30.74 (-17)	21.39 (-34)	30.74 (-17)	21.39 (-34)
65	34.71 (-17)	24.07 (-37)	34.75 (-17)	24.10 (-37)	34.80 (-17)	24.07 (-37)	34.80 (-17)	24.07 (-37)	35.23 (-16)	25.05 (-34)	35.23 (-16)	25.05 (-34)
70	39.34 (-17)	24.92 (-44)	39.37 (-17)	24.98 (-43)	39.46 (-16)	25.08 (-43)	39.46 (-16)	25.08 (-43)	39.83 (-16)	29.48 (-33)	39.83 (-16)	29.48 (-33)

(Continued)

Table A2. Peak Responses of Different Floors of the Building under Along-wind Forces when SSI is Considered (Continued)

STMD	Rigid Foundation			Dense Soil			Medium Soil			Soft Soil		
	Floor No.	Displacement (cm)	Acceleration (cm/sec ²)	Displacement (cm/sec ²)								
75	44.21 (-16)	36.03 (-31)	44.24 (-16)	36.08 (-31)	44.34 (-16)	36.00 (-31)	44.70 (-15)	36.49 (-30)				
76	45.30 (-16)	38.68 (-31)	45.45 (-16)	38.72 (-31)	45.44 (-16)	38.84 (-30)	45.79 (-15)	39.59 (-29)				
MTMDS	Rigid Foundation			Dense Soil			Medium Soil			Soft Soil		
	Floor No.	Displacement (cm)	Acceleration (cm/sec ²)	Displacement (cm/sec ²)								
1	0.06 (-33)	1.29 (-2)	0.06 (-33)	1.30 (-2)	0.06 (-33)	1.30 (-2)	0.06 (-33)	1.29 (-2)	0.06 (-33)	1.29 (-2)	0.06 (-33)	1.29 (-2)
30	7.48 (-32)	14.21 (-15)	7.79 (-30)	14.23 (-15)	7.79 (-30)	14.23 (-15)	7.53 (-32)	14.12 (-16)				
50	18.50 (-32)	14.69 (-39)	19.22 (-29)	14.82 (-38)	19.23 (-29)	14.81 (-39)	18.78 (-31)	16.35 (-32)				
55	21.87 (-32)	18.41 (-33)	22.68 (-29)	18.56 (-33)	22.69 (-29)	19.55 (-29)	22.22 (-30)	18.57 (-32)				
60	25.44 (-31)	19.26 (-41)	26.34 (-29)	19.43 (-40)	26.35 (-29)	19.42 (-40)	25.91 (-30)	18.31 (-43)				
65	29.25 (-30)	21.81 (-43)	30.19 (-28)	21.89 (-42)	30.21 (-28)	21.86 (-43)	29.82 (-29)	22.34 (-41)				
70	33.20 (-30)	23.65 (-46)	34.20 (-28)	23.80 (-46)	34.22 (-28)	23.82 (-46)	33.90 (-28)	26.46 (-40)				
75	37.38 (-29)	30.26 (-42)	38.41 (-27)	30.27 (-42)	38.43 (-27)	30.27 (-42)	38.16 (-28)	32.57 (-38)				
76	38.32 (-29)	32.14 (-42)	39.35 (-27)	32.38 (-42)	39.37 (-27)	32.40 (-42)	39.11 (-27)	35.33 (-37)				

Table A3. RMS Responses of Different Floors of the Building under Across-wind Forces when SSI is Considered

Floor No.	Rigid Foundation			Dense Soil			Medium Soil			Soft Soil		
	Displacement (cm)	Acceleration (cm/sec ²)	Displacement Acceleration (cm) (cm/sec ²)	Displacement (cm)	Acceleration (cm/sec ²)	Displacement Acceleration (cm) (cm/sec ²)	Displacement (cm)	Acceleration (cm/sec ²)	Displacement Acceleration (cm) (cm/sec ²)	Displacement (cm)	Acceleration (cm/sec ²)	Displacement Acceleration (cm) (cm/sec ²)
1	0.02 (0)	0.06 (0)	0.02 (0) 0.03 (-50)	0.02 (0)	0.03 (-50)	0.02 (0) 0.03 (-50)	0.02 (0)	0.03 (-50)	0.02 (0) 0.03 (-50)	0.02 (0)	0.03 (-50)	0.02 (0) 0.03 (-50)
30	2.15 (0)	2.02 (0)	2.67 (+24) 2.48 (+23)	2.69 (+25)	2.48 (+23)	2.67 (+24) 2.48 (+23)	2.67 (+24)	2.48 (+23)	2.67 (+24) 2.48 (+23)	2.67 (+24)	2.48 (+23)	2.67 (+24) 2.48 (+23)
50	5.22 (0)	4.78 (0)	6.46 (+24) 5.84 (+23)	6.51 (+25)	5.89 (+23)	6.59 (+26) 5.95 (+24)	6.59 (+26)	5.95 (+24)	6.59 (+26) 5.95 (+24)	6.59 (+26)	5.95 (+24)	6.59 (+26) 5.95 (+24)
55	6.11 (0)	5.59 (0)	7.55 (+24) 6.83 (+22)	7.62 (+25)	6.91 (+24)	7.78 (+27) 6.98 (+25)	7.78 (+27)	6.98 (+25)	7.78 (+27) 6.98 (+25)	7.78 (+27)	6.98 (+25)	7.78 (+27) 6.98 (+25)
60	7.02 (0)	6.42 (0)	8.69 (+24) 7.85 (+22)	8.75 (+25)	7.94 (+24)	8.79 (+25) 8.12 (+26)	8.79 (+25)	8.12 (+26)	8.79 (+25) 8.12 (+26)	8.79 (+25)	8.12 (+26)	8.79 (+25) 8.12 (+26)
65	7.97 (0)	7.31 (0)	9.85 (+24) 8.91 (+22)	9.91 (+24)	8.98 (+23)	9.99 (+25) 9.09 (+24)	9.99 (+25)	9.09 (+24)	9.99 (+25) 9.09 (+24)	9.99 (+25)	9.09 (+24)	9.99 (+25) 9.09 (+24)
70	8.92 (0)	8.18 (0)	11.03 (+24) 10.01 (+22)	11.15 (+25)	10.11 (+24)	11.21 (+26) 10.19 (+25)	11.21 (+26)	10.19 (+25)	11.21 (+26) 10.19 (+25)	11.21 (+26)	10.19 (+25)	11.21 (+26) 10.19 (+25)
75	9.92 (0)	9.14 (0)	12.26 (+24) 11.17 (+22)	12.33 (+24)	11.27 (+23)	12.38 (+25) 11.33 (+24)	12.38 (+25)	11.33 (+24)	12.38 (+25) 11.33 (+24)	12.38 (+25)	11.33 (+24)	12.38 (+25) 11.33 (+24)
76	10.14 (0)	9.35 (0)	12.53 (+24) 11.43 (+22)	12.62 (+24)	11.53 (+23)	12.71 (+25) 11.59 (+24)	12.71 (+25)	11.59 (+24)	12.71 (+25) 11.59 (+24)	12.71 (+25)	11.59 (+24)	12.71 (+25) 11.59 (+24)
STMD	Rigid Foundation			Dense Soil			Medium Soil			Soft Soil		
	Displacement (cm)	Acceleration (cm/sec ²)	Displacement Acceleration (cm) (cm/sec ²)	Displacement (cm)	Acceleration (cm/sec ²)	Displacement Acceleration (cm) (cm/sec ²)	Displacement (cm)	Acceleration (cm/sec ²)	Displacement Acceleration (cm) (cm/sec ²)	Displacement (cm)	Acceleration (cm/sec ²)	Displacement Acceleration (cm) (cm/sec ²)
1	0.01 (-50)	0.02 (-67)	0.01 (-50) 0.02 (-67)	0.01 (-50)	0.02 (-67)	0.01 (-50) 0.02 (-67)	0.01 (-50)	0.02 (-67)	0.01 (-50) 0.02 (-67)	0.01 (-50)	0.02 (-67)	0.01 (-50) 0.02 (-67)
30	1.58 (-27)	1.21 (-40)	1.58 (-27) 1.21 (-40)	1.58 (-27)	1.21 (-40)	1.56 (-27) 1.20 (-41)	1.56 (-27)	1.20 (-41)	1.56 (-27) 1.20 (-41)	1.56 (-27)	1.20 (-41)	1.56 (-27) 1.20 (-41)
50	3.82 (-27)	2.53 (-47)	3.82 (-27) 2.53 (-47)	3.82 (-27)	2.53 (-47)	3.76 (-28) 2.53 (-47)	3.76 (-28)	2.53 (-47)	3.76 (-28) 2.53 (-47)	3.76 (-28)	2.53 (-47)	3.76 (-28) 2.53 (-47)
55	4.46 (-27)	2.93 (-48)	4.46 (-27) 2.93 (-48)	4.46 (-27)	2.93 (-48)	4.39 (-28) 2.92 (-48)	4.39 (-28)	2.92 (-48)	4.39 (-28) 2.92 (-48)	4.39 (-28)	2.92 (-48)	4.39 (-28) 2.92 (-48)
60	5.12 (-27)	3.35 (-48)	5.12 (-27) 3.35 (-48)	5.12 (-27)	3.35 (-48)	5.04 (-28) 3.34 (-48)	5.04 (-28)	3.34 (-48)	5.04 (-28) 3.34 (-48)	5.04 (-28)	3.34 (-48)	5.04 (-28) 3.34 (-48)
65	5.80 (-27)	3.80 (-48)	5.80 (-27) 3.80 (-48)	5.80 (-27)	3.80 (-48)	5.70 (-28) 3.78 (-48)	5.70 (-28)	3.78 (-48)	5.70 (-28) 3.78 (-48)	5.70 (-28)	3.78 (-48)	5.70 (-28) 3.78 (-48)
70	6.48 (-27)	4.30 (-47)	6.48 (-27) 4.30 (-47)	6.48 (-27)	4.30 (-47)	6.37 (-29) 4.27 (-48)	6.37 (-29)	4.27 (-48)	6.37 (-29) 4.27 (-48)	6.37 (-29)	4.27 (-48)	6.37 (-29) 4.27 (-48)

(Continued)

Table A3. RMS Responses of Different Floors of the Building under Across-wind Forces when SSI is Considered (Continued)

STMD	Rigid Foundation			Dense Soil			Medium Soil			Soft Soil		
	Floor No.	Displacement (cm)	Acceleration (cm/sec ²)	Displacement (cm)								
75	7.20 (-27)	4.86 (-47)	7.19 (-28)	4.86 (-47)	7.19 (-28)	4.86 (-47)	7.07 (-29)	4.83 (-47)	7.22 (-29)	4.96 (-47)		
76	7.35 (-28)	5.00 (-47)	7.35 (-28)	5.00 (-47)	7.35 (-28)	4.99 (-47)	7.22 (-29)	4.96 (-47)				
MTMDS	Rigid Foundation			Dense Soil			Medium Soil			Soft Soil		
	Floor No.	Displacement (cm)	Acceleration (cm/sec ²)	Displacement (cm)								
1	0.01 (-50)	0.02 (-67)	0.01 (-50)	0.02 (-67)	0.01 (-50)	0.02 (-67)	0.01 (-50)	0.02 (-67)	0.01 (-50)	0.02 (-67)	0.01 (-50)	0.02 (-67)
30	1.48 (-31)	1.05 (-48)	1.50 (-30)	1.07 (-47)	1.50 (-30)	1.07 (-47)	1.50 (-30)	1.07 (-47)	1.50 (-30)	1.10 (-46)		
50	3.57 (-32)	2.09 (-56)	3.62 (-31)	2.16 (-55)	3.61 (-31)	2.16 (-55)	3.60 (-31)	2.16 (-55)	3.60 (-31)	2.23 (-53)		
55	4.17 (-32)	2.40 (-57)	4.22 (-31)	2.49 (-55)	4.22 (-31)	2.49 (-55)	4.21 (-31)	2.49 (-55)	4.21 (-31)	2.57 (-54)		
60	4.78 (-32)	2.74 (-57)	4.85 (-31)	2.84 (-56)	4.84 (-31)	2.84 (-56)	4.83 (-31)	2.84 (-56)	4.83 (-31)	2.94 (-54)		
65	5.42 (-32)	3.11 (-57)	5.49 (-31)	3.22 (-56)	5.48 (-31)	3.22 (-56)	5.46 (-31)	3.22 (-56)	5.46 (-31)	3.33 (-54)		
70	6.05 (-32)	3.53 (-57)	6.13 (-31)	3.66 (-55)	6.13 (-31)	3.66 (-55)	6.10 (-32)	3.66 (-55)	6.10 (-32)	3.77 (-54)		
75	6.72 (-32)	4.03 (-56)	6.80 (-31)	4.17 (-54)	6.80 (-31)	4.17 (-54)	6.77 (-32)	4.29 (-53)	6.77 (-32)	4.29 (-53)		
76	6.86 (-32)	4.15 (-56)	6.96 (-31)	4.30 (-54)	6.95 (-31)	4.30 (-54)	6.92 (-32)	4.42 (-53)	6.92 (-32)	4.42 (-53)		

Table A4. Peak Responses of Different Floors of the Building under Across-wind Forces when SSI is Considered

NC	Rigid Foundation			Dense Soil			Medium Soil			Soft Soil		
	Floor No.	Displacement (cm)	Acceleration (cm/sec ²)	Displacement (cm)								
1	0.05 (0)	0.22 (0)	0.07 (+40)	0.12 (-45)	0.07 (+40)	0.12 (-45)	0.07 (+40)	0.12 (-45)	0.07 (+40)	0.12 (-45)	0.07 (+40)	0.12 (-45)
30	6.84 (0)	7.14 (0)	8.71 (+27)	8.45 (+18)	8.71 (+27)	8.45 (+18)	8.71 (+27)	8.45 (+18)	8.71 (+27)	8.45 (+18)	8.71 (+27)	8.45 (+18)
50	16.59 (0)	14.96 (0)	21.14 (+27)	18.37 (+23)	21.14 (+27)	18.37 (+23)	21.14 (+27)	18.37 (+23)	21.14 (+27)	18.37 (+23)	21.14 (+27)	18.37 (+23)
55	19.42 (0)	17.48 (0)	24.74 (+27)	21.26 (+22)	24.74 (+27)	21.26 (+22)	24.74 (+27)	21.26 (+22)	24.74 (+27)	21.26 (+22)	24.74 (+27)	21.26 (+22)
60	22.34 (0)	19.95 (0)	28.47 (+27)	24.20 (+21)	28.47 (+27)	24.20 (+21)	28.47 (+27)	24.20 (+21)	28.47 (+27)	24.20 (+21)	28.47 (+27)	24.20 (+21)
65	25.35 (0)	22.58 (0)	32.31 (+27)	27.57 (+22)	32.31 (+27)	27.57 (+22)	32.31 (+27)	27.57 (+22)	32.31 (+27)	27.57 (+22)	32.31 (+27)	27.57 (+22)
70	28.41 (0)	26.04 (0)	36.21 (+27)	31.99 (+23)	36.21 (+27)	31.99 (+23)	36.21 (+27)	31.99 (+23)	36.21 (+27)	31.99 (+23)	36.21 (+27)	31.99 (+23)
75	31.59 (0)	30.33 (0)	40.25 (+27)	36.51 (+20)	40.25 (+27)	36.51 (+20)	40.25 (+27)	36.51 (+20)	40.25 (+27)	36.51 (+20)	40.25 (+27)	36.51 (+20)
76	32.30 (0)	31.17 (0)	41.15 (+27)	37.52 (+20)	41.15 (+27)	37.52 (+20)	41.15 (+27)	37.52 (+20)	41.15 (+27)	37.52 (+20)	41.15 (+27)	37.52 (+20)
STMD												
Floor No.	Rigid Foundation			Dense Soil			Medium Soil			Soft Soil		
	Displacement (cm)	Acceleration (cm/sec ²)	Displacement (cm)	Acceleration (cm/sec ²)	Displacement (cm)	Acceleration (cm/sec ²)	Displacement (cm)	Acceleration (cm/sec ²)	Displacement (cm)	Acceleration (cm/sec ²)	Displacement (cm)	Acceleration (cm/sec ²)
1	0.05 (0)	0.10 (-55)	0.05 (0)	0.10 (-55)	0.04 (-20)	0.10 (-55)	0.04 (-20)	0.10 (-55)	0.04 (-20)	0.10 (-55)	0.04 (-20)	0.10 (-55)
30	5.71 (-17)	4.79 (-33)	5.69 (-17)	4.79 (-33)	5.63 (-18)	4.79 (-33)	5.63 (-18)	4.79 (-33)	4.91 (-28)	4.38 (-39)	4.91 (-28)	4.38 (-39)
50	13.56 (-18)	9.63 (-36)	13.51 (-19)	9.62 (-36)	13.37 (-19)	9.60 (-36)	13.37 (-19)	9.60 (-36)	11.83 (-29)	8.75 (-42)	11.83 (-29)	8.75 (-42)
55	15.78 (-19)	11.12 (-36)	15.73 (-19)	11.13 (-36)	15.56 (-20)	11.14 (-36)	15.56 (-20)	11.14 (-36)	13.81 (-29)	10.17 (-42)	13.81 (-29)	10.17 (-42)
60	18.07 (-19)	13.39 (-33)	18.00 (-19)	13.40 (-33)	17.81 (-20)	13.42 (-33)	17.81 (-20)	13.42 (-33)	15.85 (-29)	11.87 (-41)	15.85 (-29)	11.87 (-41)
65	20.41 (-19)	15.59 (-31)	20.33 (-20)	15.60 (-31)	20.11 (-21)	15.61 (-31)	20.11 (-21)	15.61 (-31)	17.93 (-29)	13.84 (-39)	17.93 (-29)	13.84 (-39)
70	22.77 (-20)	17.57 (-33)	22.69 (-20)	17.58 (-32)	22.44 (-21)	17.60 (-32)	22.44 (-21)	17.60 (-32)	20.03 (-29)	15.60 (-40)	20.03 (-29)	15.60 (-40)

(Continued)

Table A4. Peak Responses of Different Floors of the Building under Across-wind Forces when SSI is Considered (Continued)

STMD	Rigid Foundation			Dense Soil			Medium Soil			Soft Soil		
	Floor No.	Displacement (cm)	Acceleration (cm/sec ²)	Displacement (cm)								
75	25.22 (-20)	19.58 (-35)	25.13 (-20)	19.59 (-35)	24.85 (-21)	19.61 (-35)	22.22 (-30)	17.66 (-42)				
76	25.77 (-20)	20.12 (-35)	25.67 (-21)	20.12 (-35)	25.39 (-21)	20.12 (-35)	22.73 (-30)	18.09 (-42)				
MTMDS	Rigid Foundation			Dense Soil			Medium Soil			Soft Soil		
	Floor No.	Displacement (cm)	Acceleration (cm/sec ²)	Displacement (cm)								
1	0.04 (-20)	0.10 (-55)	0.04 (-20)	0.10 (-55)	0.04 (-20)	0.10 (-55)	0.04 (-20)	0.10 (-55)	0.04 (-20)	0.10 (-55)	0.04 (-20)	0.10 (-55)
30	5.59 (-18)	4.56 (-36)	5.54 (-19)	4.69 (-34)	5.53 (-19)	4.68 (-34)	5.23 (-24)	4.56 (-36)				
50	13.28 (-20)	8.89 (-41)	13.15 (-21)	9.29 (-38)	13.13 (-21)	9.27 (-38)	11.40 (-31)	8.52 (-43)				
55	15.45 (-20)	9.80 (-44)	15.29 (-21)	10.27 (-41)	15.27 (-21)	10.25 (-41)	13.42 (-31)	9.40 (-46)				
60	17.67 (-21)	11.13 (-44)	17.49 (-22)	11.62 (-42)	17.47 (-22)	11.60 (-42)	15.48 (-31)	10.49 (-47)				
65	19.94 (-21)	12.87 (-44)	19.73 (-23)	13.42 (-41)	19.70 (-22)	13.41 (-41)	17.58 (-31)	12.27 (-46)				
70	22.23 (-22)	14.91 (-44)	21.99 (-23)	15.53 (-40)	21.96 (-23)	15.51 (-40)	19.69 (-31)	14.24 (-45)				
75	24.59 (-22)	17.01 (-44)	24.32 (-23)	17.71 (-42)	24.28 (-23)	17.69 (-42)	21.88 (-31)	16.29 (-46)				
76	25.12 (-22)	17.47 (-44)	24.84 (-23)	18.19 (-42)	24.81 (-23)	18.17 (-42)	22.37 (-31)	16.78 (-46)				

CHAPTER 4

Wind Loading on Tall Building Structures in Consideration of Performance-Based Design

U. Y. Jeong^{*}
K. Tarrant^{*}

Abstract: Tall buildings are vulnerable to wind loading, and their designs are therefore frequently governed by wind loads. In buildings' wind design, attempts have been made to apply performance-based design (PBD) in result of its potential advantages to buildings' seismic design. This paper addresses basic issues in applying PBD to tall building wind design, which were raised by investigating different characteristics between wind loading and seismic loading. The main differences lie in (i) probabilistic distribution of winds and ground accelerations, and (ii) aerodynamic effects such as vortex-shedding. Potential benefits of performance-based wind design were investigated by comparing wind loads with seismic loads for various return periods. In order to derive general discussions and conclusions, the study was applied to a generic tall building with a square plan dimension of 30 m by 30 m, and a building height of 300 m, leaving aspect ratio (slenderness ratio) of ten (10). The across-wind and along-wind loads and their responses were simulated for a range of return periods, covering service level, strength level, and collapse-prevention level events. Findings concluded that the "heavy-headed, light-tailed" probabilistic distribution of wind speeds, and building aerodynamic characteristics which generate high loads in service level winds, demerit the application of PBD to tall building wind design.

INTRODUCTION

Tall buildings are vulnerable to wind loads due to their structural and aerodynamic characteristics, and their designs are frequently governed by wind loads over other design loads such as seismic loads, even in active seismic regions. Due to the importance of wind loads in tall building design, researchers have made attempts

*Gradient Wind Engineering Inc., 127 Walgreen Road, Ottawa, ON K0A 1L0, Canada, PH (613) 836-0934; FAX (613) 836-8183; email: {unyong.jeong, kevin.tarrant}@gradientwind.com

(Griffis et al. 2012, Larsen et al. 2016, Judd and Charney 2016, Nakai et al. 2013) to apply performance-based wind design (PBWD) in result of its potential advantages in providing economically feasible building seismic design. The key component of performance-based seismic design (PBSD) lies in finding a realistic design solution which satisfies both strength level in elastic material range and ultimate level (collapse-prevention level) by allowing post-yielding hysteretic behavior of materials (FEMA 2012, PEER 2010).

Performance-based wind design (PBWD) has been suggested to overcome the drawbacks (usually conservative design) of the current building wind design practice based on allowable stress design (ASD) and/or load resistant factored design (LRFD) by explicitly satisfying performance levels set out for different level of probabilities and intensities (Griffis et al. 2012, Larsen et al. 2016, Judd and Charney 2016). According to these publications, the main efficiency of PBWD can be achieved by allowing the post-yielding behavior of materials for collapse-prevention level winds which correspond to 700-year up to 20,000-year return periods for category II buildings. Regardless of some differences in defining target return periods, the suggested procedures are similar and are in line with those of PBSD.

Several questions arise despite the generally agreeable arguments provided by the aforementioned studies, especially regarding the feasibility of introducing post-yielding behavior of materials even for considered-to-be extreme wind events at collapse-prevention level. Due to the unique nature of wind loads on tall buildings which are singular around relatively short return periods and which mildly increase thereafter, it is an instinct that once a building is designed in elastic range for the short return period, it will remain elastic even for much higher return periods. Another question considers the difference in degree of extremity between winds versus earthquakes. Earthquakes appear to be much more extreme in intensity than winds. In consideration of the above characteristics of wind loads on tall buildings, the feasibility study on PBWD presented in this paper was performed by quantifying the statistical and aerodynamic characteristics of wind loading.

The following sections acknowledge several relevant considerations for this study: the main components of PBD are identified; probabilistic distributions of wind loads are compared to the earthquake loads; wind loading on tall buildings are decomposed in to along-wind and across-wind directions and compared with the seismic loads, and; wind loading characteristics in along-wind, across-wind are described in relation to PBD. Subsequently, using a typical tall building example, the main components of PBWD are discussed and compared to those of PBSD to examine the feasibility of expected material-saving effects of PBWD.

COMPONENTS OF PERFORMANCE-BASED DESIGN

Regardless of some issues in its application, PBD has demonstrated potential advantages in recommending reductions to reinforcements for new constructions and for repairs/replacements to existing buildings by optimally satisfying performance demands such as serviceability, strength and collapse-prevention.

Although the performance objectives can be somewhat optimized between the serviceability and strength levels based on PBSD, the main efficiency of PBSD resides in allowing ductile behavior of structural members to prevent the subject building from total collapse under devastating earthquakes which have extremely low probability of occurrence, while still satisfying the strength requirements under much more frequent but smaller scale earthquakes.

Seismic load can be identified as a combination of an earthquake intensity and a dynamic transfer function of the structure, whereas wind load can also be identified as the combination of wind intensity, and dynamic and aerodynamic transfer functions. Whereas earthquake intensity is defined for a site in terms of a ground acceleration, wind intensity is mainly defined by the wind speeds measured on-site. Unlike the seismic loads, wind loads involve aerodynamic transfer functions due to the vortex shedding or motion-induced aerodynamic forces (self-excited forces), and so on. Hereafter, the noted differences between wind and seismic loads are discussed in detail.

WIND AND SEISMIC INTENSITY AND DURATION

Probabilistic distribution of seismic intensity (in terms of the design response spectrum at a given period) is characterized by “light head” and “heavy tail,” which means frequent seismic events are very low intensity, whereas extreme rare events are very high intensity. Figures 1a and 1b illustrate probabilistic distribution of seismic intensity ([FEMA 2012](#), [ASCE 2010](#)) compared to wind (pressure) distribution based on statistical analysis of wind speed data (NOAA) in Seattle, WA, as an example. In the graph, the seismic intensity and dynamic wind pressure are normalized by 50-year values for the comparison. Probabilistic distribution of seismic loads can best be represented by lognormal distribution ([FEMA 2012](#)) with typical dispersion, $\beta = 0.4$ to 0.5 , whereas wind pressure distribution is evaluated from the wind speeds (NOAA) for which distribution typically follows Type-1 Gumbel distribution, as shown in Figure 2. Figure 1a and 1b represent the differences between frequent event and the extreme event, which correspond to the low and high non-exceedance probability respectively; these differences are much larger for the seismic load than for the wind load, due to the light head and heavy tail characteristic of the seismic loads probabilistic distribution.

On another note, wind events have much longer duration than seismic events, which makes PBWD more difficult than PBSD due to the significant degradation of the material which will occur during the long-duration excitation.

ALONG-WIND AND ACROSS-WIND LOADING ON TALL BUILDINGS

Tall buildings are susceptible to winds due to their flexibility and slenderness. The main sources of wind loading on tall buildings are vortex shedding, wind-buffeting and wake buffeting. Wind buffeting and wake buffeting are generated by

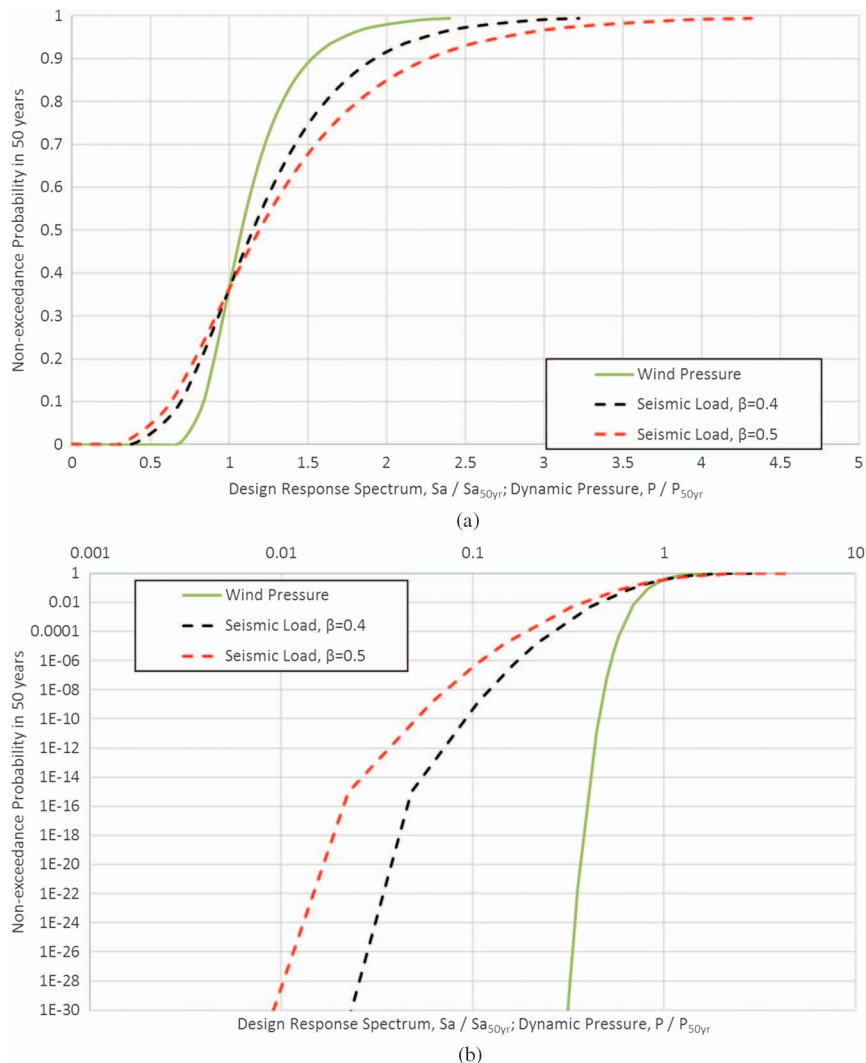


Figure 1. Non-exceedance probability of seismic and wind loads intensity normalized by 50-year values based on statistical analysis of wind speed data (Source: NOAA 2018), seismic intensity (Source: ASCE 7-10 2010) in Seattle, WA, and probabilistic distribution (Source: FEMA 2012): (a) linear scale – overall distribution, and (b) log-log scale – head behavior of the distribution

boundary-layer wind turbulence and vortices shed from upstream buildings, respectively. When the wind loads on tall buildings are decomposed into along-wind and across-wind components, wind buffeting, vortex shedding, and wake-buffeting act in the along-wind, across-wind and both directions, respectively. Torsional wind load and wake-buffeting are not addressed in this paper due to relative insignificance in tall buildings and case-dependency, respectively.

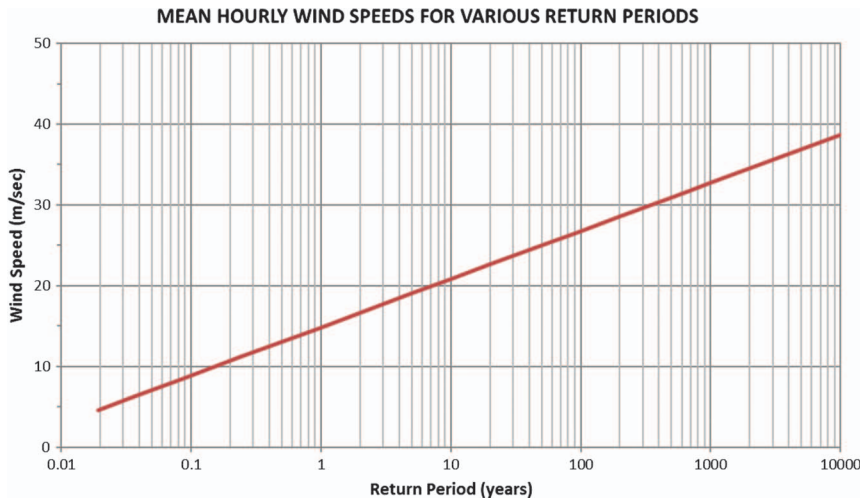


Figure 2. Mean hourly wind speeds at 10 m height for various return periods measured from King County International Airport, Seattle, WA

Source: [NOAA \(2018\)](#).

As a building becomes taller and more slender, due to the increasing flexibility and susceptibility to resonance, building response rapidly increases until it reaches a level where the motion-induced wind force (aeroelastic force) becomes significant. While along-wind aerodynamic damping can be estimated to be positive, which gives favorable effects ([Davenport 1979, Holmes 1996, 2001](#)), across-wind aerodynamic damping can be either positive or negative around the vortex-shedding wind speed. Even though this issue is important in tall building wind design, this is not addressed in the current paper because it would not change the major points which will be discussed in relation to the performance-based design. However, the author has addressed these issues and its time-domain analysis formula in another paper ([Jeong 2015](#)).

Along-wind wind loading - Along-wind response on a tall building consists of mean plus dynamic loads, which is a combination of quasi-steady load and resonant load. Since the along-wind load spectrum has more or less uniform distribution, the along-wind response increases quadratically with respect to wind speed. The estimation of the dynamic component of the along-wind loading of a building is generally obtained using the gust factor approach which has been utilized in several building codes. The basis of the gust factor approach follows from Davenport's method ([Davenport 1964](#)) whereby the maximum along-wind displacement \hat{Y} can be expressed as:

$$\hat{Y} = G\bar{Y} \quad (1)$$

where \bar{Y} is the mean static displacement and G is the gust factor, expressed as

$$G = 1 + g_y \frac{\sigma_y}{\bar{Y}} \quad (2)$$

where g_y is the peak factor and σ_y is the standard deviation of the fluctuation around the mean displacement. Details of the method to calculate G in this paper can be found in the work by Solari (1993a, 1993b). It has been assumed in the analysis that the fundamental mode primarily contributes to the building response.

Across-wind wind loading - Since the across-wind load spectrum has a peak around the 7 to 15 second period due to the vortex shedding, across-wind response of tall buildings whose natural periods fall within 5 to 10 seconds drastically increases due to resonance. As building height increases, vortex shedding wind loads increase rapidly, since the vortices and their shedding frequencies are highly correlated along the vertical axis of the building. Conversely, the along-wind buffeting loads increase moderately due to the relatively low correlation of boundary layer wind turbulence along the tower height. To calculate the across-wind load, the dynamic equation of motion of a tall building can be defined in terms of the generalized coordinate \tilde{x} as follows (Jeong 2015):

$$\ddot{\tilde{x}} + 2\xi_1\omega_1\dot{\tilde{x}} + \omega_1^2\tilde{x} = \tilde{m}^{-1}\tilde{f} \quad (3)$$

where $\ddot{\tilde{x}}$ and $\dot{\tilde{x}}$ represent the second and first order time derivatives of the generalized coordinate; ξ_1 and ω_1 represent the damping ratio and natural angular frequency respectively of the fundamental across-wind directional mode; \tilde{m} is the generalized mass that equals to $\int_0^H \phi_{x1}^2 m dz$; \tilde{f} is the generalized force in across-wind direction which is defined as $\int_0^H \phi_{x1} p(z) dz$; H is building height; ϕ_{x1} is the first across-wind directional mode shape function which is approximated with $\phi = (z/H)^\mu$; m denotes mass per unit height; $p(z)$ denotes the wind load distribution along the height. Here, since the contributions of the higher modes to the wind loads are minimal, only the first mode is considered in the analysis.

Since the wind loads can be measured as a base bending moment based on wind High-Frequency Force Balance measurements, the generalized force is derived from the base moment. By definition, base bending moment can be defined as $M = \int_0^H z p(z) dz$. Therefore, the generalized force can be defined as follows by using the previous definitions:

$$\tilde{f} = k_m M; \quad (4)$$

$$k_m = \frac{\int_0^H \phi_{x1} p(z) dz}{\int_0^H z p(z) dz} \quad (5)$$

Here, when the wind load distribution $p(z)$ is assumed to be a linear function of height, z , the mode shape correction factor is $k_m = 3 \times [H(\mu + 2)]^{-1}$.

By using Eqs. (3), (4) and the mode shape correction factor, the power spectral density (PSD) of the displacement response, $S_{\ddot{x}}$ can be calculated as follows based on random vibration theory for stationary processes (Clough and Penzien 1993):

$$S_{\ddot{x}} = \tilde{m}^{-2} k_m^2 |h(\omega)|^2 S_M(f) \quad (6)$$

$$h(\omega) = [(-\omega^2 + \omega_1^2) + i(2\xi_1\omega_1\omega)]^{-1} \quad (7)$$

where $S_M(f)$ is the PSD of the base bending moment. In the above, the generalized mass and the mode shape correction factor are time-independent variable. The PSD of the across-wind acceleration response is therefore

$$S_{\ddot{x}} = \omega^4 \tilde{m}^{-2} k_m^2 |h(\omega)|^2 S_M(f) \quad (8)$$

$S_M(f)$ can be calculated according to AIJ (AIJ, 2006) as

$$\frac{f S_M(f)}{(0.5\rho U_H^2 B H^2)^2} = C_M^2 \sum_{j=1}^k \frac{4K_j(1+0.6\varphi_j)\varphi_j}{\pi} \frac{(f_1/f_{sj})^2}{(1-(f_1/f_{sj})^2)^2 + 4\beta^2(f_1/f_{sj})^2} \quad (9)$$

where ρ , U_H are the air density and mean wind speed at the top of the building; B and H are the breadth and height of the building; and f_1 is the natural frequency for the first mode in the across-wind direction.

$$k = \begin{cases} 1, & D/B < 3 \\ 2, & D/B \geq 3 \end{cases} \quad K_1 = 0.85; K_2 = 0.02$$

$$C_M = 0.0082(D/B)^3 - 0.071(D/B)^2 + 0.22(D/B);$$

$$\varphi_1 = \frac{(D/B)^4 + 2.3(D/B)^2}{2.4(D/B)^4 - 9.2(D/B)^3 + 18(D/B)^2 + 9.5(D/B) - 0.15} + \frac{0.12}{(D/B)};$$

$$\varphi_2 = \frac{0.28}{(D/B)^{0.34}}; \quad f_{s1} = \frac{0.12}{(1 + 0.38(D/B)^2)^{0.89}}; \quad f_{s2} = \frac{0.56}{(D/B)^{0.85}}$$

where D is the depth of the building. The variance of the across-wind acceleration response of the building is

$$\sigma_{\ddot{x}}^2 = \int_0^\infty S_{\ddot{x}} df \quad (10)$$

By assuming the mode shape to be of the form $\phi_{x1}(z) = (z/H)^\mu$, the shear force and bending moment at a location αH , ($0 \leq \alpha \leq 1.0$), along the building height can be respectively expressed as

$$F(z) = \frac{mBD}{H^\mu} \sigma_{\ddot{x}}^2 \int_{\alpha H}^H z^\mu dz \quad (11)$$

$$M(z) = \frac{mBD}{H^\mu} \sigma_{\ddot{x}}^2 \int_{\alpha H}^H z^\mu (z - \alpha H) dz \quad (12)$$

where m represents the mass density of building.

SEISMIC RESPONSE OF TALL BUILDINGS

In the formulation of seismic response of tall buildings, the effect of higher modes can have a significant influence on the overall response when compared to that of the first mode response. Neglecting the effect of higher modes can lead to unconservative results. The equation of motion of a tall building subjected to ground acceleration $\ddot{x}_g(t)$ is given by

$$\ddot{\tilde{x}}_j + 2\xi_j \omega_j \dot{\tilde{x}}_j + \omega_j^2 \tilde{x}_j = -\frac{\tilde{L}_j}{\tilde{m}_j} \ddot{x}_{gj}(t) \quad (13)$$

where \tilde{x}_j is the generalized coordinate of the j th mode and $\tilde{L}_j \ddot{x}_{gj}(t)$ is the generalized excitation with

$$\tilde{L}_j = \int_0^H m(z) \phi_{xj}(z) dz \quad (14)$$

and $\phi_{xj}(z)$ is the mode shape for mode j in the x - direction. To compute the bending moments and shears associated with the displacement $x(z, t)$, the method of equivalent static forces has been used. These forces are defined as the external forces that would cause displacements $x(z)$ defined by [Chopra \(1995\)](#) as

$$f_{oj}(z) = \frac{\tilde{L}_j}{\tilde{m}_j} m(z) \phi_{xj}(z) S_{ai} \quad (15)$$

where S_{ai} is the ordinate of the acceleration design spectrum at a given period. The value of spectral acceleration is assumed to be lognormally distributed with median value θ , and dispersion β , and can be obtained according to FEMA P-58-1 ([FEMA 2012](#)) as

$$S_{ai} = \theta e^{\beta\Phi^{-1}(P_i)} \quad (16)$$

where Φ^{-1} is the inverse standardized normal distribution, and P_i is the midpoint cumulative probability for region i within the interval used to characterize the distribution of seismic demand. Thus, the shear and bending moment at a height αH , ($0 \leq \alpha \leq 1$) can be respectively expressed as

$$F_j(z) = \int_{\alpha H}^H f_{oj}(z) dz \quad (17)$$

$$M_j(z) = \int_{\alpha H}^H f_{oj}(z)[z - \alpha H] dz \quad (18)$$

for mode j . The contribution of each mode to the overall response is determined by combining the maximum effect of each mode to the response using the square root of sum of squares (SRSS) method.

EXAMPLE – DESIGN LOADS ON TALL BUILDING FOR PERFORMANCE BASED DESIGN

A tall building with a building height, H , of 300 m, with uniform square-shaped floor plates with dimensions of 30 m (B) \times 30 m (D) was analyzed in along-wind and across-wind directions for various wind speeds that corresponded from weekly to 10,000-year return period wind speeds in Seattle, Washington. The wind exposure applied was the open exposure which has turbulence intensity of approximately 10 % at the building height based on ASCE (2010) and ESDU (1984). The mass density of the building was 225 kg/m³; the mass per unit height was equal to 202.5×10^3 kg/m. Figure 3 illustrates the building's natural vibration modes and corresponding frequencies and periods for the first six modes in the direction of interest. The building's first mode frequency and structural damping ratio were 0.1 Hz (i.e., building period, $T=10.0$ s) and 0.02 respectively. For the 1st mode, the exponent of the mode shape, μ , was 1.5 which is a typical value for tall buildings, where mode shape function, $\varphi = (z/H)^\mu$, where z is elevation from the ground.

The statistical distribution of wind speeds measured at King County International Airport in Seattle is plotted in Figure 2 (NOAA). The wind speeds indicate mean hourly wind speeds at 10-meter height at open exposure. The plot shows the 50-year return period mean hourly wind speed of 25 m/s, which corresponds to 85 mph 3 second gust wind speed according to ASCE 7-05 (ASCE 2005). The empirical across-wind spectrum (AIJ 2006) has been used in this example due to the simplicity and versatility. Figure 4 illustrates across-wind spectrum in terms of base moment, as well as the vortex shedding peak value

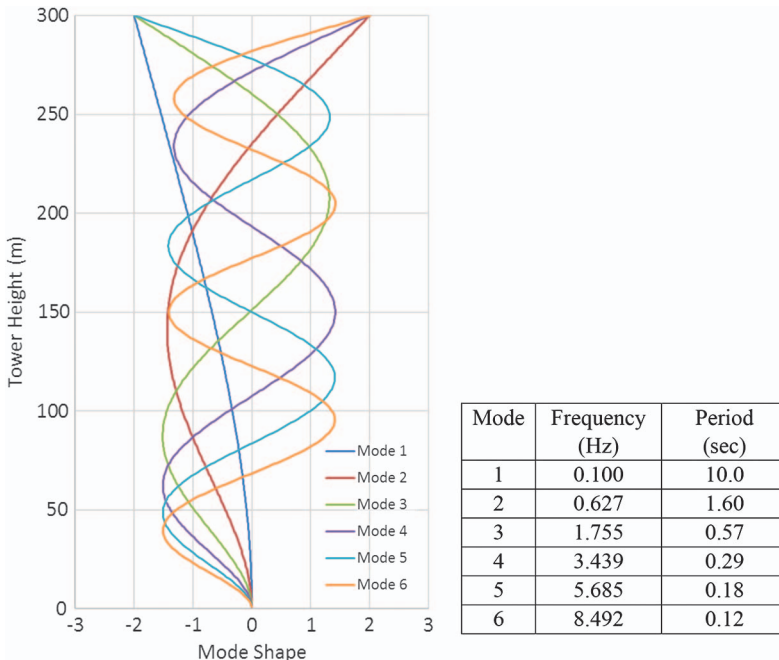


Figure 3. Natural vibration modes of the building

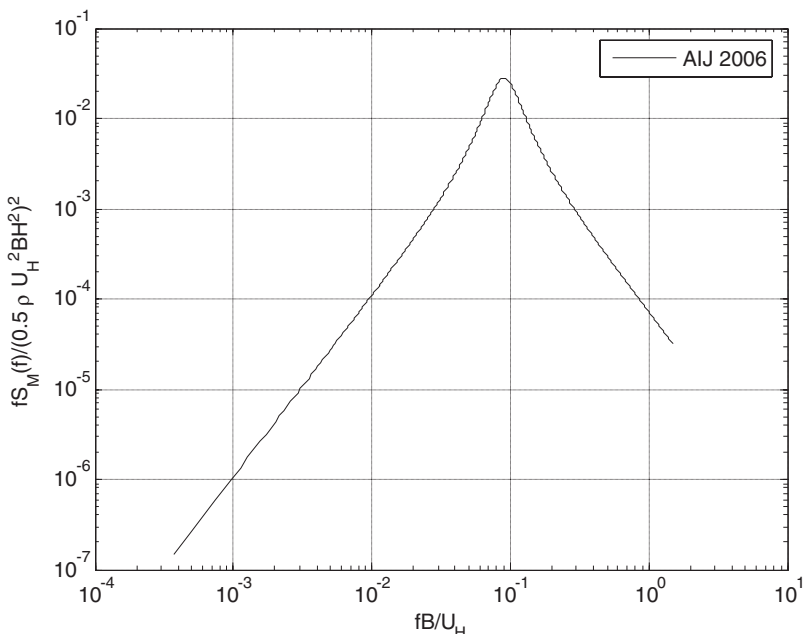


Figure 4. Normalized base moment spectra of the subject building
Source: Based on AIJ (2006).

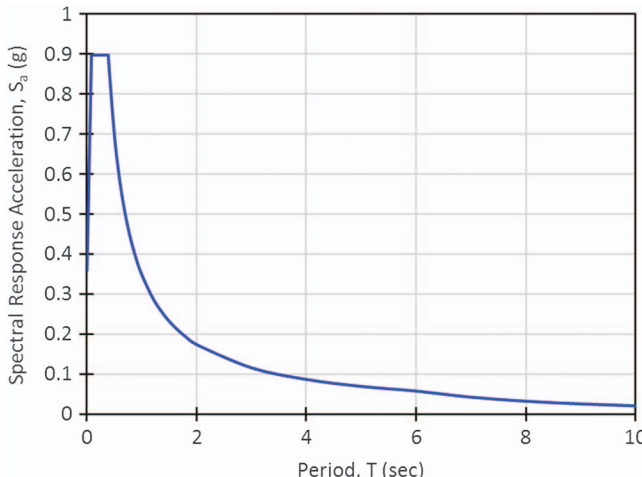


Figure 5. Design Response Spectrum at the Project Site, Seattle, WA

Source: ASCE 7-10 (2010).

occurring around the reduced frequency ($f_s B/U_H$) of 0.1 typical for buildings with a square plan (Gu and Quan 2004, Chen et al. 2014).

For the comparison, seismic loads were also estimated in terms of response spectrum according to ASCE 7-10 (ASCE 2010). Based on USGS Design Map (ASCE 7-10) as illustrated in Figure 5, the Design Spectral Acceleration Parameter, $S_{D1} = 0.348 \text{ g}$; long-period transition period, $T_L = 6 \text{ seconds}$; and corresponding Design Response Spectrum, $S_a = S_{D1} T_L / T^2 = 0.02088 \text{ g}$ for collapse probability of 1% in 50-year in Seattle (ASCE 7-10). The above values were achieved by assuming Site Class-B and Risk Category I, II, and III. The distribution of the seismic intensity was assumed to be a lognormal distribution with dispersion coefficient, β , of 0.4 to 0.5 which is a typical statistical distribution of seismic intensity (FEMA 2012). Figure 1 illustrates the probabilistic distribution of the seismic intensity for the different dispersions of 0.4 and 0.5.

Base moments during vortex-shedding (across-wind direction) and wind-buffeting (along-wind direction) were evaluated based on spectral analysis and gust buffeting theory (Solari 1993a, 1993b), respectively. In the wind analysis, only the first mode was considered since the higher mode contributions were minimal. The peak base moments and base shears were represented in Figure 6a and 6b respectively. As shown in these figures, the across-wind loads drastically increased from 1-year to 10-year return periods; however, the slope quickly reduced after 50-year return period and maintained a very mild slope beyond this point. As already briefly mentioned, those high across-wind responses were due mainly to the vortex-shedding. However, along-wind loads quadratically increased and reached the level of the across-wind load for 10,000-year return period for the base moment and 700-year for the base shear. The example represents a typical tall building behavior, which is governed by the across-wind vibration.

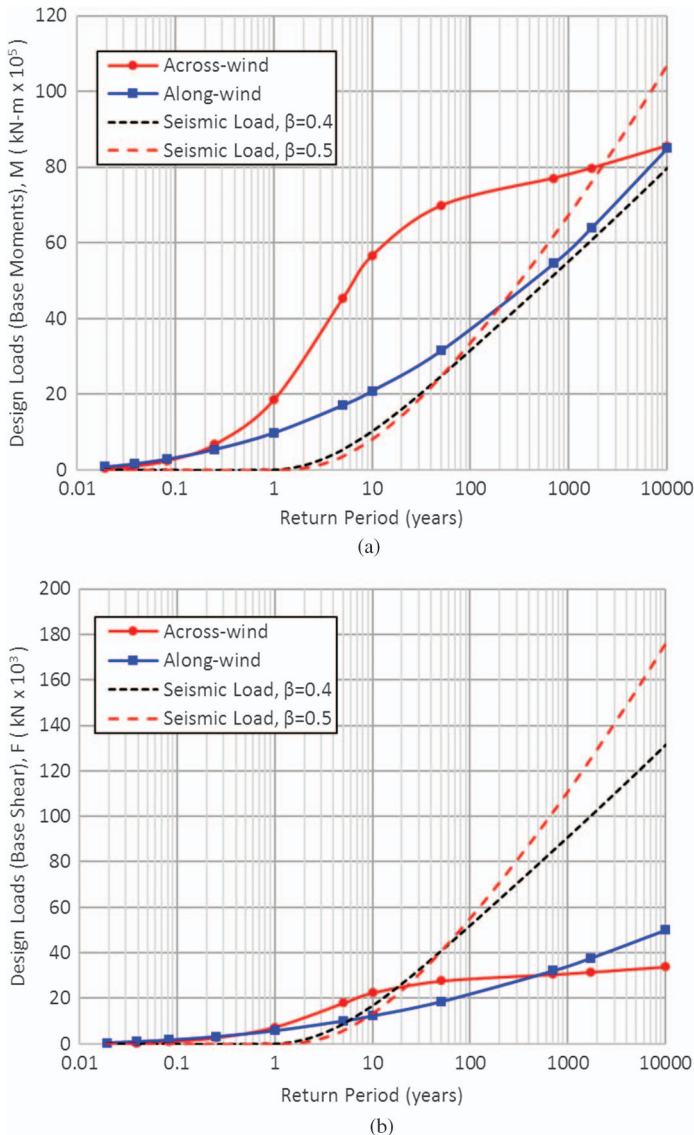


Figure 6. Peak base moment and base shear for various return period under wind and seismic loads: (a) base moment, and (b) base shear

Base moments were also calculated for the previous seismic loads, considering the six lowest vibration modes. Based on the assumption of uniform mass density, the base overturning moments were calculated using the inertia forces of the modes which were combined based on SRSS method. As shown in Figure 6a, the overall base moment caused by seismic loads were much lower than those caused by wind loads over the serviceability and strength levels, because of the long

fundamental building period (low building frequency). Meanwhile, in the case of base shear as shown in Figure 6b, seismic loads were evaluated to be higher than the wind loads beyond 20-year return period.

For the PBWD, 1-year and 10-year accelerations were limited by the industry guidelines for the serviceability; 50-year wind load for strength required the structure remain in an elastic state; 10,000-year wind load for collapse-prevention demand allowed plastic deformation of some elements. Figure 7 illustrates the design loads normalized by 50-year values. The figure displays the collapse-prevention level wind loads (10,000-year return period) compared to the corresponding strength level loads (50-year return period). As shown in this figure, the collapse-prevention level loads were 3.2 to 4.3 times larger than the strength level for seismic loads; whereas only 2.7 and 1.2 times for along-wind and across-wind loads, respectively. For the seismic loads, the structural materials could be saved by allowing plastic deformation to dissipate large seismic energy without substantial reinforcement for very high collapse-prevention level seismic loads, while keeping the structure in the elastic range up to the strength level loads. Furthermore, as briefly mentioned in the introduction, the ductile design is applicable for seismic loads because the short-duration of the seismic loads prevents complete collapse from the cyclic degradation. However, for the across-wind loads, the difference between the collapse-prevention level and the strength level loads is too small to allow ductile behavior of the material while keeping it elastic for the strength level loads, which means the material will always remain in elastic range.

The overall bending moment and shear force distributions over the entire height of the building obtained from the analysis are illustrated in Figure 8. As shown in Figures 8a and 8b, for the strength level design with 50-year return period, the across-wind load governed the design, except for a small portion at

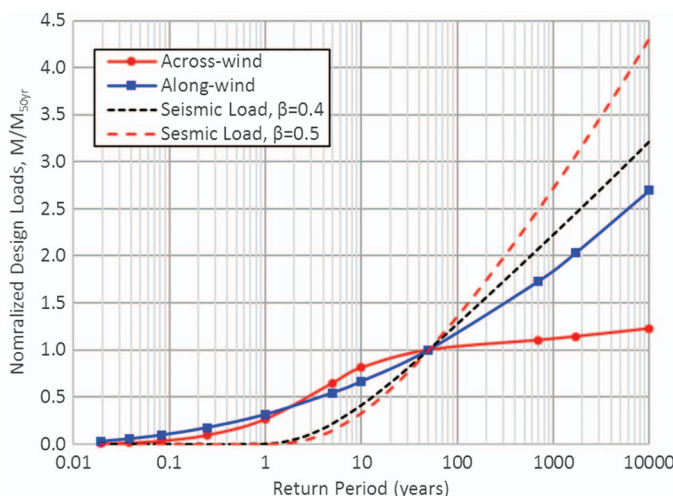


Figure 7. Peak base moment under wind and seismic loads normalized by 50-year values

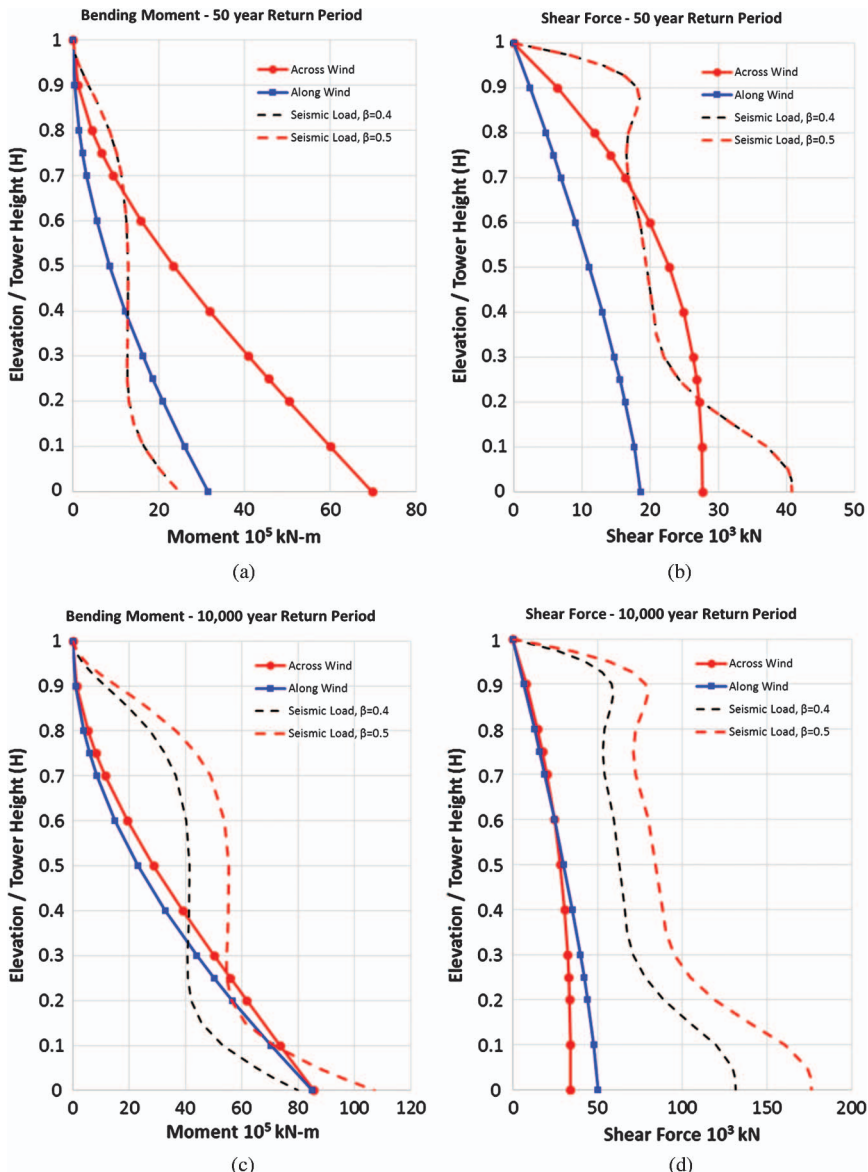


Figure 8. Moment and shear force distribution along the height under wind and seismic loads: (a) 50-year bending moment, (b) 50-year shear force, (c) 10,000-year bending moment, and (d) 10,000-year shear force

the top of the building where seismic loads exceed wind loads. For shear force, seismic loads were higher than the wind loads at the base and at the top, whereas across-wind loads were higher at the mid-height of the building. For the

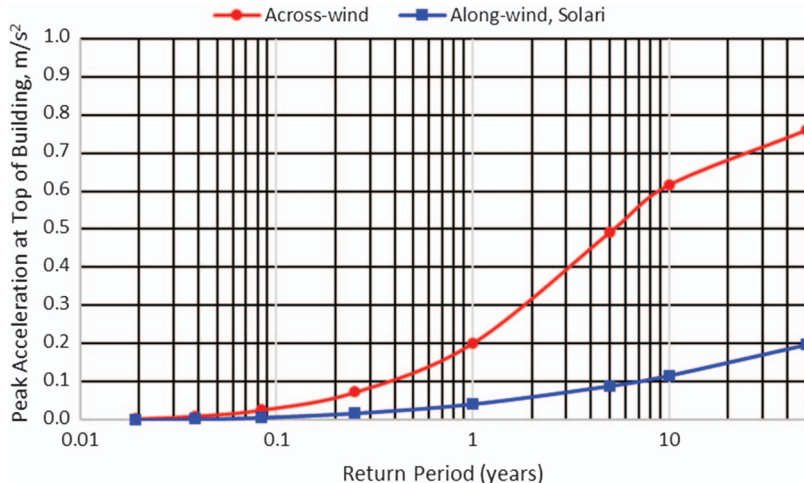


Figure 9. Peak accelerations at top floor for various return periods

collapse-prevention level design with 10,000-year return period, seismic load effects showed a significant increase compared to wind loads as shown in Figures 8c and 8d. The base moments due to seismic loads were similar at the base but much higher over the majority of the building heights, whereas shear forces from seismic loads were calculated to be much higher than those from wind loads as shown in Figure 8d.

Although the main goal of this paper is to identify the feasibility of performance objective optimization between the strength and collapse-prevention levels, there may be more potential efficiency of PBWD in optimizing the levels of serviceability and strength levels (Nakai et al. 2013, Griffis et al. 2013). To investigate the wind issues for these levels, the peak accelerations in across-wind and along-wind directions were evaluated, and the results were compared for service level winds. As shown in Figure 9, the across-wind response governed the serviceability condition due to the vortex shedding. Since the building accelerations were estimated to substantially exceed the industry guidelines (ISO; Isyumov 1993, 1995), artificial damping such as Tuned Liquid Sloshing Damper (Kareem 1987, 1990; Jeong 2015) or Tuned Mass Dampers will be required for the building to mitigate the excessive vibrations to the acceptable levels. Artificial dampers also affect the building performance, and will be invested in future research by the authors.

CONCLUSIONS

Wind design of tall buildings were investigated in consideration of PBD. Tall slender buildings were governed by the across-wind loads which very slowly increased beyond the strength level wind loads even in much longer return

periods. This characteristic of wind loads demerits the application of the conventional PBD approach to tall building wind design. The serviceability of the buildings was also governed by the across-wind vibration during vortex shedding.

References

- AIJ (Architectural Institute of Japan). 2006. *Recommendations for loads on buildings*.
- ASCE. 2005. *Minimum design loads for buildings and other structures*. ASCE/SEI 7-05. Reston, VA: ASCE.
- ASCE. 2010. *Minimum design loads for buildings and other structures*. ASCE/SEI 7-10. Reston, VA: ASCE.
- Chen, X., D. Kwon, and A. Kareem. 2014. "High-frequency force balance technique for tall buildings: A critical review and some new insights." *Wind Struct.* **18** (4): 391–422.
- Chopra, A. K. 1995. *Dynamics of structures*. Hoboken, NJ: Pearson.
- Clough, R. W., and J. Penzien. 1993. *Dynamics of structures*. 2nd ed. New York: McGraw-Hill.
- Davenport, A. G. 1964. "Note on the distribution of the largest value of a random function with application to gust loading." *Proc. Inst. Civil Eng.* **28** (2): 187–196.
- Davenport, A. G. 1979. "The influence of turbulence on the aeroelastic responses of tall structures to wind." In *IAHR-IUTAM Symp. Practical Experiences with Flow Induced Vibrations*, 681–695, Germany, Karlsruhe: Univ. of Karlsruhe.
- ESDU (Engineering Standard Data Unit). 1984. *Strong winds in the atmospheric boundary layer. Part 2: Discrete gust speeds*. ESDU 83045. ESDU.
- FEMA. 2012. *Seismic performance assessment of buildings*. FEMA P-58. Washington, DC: FEMA.
- Fujino, Y., K. Wilde, J. Masukawa, and B. Bhartia. 1995. "Rational function approximation of aerodynamic forces on bridge deck and its application to active control of flutter," In *Proc., 9th Int. Conf. on Wind Engineering*. New Delhi, India.
- Griffis, L., V. Patel, S. Muthukumar, and S. Baldava. 2012. "A framework for performance-based wind engineering," In *Proc., ATC-SEI Advances in Hurricane Engineering Conf.* Miami, FL.
- Gu, M., and Y. Quan. 2004. "Across-wind loads on typical tall buildings." *J. Wind Eng. Ind. Aerodyn.* **92** (13): 1147–1165.
- Holmes, J. D. 1996. "Along-wind response of lattice towers. II: Aerodynamic damping and deflection." *Eng. Struct.* **18** (7): 483–488.
- Holmes, J. D. 2001. *Wind loading of structures*. London: E & FN Spon.
- ISO. n.d. *Guidelines for the evaluation of the response of occupants of fixed structures, especially buildings and off-shore structures, to low frequency horizontal motion (0.063 to 1 Hertz)*. ISO 6897:1984. Geneva: ISO.
- Isyumov, N. 1993. "Criteria for acceptable wind-induced motions of tall buildings," In *Proc., Int. Conf. on Tall Buildings*. Rio de Janerio, Brazil: Council on Tall Buildings and Urban Habitat.
- Isyumov, N. 1995. "Motion perception, tolerance and mitigation," In *Proc., 5th World Congress of the Council on Tall Buildings and Urban Habitat*. Amsterdam, Netherlands.
- Jeong, U. Y. 2015. "Advances in tall building design under strong winds" In *Structures Congress 2015*. Reston, VA: ASCE/SEI.
- Judd, J. P., and F. A. Charney. 2015. "Inelastic building behavior and collapse risk for wind loads," In *Proc., Structures Congress 2015*. Reston, VA: ASCE.

- Judd, J. P., and F. A. Charney. 2016. "Wind performance assessment of buildings" In *Geotechnical and Structural Engineering Congress 2016*, 1259–1268. Reston, VA: ASCE.
- Kareem, A. 1990. "Reduction of wind induced motion utilizing a tuned sloshing damper." *J. Wind Eng. Ind. Aerodyn.* **36**: 725–737.
- Kareem, A., and W. J. Sun. 1987. "Stochastic response of structures with fluid-containing appendages." *J. Sound Vib.* **119** (3): 389–408.
- Katagiri, J., T. Ohkuma, H. Marukawa, and S. Shimomura. 2000. "Motion-induced wind forces acting on rectangular high-rise buildings with side ratio of 2." *J. Struct. Constr. Eng.* **65** (534): 25–32.
- Larsen, R., R. Klemencic, J. Hooper, and K. Aswegan. 2016. "Engineering objectives for performance-based wind design" In *Geotechnical and Structural Engineering Congress 2016*, 1245–1258. Reston, VA: ASCE.
- Nakai, M., K. Hirakawa, M. Yamanaka, H. Okuda, and A. Konishi. 2013. "Performance-based wind-resistant design for high-rise structures in Japan." *Int. J. High Rise Build.* **2**: 271–283.
- NOAA. 2018. "Climate data online." <https://www.ncdc.noaa.gov/>.
- PEER (Pacific Earthquake Engineering Research Center). 2010. *Guidelines for performance-based seismic design of tall buildings*, Berkeley, CA: PEER.
- Randall, R. B. 1987. *Frequency analysis*. Nærum, Denmark: Brüel & Kjær.
- Solari, G. 1993a. "Gust buffeting. I: Peak wind velocity and equivalent pressure." *J. Struct. Eng.* **119** (2): 365–382.
- Solari, G. 1993b. "Gust buffeting. II: Dynamic alongwind response." *J. Struct. Eng.* **119** (2): 383–398.
- Steckly, A. 1989. Ph.D. thesis, Univ. of Western Ontario.
- Watanabe, Y., N. Isyumov, and A. G. Davenport. 1997. "Empirical aerodynamic damping function for tall buildings." *J. Wind Eng. Ind. Aerodyn.* **72**: 313–321.

This page intentionally left blank

CHAPTER 5

Interrogation of Relation between Design Load Level and Lifetime of Individual Building and Its Element

Yukio Tamura, Ph.D., M.ASCE^{*}

Di Wu, Ph.D.[†]

Qingshan Yang, Ph.D.[‡]

Abstract: The common wisdom is to design cladding and components using a lower level wind load than the main structural frames, i.e. a shorter recurrence period wind load is used for cladding design than for frame design. This paper first discusses the design wind load levels for structural frames and for cladding and components. Next, the design wind loads of scaffolds for building construction, those of buildings in the construction stage, and those of so-called “temporary” structures such as site offices are discussed. In Japan, the design wind load for scaffolds is defined as 1-year-recurrence wind load, because its average setting period at one construction site is around 6 months, but this paper clearly proves the inappropriateness of this design wind load estimation concept. Then, it is shown that there is no relation between the design wind load level and its lifetime at an individual site. Finally, even for the design wind load for main structural frames, it is clearly demonstrated that the design load level may not be able to be determined based on the lifetime of an individual building. Therefore, although the LCC concept is applied in design load estimation, it is strongly recommended that the optimal design load level should be decided considering total LCC for the city or nation as a

^{*}Beijing Key Laboratory of Structural Wind Engineering and Urban Wind Engineering, School of Civil Engineering, Beijing Jiaotong University, No. 3 Shangyuan St., Haidan District, Beijing 100044, China; email: yukio@arch.t-kougei.ac.jp

[†]Beijing Key Laboratory of Structural Wind Engineering and Urban Wind Engineering, School of Civil Engineering, Beijing Jiaotong University, No. 3 Shangyuan St., Haidan District, Beijing 100044, China; email: forseti2001@163.com

[‡]Beijing Key Laboratory of Structural Wind Engineering and Urban Wind Engineering, School of Civil Engineering, Beijing Jiaotong University, No. 3 Shangyuan St., Haidan District, Beijing 100044, China; email: qshyang@bjtu.edu.cn

whole, and treat design as involving a group of buildings, rather than attempting to optimize the LCC of individual buildings. Clearly, the cost associated with social or national security must be included.

INTRODUCTION

There are several problems in the current codes and standards that need to be rectified if we are to produce wind-resistant buildings and structures. One of them is the recurrence period of the design wind load for structural frames and for cladding/components, namely the design wind load levels for structural frames and for cladding/components. The tendency is to design cladding/components using a lower wind speed than the main structural frames (i.e., a shorter recurrence wind load is used for cladding design than for frame design in some countries). For example, according to the Building Standard Law of Japan (BSLJ), allowable-stress design criteria are combined with 50-year-recurrence wind loads for structural frame design, and the same recurrence wind loads are used for cladding/components design. However, 500-year-recurrence wind loads are applied for the ultimate state structural frame design, while cladding/component design is not obligated to reach this design level. Accordingly, structural designers tend to ignore this level in cladding/component design. Some consider only 100 or 200-year-recurrence loads for cladding/components, leaving the 500-year-recurrence load for structural frames. Thus, it is implicitly understood that the design load level of cladding/components can be lower than that of structural frames. However, the validity of this understanding should be re-examined carefully.

A similar problem is seen with the design wind loads of scaffolds for building construction, and for those of so-called temporary structures such as construction site offices. For example, in Japan, the design wind load for scaffolds is defined as the 1-year-recurrence wind load, because the average setting period at a construction site is around 6 months (SCEAJ-TRSSW 1999). However, this design wind load estimation concept is completely inappropriate as discussed later.

In this paper, a very primitive problem, namely the relation between the design load level and the lifetime of individual buildings or their parts is discussed.

LOAD LEVELS FOR MAIN FRAMES AND CLADDING/COMPONENTS OF BUILDINGS

Design Wind Load Estimation. There are some problems with the wind loads used in building design, as mentioned in the Introduction, such as the different wind load levels for main frames and cladding/components. Even for just frame design, there are many problems. One of them is the Gust Loading Factor (GLF, Davenport 1967) or the Gust Response Factor (GRF) used in the majority of building codes and standards in the world. Basically, the same GLF or GRF, which

is based on the dynamic behavior of the building, is used for serviceability state design and also for ultimate state design. It is necessary to confirm conformance to “elastic GLF” or “elastic GRF” in the ultimate design stage, in which the building behaves in a plastic manner. Incidentally, in Japan, the ultimate design criteria for main structural frames allow member stresses to be within 1.1 times the allowable stress (i.e., only 10% larger than the elastic limit), so the building can behave in an “almost elastic manner.” Thus, fully plastic behavior is not permitted and is not checked in design. Further studies are needed in this regard.

Furthermore, in general, the structural design of main frames uses the aerodynamic coefficient of the pristine building without cladding damage, so that the cladding and components are implicitly assumed to keep their original integrity. Therefore, theoretically, there is no reason to accept a lower level of wind load for cladding/components, except for cases considering the possibility of change in the aerodynamic coefficient or reaching a consensus with building owners and occupants or guaranteeing preventive measures of damage coherence or chain of damage. A minor failure of cladding/components can trigger destructive damage to the entire building.

Coherent Phenomena and Chain of Wind-Induced Damage. Structural designers are interested in main frame design, but not so much in cladding design. However, wind-induced damage is generally triggered by localized damage to cladding/components. This damage can propagate to much larger scales and even damage the main frames.

In general, positive pressures act on the windward wall, but negative pressures act on the other surfaces such as side walls, leeward wall, and roof surface as shown in Figure 1a. In general, the internal pressure coefficient is negative. The wind force coefficient C_f acting on the roof structure is the difference of the external pressure coefficient C_{pe} and internal pressure coefficient C_{pi} , say $C_f = C_{pe} - C_{pi}$. Once a window pane on the windward wall is damaged, the air enters the building and the internal pressure coefficient C_{pi} becomes a high positive value. Therefore, the uplift (negative) wind force coefficient C_f suddenly becomes large through combination with the inherent negative external pressure coefficient C_{pe} . As shown in Figure 1b. The same damage progression can happen with just minor damage to the eaves.

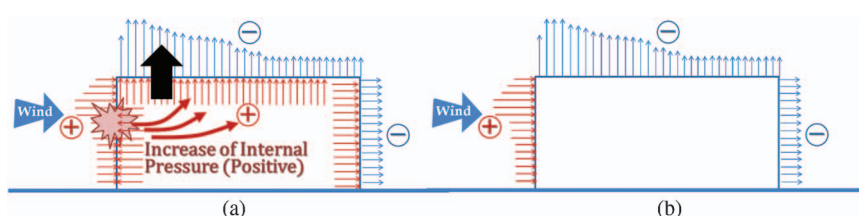


Figure 1. Wind pressure distribution and effects of sudden partial failure of the windward wall: (a) wind pressure distribution, and (b) sudden increase in roof force

This “coherent phenomenon” in damage progression is a special feature of wind-induced building damage. The separated parts of cladding and components can easily become wind-borne debris, and strike downstream buildings. Debris impacts also initiate cladding/components damage to downstream buildings. This “chain of damage” is another special feature of wind-induced damage to buildings in urban areas.

Property Losses due to Damage to Cladding/Components. If the window panes and claddings of a tall building fail, property inside the building would be seriously damaged and lose its value. This property loss can be very significant, especially if only the main structural frames remain. The miserable situation of a building with damaged window panes is often reported after extreme wind attacks in urban areas [e.g., [Brewick et al. \(2009\)](#)] (Figure 2).

Super typhoon Haiyan attacked the Philippines on November 8, 2013, and caused serious disaster to this country and other surrounding countries. The recorded maximum 3s gust was 57m/s at Roxas City, Capiz, and the lowest pressure was 910hPa at Guiuan, Samar (PAGASA). The dead and missing numbered 7,986 (NDRRMC, January 14, 2014).

Figure 3a shows a steel frame structure whose main frames suffered almost no damage but whose metal roof sheets were widely damaged. Only the claddings failed significantly but there was serious property damage inside as shown in Figure 3b. BCP (business continuity planning) was not successful and the business stopped for a long period. The cladding damage dealt a deathblow to the building owner. If one of the purposes of a building is to ensure business viability, the cladding cannot be destroyed. Even if the main frame survives without damage, it has no value. Thus, the importance of cladding/component design should be recognized, and it is essential to understand that Wind Resistant Design is equal to Cladding/Components Design.

Figure 4a shows partial damage to the metal roof sheets of a super-market due to a tornado in Nobeoka, Japan. The opening created in the roof suddenly



Figure 2. Damage due to Hurricane Ike, 2008: (a) damage to window panes, and (b) damage to interiors, furniture, facilities, and so on

Source: [Brewick et al. \(2009\)](#), photo courtesy of A. Kareem.



Figure 3. Damage to a steel structure due to Typhoon Haiyan (Palo, Leyte, Philippines, 2013): (a) damage to roof sheets of a steel structure, and (b) serious property damage inside and failure of business continuity planning (BCP)



Figure 4. Partial damage to metal roof sheets induced collapse of entrance sashes/doors, and killed one person (Nobeoka tornado, 2006): (a) partial damage to metal roof sheets, and (b) induced collapse of entrance sashes and doors

decreased the internal pressure and became negative because of the negative roof pressures, as can be understood from Figure 1a. The wind loading across the windward wall increased significantly, and the entrance sashes and doors inwardly collapsed as shown in Figure 4b. A person standing near the entrance doors was killed under the falling sashes and doors.

Cladding/component damage can propagate throughout the entire building, and can cause serious property losses to the building owners and society. Furthermore, even the partial failure of cladding/components can cause human loss.

These facts suggest that there is generally no reason to allow a lower design wind speed for cladding/components than main frames, unless property or human life are protected effectively and the damage chain is terminated. Thus, in general, the design wind load level for cladding/components should be the same as that for the main frames.

DESIGN LOADS FOR TEMPORARY-USE BUILDINGS AND STRUCTURES

Building Codes for Temporary Buildings. Design loads for temporary use buildings and structures including construction work offices are specified in the Building Standard Law of Japan. Their design loads can be lower than those of general buildings. Building codes specify the minimum requirement to keep social and national security. BSLJ specifies temporary buildings in Article 85. Temporary buildings include emergency structures after devastating disasters, emergency buildings for the public good after disasters, temporary buildings for construction works, and temporary stores/theaters/exhibition halls. [AIJ-DRBLL \(2013\)](#) recommends reduction of the design loads for the allowable stress design level excitations (almost 50y-recurrence level), if the occupants' safety is guaranteed for the ultimate limit state level excitations (almost 500y-recurrence level). ASCE 7-10 does not specify requirements for temporary structures. Accordingly, engineers may consult another standard, called ASCE 37, which addresses design loads on permanent structures in the construction stage, similar to temporary structures. For temporary structures with design life less than 6 weeks, a reduction factor of 0.75 is recommended to be applied to the design wind speeds. The Australian/New Zealand Standard (AS/NZS 1170.2:2011) defines structures with design life greater than 5 years as "permanent" and structures with design life less than or equal to 5 years as "temporary." The design wind speeds of temporary structures with varying design lifetimes are lower than is true for permanent structures. As shown in Figure 4, it might be difficult to guarantee the safety of human lives, but basically they simply believe that they can reduce the design load for temporary buildings.

Design Load for Scaffoldings. As mentioned in the Introduction, the design wind load for scaffoldings is defined as the 1-year-recurrence wind load in Japan, because of its short average setting period at one construction site, 6 months for bare scaffolding and 4.5 months if sheets are used (SCEAJ-TRSSW 1999). The British standard (BS EN 12812:2008) allows the wind pressure to be modified to take account of the period of use of the scaffolding; it is the recommendation of this standard that the minimum value of probability on a scaffolding structure be based on a two year return period. The Chinese standard (JGJ130-2011) recommends 10-year-recurrence wind loads for scaffolding design. However, this principle is not necessarily appropriate for design load estimation as mentioned in the previous section.

Figures 5a and b show damage to scaffolds in Japan and induced car accidents and damage to a neighboring building. In some cases, people working at the construction site or walking outside can be killed or injured. These facts suggest that the damage to scaffolds can cause secondary failure of/damage to others. As the structural system of scaffolding is not stand-alone, once it is damaged, the effects imposed on others are more significant than is true with general buildings.



Figure 5. Damage to scaffolding: (a) damage to scaffolding and induced car accidents, and (b) damage to scaffolding and induced damage to neighboring buildings

Source: (a) Hokkoku Shimbun (2007), and (b) Ohdo (2007).

Design Load for Construction Work Offices. Figures 6 and 7 show damage to construction work office buildings due to a tornado in Saroma, Hokkaido, 2006. Nine people died due to this damage. The foundation part is seen in Figure 7. Simple embedded short vertical posts supported wooden foundation girders and the superstructure was attached to them with iron clamps. Such buildings have

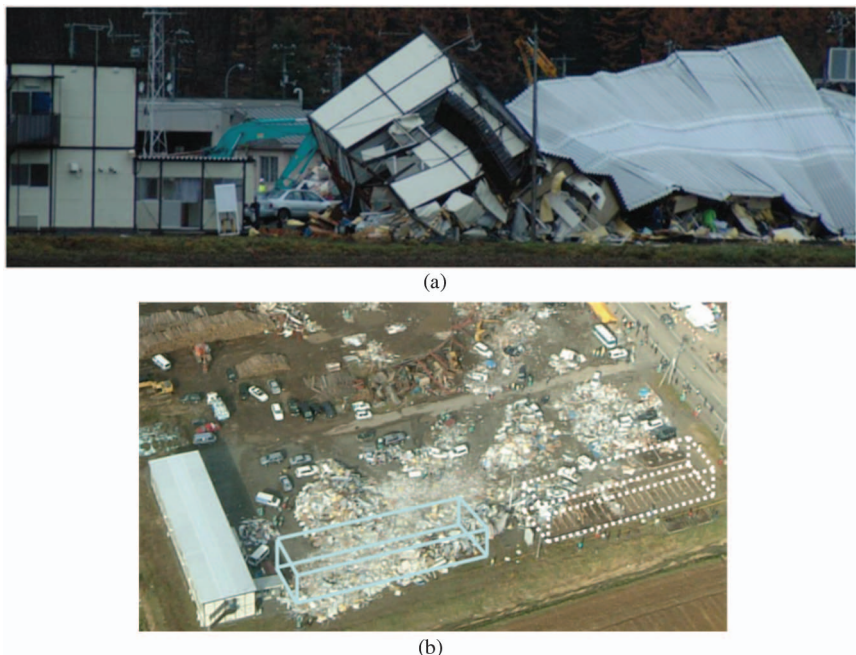


Figure 6. Damage to construction work offices due to a tornado in Saroma-cho, Hokkaido, Japan, on November 6, 2006: (a) overturned construction work office, and (b) overturned construction work office (left, after removed) and blown-off one (right)

Source: Tamura et al. (2007).



Figure 7. Simple foundation system of construction work offices shown in Figure 6: (a) foundation of construction work office blown off, and (b) close-up view of foundation pier

Source: Tamura et al. (2007).

clearly weaker ground anchorage than general buildings. As mentioned in the previous section, temporary buildings and structures can be constructed with lower design loads.

However, we cannot find any reason to accept lower design loads than general buildings. This kind of building is used in much the same way as a general building. Workers at a construction site have meetings, make drawings, conduct analyses, perform administrative works, meals, sleep, and so on in this type of building. There is no difference from other general buildings including their headquarter office building. Once a person takes a job in the construction company as a construction engineer, he should stay and work in this type of building until he retires, say for 40 years.

On the other hand, a person assigned as a designer of the same company can stay in a high quality building such as the headquarter office for the same 40 years, and do almost the same things. The site staff does not quit his job after finishing his 1- or 2-year work term at a certain construction site. He continues to work in construction work offices at different construction sites. Thus, the construction work office is a kind of permanent building for him. If the quality of the construction work office is lower than that of general buildings in term of safety level, he would face more risk than the office staff, but this should not be accepted.

LENGTH OF LIFETIME AND INDIVIDUAL USE

Can Shorter Lifetime of Temporary Building for Individual Use be Reason of Lower Design Load? Let's discuss the lifetimes of temporary buildings such as construction work offices or scaffoldings. Figure 8 shows a schematic diagram of a very simple city model, in which there are $30 \times 24 = 720$ buildings including construction sites. Each rectangular block represents a building, and green blocks indicate construction sites. The figure gives six snapshots of the city taken at

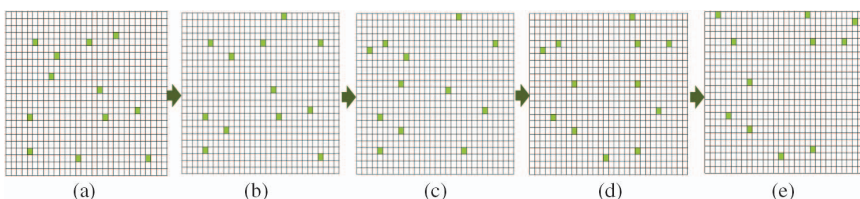


Figure 8. Schematic diagram of movement of scaffolding or construction work offices and general buildings in a city model (every 6 months snapshots): (a) present, (b) 6 months later, (c) 12 months later, (d) 18 months later, and (e) 24 months later

6 month intervals. The locations of the construction sites indicated by green blocks are basically different from snapshot to snapshot, which suggests the construction sites are moving but the number of construction sites remains basically constant. This mirrors real life.

If a strong earthquake or a strong typhoon attacks this city, all buildings, including general buildings (white blocks) and scaffolding or construction work offices (green blocks) would experience the same level of seismic load or wind load. There is no difference between the permanent and temporary blocks in terms of the existing period and the external environment.

Although a specific scaffold remains at an individual site for only a short period (i.e., average of 6 months), it moves to other places such that scaffolding is almost always present in the city or area. Although a specific scaffold is not be used for a long period, generic scaffolds always exist. The same is true for construction work offices.

If when looking at a specific construction site (e.g., “construction site i”), it disappears after a certain period, and so it seems to have a short fixed lifetime. However, if looking at construction sites in general, one or more always exist somewhere in the city the same as general buildings. Even for general buildings, a specific building has a certain lifetime, but similar structures are “always present.” Staff assigned to work at construction sites are “always working” at one or another construction work office, although the site often moves.

This suggests that the length of individual use of buildings and structures (i.e., the average period of 6 months for scaffolds or a few years for construction work offices) has no meaning with determination of design loads. We should design scaffoldings or construction work offices as permanent structures, rather than as temporary structures as they now are. The staff assigned to construction work offices do not see them as temporary, only as permanent structures.

Easier to understand examples are as follows. Even if the average rental period of an individual rental car is one day or one and a half days, the car cannot be designed based on this length of use. The renters will change, but the car itself always exists. The fact that the users are temporary (short-term) has no meaning in terms of design, only the long-term use is important for car design. Even if some parts or bolts of an airplane are replaced at predetermined intervals, those

parts and bolts cannot be designed weaker than the main body based on the replacement interval. They should have the same performance as the main body.

Replacement of Cladding/Components for Maintenance. It is said that claddings and components are replaced more frequently than main structural frames, so the existing return periods for them are shorter than that of main frames. However, as explained by rental car example and airplane example in the previous section, this replacement has no meaning. A specific cladding element may be replaced at short predetermined intervals, but identical cladding element will replace it, and the cladding itself exists as long as the building exists.

The replacement is only maintenance to keep the element's quality or resistance up to the level assumed in the design stage as shown in Figure 9. The resistance level or design load level must not predicated on the replacement interval.

Thus, short replacement periods for specific cladding elements has no meaning in terms of wind load estimation. As cladding and component damage directly impacts the safety of the building and property, the structural designer should play an important role in guaranteeing their performance during strong winds.

Removal of Nets and Sheets for Strong Tropical Cyclones. By the way, the conventional wisdom is that the early warning systems of tropical cyclones allows nets or sheets covering scaffolding to be removed if strong wind is imminent, so a lower level of wind loads can be applied for scaffolding design [e.g., 1-year recurrence wind speed as specified in SCEAJ-TRSSW (1999)]. This is also obviously wrong.

Removal of nets and sheets changes only the physical parameters such as wind force coefficient C_f and projected area A_f . It cannot be a reason for accepting a reduction of design wind speed level V_d . The resultant wind force

$$F_d = (1/2)\rho V_d^2 C_f A_f \quad (1)$$

can be smaller because of the smaller wind force coefficient C_f or the smaller projected area A_f , but the recurrence year of the design wind speed V_d cannot be smaller. Thus, we can change and use appropriate C_f and A_f values depending

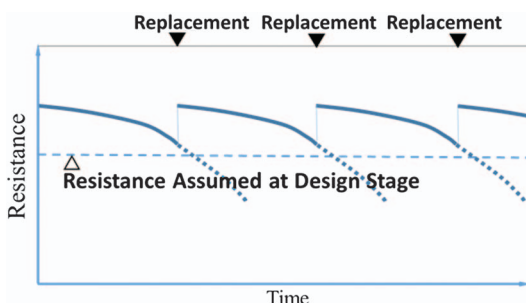


Figure 9. Replacement of elements for maintenance

upon the situation, but there is no relation between the design load level (i.e., design wind speed level V_d) and the removal of nets or sheets, and this point should be clearly noted.

Anyway, it should be clearly understood that there is no reason to use such a short design recurrence period [e.g., 1-year-recurrence wind load ([SCEAJ-TRSSW 1999](#))] for scaffolds.

Seasonal Effects, Local Effects and others. Typhoons appear in the West Pacific region mainly in the warm season as seen in Figure 10, and there are significant seasonal effects. However, this is a wind climate problem. If a particular building is utilized only in the winter season, of course you need not consider the typhoon winds when you calculate design wind speed V_d . You can estimate design wind speed V_d based on wind speed records in winter seasons, or a seasonal factor can be used. This is similar to the geographic location effects. We can estimate design wind speed V_d based on the local wind climate.

It seems needless to say that these effects cannot be a reason for accepting a reduction in the recurrence period for the design wind speed estimation.

No Relation between Individual Lifetime and Social Importance or Damage Impacts. The discussions made above make it obvious that there is no relation between the design load level and the length or lifetime of individual use of cladding/components, scaffolds, and so-called temporary buildings.

It follows that the design wind load should be determined with clear recognition of the fact that so-called temporary buildings and structures never disappear and are always “present.” Their design load level should be determined based on their acceptable collapse rate or damage rate in human society. Of course, it is not easy to determine an acceptable level of damage, because it depends on the importance of the target, social, economic and physical impacts of the damage, the economic situation of the society/nation, historical aspects, and so on.

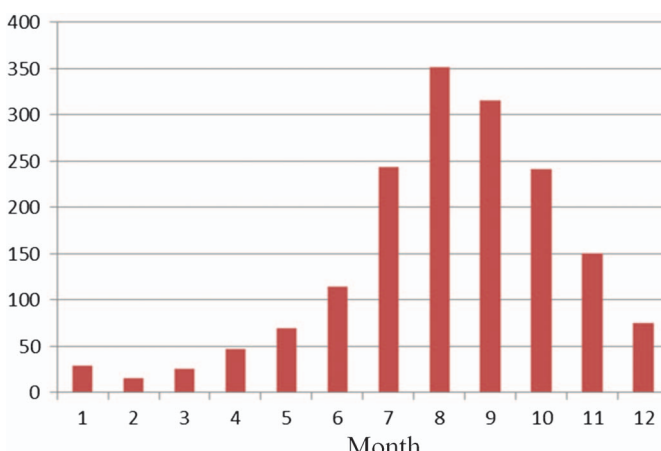


Figure 10. Monthly variation of number of typhoons (JMA, 1951–2014)

So-called temporary buildings and structures tend to be treated as less important to society, but this is not necessarily true either. There is no essential relation between the social importance and the individual lifetime of a building part or an entire building. This should also be clearly noted.

RAISED PROBLEMS OF MINIMUM LIFE CYCLE COST APPROACH

Even for designing main structural frames to resist wind loads, the design load level may not be able to be determined based on the lifetime of an individual building. We use individual buildings, but each building is an important element forming the city or nation. The function of an individual building is of course important and should be considered in the design load estimation, but the function of the city and the nation is also very important. As such, the failure or damage rate of the assemblage of elements is important, not that of any one particular element.

As is well known, there is a concept for determining the optimal design load level based on a probabilistic consideration of the minimum Life Cycle Cost (LCC) of a building including initial construction cost and estimated repair cost over its estimated lifetime. However, although each building generally belongs to an individual as private property, it is one of the cells or elements composing a city or nation, and they are strongly related to each other through economic functions as well.

Business Continuity Planning (BCP) is an important issue not only for the private sector but also for a city or a nation, and securing BCP can be a key to the security of the city or nation. In particular, tall buildings have an aspect of social property, and damage to them has significant economic and social impacts on the community.

Under the above situation and considering the fact that the design load level cannot be decided based on the lifetime or length of individual use of a building or its parts, the concept of LCC should be re-examined. This raises the following question. Can "life cycle" be the length of the lifetime of the individual building? As it has been demonstrated, we should address the assemblage of buildings rather than individual buildings. We have to re-examine whether we can decide the design load level based on the length of the individual building use.

When we make building codes or standards, we aim to specify the minimum requirements in order to keep essential and necessary security or safety level of our society which is undergirded by the vast number of buildings and structures. All of them must be designed as an assemblage and not in isolation. It is especially important that building codes and standards should be made based on this principle. It is strongly recommended that we re-examine the design load levels specified in some current codes, standards, and recommendations such as [SCEAJ-TRSSW \(1999\)](#), [BSLJ Article 85 \(2000\)](#), [AIJ-DRBLL \(2013\)](#), and so on.

Although the LCC concept has been adopted for design load estimation, the optimal design load level should be decided considering the overall LCC of the city or nation, rather than optimization of the LCC of an individual building. In that case, the costs imposed by securing social or national security should be addressed.

CONCLUDING REMARKS

The relation between the design load level and the length of individual use of a building or its parts was discussed. Most codes or standards tie the design load level to the lifetime of the individual building or building parts. However, it was clearly demonstrated that there is no rational reason for adopting this principle.

The aim of this paper was to merely clarify the problem of the relation between the design load level and the length of lifetime of buildings which has not necessarily been correctly understood.

More scientific discussion is needed to properly define so-called temporary buildings. There might be more than two different types of temporary buildings. If we wish to decide the design load level of a building based on the length of its individual use, we should find a rational reason for it. Acceptable impact to society and acceptable probability of infrastructure failure should be directly discussed when determining design load levels. The acceptable criteria can be also depend upon the nation's economic situation. Anyway, many relevant problems remain to be solved.

ACKNOWLEDGMENTS

This study is supported in part by the 111 Project of China (B13002), the National Natural Science Foundation of China (51308039, 91215302), and 1000 Foreign Experts Program. These supports are gratefully acknowledged.

References

- AIJ-DRBLL (Architectural Institute of Japan–Design recommendations for buildings with limited lifetime). 2013. *Design recommendations for buildings with limited lifetime*. Tokyo: Architectural Institute of Japan.
- ASCE. 2010. *Minimum design loads for buildings and other structures*. ASCE/SEI 7-10. Reston, VA: ASCE.
- Australian/New Zealand Standard. 2002. *Structural design actions. Part 2: Wind actions*. AS/NZS 1170.2. Australian/New Zealand Standard.
- Brewick, P., L. Divel, K. Butler, R. Bashor, and A. Kareem. 2009. “Consequences of urban aerodynamics and debris impact in extreme wind events.” In *Proc., 11th Americas Conf. on Wind Engineering*. San Juan, Puerto Rico.
- BSI (British Standards Institution). 2011. *Falsework: Performance requirements and general design*. BS EN 12812:2008. London: BSI.

- BSLJ (Building Standard Law of Japan). 2000. *Building standard law*. Buildings Center of Japan.
- Davenport, A. G. 1967. "Gust loading factor." *J. Struct. Div.* **93**, 11–34.
- Hokkoku Shimbun. 2007. "Morning issue." November 13, 2007.
- National Standard of China. 2011. *Technical code for safety of steel tubular scaffold with couplers in construction*. Ministry of Housing and Rural-Urban Development of China.
- Ohdo, K. 2007. *Wind engineering handbook*, edited by JAWE, Asakura-shoten, 232.
- SCEAJ-TRSSW (Scaffolding and Construction Equipment Association of Japan—Technical Recommendation for Safety of Scaffolding to Winds). 1999. *Technical Recommendation for Safety of Scaffolding to Winds*. Scaffolding and Construction Equipment Association of Japan (Kasetsu Kogyo Kai).
- Tamura, Y. 2009. "Wind and tall buildings." In *Proc., 5th European and African Conf. on Wind Engineering (EACWE 5)*, 25–49, Florence, Italy.
- Tamura, Y., H. Niino, O. Suzuki, Y. Fujiyoshi, H. Kawai, and Y. Okuda. 2007. *Investigation of serious tornado damage in Saroma-cho*. Special Research Promotion Grant No. 18900003. Hokkaido, Japan: JSPS.

CHAPTER 6

Simulating the Role of Axial Flow in Stay Cable Vibrations via a Perforated Wake Splitter Plate

Ran Wang^{*}
Shaohong Cheng^{*}
David S-K. Ting[†]

Abstract: The inclined and/or yawed orientation of bridge stay cables results in the formation of secondary axial flow on the leeward side of cable surface, which is believed to be one of the contributing factors exciting some unique wind-induced cable vibration phenomena. To clarify the role of axial flow in triggering aerodynamic instability of stay cables, a numerical study has been conducted to indirectly examine the axial flow effect via a perforated splitter plate placed along the central line of a circular cylinder wake. By manipulating the perforation ratio of the perforated plate at four different levels, the variation of von Kármán vortex shedding strength, which reflects the axial flow intensity, can be simulated. The impact of the splitter plate perforation ratio on the flow structure around a circular cylinder, in terms of the instantaneous vortex structure, the surface pressure distribution and the aerodynamic forces are discussed in detail by exploiting the numerical data obtained from the large eddy simulation. Results show that the presence of a perforated wake splitter plate would play a similar role as the axial flow in affecting the strength of von Kármán vortex shedding. A more solid wake splitter plate is found to cause a stronger interruption on the interaction between the shear layers formed on the two sides of the cylinder and consequently lead to a more symmetric surface pressure distribution pattern and weaker von Kármán vortex shedding strength. Reductions on the fluctuating amplitude of the instantaneous lift and drag as well as the mean drag are also observed, which would ultimately affect the aerodynamic response of the studied cylinder.

*Department of Civil and Environmental Engineering, University of Windsor (corresponding author), Tel: +15192533000, Ext. 2629, Fax: +5199713686, email: {wang1hf, shaohong}@uwindsor.ca

†Department of Mechanical, Automotive and Materials Engineering, University of Windsor 401 Sunset Avenue, Windsor, Ontario, Canada, N9B 3P4, email: dting@uwindsor.ca

Keywords: *circular cylinder; perforated wake splitter plate; von Kármán vortex shedding; axial flow; cable vibrations; cable-stayed bridges; aerodynamic instability; large eddy simulation.*

1 INTRODUCTION

Cable-stayed bridges have become progressively popular since the completion of the Stomsund Bridge in Sweden in 1955, mainly due to their modest requirement on ground anchorage condition, efficient utilization of structural material, higher stiffness and economy compared to the suspension bridges. Rapid development in materials, design and construction technology constantly push the bridge span to a new limit. Currently, the record holder of the cable-stayed bridge, the Russky Bridge in Russia, has a center span length of 1,104 m and the longest cable on the bridge is 580 m. The road deck of the highest cable-stayed bridge, the Duge Bridge in China inaugurated in 2016, sits over 565 m above the Beipan River. These great advancements are, naturally, accompanied with new engineering challenges. Owing to the low lateral stiffness, low inherent damping and small mass, stay cables on cable-stayed bridges are prone to dynamic excitations. Further, the inclined and/or yawed orientation of stay cables against the oncoming wind introduces some unique wind-induced cable vibration phenomena, the mechanisms of which are yet to be fully comprehended.

Excessive vibrations of cables on cable-stayed bridges have been frequently reported in recent years. Among these incidents, rain-wind-induced vibration (RWIV) is observed most on site. This sort of vibration was first reported by [Hikami and Shiraishi \(1988\)](#) on the Meiko-Nishi Bridge in Japan. After that, numerous similar cases were reported ([Stafford and Watson 1988](#), [Pacheco 1993](#), [Persoon and Noorlander 1999](#), [Main and Jones 2000](#), [Matsumoto et al. 2003](#), [Zuo et al. 2008](#), [Zuo and Jones 2010](#)). Extensive researches have been conducted to unveil the mystery, mainly using wind tunnel tests ([Matsumoto et al. 1992](#), [1995](#); [Flamand 1995](#); [Bosdogianni and Olivari 1996](#); [Ming 2002](#); [Gu and Du 2005](#); [Alam and Zhou 2007](#); [Li et al. 2016](#); [Jing et al. 2017](#)), theoretical ([Yamaguchi 1990](#); [Gu and Lu 2001](#); [Cao et al. 2003](#); [He et al. 2010, 2012](#); [Li et al. 2013](#)) and numerical analyses ([Seidel and Dinkler 2006](#), [Robertson et al. 2010](#), [Li et al. 2010](#), [Bi et al. 2013](#), [Wang et al. 2016](#)). While many studies have been carried out to investigate the excitation mechanisms of RWIVs, researchers held different or even conflicting ideas and no consensus has been reached so far ([Jing et al. 2017b](#)). Nevertheless, the formation of upper water rivulet on the cable surface is considered to be an important factor to induce RWIV.

Dry inclined cable galloping has been proved theoretically to be a potential safety threat to bridge stay cables ([Piccardo 1993](#), [Macdonald and Larose 2008](#), [Raeesi et al. 2014](#), [He and Macdonald 2016](#)). [Saito et al. \(1994\)](#) proposed an instability criterion which suggested that the onset condition of dry inclined cable

galloping could be easily satisfied for many stay cables on existing bridges and the unstable cable motion could not be suppressed by introducing additional damping. However, this criterion is too conservative to be applied to bridge design and field experience indicated that this was not the case. Outcomes of earlier studies indicated that the necessary conditions to trigger dry inclined cable galloping would include (a) emergence of critical Reynolds number regime (Macdonald and Larose 2006; Cheng et al. 2008a, 2008b), (b) presence of axial flow (Matsumoto et al. 1992, 1995, 2003, 2005), and (c) sustained duration of the critical flow condition (Raeesi et al. 2014). Also, high span-wise correlation of aerodynamic forces on the cable upon the onset of dry galloping was found by Cheng and Tanaka (2005). It is worth noting that, up till now, no field incident of dry inclined cable galloping has been formally confirmed, despite a few wind tunnel tests (Miyata et al. 1994; Cheng et al. 2003, 2008b; Jakobsen et al. 2012; Vo et al. 2016) observed the occurrence of this type of instability. reported both divergent and limited-amplitude cable vibrations at high reduced wind speed. Zuo and Jones (2009) suspected that the dry galloping observed in the wind tunnel test by Cheng et al. (2003, 2008a) might relate to rain-wind-induced vibration in the field. However, it is challenging in acquiring accurate onsite environment data at the occurrence of violent cable vibrations, such as the particular amount of precipitation, wind speed and direction. The possible existence of the so-called rain-wind-induced vibration in the absence of rainfall, and the possible relation between the vibrations observed on wet and dry cables is still unclear.

A circular cylinder in cross-flow has been extensively studied both experimentally and numerically. However, in the case of a bridge stay cable, though it is typically modeled as a circular cylinder in existing studies, the flow structure around it is much more complex due to its inclined and yawed orientation. This renders the formation of the secondary axial flow on the leeward side of the cable surface which disturbs the interaction between the shear layers separated from the two sides of the cylinder and suppresses the shedding of the von Kármán vortices. Shirakashi et al. (1986) investigated the aerodynamic behaviour of a yawed circular cylinder in uniform flow in the wind tunnel and concluded that the reduction of the vortex shedding frequency by yawing was attributed to the presence of the secondary flow behind the cylinder. Matsumoto et al. (1990) reported that depending on the boundary condition, the intensity of the axial flow formed on the leeward side of a circular cylinder yawed at 45° varied between 40% to 60% of the oncoming flow velocity.

From the existing studies, it is understood that a splitter plate could be used as a passive device to control the vortex formation in the wake of a cylinder (Roshko and Anato 1954, Apelt et al. 1973, Apelt and West 1975, Ozono 1999, Choi 2007, Dehkordi and Jafari 2010, Ali et al. 2012). Therefore, it is expected that a wake splitter plate would play a similar role as that of the axial flow in interrupting the communications between separated flow from the two sides of a cylinder. Due to the challenge of directly manipulating and measuring the intensity of axial flow, Matsumoto et al. (2010) installed a perforated splitter plate in the wake center of a

non-yawed circular cylinder in a wind tunnel study. By varying the perforation ratio of the splitter plate, the intensity of von Kármán vortex shedding from the cylinder body can be controlled in a stationary state. Their results implied that the generation mechanism of dry inclined cable galloping might be associated with the suppression of the von Kármán vortex shedding.

Many researchers investigated the impact of placing a solid plate in the near wake of a cylinder on its surrounding flow structure. (Roshkot 1954) discovered that the base pressure of a circular cylinder would be substantially increased if a long solid splitter plate was present in the wake. Apelt et al. (1973) and Apelt and West (1975) conducted experiments by placing solid splitter plate of different lengths downstream of a circular cylinder. They concluded that the near wake structure of the cylinder might be studied in the absence of von Kármán vortex formation. A few other studies also discussed how the communication interruption between the separated shear layers in the wake region of a cylindrical body in the presence of a solid splitter plate would affect the aerodynamic forces acting on it (Ozono 1999, Choi 2007, Dehkordi and Jafari 2010, Ali et al. 2012). On the other hand, experimental studies on the effect of a perforated/permeable wake splitter plate on the flow structure around a circular cylinder were rarely reported in literature. Cardell (1993) indicated that if a permeable splitter plate was placed in the wake of a circular cylinder, both drag and von Kármán vortex shedding frequency would drop. In addition, provided the plate solidity was high enough, the base pressure of the cylinder was found to be independent of the Reynolds number and the plate solidity. As far as the numerical simulation is concerned, the solid wake splitter plate effect was investigated by a number of researchers in the relatively low Reynolds number regime (Kwon and Choi 1996; Hwang et al. 2003, 2007; Vu et al. 2015); whereas to the best knowledge of the authors, reported numerical study on the flow structure around a circular cylinder with a perforated wake splitter plate is scarce.

Existing studies showed that the extent of communication between the separated shear layers was critical to the characteristics of the cylinder wake. Abernathy and Kronauer (1962) proposed that, in the subcritical Reynolds number region, the von Kármán vortex street could form without a wake producing body, but rather by just bringing two shear layers of opposite sign within a communicable proximity of one another. Cardell (1993) confirmed the ability of permeable splitter plate in modifying the communication across the center plane of a circular cylinder wake. The effect of axial flow, on the other hand, on interrupting the communication between the two separated shear layers in the near wake region behind a circular cylinder was reported by Matsumoto et al. (2010). It was also suspected that the formation of axial vortex on the leeward side of the cylinder and the possible interaction between the axial vortex shedding and the conventional von Kármán vortex shedding in the wake could contribute to the aerodynamic instability of the cylinder. Their results indicated that galloping could be excited by introducing artificial axial flow in the near wake of a non-yawed circular cylinder. However, quite counter intuitively, it was also found that the velocity of axial flow, which might be related to the degree of interference on shear layer communication, had an

inverse relation with the stability of the circular cylinder. Though the mechanism of axial flow on affecting the aerodynamic stability of a circular cylinder has not been fully unveiled, it is clear that part of its role is similar as that of the splitter plate, i.e. to interrupt the shear layer communication. Therefore, it is feasible to apprehend our understanding of the effect of axial flow, as well as its intensity, on the aerodynamic stability of a circular cylinder via placing a splitter plate with variable perforation ratio in its wake.

To unveil the possible relation between the von Kármán vortex shedding mitigation and the onset of dry inclined cable galloping, it is imperative to examine how change in the communication of separated shear layers would influence the flow structure around a circular cylinder and/or vice versa. In the current paper, a CFD simulation will be conducted to study flow past a non-yawed circular cylinder at a Reynolds number of 3900, with the presence of a perforated wake splitter plate. This particular Reynolds number is selected mainly due to the availability of the existing experimental and numerical data, which can be used to validate the developed numerical model. By manipulating the solidity of the perforated wake splitter plate, the variation of von Kármán vortex shedding strength can be simulated. This would allow examining the impact of axial flow intensity on the aerodynamic behaviour of a circular cylinder indirectly and shed light on the role of axial flow in the excitation mechanism of dry inclined cable galloping.

2 NUMERICAL SIMULATION

2.1 Numerical approach

All simulations presented in this paper utilize the open source CFD Toolbox: OpenFOAM V4.1 (Open Source Field Operation and Manipulation). The incompressible solver pisoFOAM uses a finite volume cell-centered discretization of the domain and handles unstructured mesh data format based on the so-called face-addressing storage using Pressure-Implicit with Splitting of Operators algorithm (PISO). Linear Green-Gauss is used for computing the gradient. The treatments of convective terms for velocity, kinematic turbulent energy, kinematic turbulent viscosity are Gauss LUST (blended 75% linear and 25% linearUpwind) and Gauss limitedLinear for the last two terms. A second-order accuracy scheme backward method is used for temporal discretization. A time step of 10^{-4} second is employed to guarantee the maximum Courant number to be smaller than 0.2 during the simulation. A geometric agglomerated algebraic multigrid solver (GAMG) with the Gauss-Seidel smooth method iteratively solves the linear algebraic system with a local accuracy of 10^{-6} for the pressure and 10^{-7} for the remaining variables at each time step.

The current study mainly focuses on the unsteady-state flow and hence the detailed instantaneous flow characteristics are critical to the investigation. In the Reynolds-averaged Navier-Stokes (RANS) approach, one only solves the averaged fluid field while the effect of all scales of instantaneous turbulent motion

is modelled by a turbulent model. The direct numerical simulation (DNS) directly solves the full Navier-Stokes equations using extremely fine spatial and temporal discretization to capture eddies at all scales in the given problems at a huge computational cost. The large eddy simulation (LES) is based on the filtered Navier-Stokes equations (Smagorinsky 1963). Instead of adopting the conventional time averaging RANS approach with additional modelled transport equations, LES simulates eddies which are larger than the smallest grid size directly, while it treats the eddies under this scale by using the subgrid-scale (SGS) model with relatively lower computational resources than DNS. A novel approach of the hybrid LES-RANS method, i.e. the detached eddy simulation (DES), solves the attached portion of the boundary layers with the traditional RANS and uses LES in the separated flow regions. However, when using DES, the treatment of the boundary layer in the vicinity of the cylinder is not sufficient to unveil the properties of the highly unsteady flow. Therefore, the LES turbulent model is adopted in the current study to investigate the effect of a perforated wake splitter plate on the flow characteristics around a circular cylinder.

The governing equations, the Navier-Stokes equations, are based on the conservation laws for mass, momentum and energy. Since only the large eddies are directly computed in LES, so a low-pass spatial filter is applied to the Navier-Stokes equations. The filtered equations for a Newtonian incompressible flow can be written in a conservative form as

$$\partial_i \bar{u}_i = 0 \quad (1)$$

$$\partial_t(\rho \bar{u}_i) + \partial_j(\rho \bar{u}_i \bar{u}_j) = -\partial_i \bar{p} + 2\partial_j(\mu \bar{S}_{ij}) - \partial_j(\tau_{ij}) \quad (2)$$

$$\bar{S}_{ij} = \frac{1}{2}(\partial_i \bar{u}_j + \partial_j \bar{u}_i) \quad (3)$$

$$\tau_{ij} = \frac{1}{2}(\bar{u}_i \bar{u}_j - \bar{u}_i \bar{u}_j) \quad (4)$$

where ρ is the density of the air, \bar{u}_i is the filtered velocity, \bar{p} is the filtered pressure, μ is the dynamics viscosity, \bar{S}_{ij} is the filtered strain rate tensor, and τ_{ij} is the unknown SGS stress tensor, which represents the small scale motions. To solve the above equations, the SGS eddy viscosity needs to be determined. The most basic model is the one originally proposed by Smagorinsky (1963):

$$\mu_t = \rho(C_s \bar{\Delta})^2 S \quad (5)$$

$$S = (2\bar{S}_{ij}\bar{S}_{ij})^{\frac{1}{2}} \quad (6)$$

$$\bar{\Delta} = (\Delta x \Delta y \Delta z)^{\frac{1}{3}} \quad (7)$$

where C_s is the Smagorinsky constant depending on the type of the flow.

2.2 Computational domain

The coordinate system, the definition of the angle θ , which represents the angular position of an arbitrary point on the cylinder surface with respect to the stagnation point, and the span-wise length are shown in the Figure 1a. Figure 1b illustrates a schematic view of the computational domain of a classic case of flow past a circular cylinder. The diameter of the studied circular cylinder is $D = 0.0889$ m. The center of the cylinder coincides with the origin of the computational domain. From the origin, the computational domain extends $10D$ toward the inlet and $20D$ toward the outlet, and from $-10D$ to $10D$ in the cross-flow direction. The span-wise extension L_z is chosen to be $\pi D/2$, which is found to be more efficient while maintaining an acceptable accuracy based on the mesh independence test.

ANSYS/ICEM is used to generate a block structured rectangular computational domain, as shown in Figure 1b. The non-dimensional viscous length scale is defined as

$$y^+ = (u_* \cdot y) / \nu \quad (8)$$

where u_* is the friction velocity at the near wall, y is the distance to the wall and ν is the local kinematic viscosity of the fluid. The height of the first cell on the cylinder is $9.57 \times 10^{-4}D$, which guarantees y^+ is smaller than 1. The no-slip condition is imposed on the surface of the cylinder and the plate. The span-wise resolution Δz is $0.05D$ with 32 nodes along the z -axis. 392 nodes are employed on the cylinder surface along the circumference for the no wake splitter plate case. The total number of control volumes for the solid plate case is 5.57×10^6 . A non-dimensional time step Δt of 7.4×10^{-4} is used, where $\Delta t = Ut/D$. A Dirichlet boundary condition for velocity ($u = 0.658$ m/s; $v = 0$; $w = 0$) and a Neumann boundary condition for zero gradient pressure are prescribed at the inlet. A Dirichlet boundary condition for zero pressure is applied at the outlet. A cyclic boundary condition is employed on the span-wise walls.

When introducing a piece of splitter plate along the central line of a circular cylinder wake, not only the perforation ratio, but also the size and the position

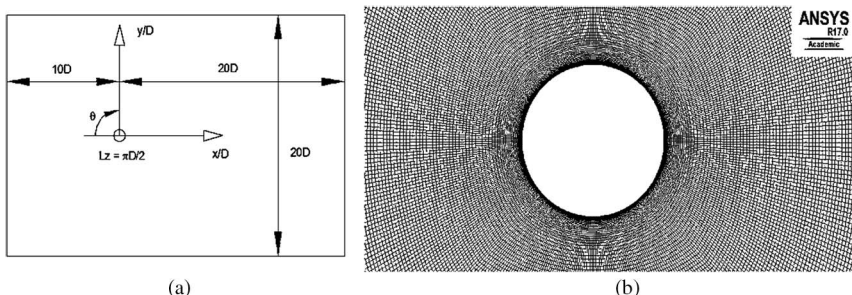


Figure 1. Computational domain and detailed mesh for flow past a circular cylinder: (a) computational domain, and (b) detailed grid in the near region of the circular cylinder

of the plate could have a sizable impact on the cylinder wake structure. (Roshko 1954) found that a splitter plate of length $5D$ (D is the cylinder diameter) inhibited the periodic formation of the von Kármán vortices, whereas it was not the case if the plate length was shortened to $1.14D$. Besides, Cardell (1993) investigated the influence of the gap size between the splitter plate and the cylinder on the flow properties around the cylinder. Results showed that if the gap was less than $0.13D$, the presence of the splitter plate would not have an appreciable effect on the cylinder mean base pressure and the von Kármán vortex shedding frequency. Based on these, to explore how the variation of the von Kármán vortex shedding strength would affect the flow structure around a circular cylinder, in the current numerical study, a wake splitter plate of length D and thickness $D/20$ was placed along the central line of the cylinder wake with a gap of $0.11D$ between the cylinder and the plate.

Figure 2 shows a 3D view of the detailed mesh near the cylinder and the solid wake splitter plate. For the perforated plate, the perforation ratio is defined as the ratio between the opening length and the total length of the splitter plate along the flow direction. A total of four perforation ratio levels, i.e. 0, $1/3$, $2/3$, and 1, are simulated in the current study, of which a perforation ratio of 0 represents the solid splitter plate case, whereas 1 represents the no splitter plate case. The mesh details of the perforation ratio cases of $1/3$ and $2/3$ are given in Figures 3a and 3b, respectively.

Regarding the mesh generation scheme in the perforated splitter plate cases, the O-shape meshes were first introduced in the near region of the cylinder. Then, based on the studied perforation ratio, the block near the splitter plate region was further divided into 7 and 16 sub-blocks, with the quadrilateral meshes generated in each sub-block. Finally, the three-dimensional meshes were generated by extending the two-dimensional plane along the span-wise direction.

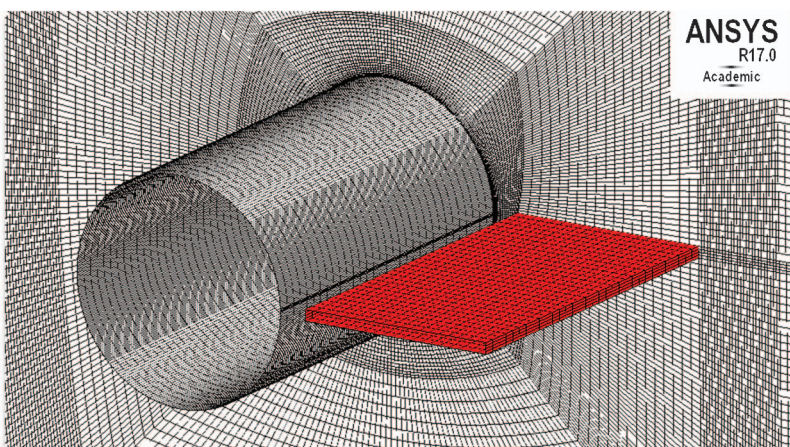


Figure 2. Detailed mesh near the cylinder and the solid splitter plate (perforation ratio of 0)

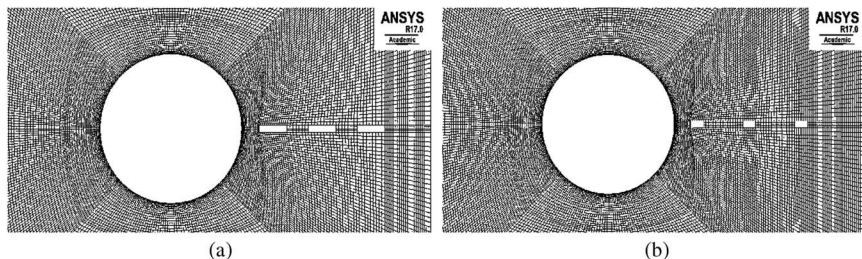


Figure 3. Mesh details of the perforated wake splitter plate cases: (a) perforation ratio of 1/3, and (b) perforation ratio of 2/3

2.3 Model validation

The validity of the developed numerical model was examined using the no splitter plate case at a Reynolds number of 3900. Two different meshes, Mesh 1 and Mesh 2 were used for the model validation test. They had the same 2-dimensional grid, but the number of nodes in the span-wise direction was taken as 16 and 32, respectively. The span-wise resolution (i.e., the distance between the two adjacent span-wise nodes) was kept the same at $\pi D/64$. The drag coefficient and the Strouhal number of the circular cylinder obtained from these two meshes are listed in Table 1, along with the data reported in literature (Lourenco and Shih 1993, Breuer 1998, Kravchenko and Moin 2000, Tremblay

Table 1. Model Validation Results

Model	Method	Number of vortex shedding periods	Number of control volume (million)	C_d	S_t
Mesh 1	LES	10	2.3	1.32	0.22
Mesh 2	LES	10	5.5	1.20	0.21
Lourenco and Shih (1993)	PIV	–	–	0.99	0.22
Breuer (1998)	LES	22	0.87 to 1.74	[0.97–1.49]	[0.21–0.22]
Kravchenko and Moin (2000)	LES	7	0.5 to 2.4	[1.04–1.36]	[0.19–0.21]
Tremblay et al. (2002)	LES	–	–	[1.14–1.31]	[0.21–0.22]
Prsic et al. (2012)	LES	60	5 to 11	[1.10–1.24]	0.21

et al. 2002, Prsic et al. 2012). It can be seen from Table 1 that the Strouhal number obtained from the current numerical models, both Mesh 1 and Mesh 2, agree very well with those in the literature. In terms of the drag coefficient, though the results yielded from both meshes fall within the range documented in the existing studies, the relatively higher drag coefficient obtained from Mesh 1 suggests that the span-wise length used in Mesh 1 could be insufficient. By doubling the span-wise length in Mesh 2, the drag coefficient drops from 1.32 to 1.20 by 10% and has a better agreement with the literature data. Therefore, Mesh 2 is used in the rest of the study.

3 RESULTS AND DISCUSSIONS

3.1 Instantaneous vortex structure

Flow around a non-yawed circular cylinder with the presence of a perforated wake splitter plate is investigated numerically at a Reynolds number of 3900. The effect of axial flow on the flow structure around the cylinder is examined indirectly by placing a perforated splitter plate in the near wake of the cylinder. Since the strength of the von Kármán vortex shedding is dictated by the perforation ratio of the wake splitter plate, four different perforation ratios [i.e., 0 (solid splitter plate), 1/3, 2/3, and 1 (no splitter plate)] are simulated in the current study to examine the impact of the axial flow intensity on the aerodynamic behaviour of a circular cylinder.

The Galilean-invariant vortex criterion is commonly used to investigate the vortex structure in LES. In this criterion, the velocity gradient $\nabla\mathbf{v}$ is decomposed into

$$\nabla\mathbf{v} = \mathbf{S} + \boldsymbol{\Omega} \quad (9)$$

where $\mathbf{S} = \frac{1}{2}[\nabla\mathbf{v} + (\nabla\mathbf{v})^T]$ is the rate-of-strain tensor, and $\boldsymbol{\Omega} = \frac{1}{2}[\nabla\mathbf{v} - (\nabla\mathbf{v})^T]$ is the vorticity tensor. The first three-dimensional vortex criterion using Eq. (9) is the *Q-criterion* by Hunt et al. (1988). The definition of *Q* is given as

$$Q = \frac{1}{2} [|\boldsymbol{\Omega}|^2 - |\mathbf{S}|^2] \quad (10)$$

The *Q* value of the isosurfaces is 300 (s^{-2}), and its contour range of the vorticity varies from -30 to 30 (s^{-1}). Figure 4 shows the span-wise component, ω_z , of the instantaneous vorticity for the no splitter plate (perforation ratio = 1) and the solid splitter plate (perforation ratio = 0) cases. The span-wise vorticity component ω_z describes the formation structure of the two shear layers on both sides of the circular cylinder. The numerical simulation results in Figure 4 demonstrate that the presence of a solid splitter plate would change the cylinder near wake structure by

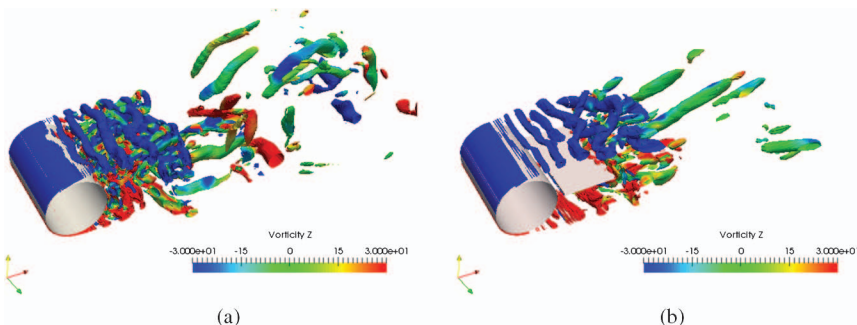


Figure 4. Instantaneous vortex structures ($Q = 300 \text{ [s}^{-2}\text{]}$): (a) perforation ratio = 1 (no splitter plate), and (b) perforation ratio = 0 (solid splitter plate)

interrupting the communications between the two separated shear layers and extend their development range in the wake. Thus, a wake splitter plate could have a similar role as the axial flow on the leeward side of the cylinder.

The variations of the instantaneous vortex contour in the cylinder near wake at $z = D/4$ within one cycle of vortex shedding are illustrated in Figure 5 for the four perforation ratio cases. It can be observed from the figure that as the perforation ratio of the splitter plate decreases, the recirculation length gradually becomes longer. As a consequence, the near wake becomes more stable since the interaction between the two separated shear layers is more constrained. This clearly indicates that the intensity of von Kármán vortex shedding is controlled by the perforation ratio of the wake splitter plate.

3.2 Surface pressure distribution

Figure 6 shows snap shots of the instantaneous surface pressure distribution along the circumference of the studied circular cylinder at its middle plane, in terms of the non-dimensional surface pressure coefficient C_p , for the four different perforation ratio cases at time instants of 6.0, 6.2, 6.4 and 6.6 second. They cover approximately a full period of von Kármán vortex shedding. It is worth mentioning that time instant 6.0 second is slightly lag behind that corresponding to zero instantaneous lift. The black solid line represents the cylinder surface. The non-dimensional surface pressure coefficient C_p is defined as

$$C_p = \frac{p - p_0}{\rho U_{\infty}^2 / 2} \quad (11)$$

where p is the instantaneous surface pressure of the cylinder, p_0 is the reference pressure at the infinite upstream, ρ is the density of the fluid, and U_∞ is the freestream velocity of the flow. As can be seen from Figure 6a, when the splitter plate is solid (i.e., the perforation ratio is 0), the instantaneous surface pressure distribution profiles at the four studied time instants within one vortex shedding

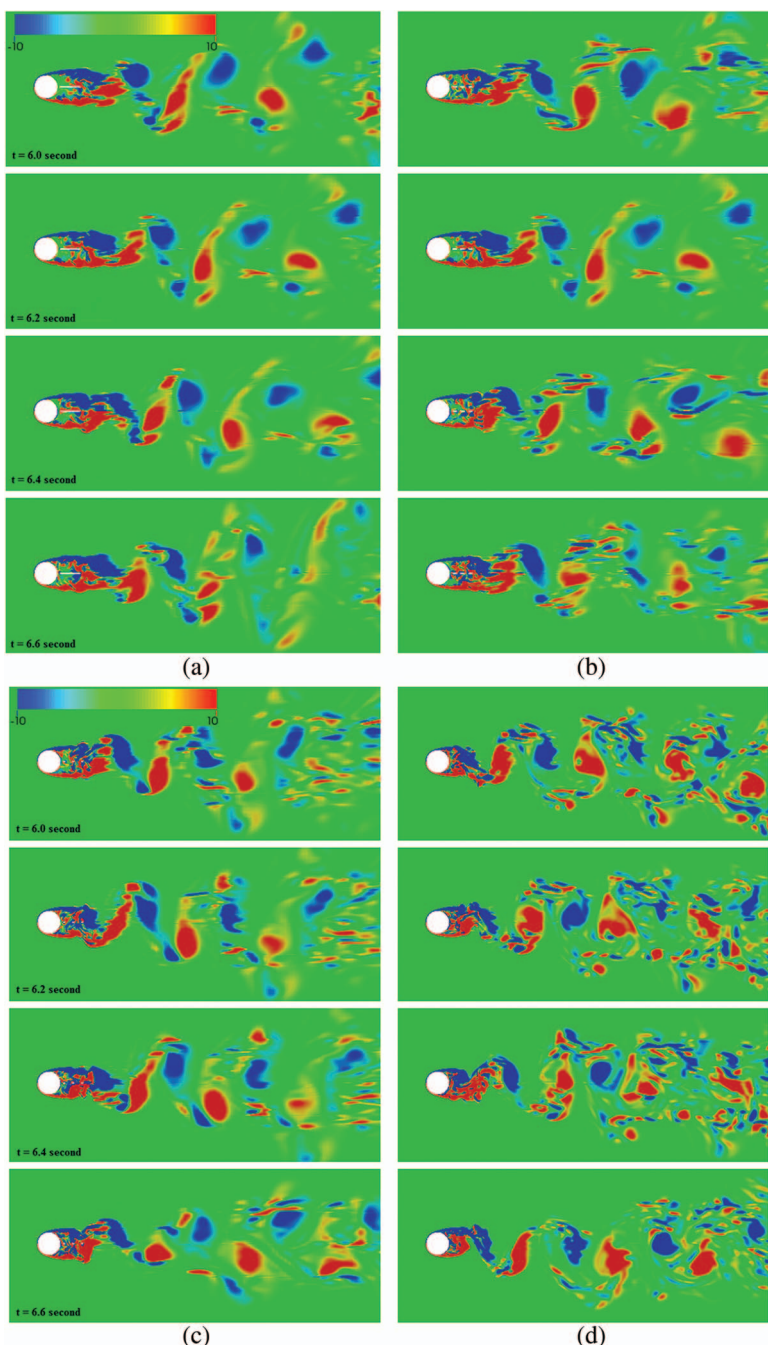


Figure 5. Instantaneous z-axis vortex contour ($Q = 300 \text{ [s}^{-2}\text{]}$) at mid-plane ($z = D/4$):
 (a) perforation ratio = 0 (solid splitter plate), (b) perforation ratio = 1/3,
 (c) perforation ratio = 2/3, and (d) perforation ratio = 1 (no splitter plate)

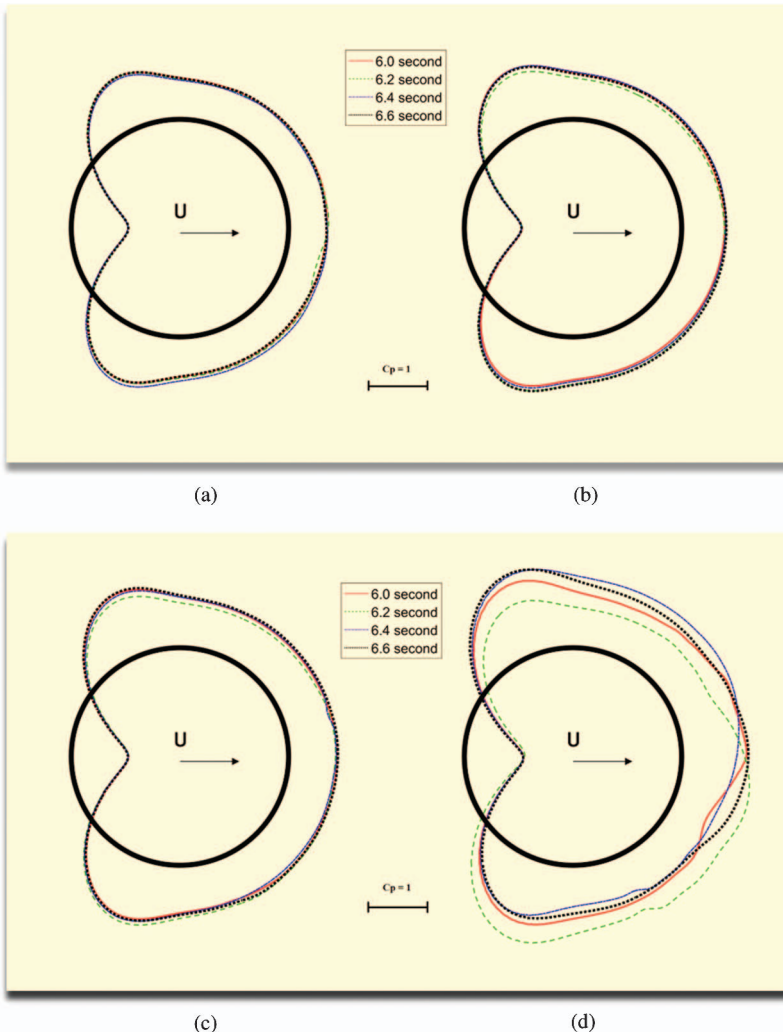


Figure 6. Instantaneous surface pressure distribution profile at cylinder mid-plane ($z = D/4$): (a) perforation ratio = 0, (b) perforation ratio = 1/3, (c) perforation ratio = 2/3, and (d) perforation ratio = 1

period has no sizable difference and remain symmetric. With the decrease of the plate perforation ratio, the difference between them within approximately one vortex shedding period, though still small, increases gradually, as shown in Figures 6b and 6c. When the splitter plate is removed from the wake (perforation ratio of 1), a clear variation of the instantaneous surface pressure distribution profile within approximately one vortex shedding period can be observed from Figure 6d. In particular, the surface pressure distribution pattern becomes asymmetric at time instant 6.2 second, which is approximately at 1/4 of a vortex

shedding period. This suggests that by placing a piece of more solid wake splitter plate, it would “stabilize” the variation of the instantaneous surface pressure distribution and alter the associated pattern to be more symmetric about the flow direction. Therefore, the strength of the von Kármán vortex shedding would be weakened. In addition, the base pressure of the cylinder is found to gradually increase with a more solid wake splitter plate.

Figure 7 shows the influence of the wake splitter plate perforation ratio on the mean surface pressure coefficient distribution pattern of the circular cylinder. Similarly, it can be clearly seen from the figure that when no wake splitter plate is present (perforation ratio of 1), the distribution of the cylinder surface pressure is symmetric about the flow direction. With the gradual decrease of the perforation ratio (i.e., the wake splitter plate being more and more solid), the absolute value of the pressure coefficients gradually decrease, implying the strength of the von Kármán vortex shedding is weakened. In addition, it can be seen from Figure 7 that as the perforation ratio increases, the absolute value of the mean surface pressure coefficient would increase accordingly, except for the perforation ratio case 2/3, of which the surface pressure at the bottom side of the cylinder is found to be slightly higher than the other cases. This could be associated with the time duration over which the mean surface pressure coefficient is computed. In the current study, it is calculated based on 10 von Kármán vortex shedding periods. Further, such a change in the plate perforation ratio would result in a decrease in the base pressure.

In general, the results in Figures 6 and 7 indicate that the perforation ratio of the wake splitter plate would dictate the symmetry of the surface pressure distribution pattern around a circular cylinder and the magnitude of the base pressure, and thus affect the flow structure around the cylinder. The formation of axial flow on the leeward side of an inclined and/or yawed stay cable is suspected to play a similar role as the wake splitter plate in mitigating the strength of von Kármán vortex shedding, which would consequently affect the cable surface pressure distribution pattern and ultimately its wind-induced forces and responses.

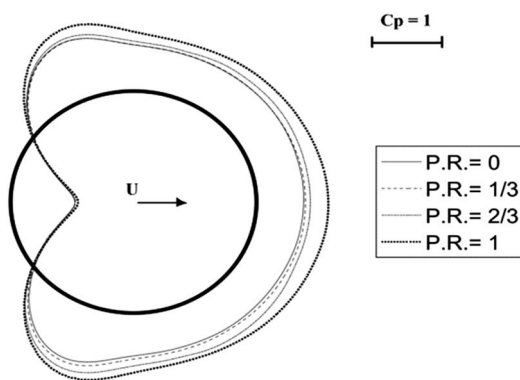


Figure 7. Ten periods mean surface pressure distribution profile of the cylinder

3.3 Aerodynamic forces

When flow past a solid body, it would exert pressure forces normal to the body surface and shear forces tangent to it. The resultant force of these two is usually decomposed into an along-flow component, i.e. the drag force, and a cross-flow component, i.e. the lift force. For the Reynolds number 3900 scenario studied in the current paper, the viscous shear force can be neglected. Thus, the lift force and the drag force acting on the circular cylinder can be evaluated by integrating the normal pressure over the cylinder circumferential surface. The sectional lift and drag forces can be computed from

$$F_l = \int_0^{2\pi} p \cdot \vec{n}_y \cdot r \cdot d\theta = \sum_0^n p \cdot \vec{n}_y \cdot r \cdot \Delta\theta \quad (12)$$

$$F_d = \int_0^{2\pi} p \cdot \vec{n}_x \cdot r \cdot d\theta = \sum_0^n p \cdot \vec{n}_x \cdot r \cdot \Delta\theta \quad (13)$$

where F_l and F_d are respectively the sectional lift and drag forces, p is the surface pressure at a specific point on the cylinder surface, \vec{n}_x and \vec{n}_y are respectively the wall normal vector in the x -and y -direction at that surface point, r is the radius of the cylinder, n is the total number of nodes along the cylinder circumference, which is 392 in the current study, and $\Delta\theta = 2\pi/n$. The non-dimensional form of the time t , the sectional lift force F_l , the sectional drag force F_d , and the von Kármán vortex shedding frequency f are designated as T^* , C_l , C_d , and S_t respectively. They are defined as follows:

$$T^* = T \cdot U_\infty / D \quad (14)$$

$$C_l = \frac{F_l}{\rho U_\infty^2 / 2} = \frac{1}{2} \sum_0^n C_p \cdot \vec{n}_y \cdot \Delta\theta \quad (15)$$

$$C_d = \frac{F_d}{\rho U_\infty^2 / 2} = \frac{1}{2} \sum_0^n C_p \cdot \vec{n}_x \cdot \Delta\theta \quad (16)$$

$$S_t = f \cdot D / U_\infty \quad (17)$$

where C_p is the non-dimensional surface pressure coefficient defined by Eq. (11), ρ is the density of the fluid, U_∞ is the freestream velocity of the flow, t is the dimensional time and D is the cylinder diameter.

Figures 8 and 9 depict respectively the time history of the lift and drag coefficients over a time duration of approximately 10 vortex shedding periods for the four studied wake splitter plate perforation ratio cases. The mean drag coefficient, the root-mean-square and the maximum instantaneous lift coefficient,

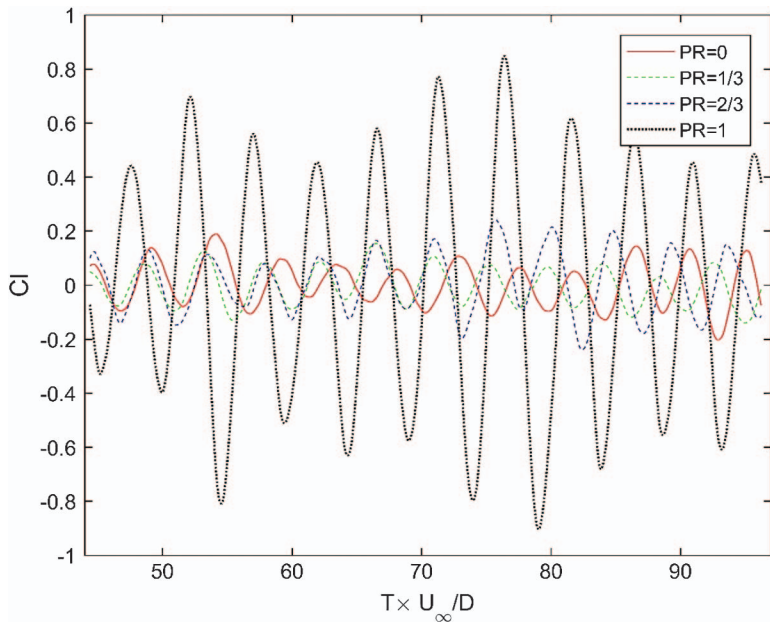


Figure 8. Lift coefficient time histories for the four wake splitter plate perforation ratio cases

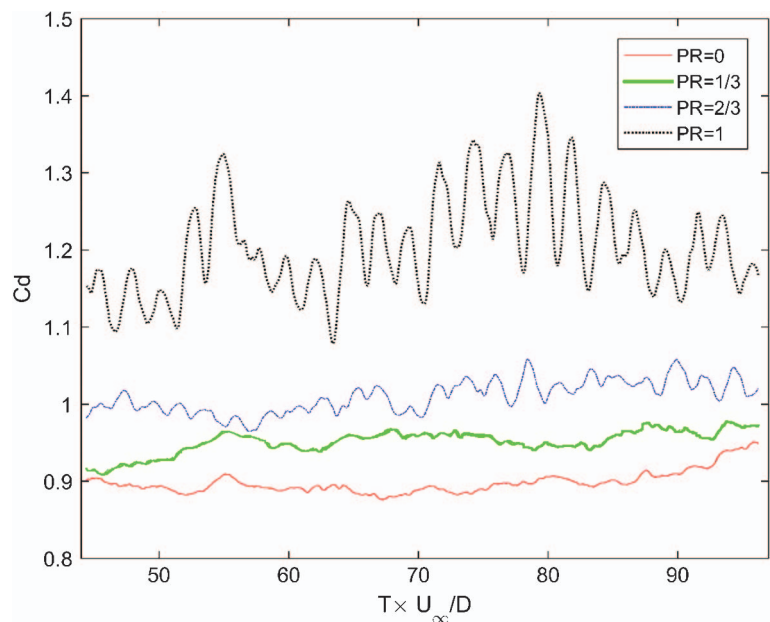


Figure 9. Drag coefficient time histories for the four wake splitter plate perforation ratio cases

which are computed based on the simulated time history of 10 vortex shedding periods, are summarized in Table 2. In terms of the statistical convergence, the averaging time used for computing these statistics differ significantly from one to the other in the existing studies (Parnaudeau et al. 2008). For instance, (Kravchenko and Moin 2000) considered only 7 vortex shedding periods, whereas Franke (2002) suggested to use 40 vortex shedding periods to obtain accurate mean flow in the neighborhood of a cylinder. In the case of Dong et al. (2006), 40-50 vortex shedding cycles were simulated. However, Parnaudeau et al. (2008) observed that the convergence level of a given set of data is very delicate to evaluate. They could compute a set of first and second order statistics in excellent agreement with their experimental data based on a simulated time history of 12 vortex shedding periods instead of 52 periods. In the current study, it is found that the mean drag coefficient of 1.2054 computed based on a time history of 10 vortex shedding periods does not differentiate too much from that based on a time history of 30 vortex shedding periods, which is 1.2436. Therefore, the current results will be based on a simulated time history of 10 vortex shedding periods.

The lift coefficient time histories depicted in Figure 8 show that the fluctuation amplitude of the instantaneous lift is significantly affected by the presence of a perforated wake splitter plate. As given in Table 2, by decreasing the plate perforation ratio from 1 (no plate) to 0 (solid plate), the maximum instantaneous lift coefficient would reduce from 0.84 to 0.19 by 4.4 times, whereas the root-mean-square of the lift coefficient would drop more than 5 times from 0.44 to 0.08. This set of results indicates that a more solid wake splitter plate would discourage the shedding of the von Kármán vortex in the wake.

The mean drag results in Table 2 and the drag coefficient time histories in Figure 9 indicate that the presence of a wake splitter plate would decrease the drag on a circular cylinder. This reduction effect becomes more considerable should the perforation ratio of the plate gradually decrease, i.e. the plate being more and more solid. The same phenomenon was reported in the literature by Apelt et al. (1973) who used a solid wake splitter plate, and Cardell (1993) who used a permeable wake splitter plate having a solidity of 0.65. The latter is close to the current case of perforation ratio 1/3. Cardell (1993) conducted an experimental study at Reynolds number 4800 and found that compared to the no-plate case, the installation of a permeable wake splitter plate of solidity 0.65 caused a reduction in the cylinder

Table 2. Summary of the Aerodynamic Force Coefficients

Force coefficient	Perforation ratio			
	0	1/3	2/3	1
$C_{d,mean}$	0.90	0.95	1.01	1.20
$C_{l,rms}$	0.08	0.07	0.10	0.44
$C_{l,max}$	0.19	0.15	0.24	0.84

mean drag coefficient from 1.00 to 0.76 by 24%. Whereas in the current simulation, a mean drag coefficient of 1.20 and 0.95 was obtained respectively for the no-plate and the perforation ratio 1/3 cases at Reynolds number 3900, which leads to a drag reduction of 21%. Further, the pattern of the four drag coefficients time history curves in Figure 9 suggests that the fluctuation of the instantaneous drag is mitigated by the existence of a wake splitter plate, and the suppression effect is enhanced with the decrease of perforation ratio. This implies that the installation of a more solid wake splitter plate would result in a stronger interruption in the communications between two separated shear layers.

4 CONCLUSIONS

Vulnerability of bridge stay cables to dynamic excitations like wind is one of the contemporary challenges in the design of modern cable-stayed bridges. Though dry inclined cable galloping has only been observed in a few wind tunnel tests so far, its possible occurrence on site should not be disregarded due to its significant consequence. Research effort in the past two decades identified a number of factors that could possibly contribute to the generation mechanism of this type of aerodynamic instability, and the presence of axial flow on the leeward side of the cable surface, which is resulted from the inclined and/or yawed orientation of a stay cable against the oncoming wind, is one of them. It was speculated by some researcher that the onset of dry inclined cable galloping could be associated with the mitigation of von Kármán vortex shedding in the presence of axial flow, the intensity of which would directly affect the strength of von Kármán vortex shedding. To better understand the role of axial flow in exciting dry inclined cable galloping, how the change in axial flow intensity, or in other words, the strength of von Kármán vortex shedding in the wake, would influence the flow structure around a stay cable needs to be fully explored.

A numerical simulation has been conducted in the current paper to study flow past a non-yawed circular cylinder at a Reynolds number of 3900, with the presence of a perforated wake splitter plate. The strength of von Kármán vortex shedding is simulated by manipulating the perforation ratio of the perforated wake splitter plate. A total of four different perforation ratios of 0, 1/3, 2/3, and 1 have been considered in the current study. Results show that the change in the von Kármán vortex shedding strength could have a sizable impact on the flow structure around a circular cylinder and the aerodynamic forces acting on it. With the gradual decrease of the plate perforation ratio (i.e., the presence of a more solid wake splitter plate), a stronger interruption on the interaction between the shear layers formed on the two sides of the cylinder is observed, which subsequently alters the surface pressure distribution pattern to be more symmetric about the oncoming flow and reduces the strength of von Kármán vortex shedding in the wake. Such a change in the surrounding flow structure results in a decrease in the fluctuating amplitude of the instantaneous lift and drag acting on

the cylinder and also the mean drag, which would ultimately affect the flow-induced responses of the cylinder. On site, if the combination of the oncoming wind speed and cable orientation intensifies the axial flow strength to a certain level, it could possibly mitigate von Kármán vortex shedding and therefore influence the wind-induced forces acting on the stay cable and thus its aerodynamic responses. In the next phase of the study, the numerical simulation will be extended to higher Reynolds number close to and within the critical regime to further explore how weakening in the von Kármán vortex shedding would trigger the onset of galloping instability on a stay cable.

ACKNOWLEDGMENTS

The authors are grateful to Natural Sciences and Engineering Research Council of Canada (NSERC) for supporting this project. This work was made possible by supercomputer mp2 from Université de Sherbrooke, managed by Calcul Québec and Compute Canada, the operation of this supercomputer is funded by the Canada Foundation for Innovation (CFI), the ministère de l'Économie, de la science et de l'innovation du Québec (MESI) and the Fonds de recherche du Québec - Nature et technologies (FRQ-NT). The computational support by the visualization systems vdi-ferdora20 managed by Shared Hierarchical Academic Research Computing Network (SHARCNET: www.sharcnet.ca) is greatly acknowledged.

References

- Abernathy, F. H., and R. E. Kronauer. 1962. "The formation of vortex streets." *J. Fluid Mech.* **13** (1): 1.
- Alam, M. M., and Y. Zhou. 2007. "Turbulent wake of an inclined cylinder with water running." *J. Fluid Mech.* **589**: 261–303.
- Ali, M. S. M., C. J. Doolan, and V. Wheatley. 2012. "Low Reynolds number flow over a square cylinder with a detached flat plate." *Int. J. Heat Fluid Flow* **36**: 133–141.
- Apelt, C. J., and G. S. West. 1975. "The effects of wake splitter plates on bluff-body flow in the range 10^{44} : Part 2." *J. Fluid Mech.* **71** (1): 145.
- Apelt, C. J., G. S. West, and A. A. Szewczyk. 1973. "The effects of wake splitter plates on the flow past a circular cylinder in the range 10^{44} ." *J. Fluid Mech.* **61** (1): 187.
- Bi, J., J. Wang, Q. Shao, P. Lu, J. Guan, and Q. Li. 2013. "2D numerical analysis on evolution of water film and cable vibration response subject to wind and rain." *J. Wind Eng. Ind. Aerodyn.* **121**: 49–59.
- Bosdogianni, A., and D. Olivari. 1996. "Wind- and rain-induced oscillations of cables of stayed bridges." *J. Wind Eng. Ind. Aerodyn.* **64** (2–3): 171–185.
- Breuer, M. 1998. "Large Eddy simulation of the subcritical flow past a circular cylinder: Numerical and modeling aspects." *Int. J. Numer. Methods Fluids* **28** (9): 1281–1302.
- Cao, D., R. W. Tucker, and C. Wang. 2003. "A stochastic approach to cable dynamics with moving rivulets." *J. Sound Vib.* **268** (2): 291–304.
- Cardell, G. S., 1993. "Flow past a circular cylinder with a permeable wake splitter plate." Ph.D. thesis, Lehigh Univ.

- Cheng, S., P. Irwin, and H. Tanaka. 2008b. "Experimental study on the wind-induced vibration of a dry inclined cable. II: Proposed mechanisms." *J. Wind Eng. Ind. Aerodyn.* **96** (12): 2231–2253.
- Cheng, S., G. L. Larose, M. G. Savage, and H. Tanaka. 2003. "Aerodynamic instability of inclined cables." In *Proc., 5th Int. Symp.on Cable Dynamics*, 69–76.
- Cheng, S., G. L. Larose, M. G. Savage, H. Tanaka, and P. A. Irwin. 2008a. "Experimental study on the wind-induced vibration of a dry inclined cable. I: Phenomena." *J. Wind Eng. Ind. Aerodyn.* **96** (12): 2231–2253.
- Cheng, S., and H. Tanaka. 2005. "Correlation of aerodynamic forces on an inclined circular cylinder." *Wind Struct.* **8** (2): 135–146.
- Choi, H., 2007. "Control of flow over a bluff body." In *Proc., Fifth Int. Symp.on Turbulence and Shear Flow Phenomena*. Begel House Inc.
- Dehkordi, B. G., and H. H. Jafari. 2010. "On the suppression of vortex shedding from circular cylinders using detached short splitter-plates." *J. Fluids Eng.* **132** (4): 44501.
- Dong, S., G. E. Karniadakis, A. Ekmekci, and D. Rockwell. 2006. "A combined direct numerical simulation–particle image velocimetry study of the turbulent near wake." *J. Fluid Mech.* **569**: 185–207.
- Flamand, O. 1995. "Rain-wind induced vibration of cables." *J. Wind Eng. Ind. Aerodyn.* **57** (2–3): 353–362.
- Franke, J. 2002. "Large Eddy simulation of the flow past a circular cylinder at Re=3900." *J. Wind Eng. Ind. Aerodyn.* **90** (10): 1191–1206.
- Gu, M., and Q. Du. 2005. "Testing investigation for rain-wind induced vibration and its control of cables of cable-stayed bridges." *J. Wind Eng. Ind. Aerodyn.* **93** (1): 79–95.
- Gu, M., and Q. Lu. 2001. "Theoretical analysis of wind-rain induced vibration of cables of cable-stayed bridges." *J. Wind Eng. Ind. Aerodyn.* **89**: 125–28.
- He, X., J. Fang, A. Scanlon, and Z. Chen. 2010. "Wavelet-based nonstationary wind speed model in dongting lake cable-stayed bridge." *Engineering* **2** (11): 895–903.
- He, M., and J. H. G. Macdonald. 2016. "An analytical solution for the galloping stability of a 3 degree-of-freedom system based on quasi-steady theory." *J. Fluids Struct.* **60**: 23–36.
- He, X., X. Yu, and Z. Chen. 2012. "Nonstationarity analysis in wind-rain-induced vibration of stay cables." *J. Civil Eng. Manage.* **18** (6): 821–827.
- Hikami, Y., and N. Shiraishi. 1988. "Rain-wind induced vibrations of cables stayed bridges." *J. Wind Eng. Ind. Aerodyn.* **29** (1): 409–418.
- Hunt, J. C. R., A. Wray, and P. Moin. 1988. "Eddies, streams, and convergence zones in turbulent flows." In *Proc., Summer Program*, 193–208. Center for Turbulence Research.
- Hwang, J., and K. Yang. 2007. "Drag reduction on a circular cylinder using dual detached splitter plates." *J. Wind Eng. Ind. Aerodyn.* **95** (7): 551–564.
- Hwang, J., K. Yang, and S. Sun. 2003. "Reduction of flow-induced forces on a circular cylinder using a detached splitter plate." *Phys. Fluids* **15** (8): 2433–2436.
- Jakobsen, J. B., T. L. Andersen, J. H. Macdonald, G. N. Nikitas, G. L. Larose, M. G. Savage, and B. R. McAuliffe. 2012. "Wind-induced response and excitation characteristics of an inclined cable model in the critical Reynolds number range." *J. Wind Eng. Ind. Aerodyn.* **110**: 100–112.
- Jing, H., Y. Xia, H. Li, Y. Li, and Y. Xu. 2017. "Excitation mechanism of rain-wind induced cable vibration in a wind tunnel." *J. Fluids Struct.* **68**: 32–47.
- Kravchenko, A. G., and P. Moin. 2000. "Numerical studies of flow over a circular cylinder at $\{R\}e = 3900$." *Phys. Fluids* **12** (2): 403–417.

- Kwon, K., and H. Choi. 1996. "Control of laminar vortex shedding behind a circular cylinder using splitter plates." *Phys. Fluids* **8** (2): 479–486.
- Li, H., W. Chen, F. Xu, F. Li, and J. Ou. 2010. "A numerical and experimental hybrid approach for the investigation of aerodynamic forces on stay cables suffering from rain-wind induced vibration." *J. Fluids Struct.* **26** (7–8): 1195–1215.
- Li, S., Z. Chen, W. Sun, and S. Li. 2016. "Experimental investigation on quasi-steady and unsteady self-excited aerodynamic forces on cable and rivulet." *J. Eng. Mech.* **142** (1): 06015004.
- Li, S., Z. Chen, T. Wu, M. A. Kareem, et al. 2013. "Influence of dynamic properties and position of rivulet on rain-wind-induced vibration of stay cables." **139**: 1688–1698.
- Lourenco, L. M., and C. Shih. 1993. "Characteristics of the plane turbulent near wake of a circular cylinder, a particle image velocimetry study." Private Communication.
- Macdonald, J. H. G., and G. L. Larose. 2006. "A unified approach to aerodynamic damping and drag/lift instabilities, and its application to dry inclined cable galloping." *J. Fluids Struct.* **22** (2): 229–252.
- Macdonald, J. H. G., and G. L. Larose. 2008. "Two-degree-of-freedom inclined cable galloping. Part 1: General formulation and solution for perfectly tuned system." *J. Wind Eng. Ind. Aerodyn.* **96** (3): 291–307.
- Main, J. A., and N. P. Jones. 2000. "A comparison of full-scale measurements of stay cable vibration." In *Proc., Structures Congress 2000*.
- Matsumoto, M., T. Saitoh, M. Kitazawa, H. Shirato, and T. Nishizaki. 1995. "Response characteristics of rain-wind induced vibration of stay-cables of cable-stayed bridges." *J. Wind Eng. Ind. Aerodyn.* **57** (2–3): 323–333.
- Matsumoto, M., N. Shiraishi, M. Kitazawa, C. Knisely, H. Shirato, Y. Kim, and M. Tsujii. 1990. "Aerodynamic behavior of inclined circular cylinders-cable aerodynamics." *J. Wind Eng. Ind. Aerodyn.* **33** (1): 63–72.
- Matsumoto, M., N. Shiraishi, and H. Shirato. 1992. "Rain-wind induced vibration of cables of cable-stayed bridges." *J. Wind Eng. Ind. Aerodyn.* **43** (1): 2011–2022.
- Matsumoto, M., H. Shirato, T. Yagi, M. Goto, S. Sakai, and J. Ohya. 2003. "Field observation of the full-scale wind-induced cable vibration." *J. Wind Eng. Ind. Aerodyn.* **91** (1–2): 13–26.
- Matsumoto, M., T. Yagi, H. Hatsuda, T. Shima, M. Tanaka, and H. Naito. 2010. "Dry galloping characteristics and its mechanism of inclined/yawed cables." *J. Wind Eng. Ind. Aerodyn.* **98** (6–7): 317–327.
- Matsumoto, M., T. Yagi, Q. Liu, T. Oishi, and Y. Adachi. 2005. "Effects of axial flow and Karman vortex interference on dry-state galloping of inclined stay-cables." In *Proc., 6th Int. Symp.on Cable Dynamics*, 247–254.
- Ming, G. U. 2002. "Response characteristic of wind excited cables with artificial rivulet." *Appl. Math. Mech.* **23** (10): 1176–1187.
- Miyata, T., H. Yamada, and T. Hojo. 1994. "Aerodynamic response of pe stay cables with pattern-indent surface." In *Proc., Int. Conf. on Cablestayed and Suspension Bridges (AFPC)*, 515–522.
- Ozono, S. 1999. "Flow control of vortex shedding by a short splitter plate asymmetrically arranged downstream of a cylinder." *Phys. Fluids* **11** (10): 2928–2934.
- Pacheco, B. M. 1993. "Keeping cables calm." *Civil Eng.* **63** (10): 56–58.
- Parnaudeau, P., J. D. Heitz, and E. Lamballais. 2008. "Experimental and numerical studies of the flow over a circular cylinder at reynolds number 3900." *Phys. Fluids* **20** (8): 085101.
- Persoon, A. J., and K. Noorlander. 1999. *Full-scale measurements on the Erasmus bridge after rain/wind induced cable vibrations*. Amsterdam, Netherlands: Nationaal Lucht-en Ruimtevaartlaboratorium.

- Piccardo, G. 1993. "A methodology for the study of coupled aeroelastic phenomena." *J. Wind Eng. Ind. Aerodyn.* **48** (2): 241–252.
- Prsic, M., M. C. Ong, B. Pettersen, and D. Myrhaug. 2012. "Large Eddy simulations of three-dimensional flow around a pipeline in a uniform current." In *ASME 2012 31st Int. Conf. on Ocean, Offshore and Arctic Engineering*, 539–548.
- Raeesi, A., S. Cheng, and D. S. Ting. 2014. "A two-degree-of-freedom aeroelastic model for the vibration of dry cylindrical body along unsteady air flow and its application to aerodynamic response of dry inclined cables." *J. Wind Eng. Ind. Aerodyn.* **130**: 108–124.
- Robertson, A. C., I. J. Taylor, S. K. Wilson, B. R. Duffy, and J. M. Sullivan. 2010. "Numerical simulation of rivulet evolution on a horizontal cable subject to an external aerodynamic field." *J. Fluids Struct.* **26** (1): 50–73.
- Roshkot, A. 1954. *On the drag and shedding frequency of two-dimensional bluff bodies*. Washington DC: National Advisory Committee on Aeronautics.
- Saito, T., M. Matsumoto, and M. Kitazawa. 1994. "Rain-wind excitation of cables on cable-stayed higashi-kobe bridge and cable vibration control." In Vol. 2 of *Proc., Int. Conf. on Cable-Stayed and Suspension Bridges* (AFPC), 507–510.
- Seidel, C., and D. Dinkler. 2006. "Rain-wind induced vibrations: Phenomenology, mechanical modelling and numerical analysis." *Comput. Struct.* **84** (24–25): 1584–1595.
- Shirakashi, M., A. Hasegawa, and S. Wakiya. 1986. "Effect of the secondary flow on kármán vortex shedding from a yawed cylinder." *Bull. JSME* **29** (250): 1124–1128.
- Smagorinsky, J. 1963. "General circulation experiments with the primitive equations." *Mon. Weather Rev.* **91** (3): 99–164.
- Stafford, D. G., and S. C. Watson. 1988. "Cables in trouble." *Civil Eng.* **58** (4): 38.
- Tremblay, F., M. Manhart, and R. Friedrich. 2002. "LES of flow around a circular cylinder at a subcritical reynolds number with cartesian grids." In *Advances in LES of complex flows*, 133–50. Springer.
- Vo, H. D., H. Katsuchi, H. Yamada, and M. Nishio. 2016. "A wind tunnel study on control methods for cable dry-galloping." *Front. Struct. Civil Eng.* **10** (1): 72–80.
- Vu, H. C., J. Ahn, and J. H. Hwang. 2015. "Numerical investigation of flow around circular cylinder with splitter plate." *KSCE J. Civil Eng.* 1–10.
- Wang, J., P. Lu, J. Bi, H. J. Guan, and H. Y. Qiao. 2016. "Three-phase coupled modelling research on rain: Wind induced vibration of stay cable based on lubrication theory." *J. Fluids Struct.* **63**: 16–39.
- Yamaguchi, H. 1990. "Analytical study on growth mechanism of rain vibration of cables." *J. Wind Eng. Ind. Aerodyn.* **33** (1): 73–80.
- Zuo, D., and N. P. Jones. 2009. "Wind tunnel testing of yawed and inclined circular cylinders in the context of field observations of stay-cable vibrations." *J. Wind Eng. Ind. Aerodyn.* **97** (5–6): 219–227.
- Zuo, D., and N. P. Jones. 2010. "Interpretation of field observations of wind- and rain-wind-induced stay cable vibrations." *J. Wind Eng. Ind. Aerodyn.* **98** (2): 73–87.
- Zuo, D., N. P. Jones, and J. A. Main. 2008. "Field observation of vortex- and rain-wind-induced stay-cable vibrations in a three-dimensional environment." *J. Wind Eng. Ind. Aerodyn.* **96** (6–7): 1124–1133.

CHAPTER 7

Longitudinal Forces on Transmission Towers due to Non-Symmetric Downburst Ground Wire Loads

Amal Elawady^{*}
Ashraf El Damatty[†]

Abstract: Spatial localization of downbursts causes unique oblique load cases on long span structures such as transmission lines that do not occur during synoptic winds. This loading scenario causes an unsymmetrical wind loading along the spans of the cables resulting in an unbalanced longitudinal force acting on the transmission tower of interest. This longitudinal force is highly nonlinear; it depends on the material and geometrical properties of the cables. Therefore, a nonlinear analysis should be conducted considering the various possibilities of downburst-cable configurations and the cable material and geometrical properties. The current paper focuses on developing a simplified and manual approach to estimate this damaging longitudinal force, which develops in ground wires of transmission lines. A literature review regarding the downburst wind field and the oblique configurations that cause the peak longitudinal forces in the cables is provided. Then, the study systematically examined the effect of the variations of the ground wire parameters on their longitudinal response. Based on the findings of the assessment study, a set of charts is developed and linear interpolation equations are presented to estimate the power of such a force. This approach can address a current gap in the available transmission line standards.

Keywords: High Intensity Wind; Transmission Line; Ground wire; Conductor; Longitudinal Force; Downburst.

^{*}Department of Civil and Environmental Engineering, Florida International University, 10555 W Flagler St, Miami, FL 33174; email: aelawady@fiu.edu

[†]Department of Civil and Environmental Engineering, Western University, 1151 Richmond St., London, ON N6A 3K7; email: damatty@uwo.ca

1 INTRODUCTION

Downburst thunderstorms are localized high intensity wind events that are formed by an intensive downdraft of cold air that impinges on the ground causing high radial wind speeds (Fujita 1985). Previous reports confirmed that the majority of failures of transmission lines are caused by high intensity wind events including downburst. In Manitoba, Canada, failure and weather reports confirmed that the failure of 20 towers was related to a downburst event (McCarthy and Melsness 1996). Similar incidents were replicated in Ontario in 2006 where two guyed towers failed during a downburst event with an estimated wind speed of 50 m/s according to Environment Canada. In China, Zhang (2006) reported several failures of different transmission line systems that were subjected to downburst events. A report released by the Office of the President of the United States, emphasized that power outages due to severe weather events cause annual economic loses ranging between \$18 billion and \$33 billion (The White House report 2013). Most recently, in September 2016, a series of 23 high voltage towers failed in South Australia due to downburst event. The incident caused a blackout in South Australia for several hours (Australian Wind Alliance 2016). One of the major challenges in solving this problem is that current design guidelines do not provide sufficient information about the critical wind profiles of a downburst that act on a tower and the attached cables. The current study focuses specifically on the behavior of ground wires of transmission line systems during downburst events.

Several numerical studies reported possible failure modes of transmission lines due to downburst loads. Wang et al. (2013), Mara and Hong (2013), and Yang and Zhang (2016) evaluated the capacity of lattice transmission towers under peak wind forces resulting from the maximum downburst radial velocity, V_{RDmax} . Although of the merit provided by those studies, the effect of the spatial variations of the downburst was ignored. Shehata and El Damatty (2007, 2008) studied the behavior of a guyed tower subjected to varying downburst loading scenarios; while Darwish and El Damatty (2011) conducted a similar study on a self-supported tower. Both studies focused on addressing the effect of localization aspects of downburst events with respect to the length of the line. The studies showed that the maximum responses of the tower and the attached cables depend on the distance between the center of the downburst and the tower “R”, the angle of attack “ Θ ”, and the downburst jet diameter “ D_j ” as illustrated in Figure 1.

Failure modes of transmission line systems depend not only on the downburst configuration but also on the structural properties. One of the failure modes may occur due to an “oblique” load case of a downburst where the downburst touchdown point is located close to one side of the line spans with respect to the tower of interest. This leads to an unsymmetrical distribution of the wind forces on the spans adjacent to the tower of interest from each side as illustrated in Figure 2. Therefore, uneven tension forces develop on each side of the cables causing an unbalanced tension or a “longitudinal” force in the cables (R_{XG} in Figure 2) acting on the tower of interest. This longitudinal force does not exist in synoptic wind cases where the spans are equally loaded. Although this longitudinal force can be destructive to transmission lines, none of the available guidelines

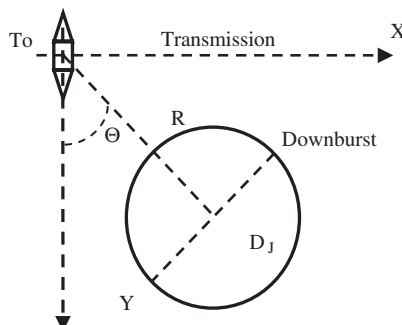


Figure 1. Downburst characteristic parameters

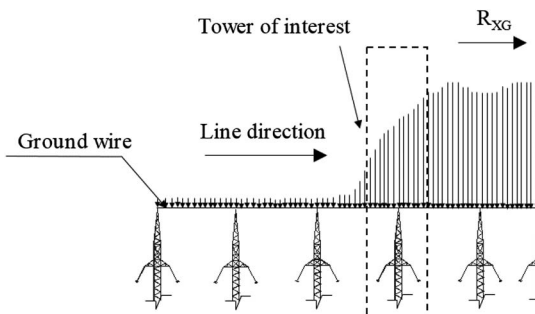


Figure 2. Schematic of the non-symmetrical loading of downbursts on the ground wires

addresses the effect of this oblique downburst load case. [Aboshosha and El Damatty \(2015\)](#) and [Elawady and El Damatty \(2016\)](#) indicated that this longitudinal force, which develops in the conductors, can reach more than 60% of the conductor's transverse force. [McCarthy and Melsness \(1996\)](#) reported an obvious cross arm failure, shown in Figure 3, caused by the effect of this force. The previous studies conducted by [Aboshosha and El Damatty \(2015\)](#) and [Elawady and El Damatty \(2016\)](#) showed that this longitudinal force is highly nonlinear. It highly depends on the configurations of the downburst (D_J , R , Θ) and the cable properties.

Therefore, evaluating this force requires a nonlinear iterative analysis while considering the cable's material and geometrical nonlinearity. This makes the evaluation of the ground wire forces, due to the effect of the non-stationary downburst oblique case, a time-consuming task for design engineers. The ultimate goal of this study is to provide a simplified approach that can be used to evaluate the longitudinal force in transmission line ground wires.

Several numerical studies discussed possible modeling approaches for transmission line cables. [Shehata et al. \(2005\)](#) used a nonlinear cable element to model the conductors and the ground wires of the transmission lines subjected to downbursts. In their study, [Shehata et al. \(2005\)](#) considered six spans of the line in order to accurately evaluate the longitudinal response of the conductors and



Figure 3. Cross arm failure due to downburst oblique loading

Source: McCarthy and Melsness, (1996)

ground wires. Later, Aboshosha and El Damatty (2014) developed a closed form solution and simulated six spans of the cables taking into consideration their pretension forces and the insulator flexibility. Unlike Finite Element Modelling of cables, this solution was found to be computationally inexpensive; however, the solution required coding for a number of coupled nonlinear equations. This complexity motivated Elawady and El Damatty (2016) to develop a manual approach to calculate the longitudinal forces developing in the conductors due to the downburst critical oblique case using a simple set of linear interpolation equations together with force charts.

Although of their small diameters compared to those of the conductors, ground wires may experience high longitudinal forces due to their rigid boundary conditions where the cables are fixed to the tower directly with no insulators. This motivated the authors of this study to develop a simplified approach to evaluate the longitudinal force developing in the ground wires of transmission line structures due to the critical oblique downburst load case.

The current paper is divided into five main sections. In the first section, the downburst wind field and the critical oblique downburst configuration are discussed. In the second section, dependency of the longitudinal force of ground wires on their properties is studied. Based on the observations obtained in section two, a set of charts is developed in section three to help practitioners to manually calculate the longitudinal forces developing in ground wires subjected to the critical downburst oblique load case. In section four, a validation of the proposed procedure is conducted. Finally, the conclusions to the entire study are presented.

2 DOWNBURST WIND FIELD

The localized dimension of a downburst compared to the long length of the transmission line affects the values of the forces acting on the conductors and the tower members and, consequently, the overall structural response of the line.

The downburst dimensions are characterized by the size (jet diameter, D_J) and the polar coordinates of the center of the downburst relative to the center of the tower of interest (R and Θ), as shown in Figure 1. The intensity of the downburst is represented by the jet velocity (V_J). Different numerical modeling techniques were reported in the literature to simulate the downburst wind field. The current study utilizes the impinging jet model developed and validated by Kim and Hangan (2007) to simulate the downburst's radial and vertical velocities. The model provides time histories of the mean radial and vertical velocities of the downburst wind field. A sample time history of the radial velocity of a downburst at a point in space is provided in Figure 4. The figure shows the temporal localization of the radial velocity along the time history of the event. The variations in the normalized radial (V_{RD}) and vertical (V_{VR}) velocities with respect to the distance ratio R/D_J along the height is provided in Figures 5 and 6, respectively. These wind profiles are plotted at the time instants corresponding

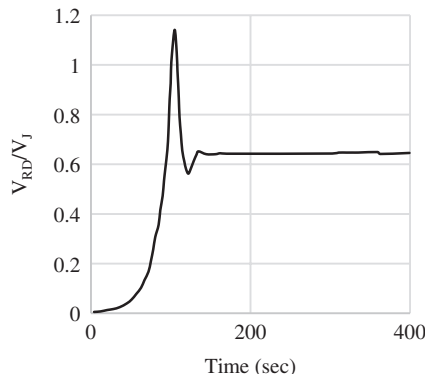


Figure 4. Time history of the radial velocity at a point in space

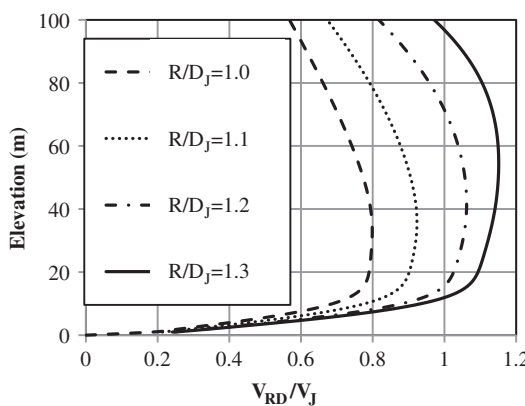


Figure 5. Radial velocity profile along the height

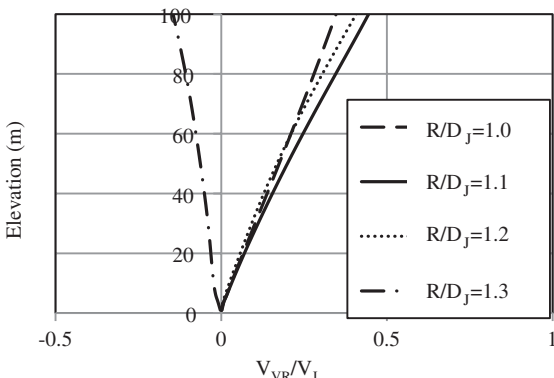


Figure 6. Vertical velocity profile along the height

to the maximum radial or vertical velocities at a specific elevation. Figure 5 shows that the maximum radial velocity occurs at R/D_J equal 1.3 and at a height of approximately 60 m. Since no significant variation of the V_{RD} is found in the vicinity of the typical height of ground wires (i.e., 40–60 m, the height factor is eliminated from this study and a constant ground wire height of 60 m is assumed). In the next section, the downburst configurations that cause the peak longitudinal forces developing in the ground wires due to the non-symmetrical wind loading on the spans of the line adjacent to the tower of interest are discussed.

The Computational Fluid Dynamics (CFD) model utilized in the current study does not provide the turbulence component. Turbulence is intrinsic to evaluate the peak forces acting on the tower and the conductors. In general, transmission towers are not susceptible to dynamic excitation, which results from the mean wind component, due to their high frequencies (typically > 1 Hz according to ASCE-74 2010). However, ground wires are more prone to the dynamic excitation of wind loads in general and to downbursts in particular because of their low frequencies (typically < 0.2 Hz according to Loredo-Souza and Davenport 1998). Different studies, such as those of Gattulli et al. (2007) and Darwish et al. (2010), showed that the aerodynamic damping of transmission line conductors helps to attenuate the dynamic response of the line at high wind speeds. Elawady (2016) conducted an aero-elastic testing for a multi-spanned lattice transmission system under simulated downburst wind field. The results reported from this test showed that the dynamic response of the conductors of the system is in the order of 10% to 12% at the expected high wind speeds. This means that quasi-static analysis for such systems may be sufficient in cases of downbursts winds. Therefore, the current study accounts only for the background component of the response by scaling-up the mean wind field to the gust wind speed. The study assumes a full turbulence correlation along the line spans which agrees with the findings reported by Holmes et al. (2008).

2.1 Critical configurations of downburst causing maximum R_{XG}

This section discusses the downburst wind profile acting on the ground wire spans that is used in the current study. As mentioned earlier, the downburst configurations that affect the wind forces acting on the ground wires are D_J , R , Θ , V_{RD} , and the time instant. In addition, [Elawady and El Damatty \(2016\)](#) revealed that the longitudinal force developing in the cables due to the non-symmetrical downburst loading is proportional to the difference between the integrated wind forces acting on the right and left hand side spans adjacent to the tower of interest, respectively. In their study, [Elawady and El Damatty \(2016\)](#) conducted an extensive parametric study to determine the critical downburst configuration that causes the maximum longitudinal force in the cables. Based on that parametric study, [Elawady and El Damatty \(2016\)](#) reported that the V_{RD} distribution corresponding to a downburst of $D_J = 500$, $R/D_J = 1.6$, and $\Theta = 30^\circ$, shown in Figure 7, is the most critical. The current study adopts this velocity distribution in order to evaluate the corresponding ground wire longitudinal force.

3 GROUND WIRE PROPERTIES AFFECTING THE LONGITUDINAL FORCE

The current study utilizes the iterative semi-analytical technique developed and validated numerically by [Aboshosha and El Damatty \(2014\)](#) and experimentally by [Elawady \(2016\)](#) to estimate reactions of ground wires. In this section, the ground wires properties are varied in a systematic approach in order to assess the sensitivity of ground wire longitudinal force, R_{XG} , to those parameters. For each of the examined parameters, the practical range is determined based on recommendations received from Hydro One, Ontario and other utility companies in the United States. Two ground wires, GW1 and GW2, are used in the parametric

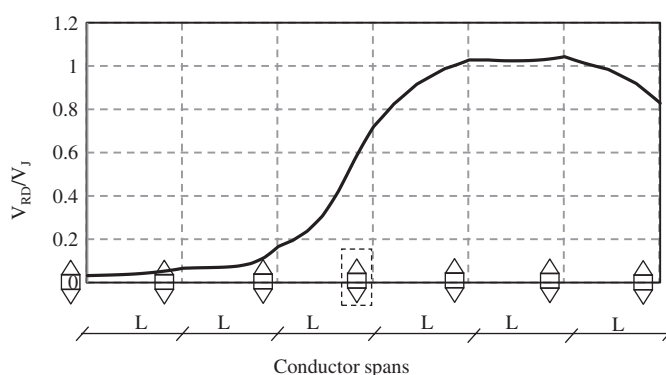


Figure 7. Radial velocity distribution along multiple spans in the case of an oblique downburst

Table 1. Selected Conductors used to Assess the Effect of the Conductor's Parameters on R_{XG}

Ground wire index	w (N/m)	α (kg/sec^2)	EA (N)	S	L (m)
GW1	3	18	2.00E+07	4%	300, 400,
GW2	15	62	6.00E+07	2.5%	and 500

study. The weight per unit length “w”, span “L”, wind pressure “ α ”, sag to span ratio “S” and axial stiffness “EA” of the two ground wires are given in Table 1. It is important to mention that, for the case of the longitudinal force developing in the ground wires “ R_{XG} ”, the towers (point of supports of the cables, are assumed to be hinged which implies the case of no insulator (e.g., ground wire case).

3.1 Effect of the ground wire weight per unit length

The ground wire’s weight per unit length (w) is considered to vary between 3 N/m and 15 N/m. For this range of ground wire weights, the analysis showed that the longitudinal force decreases with an increase of w as shown in Figure 8. The figure shows that R_{XG} linearly reduces with the increase of w. This is justified since the increase in w results in an increase in the cable pretension force and accordingly an increase in the cable axial stiffness. Therefore, the increase in w results in a reduction in the lateral deflection of the cable and consequently a reduction in the longitudinal force of the cable.

3.2 Effect of the wind pressure

In this study, the wind pressure, α , is varied from 18 kg/sec^2 to 62 kg/sec^2 . Assuming wire diameters ranging between 0.006 m to 0.02 m, the considered wind

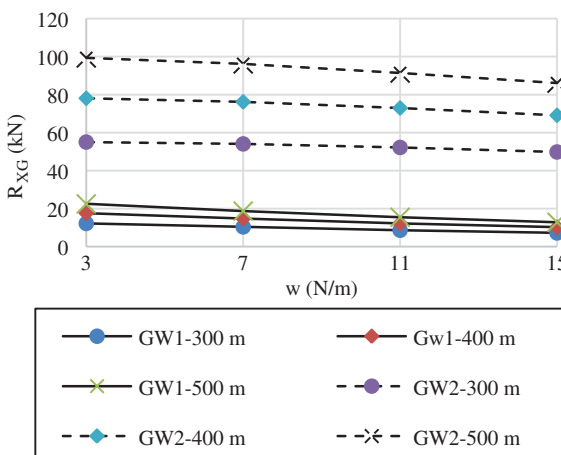


Figure 8. Variation of R_{XG} with w

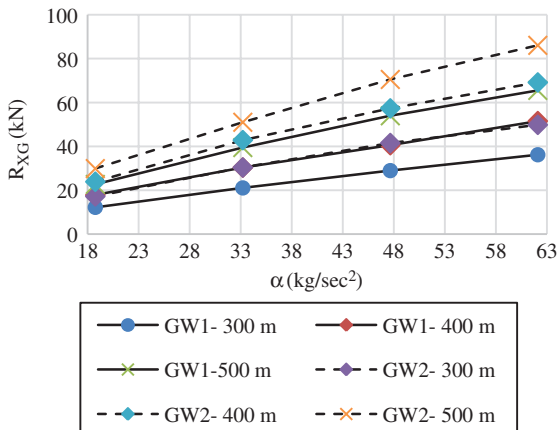


Figure 9. Variation of R_{XG} with α

pressure corresponds to a varying downburst jet velocity up to and including 70 m/s. Figure 9 shows that R_{XG} increases with the increase of α in a linear manner. Elawady and El Damatty (2016) reported similar results. However, the variation was found to be nonlinear. This is because the range of α is significantly greater than that considered in the ground wire cases.

3.3 Effect of the ground axial stiffness

Elawady and El Damatty (2016) reported that the effect of the conductor's axial stiffness, EA, is negligible with respect to the value of R_X . This can be interpreted as follows: under the same level of loading, a reduction in EA will result in an increase in the deformation of the cable, and, consequently, an increase in the strains developing in the conductor; strains are determined by comparing the difference between the deformed length and the initial length of the wire. This may not be valid in case of ground wires where the axial stiffness is low compared to conductor cases. The small value of EA may result in a second order deformation causing a different trend than that found in the conductor cases reported previously by Elawady and El Damatty (2016). Therefore, the axial stiffness of the ground wires, EA, is considered, in the charts developed and discussed in the next section, to vary between $2E+07$ and $6E+07$ N. Figure 10 shows the variations of the R_{XG} with respect to the considered values of EA. The figure shows that R_{XG} increases with the linearly increase of EA.

3.4 Effect of the ground wire sag

The sag to span ratio "S" is considered to vary from 2.5% to 4%. Figure 11 shows the variations of R_{XG} with S. The figure shows that R_{XG} is inversely proportional to S in a linear manner. Although the increase in S will reduce the cable stiffness, R_{XG} is reduced with the increase in S due to the increase in cable flexibility and the rigid boundary conditions at the ground wire-tower connections.

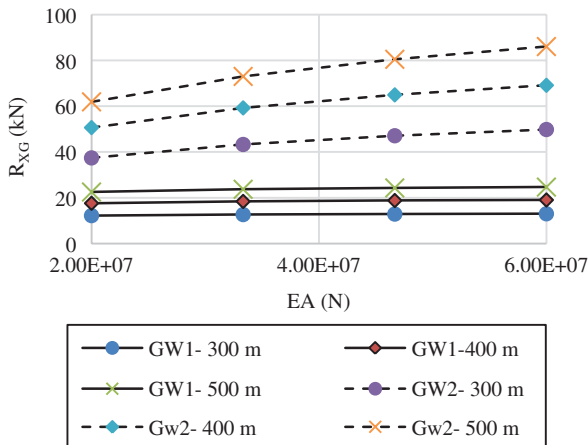


Figure 10. Variation of R_{XG} with EA

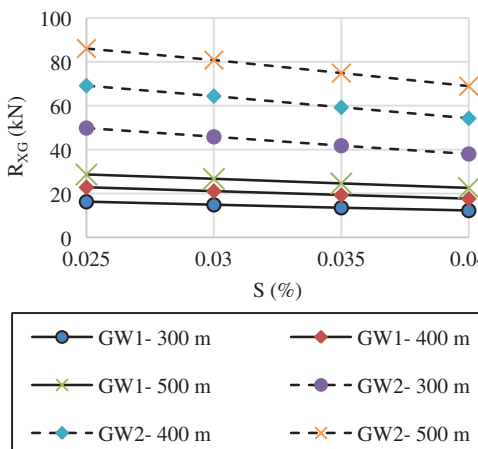


Figure 11. Variation of R_{XG} with S

4 LONGITUDINAL FORCE CALCULATION APPROACH

In this section, a set of charts is developed to evaluate the ground wire's maximum longitudinal force, R_{XG} , due to the critical oblique downburst case mentioned previously. The charts are developed based on the assumption that the structure is a tangent transmission line and the ground wires are directly attached to the tower with no insulators. As such, these charts are not applicable for the case of conductors. The charts are developed in light of the findings discussed in the assessment study conducted in the previous section. The charts are developed

to cover the practical range of the properties of ground wires in terms of w , L , S , and α . The assessment study showed that in the practical range of each of the studied properties, R_{XG} , varies in a linear manner with the variation of each of EA, α , S , and w .

In view of the above, eight charts covering a wide range of EA, α , and w are developed as shown in Figure 12. Ranges of each of the charts parameters are provided in Table 2. The eight charts developed cover all of the possible combinations of α_{\min} , α_{\max} , w_{\min} , w_{\max} , EA_{min}, and EA_{max}. The eight charts

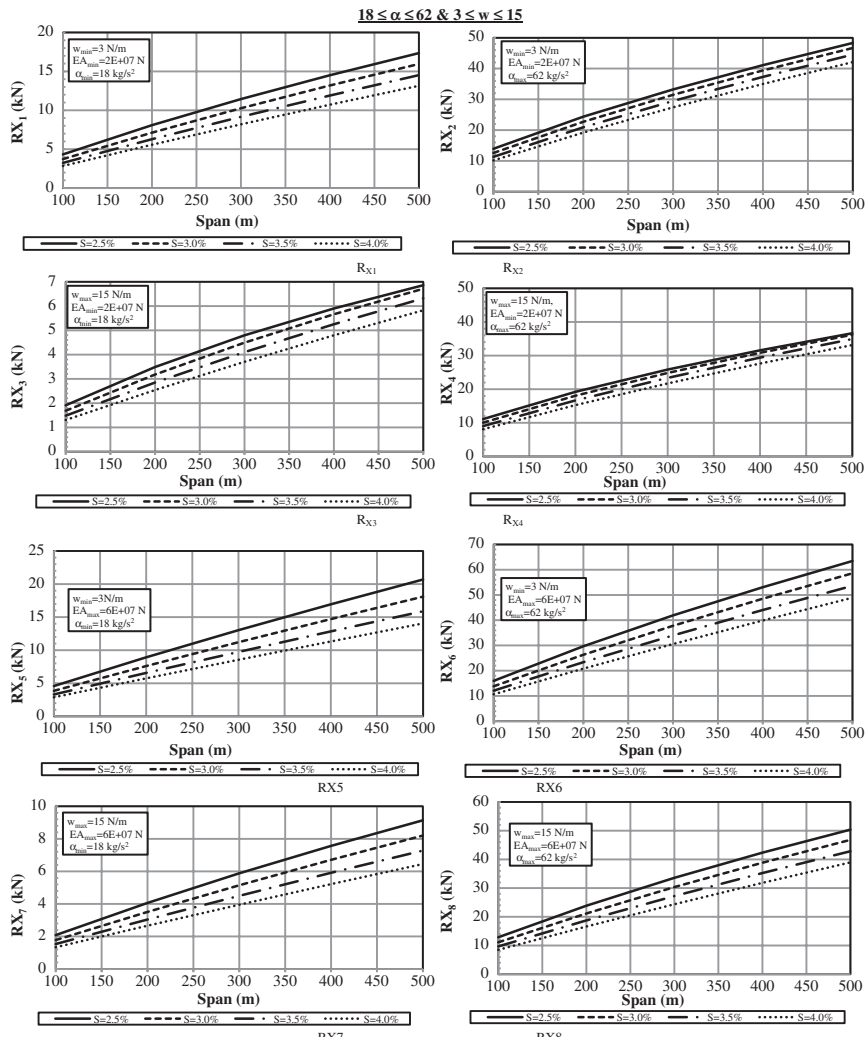


Figure 12. Ground wire maximum longitudinal force due to downburst oblique load case

Table 2. Group range for the evaluation of RX

α (kg/sec ²)		w (N/m)		EA (N)	
α_{min}	α_{max}	w_{min}	w_{max}	EA_{min}	EA_{max}
18	62	3	15	2E07	6E07

illustrate the relationship between R_{XG} and L, for the different S ratios, for the upper and the lower limits of α , w, and EA. Since R_{XG} varies linearly with α , w, and EA, a three-dimensional linear interpolation can be carried out to obtain the value of R_{XG} corresponding to the arbitrary values for L, S, EA, w, and α .

According to the developed manual approach, the following steps can be used to evaluate the maximum longitudinal force (R_{XG}) of a ground wire subjected to the critical oblique downburst load case reported previously by [Elawady and El Damatty \(2016\)](#).

1. Calculate $\alpha = 0.5 * \rho * V_J^2 * d_p$.
2. Based on the line span and the sag ratio, a user can determine eight longitudinal forces using the provided eight charts. Those are labeled as

R_{XG1} = force corresponding to $(w_{min}, EA_{min}, \alpha_{min})$

R_{XG2} = force corresponding to $(w_{min}, EA_{min}, \alpha_{max})$

R_{XG3} = force corresponding to $(w_{max}, EA_{min}, \alpha_{min})$

R_{XG4} = force corresponding to $(w_{max}, EA_{min}, \alpha_{max})$

R_{XG5} = force corresponding to $(w_{min}, EA_{max}, \alpha_{min})$

R_{XG6} = force corresponding to $(w_{min}, EA_{max}, \alpha_{max})$

R_{XG7} = force corresponding to $(w_{max}, EA_{max}, \alpha_{min})$

R_{XG8} = force corresponding to $(w_{max}, EA_{max}, \alpha_{max})$

Based on the properties of the ground wire under examination in terms of α , EA, and w, and the above-evaluated eight forces, a linear interpolation can be conducted using the set of equations as shown:

$$R_{X(1-2)} = R_{X1} + (R_{X2} - R_{X1}) * \frac{(\alpha - \alpha_{min})}{(\alpha_{max} - \alpha_{min})} \quad (2)$$

$$R_{X(3-4)} = R_{X3} + (R_{X4} - R_{X3}) * \frac{(\alpha - \alpha_{min})}{(\alpha_{max} - \alpha_{min})} \quad (3)$$

$$R_{X(EA_{\min})} = R_{X(3-4)} + (R_{X(1-2)} - R_{X(3-4)}) * \frac{(w_{\max} - w)}{(w_{\max} - w_{\min})} \quad (4)$$

$$R_{X(5-6)} = R_{X5} + (R_{X6} - R_{X5}) * \frac{(\alpha - \alpha_{\min})}{(\alpha_{\max} - \alpha_{\min})} \quad (5)$$

$$R_{X(7-8)} = R_{X7} + (R_{X8} - R_{X7}) * \frac{(\alpha - \alpha_{\min})}{(\alpha_{\max} - \alpha_{\min})} \quad (6)$$

$$R_{X(EA_{\max})} = R_{X(7-8)} + (R_{X(5-6)} - R_{X(7-8)}) * \frac{(w_{\max} - w)}{(w_{\max} - w_{\min})} \quad (7)$$

$$R_X = R_{X(EA_{\min})} + \frac{(R_{X(EA_{\max})} - R_{X(EA_{\min})})}{(EA_{\max} - EA_{\min})} * (EA - EA_{\min}) \quad (8)$$

5 VALIDATION

The proposed procedure is validated by comparing the R_{XG} values, for the selected ground wires, obtained in the proposed procedure, to those values estimated using the semi-analytical technique developed by [Aboshosha and El Damatty \(2014\)](#) and validated using experimental data reported by [Elawady et al. \(2017\)](#), R_{XG} exact, as shown in Table 3. The ground wires used in this section are selected from Hydro One, Ontario data base. The jet velocity of the downburst is assumed to equal 70 m/s. The comparison table shows that there is a good agreement between the two longitudinal forces where a maximum error of approximately 9% is found.

Table 3. Validation for the RXG Values Obtained from the Proposed Approach

α (kg/s ²)	EA (N)	w (N/m)	span (m)	Sag ratio (%)	R_{XG} (kN)	R_{XG} exact (kN)	% Error
43.49	2.52E+07	10.40	213.36	2.5	13.9	12.77	8.70
27.56	2.52E+07	3.90	480	2.8	19.8	18.97	4.17
29.19	2.66E+07	3.90	400	3	16.4	15.28	7.53
29.19	2.894E+07	3.90	460	3	21.9	21.24	3.09
42.86	3.16E+07	10.40	213.36	1.5	18.2	18.61	-1.96
27.56	3.96E+07	3.82	450	3	40.0	38.01	5.26

6 CONCLUSIONS

A manual approach is developed to evaluate the maximum longitudinal force, R_{XG} , which develops in transmission line ground wires due to a critical oblique downburst load case. This longitudinal force is the result of the non-symmetrical distribution of the downburst radial velocities along the spans adjacent to the tower of interest. First, the study describes the downburst wind field and particularly the oblique configurations of the downburst causing this unique force in the ground wires. Using the critical oblique configurations causing the maximum R_{XG} , a study is conducted to assess the effect of the variations of the ground wire parameters on the value of R_{XG} . The study shows that R_{XG} is linearly proportional to the wind pressure, α , and the axial stiffness, EA, of the cable and is inversely proportional to the cable sag, S, and the weight per unit length, w. Based on the findings of the assessment study, a group of charts is developed to estimate R_{XG} , which covers the upper and lower limits for the practical range of the ground wire parameters. The force R_{XG} can be estimated by applying a three-dimensional linear interpolation between the values corresponding to the upper and lower limits of α , w, and EA. The procedure is then validated by comparing R_{XG} value for a number of real ground wires to those values estimated using an iterative nonlinear semi-analytical technique. The procedure is found to be simple and reasonably accurate. The outcomes of this study can help in mitigating transmission line failures during downburst events.

References

- Aboshoshaa, H., and A. El Damatty. 2014. "Effective technique to analyze transmission line conductors under high intensity winds." *Wind Struct.* **18** (3): 235–252.
- Aboshosha, H., and A. El Damatty. 2015. "Engineering method for estimating the reactions of transmission line conductors under downburst winds." *J Eng Struct.* **142**: 198–216.
- ASCE. 2010. *Guidelines for electrical transmission line structural loading*. ASCE Manuals and Reports on Engineering Practice, No. 74. New York: ASCE.
- Australian Wind Alliance. 2016. <http://www.windalliance.org.au/>.
- Darwish, M. M., and A. A. El Damatty. 2011. "Behavior of self supported transmission line towers under stationary downburst loading." *Wind Struct.* **14** (5): 481–498.
- Darwish, M. M., A. A. El Damatty, and H. Hangan. 2010. "Dynamic characteristics of transmission line conductors and behaviour under turbulent downburst loading." *Wind Struct.* **13** (4): 327–346.
- Elawady, A. 2016. "Development of design loads for transmission line structures subjected to downbursts using aero-elastic testing and numerical modeling." Ph.D. thesis Univ. of Western Ontario.
- Elawady, A., H. Aboshosha, A. El Damatty, G. Bitsuamlak, H. Hangan, and A. Elatar. 2017. "Aero-elastic testing of multi-spanned transmission line subjected to downbursts." *J. Wind Eng. Ind. Aerodyn.* **169**: 194–216.
- Elawady, A., and A. El Damatty. 2016. "Longitudinal force on transmission towers due to non-symmetric downburst conductor load." *J. Eng. Struct.* **127**: 206–226.

- Fujita, T.T. 1985. *The downburst: Microburst and macroburst: SMRP Research Paper 210.* Chicago: Univ. of Chicago.
- Gattulli, V., L. Martinelli, F. Perotti, and F. Vestroni. 2007. "Dynamics of suspended cables under turbulence loading: reduced models of wind field and mechanical system." *J. Wind Eng. Ind. Aerodyn.* **95** (3): 183–207.
- Holmes, J. D., H. M. Hangan, J. L. Schroeder, C. W. Letchford, and K. D. Orwig. 2008. "A forensic study of the Lubbock-Reese downdraft of 2002." *Wind Struct.* **11** (2): 137–152.
- Kim, J., and H. Hangan. 2007. "Numerical simulations of impinging jets with application to downbursts." *J. Wind Eng. Ind. Aerodyn.* **95** (4): 279–298.
- Loredo-Souza, A. M., and A. G. Davenport. 1998. "The effects of high winds on transmission lines." *J. Wind Eng. Ind. Aerodyn.* **74**: 987–994.
- Mara, T., and H. Hong. 2013. "Effect of wind direction on the response and capacity surface of a transmission tower." *Eng. Struct.* **57**: 493–501.
- McCarthy, P., and M. Melsness. 1996. *Severe weather elements associated with September 5, 1996 hydro tower failures near Grosse*. Manitoba Environmental Service Centre.
- Shehata, A. Y., and A. A. El Damatty. 2007. "Behaviour of guyed transmission line structures under downburst wind loading." *Wind Struct.* **10** (3): 249–268.
- Shehata, A. Y., and A. A. El Damatty. 2008. "Failure analysis of a transmission tower during a microburst." *Wind Struct.* **11** (3): 193–208.
- Shehata, A. Y., A. A. El Damatty, and E. Savory. 2005. "Finite element modeling of transmission line under downburst wind loading." *Finite Elem. Anal. Des.* **42** (1): 71–89.
- The White House. 2013. "Economic benefits of increasing electric grid resilience to weather outages." Executive Office of the President, Washington. http://energy.gov/sites/prod/files/2013/08/f2/Grid%20Resiliency%20Report_FINAL.pdf.
- Wang, X., W. Lou, H. Li, and Y. Chen. 2009. "Wind-induced dynamic response of high-rise transmission tower under downburst wind load." *J. Zhejiang Univ.* **43** (8): 1520–1525.
- Yang, F., and H. Zhang. 2016. "Two case studies on structural analysis of transmission towers under downburst." *Wind Struct.* **22** (6): 685–701.
- Zhang, Y. 2006. "Status quo of wind hazard prevention for transmission lines and counter measures." *East China Electric Power* **34** (3): 28–31.

This page intentionally left blank

CHAPTER 8

Effects of Chamber Shape on Simulation of Tornado-like Flow in a Laboratory

Fangping Yuan^{*}

Guirong Yan[†]

Ryan Honerkamp[‡]

Kakkattukuzhy M. Isaac[§]

Ruoqiang Feng[¶]

Abstract: Considering that it is difficult to capture the characteristics of the wind field during a tornado event, especially the wind field near ground, it is important to reproduce the tornado-like vortices in the laboratory tornado simulator to systematically study the violent tornadic wind field and its effect on civil engineering structures. The tornado simulator studied here follows the same mechanism to generate the tornado-like vortices as the one at Iowa State University (ISU). That is, the flow, driven by the fan, self-circulates inside the simulator, and angular momentum is introduced by the guide vanes set at an angle with respect to the radius. A high-fidelity numerical model of this tornado simulator is established by modeling all the major mechanical components of the tornado simulator in the simulation, including the chamber/duct, guide vanes, fan, and honeycomb section. In order to identify the optimal shape for the laboratory tornado simulator, three tornado simulators with different geometric shapes of chambers are simulated. For each tornado simulator, both overall and near-floor tornadic wind fields are

^{*}Department of Mechanical and Aerospace Engineering, Missouri University of Science and Technology, Rolla, MO 65409, email: fy337@mst.edu

[†]Department of Civil, Architectural and Environmental Engineering, Missouri University of Science and Technology, Rolla, MO 65409 (corresponding author), email: yang@mst.edu

[‡]Department of Civil, Architectural and Environmental Engineering, Missouri University of Science and Technology, Rolla, MO 65409, email: rh7v7@mst.edu

[§]Department of Mechanical and Aerospace Engineering, Missouri University of Science and Technology, Rolla, MO 65409, email: isaac@mst.edu

[¶]The Key Laboratory of Concrete and Prestressed Concrete Structures of Ministry of Education, Southeast University, Nanjing, Jiangsu, China 210096, email: hitfeng@163.com

extracted. The obtained results show that the curved chamber provides a more stable flow compared with the multi-sided chamber that is used in the tornado simulator of ISU. The developed numerical model here helps gain more physical insights into tornado simulators, and impels the design optimization of this type of laboratory tornado simulator so that controllable tornado-like vortices can be better understood.

Keywords: Tornado; Tornado Simulator; Wind Effects; CFD simulations.

1 INTRODUCTION

Tornadoes strike the United States very frequently, about 1200 tornadoes per year based on the NOAA statistics ([NOAA n.d.](#), [Grazulis and Grazulis 1993](#)). They result in incredible amounts of property damage and significant numbers of fatalities each year. During the period of 1949–2006, the average annual economic loss due to tornadoes is about \$1 billion ([Changnon 2009](#), [McCarthy and Schaefer 2004](#), [Storm Prediction Center 2014](#)); annually, tornadoes cause 90 fatalities and 1,500 injuries ([Simmons et al. 2013](#)). In 2011 alone, the tornado-induced damage loss exceeded \$20 billion, and several hundred people lost their lives ([Lott et al. 2012](#), [FEMA 2012](#)). The devastation from recent tornadoes (e.g., Joplin, MO, in 2011; Tuscaloosa, AL, in 2011; and Moore, OK, in 2013) left no doubt as to the vulnerability of the Central United States to tornadoes, and prompted an urgent need for research on tornadoes in all aspects by different research fields.

A tornado is a rotating column of air extending from a cumulonimbus cloud to the ground ([Tornado 2018](#)) (see Figure 1). It is claimed to be one of the most violent natural hazards ([Figures 2 and 3](#)). Considering that it is difficult to capture the characteristics of the wind field during a tornado event, especially the wind field near ground, it is important to reproduce the tornado-like vortices in the laboratory to systematically study the violent tornadic wind field and its effect on civil engineering structures. The facility to reproduce tornado-like vortices is called a tornado simulator.

Besides the previous Ward-type tornado simulator ([Chang 1966](#), [Ward 1972](#)) and its updated versions ([Church et al. 1979](#), [Leslie 1977](#), [Jischke and Light 1983](#), [Diamond and Wilkins 1984](#)), the recently developed ones in North America are



Figure 1. A tornado

Source: Photo courtesy of NEW8.

@Seismicisolation



Figure 2. Damage due to EF-5 Joplin tornado in 2012

Source: Photo courtesy of FEMA.



Figure 3. Collapse due to Vilonia tornado in 2011

Source: Photo courtesy of ArkansasOnline.

located at Iowa State University (ISU) (Haan et al. 2008), Texas Tech University (Mishra et al. 2008) and Western University (WU) (Refan 1923). Using the tornado simulator at ISU, the wind flow around a one-story, gable-roofed building in tornado-like winds (Hu et al. 2011) and the wind effects on this structure (Haan et al. 2009) have been studied. It showed that the tornado-induced lateral forces were about 50% larger than those by ASCE 7-05 and the tornado-induced vertical force (uplift) were two or three times as large as those by the provision. Other similar research can be found in (Chang 1971, Bienkiewicz and Dudhia 1993, Fouts et al. 2003, Mishra et al. 2008). Using the capability of generating translating tornado-like winds in the tornado simulator at ISU, the influence of the translating speed on wind effects was investigated on a cubic building. It showed that a lower translating speed induces greater wind loading on the structure than a higher translating speed (Sengupta et al. 2008). Using the tornado simulator of WU, the effects of translation and surface roughness on tornado-like vortices were studied. It suggests that (1) translation reduces the mean value of the maximum tangential velocity for lower swirl ratios whereas it causes a slight increase in the mean value of the maximum tangential velocity for high swirl ratios, (2) surface roughness causes an overall effect similar to reducing the swirl ratio (Natarajan and Hangan 2012). Using the tornado simulator at Tokyo Polytechnic U., an experimental investigation was conducted to

gain a better understanding of the effect of building location with respect to the tornado center (Rajasekharan et al. 2013), and the effect of ground surface roughness on the internal pressures developed inside a building model (Sabareesh et al. 2013).

Due to the small size of laboratory tornado simulators and the low wind speed that can be generated, research based on experimental test data has its own limitations. Therefore, computational fluid dynamics (CFD) simulation has also been employed to simulate the tornadic wind field and determine wind effects on structures. Kuai et al. (2008) simulated the flow field of full-scale and laboratory-scale tornadoes and verified the ability of their CFD model to capture the flow characteristics of both. Natarajan (2012) investigated the flow characteristics of tornadoes by numerically simulating three types of laboratory simulators, Ward-type Tornado Vortex Chamber, WindEEE Dome, and Atmospheric Vortex Engine. Ishihara et al. (2011) studied how the swirl ratio affects the structure (single-cell, double-cell, or multiple vortices) of the generated tornado-like vortices by using Large Eddy Simulation (LES) to model turbulence (Ishihara et al. 2011, Liu and Ishihara 2012). Lewellen and Lewellen (1997) numerically simulated a full-scale tornado for a high swirl ratio ($S = 0.94$) and observed that introducing translation resulted in a slight increase in the maximum mean velocity. How a tornado flow is affected by a structure was investigated on a cubic building using CFD (Selvan and Millett 2003). It showed that when the tornado reached the building, the wind changed from horizontal to highly concentrated vertical wind; as the high-velocity vertical wind flowed past the corners of the building, flow separation and vortex shedding were observed.

Although numerical models have been developed for some tornado simulators, the previous numerical simulation was mainly focused on the convergence region, instead of modeling all the mechanical components in the tornado simulator. In this study, to simulate the tornado simulator more accurately, all mechanical components in the tornado simulator will be modeled. Considering that the tornado simulator at ISU can produce a tornado that can translate, the tornado simulator numerically simulated here will follow the same mechanism of generating a tornado as the tornado simulator of ISU. To achieve a better performance than the tornado simulator at ISU and to identify the best configuration of the laboratory tornado simulator, three tornado simulators with different shapes of chambers will be simulated and compared. The remaining of the paper is organized as follows. First, the dimensions and properties of the three tornado simulators to be numerically simulated are introduced. Then, how to model each mechanical component in the tornado simulator using ANSYS FLUENT (n.d.) is discussed. Finally, the generated overall wind flow and near-ground wind field are presented and compared among the three simulated cases. This study is expected to achieve in-depth insights into this type of tornado simulator, and to provide a guidance to optimize the design of a tornado simulator to better simulate tornado-like wind flow in the laboratory.

2 TORNADO SIMULATORS TO BE SIMULATED NUMERICALLY

The tornado simulator at Iowa State University (ISU) has successfully generated tornado-like vortices in their laboratory tornado simulator to simulate tornadic wind field (Haan et al. 2008, 2009; Kuai et al. 2008). The tornado simulators to be numerically simulated in this study follow the same mechanism to generate tornado-like vortices as ISU. The diameter of the tornado simulators considered here is slightly smaller than the one at ISU, as this is the size of the tornado simulator that the current authors will build in their institute. To identify the optimal design of the tornado simulator, three geometric shapes of the chamber are investigated here, as shown in Figure 4. Figure 4a presents the tornado simulator with the same chamber shape as the one at ISU (multi-sided chamber). Figure 4b presents the tornado simulator with a curved chamber, and Figure 4c presents the one with a curved chamber and a cone on the top. The details of the tornado simulator presented in Figure 4b are shown in Figure 5.

Among the three tornado simulators, except the difference in the shape of the chamber, the properties of all other components are kept the same. The dimensions of each component are listed in Table 1. By taking the tornado simulator presented in Figure 4b as an example, the schematic diagram of the tornado simulator and its corresponding 3D CAD model are presented in Figures 5a and 5b, respectively. Each tornado simulator consists of the chamber/duct, 37 vanes, and the inner cylinder with the fan and honeycomb section, as shown in Figure 5. The fan generates 86,000 cubic feet per minute ($Q \approx 40.587 \text{ m}^3/\text{s}$) flow rate with a static pressure increase of 1.5 inches of water ($\Delta P \approx 373 \text{ Pa}$) at RPM = 1770. The honeycomb section placed at the bottom of the inner cylinder is to straighten the upward air flow.

A cylindrical coordination system is used to describe the simulator, and the r- and z- axes are presented in Figure 5a. The flow circulation in a radial-vertical plane is illustrated in Figure 5b. The mechanism to generate the swirling flow is described as follows. The fan is positioned to suck the air from the bottom to the top region of the simulator, providing the driving force to establish the flow circulation. After the flow passes through the guide vanes, an angular momentum is added to the flow. Then the flow with the swirling motion is up-drafted back into the inner cylinder, where it is straightened by the honeycomb section before entering the fan inlet. The above flow circulating mechanism will be verified by the numerical simulations, which will be presented in the following sections.

For the tornado simulator with a curved chamber (presented in Figures 4b and 4c), the use of the curved chamber/duct is expected to reduce energy loss due to the abrupt change of the air-flow direction when the multi-sided chamber is used; the vanes follow the contour of the curved chamber/duct, which is

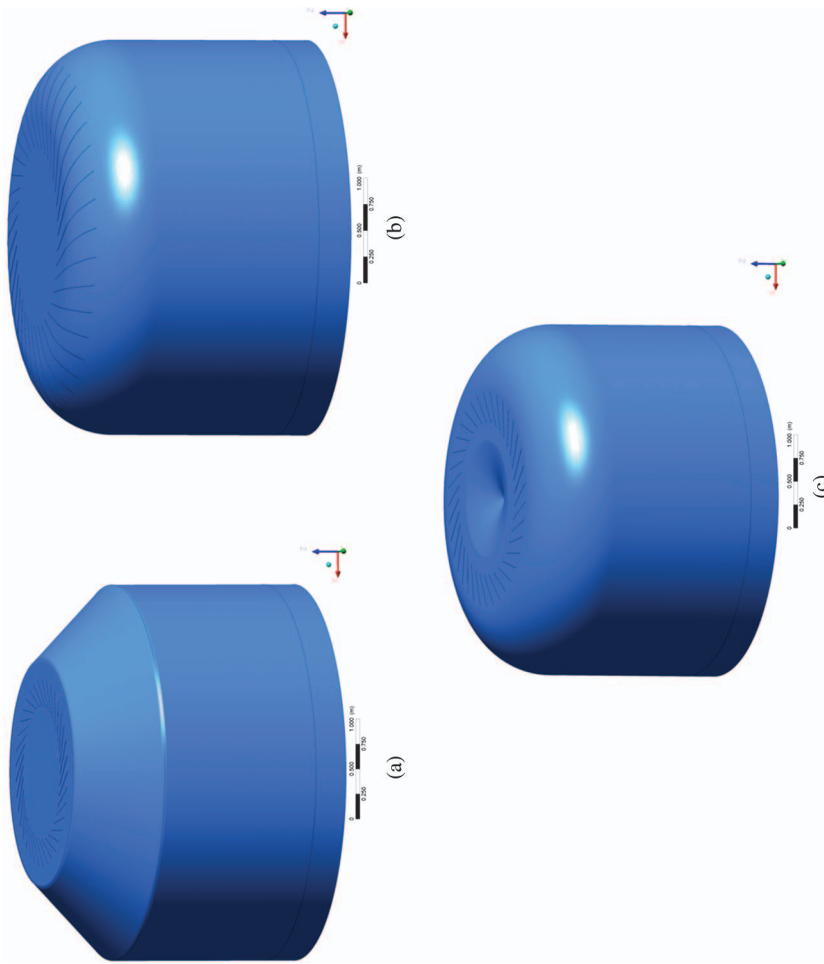


Figure 4. Tornado simulators with different chamber shapes: (a) multi-sided chamber (same chamber shape as ISU), (b) curved chamber, and (c) curved chamber with cone on the top

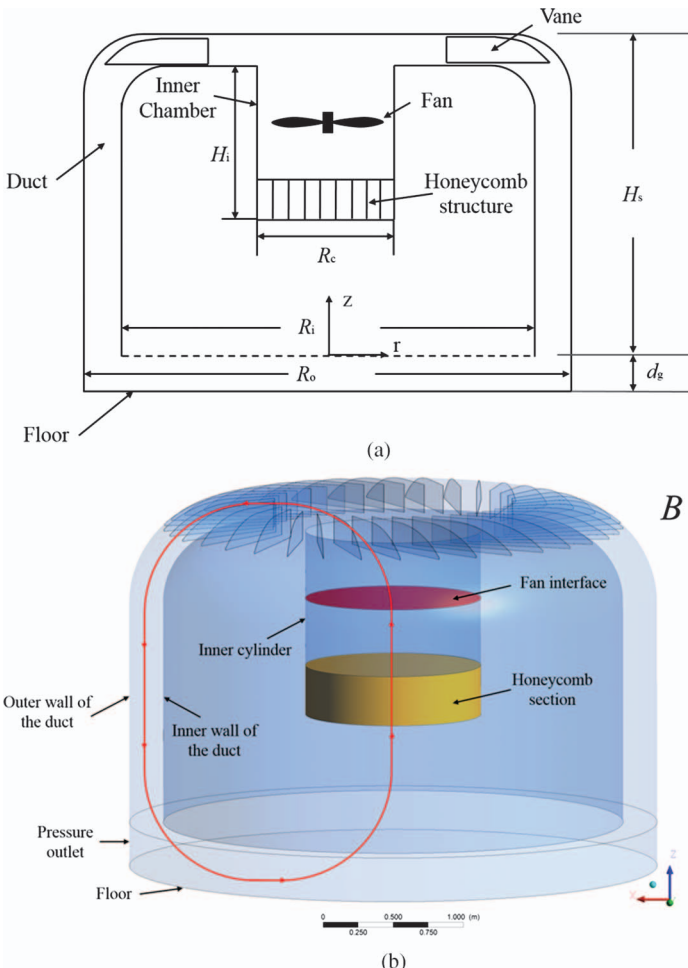


Figure 5. Tornado simulator with a curved chamber: (a) schematic diagram, and (b) 3D CAD model

expected to mitigate flow separation and decrease turbulence generated in the duct as the flow changes direction. Through the above modifications, it is expected to achieve better overall efficiency and higher potential circulation velocities than the tornado simulator at ISU.

The dimensions of the overall facility simulated here are presented in Figure 6. The entire chamber can maneuver freely along a straight path using an overhead crane to simulate the translation of a tornado. The floor plane can be raised or lowered to achieve variations of floor height and observe changes associated with different tornado conditions.

Table 1. Dimensions of the Components in the Tornado Simulator

Height of the simulator, H_s	91.13 in./2.315 m
Diameter of the outer wall of the duct, R_o	148.16 in./3.763 m
Diameter of the inner wall of the duct, R_i	131.10 in./3.330 m
Diameter of the inner cylinder, R_c	49.25 in./1.251 m
Height of the inner cylinder, H_i	51.90 in./1.318 m
Thickness of the honeycomb section, d_h	13.90 in./0.353 m
Distance between the chamber and the floor, d_g	12.40 in./0.315 m
Length of the vane, L_v	29.42 in./0.747 m
Height of the vane, H_v	8.03 in./0.204 m
Thickness of the vane, T_v	0.0625 in./1.588 mm
Vane setting angle (from radial direction)	30°

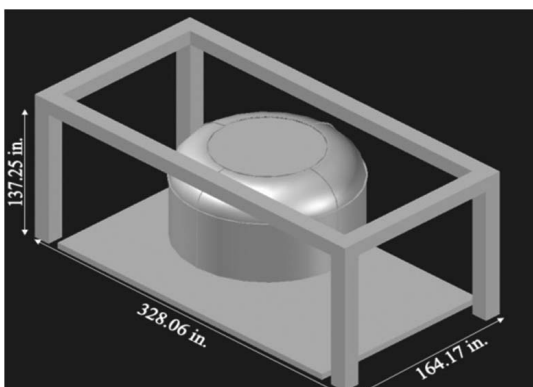


Figure 6. The overview of the entire tornado simulator facility

3 CFD MODELING OF THE TORNADO SIMULATOR

3.1 CAD model and mesh

For each tornado simulator, a 3D CAD model is created in the solids modeling package, SOLIDWORKS. The 3D CAD model is then exported into the meshing software package, POINTWISE, to generate a high-quality mesh. A hybrid mesh strategy is adopted with tetrahedral cells in the chamber and hexahedral cells in the “near-ground domain” (the computational domain between the bottom of the chambers and the ground plane). The total number of cells of this mesh is approximately 5.5 million. Because the geometric features of the computational domain span a large size range, from 0.0625 in. (thickness of the vanes) to 49.25 in. (diameter of the inner cylinder), the mesh has a transition from very fine in the vane region to coarser away from it. A zoomed-in view of the vane region on the top of the simulator is shown in Figure 7. Furthermore, since the primary objective

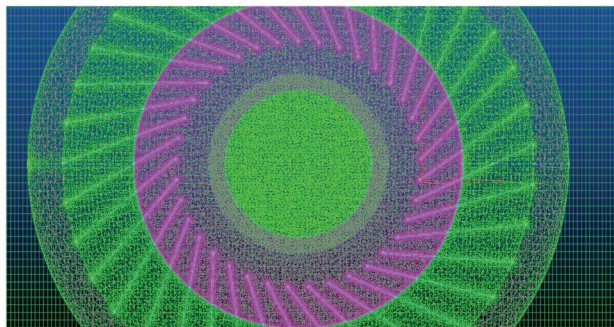


Figure 7. Zoomed-in view of mesh in the vane region

of the simulation is to capture the flow near the floor, the mesh is finer near the floor than that at higher elevations.

3.2 Modeling of the fan and honeycomb section

In this study, the fan is modeled using the fan boundary condition in FLUENT ([ANSYS FLUENT n.d.](#)). To be specific, the fan is treated as an interface, across which a static pressure jump is applied. In the present simulations, a pressure jump $\Delta P = 373\text{Pa}$ at $\text{RPM} = 1770$ is applied, which is taken from the fan performance data sheet provided by the manufacturer. The honeycomb section is modeled using the porous media model in FLUENT. The empirical model of turbulent flow passing through a perforated plate is used to determine the resistant factor ([ANSYS FLUENT n.d.](#)). And because of large Reynolds number ($\text{Re} \approx 5.15 \times 10^6$) of the highly turbulent flow, only the inertial loss term is included in the porous media model. Here, the Reynolds number is defined as $\text{Re} = \rho U R_c / \mu$, where, U is the magnitude of the maximum tangential velocity, which is about 10 m/s in this case; R_c is the diameter of the outer chamber, which is 3.763 m; μ is the dynamic viscosity of the air, which is $1.789 \times 10^{-5} \text{ kg/m-s}$ and ρ is the density of the air, which is 1.225 kg/m^3 . Therefore, the Reynolds number of this system is approximately $\text{Re} = 2.6 \times 10^6$.

3.3 Initial and boundary conditions

The tornado simulator is designed as a flow generator with the air circulating inside, driven by the fan. Therefore, no inflow and outflow boundary conditions are applied to this numerical model. The vanes, inner cylinder, duct walls, and floor are all setup as no-slip boundary conditions (no-slip walls), which indicates zero velocity at the walls. The side wall of the “near-ground domain” is setup as a wall with zero shear stress, which indicates a zero velocity gradient there. The fan is treated as an interface across which a constant static pressure drop is applied. The fan, therefore, drives the flow. Initially, the velocity is zero everywhere inside the simulator.

3.4 Simulation setup

Transient, incompressible, three-dimensional CFD simulation is conducted in this work using the commercial software, ANSYS FLUENT. Since tornado-like vortices are highly turbulent flow, an appropriate turbulence model is required to accurately capture the flow field. Large-eddy-simulation (LES), $k-\epsilon$, and $k-\omega$ are the most popular turbulent models in simulating tornado-like flow. In this study, since the main objective of this study is to develop a numerical model of the laboratory tornado simulator and to optimize its design using CFD simulations, $k-\epsilon$ model with a scalable wall function is adopted due to its low computational cost. Standard sea-level atmospheric conditions (pressure = $101,325 \text{ N/m}^2$, temperature 298 K , dynamic viscosity = $1.789 \times 10^{-5} \text{ kg/m-s}$) are used in the simulations. The finite volume-based SIMPLE scheme is used for the numerical solution, with $\Delta t = 0.01\text{s}$ as the time-step size and 200 time steps as the simulation duration, at which time instant the system reaches steady state conditions.

The height of the first layer of the cell adjacent to the ground plane is 0.0105 m , which leads to a $y+$ value of around 500 (the freestream velocity is selected to be 20 m/s , and the reference length is 3.763 m , which is the diameter of the outer wall of the duct). The mesh sensitive study has been conducted on the curved chamber model, with three different mesh sizes inside the “near-ground domain”. To be more specific, the height of the “near-ground domain” ($dg = 0.315 \text{ m}$) is uniformly divided into 20, 30, and 40 divisions, which leads to the height of a cell as 0.0158 m , 0.0105 m and 0.00788 m , respectively. The obtained results show that the difference in the maximum tangential velocity and core radius among the three cases with different sizes of meshes is below 5%.

3.5 Discussion on determination of $y+$ value

In CFD simulation, the value of $y+$ is used to measure the coarseness/fineness of the cells near walls. The value of $y+$ should be lower enough to ensure the proper simulation of the wind flow near the walls. However, a lower $y+$ is achieved at the cost of a higher computational cost. A $y+$ value less than 1 is recommended for the simulation of viscous sublayer, especially when skin friction or heat transfer is involved (Frank 2005), which is not the case in our simulation. In our simulation, if the desired $y+$ value is set as 1, the height of the first layer of cells near the wall will be around 0.02 mm , which will be prohibitively expensive in terms of computation amount. Thus, to balance the simulation resolution/accuracy and the computational cost, the value of $y+$ is chosen as 500 in our simulation. In addition, the value of $y+$ mainly affects the wind flow simulation near walls. The main purpose of this study is to compare the wind flow generated in the chambers with different shapes, i.e., the flow of interest is mainly in the region in the middle of the chamber. Since no civil structures are included in the computational domain and thus no walls are included in the region. Therefore, in this study, with the $k-\epsilon$ turbulence modeling and a scalable wall function, the $y+$ value of 500 is reasonable. In our future work, when a civil structure is included in the computational domain, LES model will be used to simulate turbulence and a lower $y+$ value (finer mesh) will be applied to

ensure that the flow near the walls (structural surface) and away from the walls (wind field) are both simulated properly.

4 COMPARISON ON GENERATED TORNADIC WIND FIELD

4.1 General flow field

When the tornado simulator is not translating, a stationary tornadic wind flow can be generated. This section presents the overall flow field inside the simulator. Figure 8 shows the overall streamlines for all three cases. In each figure, swirling flow is successfully produced. That is, the air is first driven by the fan to be sucked up and then gains the angular momentum by passing through the vanes; then flows back to the inner cylinder, where it is straightened by going through the honeycomb section, to complete a cycle of air circulation.

From Figure 8a, when a multi-sided chamber is used, although a larger maximum velocity magnitude is achieved on the top of the simulator (23 m/s compared to 18.1 m/s and 19.8 m/s), the generated flow is more chaotic. On the contrast, the tornado simulator with a curved chamber produces a more stable flow, as shown in Figures 8b and 8c, which verifies that the application of a curved chamber can help achieve the production of more stable tornadic wind flow.

By comparing the three figures in Figure 8, the big difference in velocity is mainly located at the top of the simulator. At near-ground region, the difference in tangential velocity is small (so is the difference in the resultant velocity), which can be seen in Figure 11. The difference in velocity at the top of the simulator is caused by the different shape of the chamber. For the multi-sided chamber and curved chamber with the cone (see Figure 8a and 8c), the horizontal sliced surface area at the top is smaller than that in the simulator with the curved chamber [see Figure 8(b)]. Accordingly, based on the conservation of mass, a larger velocity magnitude at the top of the simulator should be found for the cases with the multi-sided chamber and the curved chamber with the cone.

Figure 9 shows the pressure contours on the radial-vertical plane at $y=0$ for the three simulated cases. It can be observed that there are two regions inside the domain associated with significant pressure change. One is the fan interface, across which a static pressure rise from the fan inlet to the fan outlet is applied, and the other one is a pressure drop across the honeycomb section, which is modeled as a porous medium. Similar pressure distributions can be found in the domain under the honeycomb section among these three cases. That is, if looking at the area below the honeycomb section, a pressure drop can be observed in the middle where the vortex core is existing compared to the pressure far away from the core in all three cases. This pressure drop in the radial direction verifies that a vortex core is generated in the middle under the honeycomb section.

Figure 10 presents the velocity vectors in the three cases on the radial-vertical plane at $y=0$. The velocity presented here is the resultant velocity. Apparent

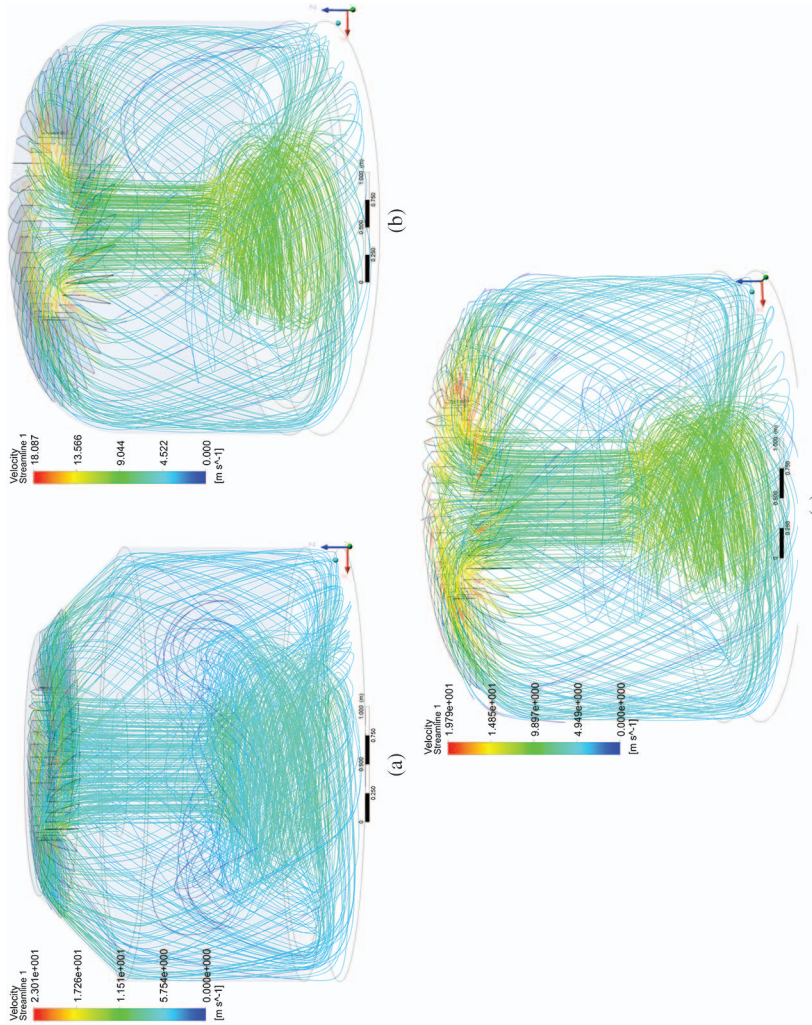


Figure 8. Streamlines inside the simulators with different chamber shapes: (a) multi-sided chamber (same chamber shape as ISU), (b) curved chamber, and (c) curved chamber with cone at the top

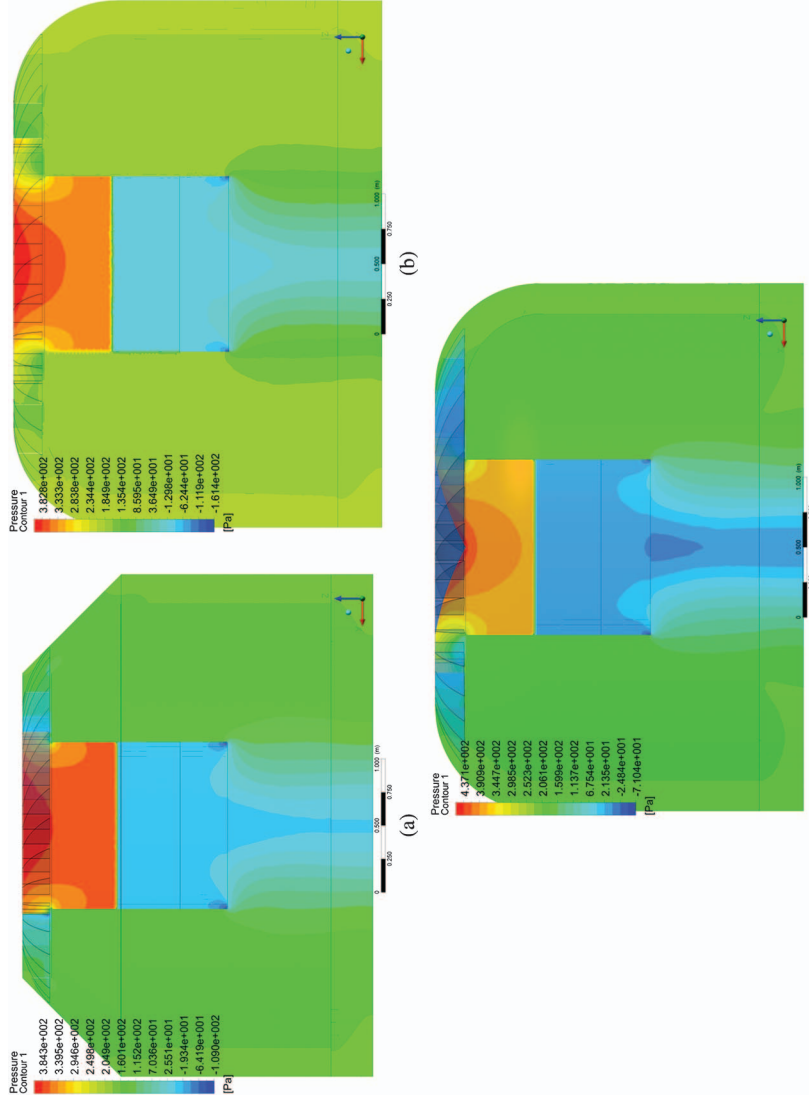


Figure 9. Pressure contours on the radial-vertical plane at $y=0$: (a) multi-sided chamber (same chamber shape as ISU), (b) curved chamber, and (c) curved chamber with cone at the top

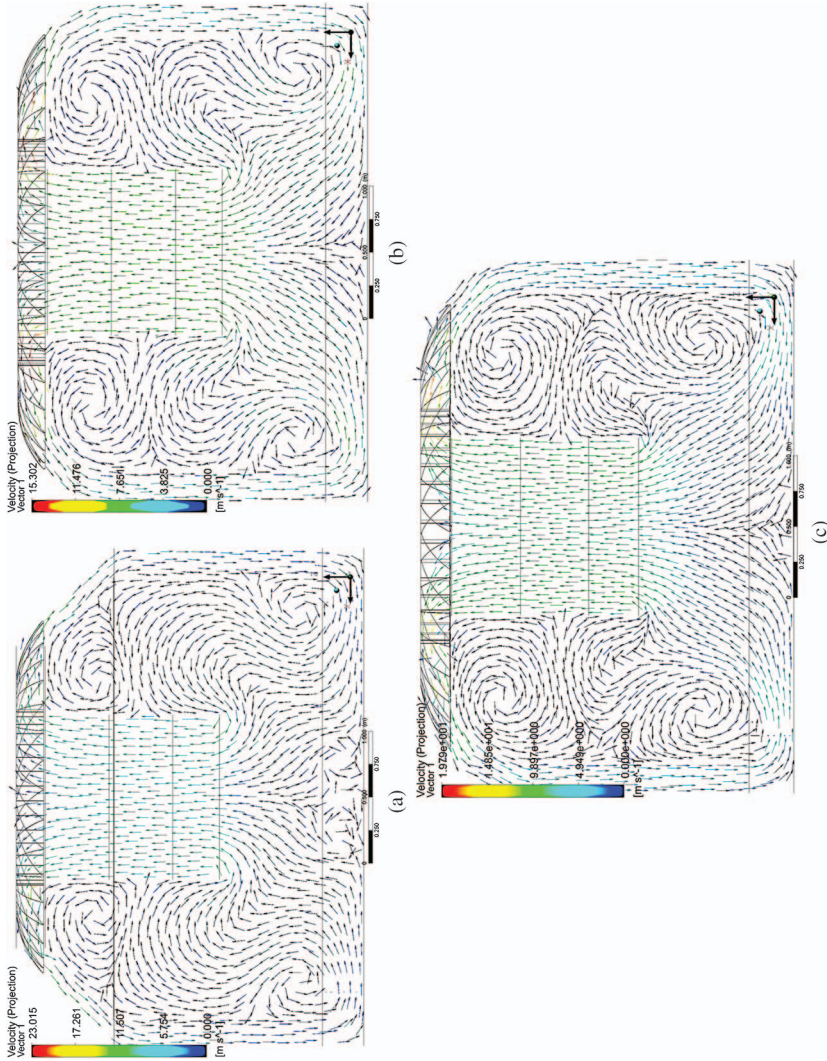


Figure 10. Velocity vectors on the radial-vertical plane at $y=0$. Color of arrows represents the projected velocity magnitude in that plane: (a) multi-sided chamber (same chamber shape as ISU), (b) curved chamber, and (c) curved chamber with cone at the top

difference among the three cases can be found. For the tornado simulator with a curved chamber, the near-floor flow is directly going up from the floor into the inner cylinder, as shown in Figures 10b and 10c. However, for the tornado simulator with multi-sided chamber, some vortices are generated near the floor, as shown in Figure 10a, which is consistent with the chaotic streamlines observed in Figure 8a. Therefore, the curved chamber will facilitate the generation of stable tornadic wind flow.

4.2 Near-floor wind field

One purpose of conducting testing in a laboratory tornado simulator is to controllably reproduce the near-ground tornadic wind field, since the wind flow in this region has the most impact on civil structures in a tornado event. Figure 11 presents the tangential velocity contours and velocity vectors from the bottom of the inner cylinder to the ground. It can be observed that the air flows to the center from outside and then elevates back to the honeycomb section in all three cases. However, more turbulence (represented by the irregularity of flow patterns near the vortex core) is found near the ground in the tornado simulator with a multi-sided chamber, as shown in Figure 11a. For the other two cases, as shown in Figures 11b and 11c, similar flow patterns can be found. However, the air flow is more stable. By comparing Figures 11b and 11c, the magnitude of the maximum tangential velocity in Figure 11c is slightly greater than that observed in Figure 11b (10.33 m/s compared to 9.52 m/s). This can be explained by the Mass Conservation. Between the two models associated with Figures 11b and 11c, the horizontal sliced surface area at the top of the curved chamber is greater than that of the curved chamber with a cone at the top, leading to a smaller velocity in the case of the curved chamber (associated with Figure 11b). From both the general and near-ground wind fields, it can be concluded that that the tornado simulator with a curved chamber generates a more stable flow, which better reproduces the tornado-like vortices to simulate the tornadic wind field around civil structures. By comparing Figure 11b and 11c, although the tornado simulator with a curved chamber and a cone at the top generates a slightly higher tangential velocity near the floor, due to the complication of building the cone at the top, the tornado simulator with a curved chamber (see Figure 4b) is identified as the optimal design of this type of tornado simulator.

5 CONCLUSIONS AND FUTURE WORK

This study provides a comprehensive numerical model of a type of laboratory tornado simulator to study the induced tornadic wind field. All the mechanical components in the physical tornado simulator, such as the chamber/duct, fan, honeycomb section, and the guide vanes, are simulated in this model. This way, less numbers of assumptions need to be made in our numerical simulation. Therefore, a

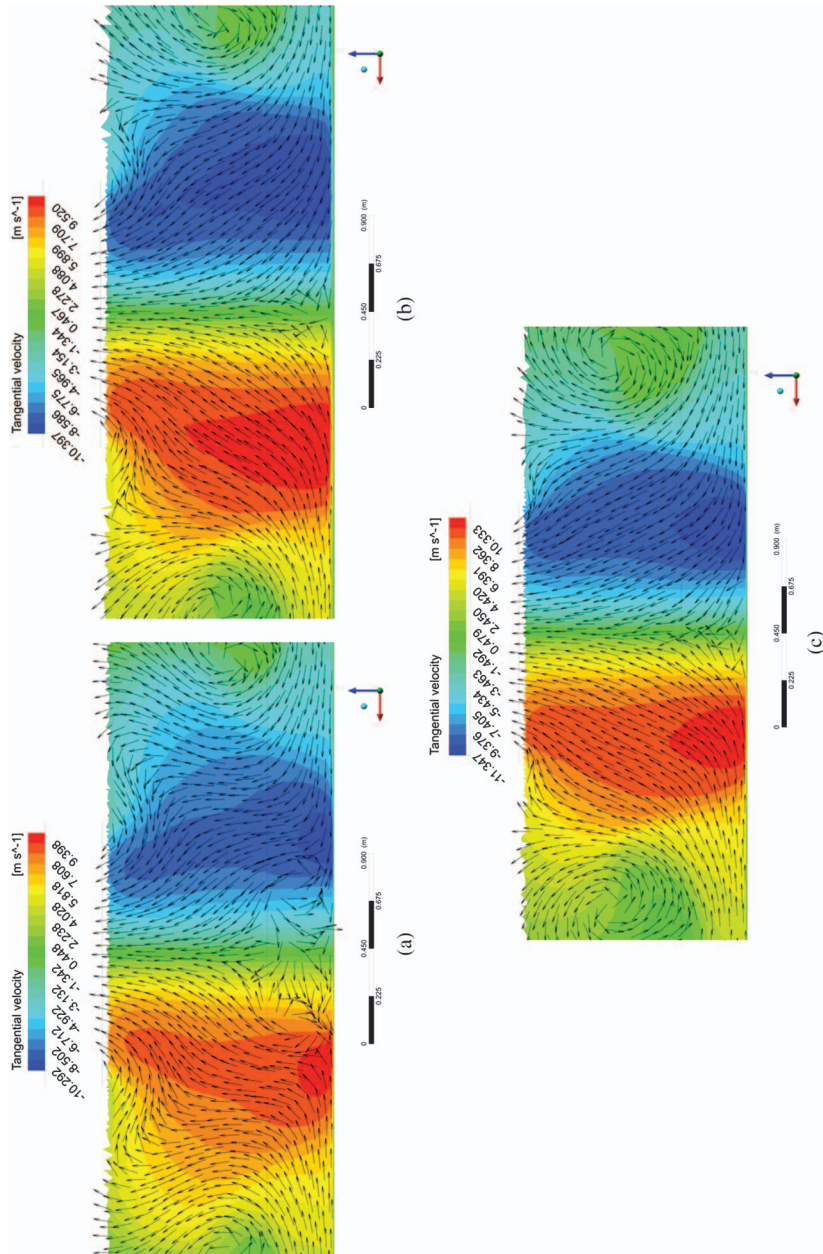


Figure 11. Tangential velocity contours and velocity vector on a radial-vertical plane $y = 0$ between the bottom of inner cylinder and the floor (The vectors are normalized and they do not indicate the magnitude of the velocity): (a) multi-sided chamber (same chamber shape as ISU), (b) curved chamber, and (c) curved chamber with cone at the top

self-circulating air flow is generated inside the simulator without applying any inflow/outflow boundaries. To achieve a better performance and to identify the best configuration of the laboratory tornado simulator, three tornado simulators with different shapes of chambers have been simulated. Both the overall wind field inside the chamber and the near-floor wind field are extracted and compared among the three tornado simulators. The obtained results verify that tornado-like vortices are produced by self-circulating the air driven by the fan in all three tornado simulators. The obtained results also demonstrate that the tornado simulator with a curved chamber produces more stable tornado-like vortices, exhibiting better performance. By using the numerical model developed here, in-depth insights into this type of laboratory-scale tornado simulator can be achieved.

Although numerical simulations conducted here offer a set of rich and high-resolution data of simulated tornadic wind fields at a low cost, experiments in a laboratory tornado simulator will be conducted to validate the obtained numerical simulation results. It should be noted that it is challenging to validate the CFD model of the tornadic wind field using experiments due to the following two reasons. First, the laboratory tornado simulator itself may not simulate the tornado-like vortex well. Second, the laboratory tornado simulators built by different research groups may follow different mechanism to generate the tornado-like vortex and it is difficult to across-compare them. To address this, the present authors are building a laboratory tornado simulator in their institute and will validate their laboratory tornado simulator by radar-measured data to ensure the high-quality simulation in the physical tornado simulator.

Besides the experimental validation, in the future, parametric studies by changing the turbulence model, angle of guide vanes, porous medium model constants of the honeycomb section, translating speed and surface roughness will be conducted to better understand the working mechanism of this type of tornado simulator.

ACKNOWLEDGMENTS

The authors greatly appreciate the financial support from National Science Foundation, the Hazard Mitigation and Structural Engineering program, through the project, “Damage and Instability Detection of Civil Large-scale Space Structures under Operational and Multi-hazard Environments” (Award No.: 1455709).

References

- [1] NOAA (National Severe Storms Laboratory of National Oceanic and Atmospheric Administration). n.d. <http://www.nssl.noaa.gov/education/swrx101/tornadoes/>.
- [2] Grazulis, T. P., and T. P. Grazulis. 1993. *Significant tornadoes, 1680–1991*. St. Johnsbury, VT: Environmental Films.
- [3] Changnon, S. A. 2009. “Tornado losses in the United States.” *Nat. Hazard. Rev.* **10** (4): 145–150.

- [4] McCarthy, D., and J. Schaefer. 2004. "Tornado trends over the past 30 years." In *14th Conf. on Applied Climatology*. Seattle: American Meteor Society.
- [5] Storm Prediction Center. 2014. "Storm prediction center WCM page." Accessed March 20, 2015. www.spc.noaa.gov/wcm.
- [6] Simmons, K. M., D. Sutter, and R. Pielke. 2013. "Normalized tornado damage in the United States: 1950–2011." *Environ. Hazard.* **12** (2): 132–147.
- [7] Lott, N., A. Smith, T. Houston, K. Shein, and J. Crouch. 2012. "Billion dollar US weather/climate disasters, 1980–2011." National Climatic Data Center. <http://www.ncdc.noaa.gov/oa/reports/billionz.html>.
- [8] FEMA. 2012. "Spring 2011 tornadoes: April 25–28 and May 22, Building performance observations, recommendations, and technical guidance." Mitigation Assessment Team Report, FEMA P-908, 512. <http://www.fema.gov/library/viewRecord.do?>
- [9] <https://en.wikipedia.org/wiki/Tornado>.
- [10] Chang, C. C. 1966. *First real man made tornado is generated in laboratory cage by space scientists at the catholic University of America*. News item of PI of CUA.
- [11] Ward, N. B. 1972. "The exploration of certain features of tornado dynamics using a laboratory model." *J. Atmos. Sci.* **29** (6): 1194–1204.
- [12] Church, C., J. T. Snow, G. L. Baker, and E. M. Agee. 1979. "Characteristics of tornado-like vortices as a function of swirl ratio: A laboratory investigation." *J. Atmos. Sci.* **36** (9): 1755–1776.
- [13] Leslie, F. W. 1977. "Surface roughness effects on suction vortex formation: A laboratory simulation." *J. Atmos. Sci.* **34** (7): 1022–1027.
- [14] Jischke, M. C., and B. D. Light. 1983. "Laboratory simulation of tornadic wind loads on a rectangular model structure." *J. Wind Eng. Ind. Aerodyn.* **13** (1): 371–382.
- [15] Diamond, C. J., and E. M. Wilkins. 1984. "Translation effects on simulated tornadoes." *J. Atmos. Sci.* **41** (17): 2574–2580.
- [16] Haan, F. L., P. P. Sarkar, and W. A. Gallus. 2008. "Design, construction and performance of a large tornado simulator for wind engineering applications." *Eng. Struct.* **30** (4): 1146–1159.
- [17] Mishra, A. R., D. L. James, and C. W. Letchford. 2008. "Physical simulation of a single-celled tornado-like vortex. Part A: Flow field characterization." *J. Wind Eng. Ind. Aerodyn.* **96** (8): 1243–1257.
- [18] Refan, M. 1923. "Physical simulation of tornado-like vortices." Ph.D. dissertation, Univ. of Western Ontario.
- [19] Hu, H., Z. Yang, P. Sarkar, and F. Haan. 2011. "Characterization of the wind loads and flow fields around a gable-roof building model in tornado-like winds." *Exp. Fluids* **51** (3): 835–851.
- [20] Haan, F. L., Jr., V. K. Balaramudu, and P. P. Sarkar. 2009. "Tornado-induced wind loads on a low-rise building." *J. Struct. Eng. Eng.* **136** (1): 106–116.
- [21] Chang, C. C. 1971. "Tornado wind effects on buildings and structures with laboratory simulation." In *Proc., Third Int. Conf. on Wind Effects on Buildings and Structures*, 231–240.
- [22] Bienkiewicz, B., and P. Duhdia. 1993. "Physical modeling of tornado-like flow and tornado effects on building loading." In *Proc., 7th US National Conf. on Wind Engineering*, 95–106.
- [23] Fouts, J. L., D. L. James, and C. W. Letchford. 2003. "Pressure distribution on a cubical model in tornado-like flow." In Vol. 10 of *11th Int. Conf. on Wind Engineering*.

- [24] Mishra, A. R., D. L. James, and C. W. Letchford. 2008. "Physical simulation of a single-celled tornado-like vortex. Part B: Wind loading on a cubical model." *J. Wind Eng. Ind. Aerodyn.* **96** (8): 1258–1273.
- [25] Sengupta, A., F. L. Haan, P. P. Sarkar, and V. Balaramudu. 2008. "Transient loads on buildings in microburst and tornado winds." *J. Wind Eng. Ind. Aerodyn.* **96** (10): 2173–2187.
- [26] Natarajan, D., and H. Hangan. 2012. "Large eddy simulations of translation and surface roughness effects on tornado-like vortices." *J. Wind Eng. Ind. Aerodyn.* **104**: 577–584.
- [27] Rajasekharan, S. G., M. Matsui, and Y. Tamura. 2013. "Characteristics of internal pressures and net local roof wind forces on a building exposed to a tornado-like vortex." *J. Wind Eng. Ind. Aerodyn.* **112**: 52–57.
- [28] Sabareesh, G. R., M. Matsui, and Y. Tamura. 2013. "Ground roughness effects on internal pressure characteristics for buildings exposed to tornado-like flow." *J. Wind Eng. Ind. Aerodyn.* **122**: 113–117.
- [29] Kuai, L., F. L. Haan Jr., W. A. Gallus Jr., and P. P. Sarkar. 2008. "CFD simulations of the flow field of a laboratory-simulated tornado for parameter sensitivity studies and comparison with field measurements." *Wind Struct.* **11** (2): 75–96.
- [30] Natarajan, D. 2011. "Numerical simulation of tornado-like vortices." Ph.D. dissertation, Univ. of Western Ontario.
- [31] Ishihara, T., S. Oh, and Y. Tokuyama. 2011. "Numerical study on flow fields of tornado-like vortices using the LES turbulence model." *J. Wind Eng. Ind. Aerodyn.* **99** (4): 239–248.
- [32] Liu, Z., and T. Ishiharab. 2012. "Effects of the swirl ratio on the turbulent flow fields of tornado-like vortices by using LES turbulent model." In *Proc., 7th Int. Colloquium on Bluff Body Aerodynamics and Applications*.
- [33] Lewellen, W. S., and D. C. Lewellen. 1997. "Large-Eddy simulation of a Tornado's Interaction with the surface." *J. Atmos. Sci.* **54** (5): 581–605.
- [34] Selvan, R. P., and P. C. Millett. 2003. "Computer modeling of Tornado forces on a cubic building using large Eddy simulation." *J. Arkansas Acad. Sci.* **57**: 140–146.
- [35] ANSYS FLUENT. n.d. *FLUENT fan boundary user guide*. Canonsburg, PA: ANSYS FLUENT.
- [36] ANSYS FLUENT. n.d. *FLUENT porous media user guide*. Canonsburg, PA: ANSYS FLUENT.
- [37] Frank, M. 2005. *White's viscous fluid flow*. 3rd ed. Boston: McGraw-Hill Education.

This page intentionally left blank

CHAPTER 9

Computational versus Wind Tunnel Simulation of Atmospheric Boundary Layer Flow for Structural Engineering Applications

DongHun Yeo, M.ASCE*

Liang Shi*

Abstract: Atmospheric Boundary Layer (ABL) flow simulations have been performed using Large Eddy Simulation (LES) to assess the suitability of the simulated flow for structural wind engineering applications. The governing equations of straight ABL flow for structural engineering purposes were formulated based on state-of-the-art meteorological studies. The balance of the horizontal pressure gradient force and the ground friction was used in the Computational Fluid Dynamics (CFD) solver to achieve dynamic equilibrium throughout the ABL flow. In the simulation using the precursor method, turbulent ABL flow was developed naturally to achieve horizontally homogenous ABL flow. To reduce computational resource requirements this study employed a model scale approach, similar to the approach used in wind tunnel simulations.

Based on the assessment of the simulated results via comparisons with measurements reported in the literature and values recommended in the ASCE 49-12 Standard for wind tunnel testing, the quality of the simulations for structural engineering applications was found to be comparable with the quality of their wind tunnel counterparts. The results also identified issues, mainly due to grid resolution and inaccurate SGS modeling, that need to be addressed by future research.

Keywords: Atmospheric boundary layer (ABL); Large eddy simulation (LES); Model scale simulation; Standards; Structural engineering; Turbulence; Wind tunnel testing.

*Engineering Laboratory, National Institute of Standards and Technology, Gaithersburg, MD 20899, USA (corresponding author), Tel: 1-301-975-8103, Fax: 1-301-869-6275, email: donghun.yeo@nist.gov

1 INTRODUCTION

Wind loads on structures can be determined by using analytical, experimental, and/or numerical simulation approaches. The analytical approach typically specified in codes and standards is widely used in engineering practice. For special structures, however, ad-hoc wind tunnel tests are generally used. Given the cost, turnover times, and reliability issues inherent in wind tunnel testing at the typically small scales required in practice on the one hand, and the rapid development of Computational Fluid Dynamics (CFD) techniques on the other, CFD is increasingly being regarded as a potentially viable simulation option for structural engineering applications. Structural engineers have expressed strong interest in the possibility of using this option, at least for preliminary designs. The UK Design Manual for Roads and Bridges (BD 49/01, HE 2001), the Eurocode (prEN 1991-1-4, CEN 2005), and the Architectural Institute of Japan guidebook (AIJ 2017) allow the use of proven CFD procedures to provide additional design guidance.

With a view to advancing the prospects of using CFD techniques for structural engineering purposes, the National Institute of Standards and Technology (NIST) is engaged in an effort aimed to develop CFD algorithms as a substitute for wind tunnel testing. In this paper we report results achieved within the framework of this effort in the Large Eddy Simulation (LES) of Atmospheric Boundary Layer (ABL) flow. For the simulations to be compatible with currently available computational resources, they need to be performed at scales comparable to those used in wind tunnel simulations. Since the latter are achieved by using empirical devices such as roughness elements, spires, and castellated walls, it was hypothesized that CFD simulations would perform at least as well as their wind tunnel counterparts.

Three approaches have been used to generate neutrally stratified ABL flows in LES studies for wind/structural engineering applications: synthetic turbulence approach, recycling and rescaling approach, and precursor database approach. For reviews of these approaches see [Tabor and Baba-Ahmadi \(2010\)](#), [Wu \(2017\)](#), and [Vasaturo et al. \(2018\)](#).

The synthetic turbulence approach generates at the inflow boundary artificially synthesized wind fluctuations based on target flow characteristics and a predefined mean wind velocity profile ([Hémon and Santi 2007](#), [Huang et al. 2010](#), [Kondo et al. 1997](#), [Xie and Castro 2008](#)). This method is computationally efficient and makes it easy to deal with any target characteristics. However, synthetic turbulence structures are less accurate and dissipate faster within the computational domain than naturally developed ones.

The recycling and rescaling method usually prescribes a time-averaged wind velocity profile on the inflow boundary, rescales wind fluctuations collected on a downstream plane, and reintroduces them to the inflow boundary ([Kataoka and Mizuno 2002](#), [Nozawa and Tamura 2001](#)). This method has been used for spatially

evolving boundary-layer flows with a zero-pressure gradient, thus reproducing the generation of boundary layer flow in conventional wind tunnel testing facilities, as opposed to the generation of neutrally stratified, horizontally homogeneous ABL flow that, owing to the action of a horizontal pressure gradient, maintains a constant boundary layer height.

The precursor database method generates turbulence in the computational domain by embedding the flow driving mechanism into the cyclic domain without rescaling to achieve fully developed turbulent equilibrium flow (Berthaut-Gerentès et al. 2014, Churchfield et al. 2010; Munters et al. 2016). This precursor method produces a database in auxiliary simulations or in the upstream domain of the main simulation. It entails additional computational costs, but simulates turbulence of the equilibrium ABL flow more realistically than the synthetic turbulence generating methods.

Since straight ABL flow is driven by the balance of horizontal pressure gradient, Coriolis, and ground friction forces, the underlying dynamic equilibrium of the ABL flow can be more accurately achieved by “balanced-force-driven” simulations (Cai et al. 2014, Porté-Agel et al. 2000), rather than by the widely used “boundary-driven” simulations (Aboshosha et al. 2015, Blocken et al. 2007, Huang et al. 2010, Kataoka and Mizuno 2002, Richards and Hoxey 1993, Tominaga 2015).

The simulations considered in this study employed the precursor database method as applied to a neutral balance-force driven ABL. The aim of this paper is to assess the quality of the ABL flow simulated by this technique and compare it to quality of ABL-like flows achieved by conventional boundary-layer wind tunnels techniques as described in standard provisions on the wind tunnel testing procedure.

In this paper, we first describe the numerical simulation of the governing equations of ABL flow, including simulation details. We then present simulation results on the ABL flow characteristics of interest of structural engineering and compare those results with reference data from the literature and standard provisions. ABL simulation features are then discussed, and a flow assessment is presented. The paper ends with concluding remarks.

2 NUMERICAL SIMULATION

2.1 Governing equations of ABL flow

Governing equations for incompressible, neutrally stratified ABL flow are the continuity equation and the momentum equations for Newtonian fluid (i.e., fluid with constant density ρ and kinematic viscosity ν) (e.g., Stull 1988):

$$\nabla \cdot \mathbf{U} = 0 \quad (1)$$

$$\frac{\partial U}{\partial t} + \mathbf{U} \cdot \nabla U + \frac{1}{\rho} \frac{\partial p}{\partial x} - \nu \nabla^2 U + S_x - f V + f^* W \mp V \frac{|\mathbf{U}|}{r} = 0 \quad (2)$$

$$\frac{\partial V}{\partial t} + \mathbf{U} \cdot \nabla V + \frac{1}{\rho} \frac{\partial p}{\partial y} - \nu \nabla^2 V + S_y + f U \pm U \frac{|\mathbf{U}|}{r} = 0 \quad (3)$$

$$\frac{\partial W}{\partial t} + \mathbf{U} \cdot \nabla W + \frac{1}{\rho} \frac{\partial p}{\partial z} - \nu \nabla^2 W + S_z - f^* U = 0 \quad (4)$$

I II III IV V VI VII VIII

where the velocity vector \mathbf{U} consist of two horizontal velocity components of (U, V) in the (streamwise) x and (lateral) y directions and one vertical component of (W) in the (upward positive) z direction. Term I is the temporal acceleration of the wind flow, Term II expresses the nonlinear interaction of convective accelerations of the flow, Term III expresses the pressure forces induced by the flow (p is the pressure), Term IV expresses the effects of molecular viscosity, Term V represents the source terms (S_x and S_y are the external horizontal pressure gradient forces in the x and y directions; S_z is the body force due to gravity so that $S_z = -g$, where g is the gravity acceleration, Terms VI and VII represent the horizontal and vertical Coriolis forces due to the Earth's rotation (f and f^* are the horizontal and vertical Coriolis force parameters, respectively), and Term VIII denotes the centrifugal force in non-straight winds (r is the radius of curvature of air trajectory).

According to recent studies (Hess 2004, Zilitinkevich 2012, Zilitinkevich et al. 2007, Zilitinkevich and Esau 2002) summarized for structural engineering purposes in Simiu et al. (2016), the contribution of the wind velocity component normal to the surface stress to the resultant mean wind speed is negligible at mid-latitudes. For example, at elevations of the order of, say, 1 km or less, the veering angle is of the order of 5 degrees or less. Thus, Terms VI and VII are not considered in this study. Term VIII is not taken into account because this study only considers the case of non-rotating flows.

This study also assumes that (i) the wind velocity is parallel to the x direction, (ii) the air density is constant throughout the flow, and (iii) the flow is barotropic, that is, the horizontal pressure gradient force is independent of height. Thus, the steady state equilibrium of the fully developed ABL flow can be reached by the external horizontal pressure gradient force (S_x) as a driving force and the friction force on the ground as a retarding force. Thus, the wall-shear stress at the ground is

$$\tau_w = - \frac{\partial p_h}{\partial x} H \quad (5)$$

where H is the height of the computational domain and $\partial p_h / \partial x$ is the external horizontal pressure gradient. Since $\tau_w = \rho u_*^2$ where u_* is the friction velocity, it

follows from Eq. (5) and the logarithmic law describing the dependence of the mean wind speed with height that:

$$\begin{aligned}\frac{\partial p_h}{\partial x} &= -\frac{\rho}{H} u_*^2 \\ &= -\frac{\rho}{H} \left[\frac{\kappa U(z_{\text{ref}})}{\ln(z_{\text{ref}}/z_0)} \right]^2\end{aligned}\quad (6)$$

where $U(z_{\text{ref}})$ is the longitudinal wind velocity at height z_{ref} , z_0 is the surface roughness length, and $\kappa = 0.41$ is the von Kármán constant.

Therefore, Eqs. (2) through Eq. (4) become

$$\frac{\partial U}{\partial t} + \mathbf{U} \cdot \nabla U + \frac{1}{\rho} \frac{\partial p}{\partial x} - \nu \nabla^2 U + \frac{1}{\rho} \frac{\partial p_h}{\partial x} = 0 \quad (7)$$

$$\frac{\partial V}{\partial t} + \mathbf{U} \cdot \nabla V + \frac{1}{\rho} \frac{\partial p}{\partial y} - \nu \nabla^2 V = 0 \quad (8)$$

$$\frac{\partial W}{\partial t} + \mathbf{U} \cdot \nabla W + \frac{1}{\rho} \frac{\partial p}{\partial z} - \nu \nabla^2 W + g = 0. \quad (9)$$

2.2 Large-Eddy Simulation

Through a spatial low-pass filter based on the scale of grid spacing, Eqs. (7) through Eq. (9) can be converted to the filtered equations for LES:

$$\nabla \cdot \tilde{\mathbf{U}} = 0 \quad (10)$$

$$\frac{\partial \tilde{\mathbf{U}}}{\partial t} + \tilde{\mathbf{U}} \cdot \nabla \tilde{\mathbf{U}} + \frac{1}{\rho} \nabla \tilde{P} - \nu \nabla^2 \tilde{\mathbf{U}} + \nabla \cdot \boldsymbol{\tau}^d + \mathbf{F} = 0 \quad (11)$$

where the filtered quantity is denoted by a tilde, P consists of pressure p and the isotropic component of the subgrid-scale (SGS) stress $\boldsymbol{\tau}$, $\boldsymbol{\tau}^d$ is the deviatoric component of the SGS stress, and \mathbf{F} is the external body force [i.e., $-(1/\rho)\partial p_h/\partial x$ in the x direction and $-g$ in the z directions, as shown in Eqs. (7) and (9) respectively]. To close the LES equations, a model for the SGS stress tensor $\boldsymbol{\tau}$ is required, to simulate the energy transfer between resolved motions and SGS modeled motions.

2.3 Simulation details

All the simulations were performed using LES with the one-equation turbulent energy SGS model (Yoshizawa and Horiuti 1985) in OpenFOAM v. 2.4.0 (2015). In this study it was assumed that the pressure gradient and temperature do not vary

with height. The model length scale was 1:1000 as in wind tunnel tests for high-rise buildings (e.g., Tanaka et al. 2013). The terrain exposure was assumed to be open (roughness length $z_0 = 0.03\text{m}$ at full scale, ASCE 2010). The target mean along-wind speed at the top was set to $\bar{U}(H) = 10\text{ m/s}$. The surface friction velocity was calculated from the logarithmic velocity profile $u_* = \kappa \bar{U}(H) / \ln(H/z_0) = 0.394\text{ m/s}$. The wall-shear stress on the ground and the horizontal pressure gradient were determined from the balance of forces [Eqs. (5) and (6)], respectively. The kinematic viscosity of air was assumed to be $\nu = 1.455 \times 10^{-5}\text{ m}^2/\text{s}$.

As shown in Figure 1, the dimensions of the computational domain were $L:W:H = 2:1:1$ where $H = 1\text{ m}$. The grid was uniform ($\Delta/H = 0.01$) in all directions, and the total number of cells was 2×10^6 (200, 100 and 100 cells in the x , y , and z direction, respectively). The non-dimensional time step Δt^* (defined as $\Delta t^* = U(H)\Delta t/H$) was 0.0025, and the total non-dimensional time for analysis was approximately 200.

Periodic boundary conditions were employed in all horizontal directions so that the ABL flow is fully developed regardless of the along-wind dimension of the domain. The slip wall condition was imposed on the top boundary for velocity (i.e., zero normal velocity and zero gradient tangential velocity). The zero-gradient boundary condition was applied to the ground and top boundaries for pressure. The wall-shear model (Schumann 1975) was employed at the center of the first grid above the ground (denoted by subscript $\Delta 1$) in the xz and yz directions to achieve local equilibrium in the near wall-region:

$$\begin{aligned}\tau_{xz,\text{wall}}(x_{\Delta 1}, y_{\Delta 1}, t) &= -\rho u_*^2 \frac{U_{\Delta 1}(x_{\Delta 1}, y_{\Delta 1}, t)}{|\mathbf{U}_{\Delta 1}|} \\ &= -\rho \left[\frac{\kappa |\mathbf{U}_{\Delta 1}|}{\ln(z_{\Delta 1}/z_0)} \right]^2 \frac{U_{\Delta 1}(x_{\Delta 1}, y_{\Delta 1}, t)}{|\mathbf{U}_{\Delta 1}|} \\ \tau_{yz,\text{wall}}(x_{\Delta 1}, y_{\Delta 1}, t) &= -\rho u_*^2 \frac{V_{\Delta 1}(x_{\Delta 1}, y_{\Delta 1}, t)}{|\mathbf{U}_{\Delta 1}|} \\ &= -\rho \left[\frac{\kappa |\mathbf{U}_{\Delta 1}|}{\ln(z_{\Delta 1}/z_0)} \right]^2 \frac{V_{\Delta 1}(x_{\Delta 1}, y_{\Delta 1}, t)}{|\mathbf{U}_{\Delta 1}|} \quad (12)\end{aligned}$$

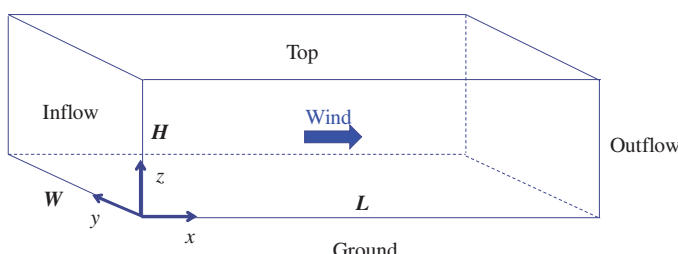


Figure 1. Computational domain of simulation

where $|\mathbf{U}_{\Delta 1}|$ is the spatial average of \mathbf{U} on the xy -plane at the height of $z_{\Delta 1}$. The friction velocity in this model was obtained from the horizontally averaged velocity at each time step by assuming a logarithmic mean profile near the ground (Grötzbach 1987) instead of a fixed value from the momentum balance in the original Schumann model. The initial conditions for the velocity consist not only of the target logarithmic along-wind wind velocity in the domain but also of small perturbations near the ground, which expedite the development of the turbulence in the simulations. Details of this model-scale ABL simulation are provided in Shi and Yeo (2016, 2017).

3 CHARACTERISTICS OF SIMULATED ABL FLOWS

The characteristics of the simulated ABL flow assumed in this study for structural engineering applications are compared with their counterparts in the literature and the ASCE 49-12 Standard for wind tunnel (ASCE 2012).

The simulated ABL wind velocities (U , V , W) were decomposed into mean velocities (\overline{U} , \overline{V} , \overline{W}) and wind velocity fluctuations (u , v , w) along the x -, y -, and z -axes, respectively, corresponding to the streamwise, lateral, and vertical directions:

$$U(z, t) = \overline{U}(z) + u(z, t), V(z, t) = \overline{V}(z) + v(z, t), W(z, t) = \overline{W}(z) + w(z, t). \quad (13)$$

The following subsections examine the characteristics of the mean velocities and fluctuating components of the simulated flow.

3.1 Mean wind speed profile

The ABL flow was assumed to follow the logarithmic law:

$$\overline{U}(z) = \frac{u_*}{\kappa} \ln \left(\frac{z}{z_0} \right). \quad (14)$$

Figure 2 shows the mean streamwise velocity profile of the simulated flow at $x/H = 1$ and $y/H = 0.5$ and the logarithmic law fit to the velocity data. The friction velocity u_* and the reference mean wind speed $\overline{U}(H)$ in Eq. (14) were estimated from the simulation result to be 0.438 m/s and 11.124 m/s, respectively, which are higher than the target values of 0.394 m/s and 10 m/s. The differences could be ascribed to the well-known log-layer mismatch due to the inaccuracy of the SGS model near the ground in the LES simulation (Mason and Thomson 1992). The simulated values are employed hereinafter for normalizing the flow characteristics.

The ASCE 49-12 Standard specifies the wind speed profile of the incoming ABL flow for the use of wind tunnel testing as

$$\overline{U}_{ASCE49}(z) = \overline{U}(z_{ref}) \left(\frac{z}{z_{ref}} \right)^{\bar{\alpha}} \quad (15)$$

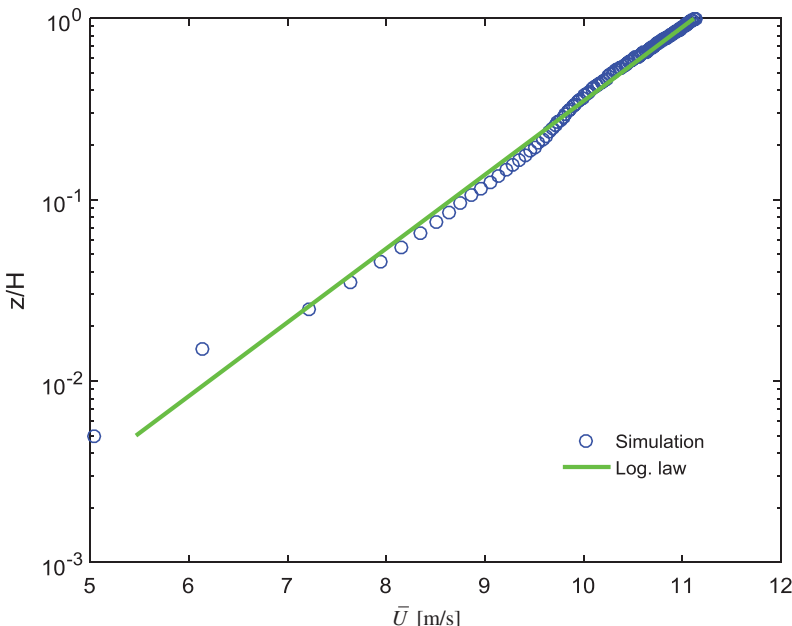


Figure 2. Logarithmic fit to mean streamwise velocity profile

where $\bar{\alpha} = 0.14$ for the open terrain exposure. ASCE 49-12 states that the mean wind speed power law exponent shall be within $\pm 15\%$ of the target value. Because the gradient height provision ($z_g = 274$ m in open terrain exposure) in the standard is not consistent with the state-of-the-art ABL flow description in the meteorological literature (see, e.g., Simiu et al. 2016 for a summary and an application to high-rise building design), the gradient height is not considered in the plot of the wind speed profile.

Figure 3 shows the mean wind speed profile as simulated in this study, the target logarithmic law profile, and the profiles accepted by ASCE 49-12. The simulation results in differences with respect to the logarithmic profile up to 5% near the ground (i.e., $z/H < 0.02$) and less than 2% at the other elevations. Those differences are well within the accepted range considered by the ASCE 49-12 Standard to be acceptable and are lower than those typical of wind tunnel tests (Kozmar 2011, Samali et al. 2004).

3.2 Turbulence intensity

The turbulence intensity at a point with height z is defined as the ratio of the root-mean-square of the velocity fluctuations to the longitudinal mean wind speed at that height:

$$I_u(z) = \frac{\sqrt{u^2(z)}}{\bar{U}(z_{ref})}, \quad I_v(z) = \frac{\sqrt{v^2(z)}}{\bar{U}(z_{ref})}, \quad I_w(z) = \frac{\sqrt{w^2(z)}}{\bar{U}(z_{ref})} \quad (16)$$

where in this study z_{ref} is the ABL height H .

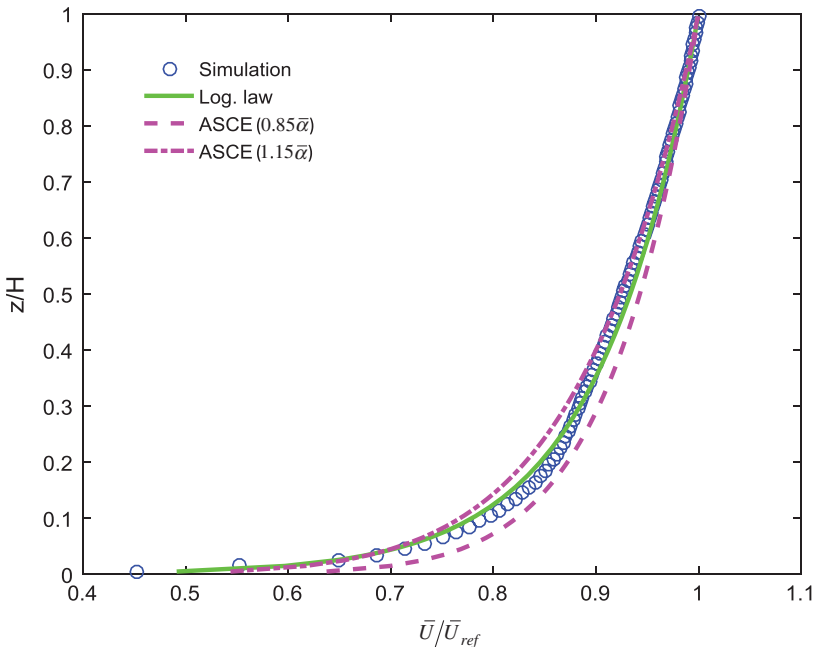


Figure 3. Mean streamwise velocity profiles

Turbulence intensities over open terrain exposure in the Atmospheric Surface Layer (ASL) e.g., $z/H \lesssim 0.1$) are, according to ASCE 49-12

$$I_u(z) = \frac{1}{\ln(z/z_0)}, \quad I_v(z) = \frac{0.8}{\ln(z/z_0)}, \quad I_w(z) = \frac{0.5}{\ln(z/z_0)} \quad (17)$$

The turbulence intensity profiles in the neutral ABL flow suggested by Stull (1988) are

$$\begin{aligned} I_u(z) &= u_* \left[6 \left(1 - \frac{z}{H} \right)^2 + \frac{\overline{u^2}(H)}{u_*^2} \frac{z}{z_H} \right]^{1/2} / U(z) \\ I_v(z) &= u_* \left[3 \left(1 - \frac{z}{H} \right)^2 + \frac{\overline{v^2}(H)}{u_*^2} \frac{z}{z_H} \right]^{1/2} / U(z) \\ I_w(z) &= u_* \left(1 - \frac{z}{H} \right)^{1/4} / U(z). \end{aligned} \quad (18)$$

Figure 4 presents the turbulence intensities determined from Eqs. (17) and (18) and obtained in the simulations. For $0.03 \leq z/H \leq 0.8$, the simulation yields I_u values that deviate from target values by approximately -5% to 10%, I_w values

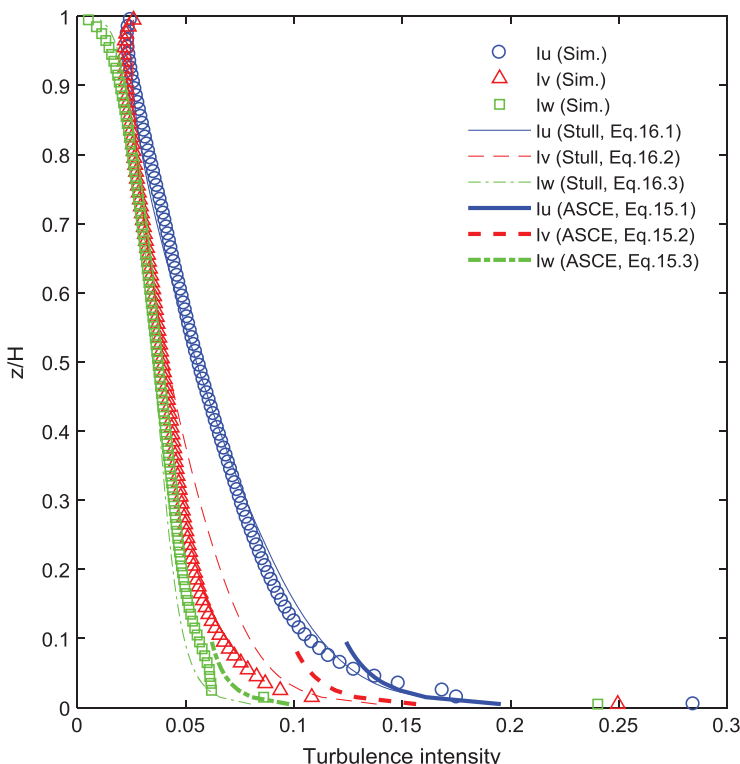


Figure 4. Turbulence intensities

that exceed target values by less than 14%, and I_v values that are smaller than target values by less than 20%, where the target values are given by Eq. (18). The turbulence intensity simulations in the study outperform their counterparts simulated in typical wind tunnel tests (Kozmar 2011, Samali et al. 2004, Tanaka et al. 2013).

The ratios of the three turbulence intensities ($I_v/I_u, I_w/I_u$) in the lower ABL are shown in Figure 5. The ratios from the simulations are 0.62:0.53 for $0.07 < z/H < 0.2$, which are comparable with the ratios of 0.7:0.45 from Stull (Eq. 18), 0.75~0.8:0.5 from ASCE 49-12 (Eq. 17), 0.5~0.6:0.3~0.4 from Counihan (1975), and 0.78~0.82:0.55~0.63 from ESDU 85020 (2001). Note that the ratio I_v/I_u is smaller by 14% than its counterpart suggested by Stull because the turbulence intensity in the lateral direction (I_v) is relatively low in the simulations.

3.3 Wind velocity spectra

The spectral density functions of wind velocity fluctuations are a measure of the contribution of each frequency component of the fluctuations to the variance of the fluctuations. Among several proposed spectral density functions for wind engineering purpose, useful non-dimensional spectra for the longitudinal, lateral,

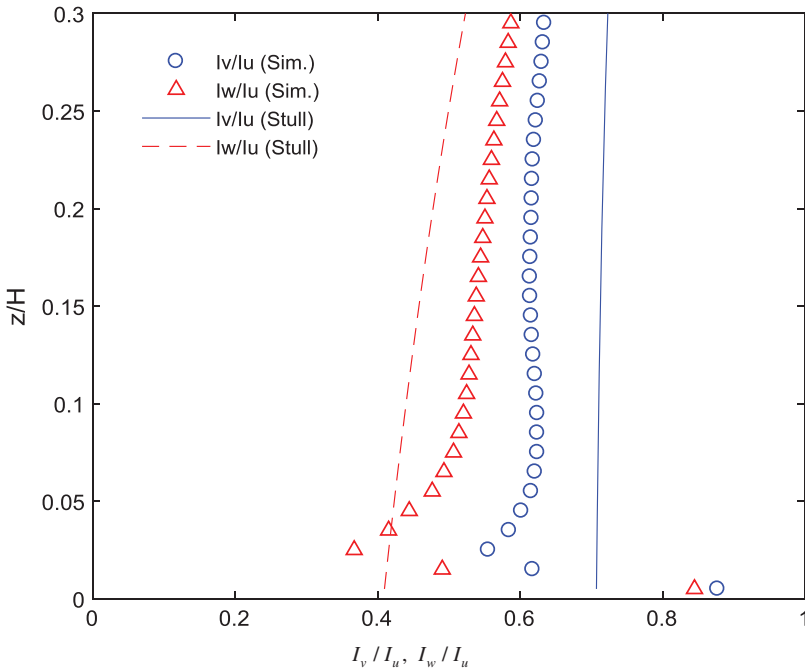


Figure 5. Ratios of turbulence intensities

and vertical turbulence at elevation z are expressed respectively as (Kaimal et al. 1972, Simiu 2011)

$$\frac{nS_u(z,n)}{u_*^2} = \frac{200f}{(1+50f)^{5/3}}, \quad \frac{nS_v(z,n)}{u_*^2} = \frac{15f}{(1+10f)^{5/3}}, \quad \frac{nS_w(z,n)}{u_*^2} = \frac{3.36f}{1+10f^{5/3}} \quad (19)$$

where f is the Monin coordinate defined as $f = nz/\bar{U}(z)$ where n is the frequency of wind velocity fluctuations. Equation (19, Part 1) differs slightly from its Kaimal et al. (1972) counterpart in that it corresponds to a mean square value of the turbulence fluctuations equal to $6u_*^2$, a value widely accepted for wind engineering purposes (Simiu and Scanlan 1996).

Figure 6 shows the non-dimensional spectra at $z/H = 0.1$. The resolved fluctuations in LES follow Eq. (19) in the inertial subrange (the slope of $-2/3$ in the plot). Note that the lower limit of the inertial subrange is on the order of $f \approx 0.1 - 0.2$ (Busch and Panofsky 1968, Drobinski et al. 2004, Fichtl and McVehil 1970, Singer et al. 1968). The deficit is also observed in the simulated flow of low-frequency and high-frequency components.

The low-frequency spectrum deficit problem is related to the size of the computational domain and the length of simulation time (Nozawa and Tamura 2001). This is experienced not only in CFD simulations but also in wind tunnel

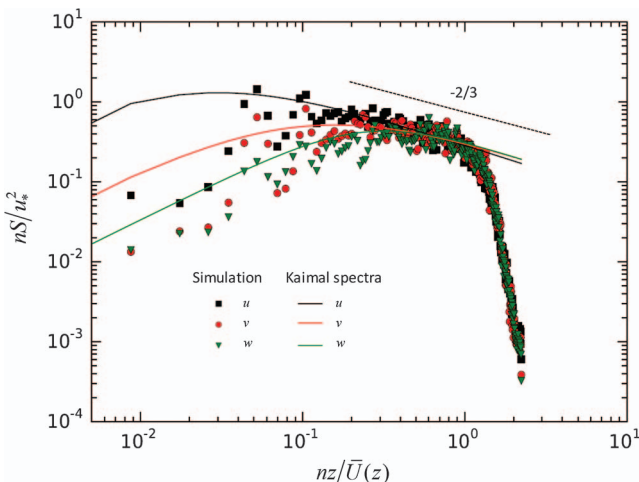


Figure 6. Spectra of wind velocity components at $z/H = 0.1$

Source: Shi and Yeo (2017).

testing (Simiu et al. 2011). The missing low-frequency components have little or no influence on the signature turbulence of structures immersed in the ABL flow but produce quasi-static effects on the response to the structures. The contribution of low-frequency component to the peak structural response can therefore be taken into account via post-processing (Asghari Mooneghi et al. 2016, Yeo and Chowdhury 2013). This approach can be applied not only to wind tunnel simulations, but to CFD simulations as well.

The high-frequency spectrum deficit problem is mainly caused by insufficient grid resolution and inaccurate SGS modeling of LES. LES resolves large-scale fluctuations up to a frequency related to grid scales, $f \approx 2.5$ (Figure 6). As shown in Figure 6, the resolved eddies follow the target spectra up to $f \approx 1$ and deviate from them for $f > 1$. This deviation is mainly caused by performance of the imperfect SGS modeling (e.g., by excessive SGS dissipation that moves too much energy from the resolved motions to the SGS motions). Such SGS modeling causes the logarithmic layer mismatch (LLM) near the ground, which generates “overshoot” peak wind shear, oversized streamwise coherence and, ultimately, inaccurate prediction of wind velocity field near the ground (Brasseur and Wei 2010, Mason and Thomson 1992, Yang et al. 2017). However, Because the overshoot occurs close to the ground, its effect is typically modest from a structural engineering point of view and is negligible for tall building design.

3.4 Wind velocity cross-spectra

The cross-spectral density functions of the wind velocity fluctuations at two different points are measures of the coherence of harmonic fluctuating components with frequencies n at those points. Since the cross-spectral density function is a function of the co-spectrum and the quadrature spectrum is negligible in

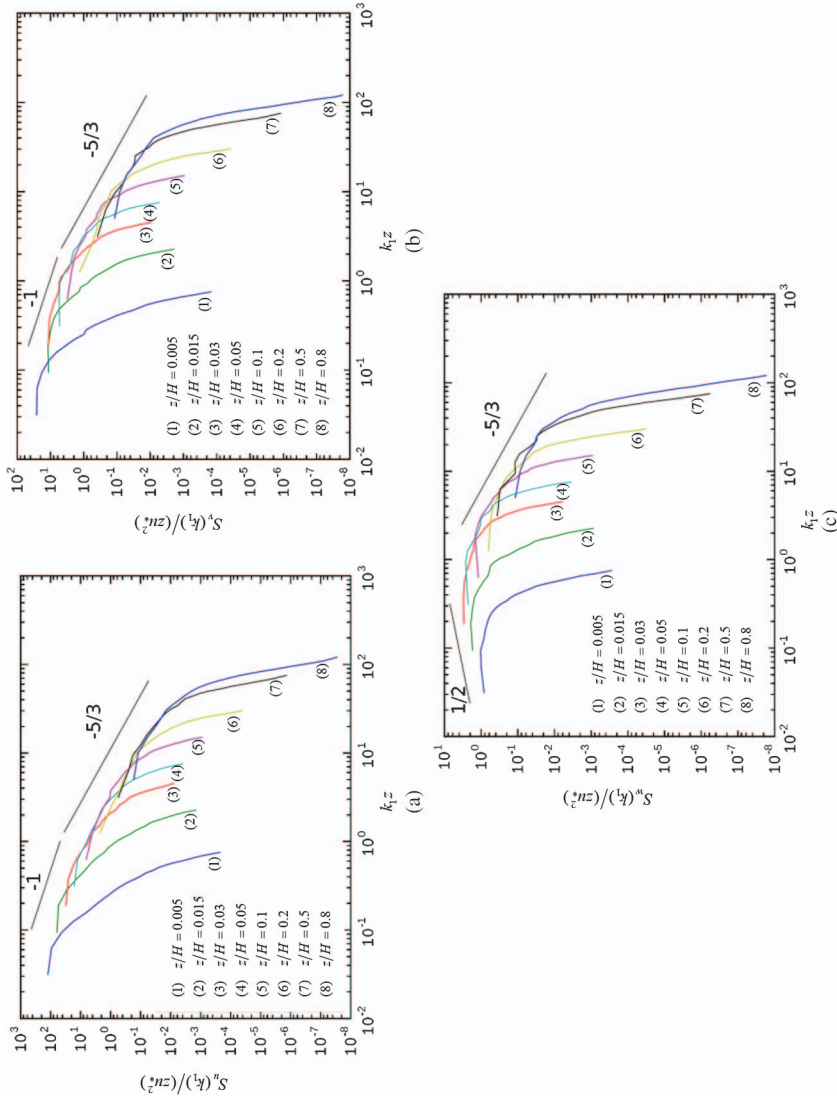


Figure 7. Spatial spectra of wind velocity components over elevations: (a) $S_u(k_z)$, (b) $S_v(k_z)$, and (c) $S_w(k_z)$

homogeneous turbulent ABL flows (Teunissen 1970), the co-spectrum can be expressed as (Simiu and Scanlan 1996)

$$S_{ii}^c(y_1, z_1; y_2, z_2; n) = S_i^{1/2}(z_1, n) S_i^{1/2}(z_2, n) e^{-\hat{f}} \quad (20)$$

where (y_1, z_1) and (y_2, z_2) denotes the coordinates in the lateral and vertical directions of two different points in a plane normal to the wind direction, the subscript i stands for the u , v , and w components, and $e^{-\hat{f}}$ describes the coherence of velocity components at those points. The expression for the exponent \hat{f} proposed by Davenport (1968) is

$$\hat{f} = \frac{n[C_z^2(z_1 - z_2)^2 + C_y^2(y_1 - y_2)^2]^{1/2}}{\frac{1}{2}[U(z_1) + U(z_2)]} \quad (21)$$

where C_z and C_y are exponential decay coefficient. Their values differ considerably from study to study (Simiu and Scanlan 1996). Commonly accepted values for the decay coefficients are $C_z = 10$, $C_y = 16$ (Vickery 1970). A similar expression was proposed for the exponential decay function in the x direction with a suggested exponential decay coefficient $C_x = 3$ to 6 (see, e.g., Simiu and Scanlan 1996).

Figure 8 shows the coherence functions $e^{-\hat{f}}$ for $u(t)$ at two locations along the directions x , y , and z . The mean streamwise velocity $\bar{U}(z)$ for C_z is the average of the mean velocities at two locations, as shown in Eq. (21). The estimated exponential decay coefficients of the simulated flow: $C_x = 1.00 \pm 0.03$, $C_y = 14.1 \pm 0.4$, and $C_z = 11.5 \pm 0.4$, where the sign \pm denotes the standard deviation with respect to the fitted curve. The coefficients of C_y and C_z in the simulations are in agreement to within 15% from the suggested values. However, C_x from the simulation is lower by a factor of at least 3 than the suggested value, which implies that the simulation produces significantly larger streamwise turbulence eddies at $z/H = 0.1$. This could be explained by the LLM problem in LES, which leads to excessive streamwise coherence near the ground.

3.5 Integral length scales

The integral length scales of turbulence are a measure of the representative size of the energy-bearing eddies in the flow and consist of nine components corresponding to the three dimensions (i.e., x , y , and z) of eddies associated with the three velocity fluctuation components. For example, L_u^x , L_u^y , and, L_u^z are the characteristic eddy sizes in the x , y , and z directions, respectively, associated with the longitudinal wind velocity fluctuations u . The length scale of L_u^x , which is the most common measure in wind engineering practice, is defined as (Counihan 1975, Simiu and Scanlan 1996)

$$L_u^x = \frac{1}{u^2} \int_0^\infty R_{u_1 u_2}(x) dx \quad (22)$$

where $R_{u_1 u_2}(x)$ is the cross-covariance function of the two longitudinal velocity components at two spatial positions of $u_1 = u(x_1, y_1, z_1, t)$ and

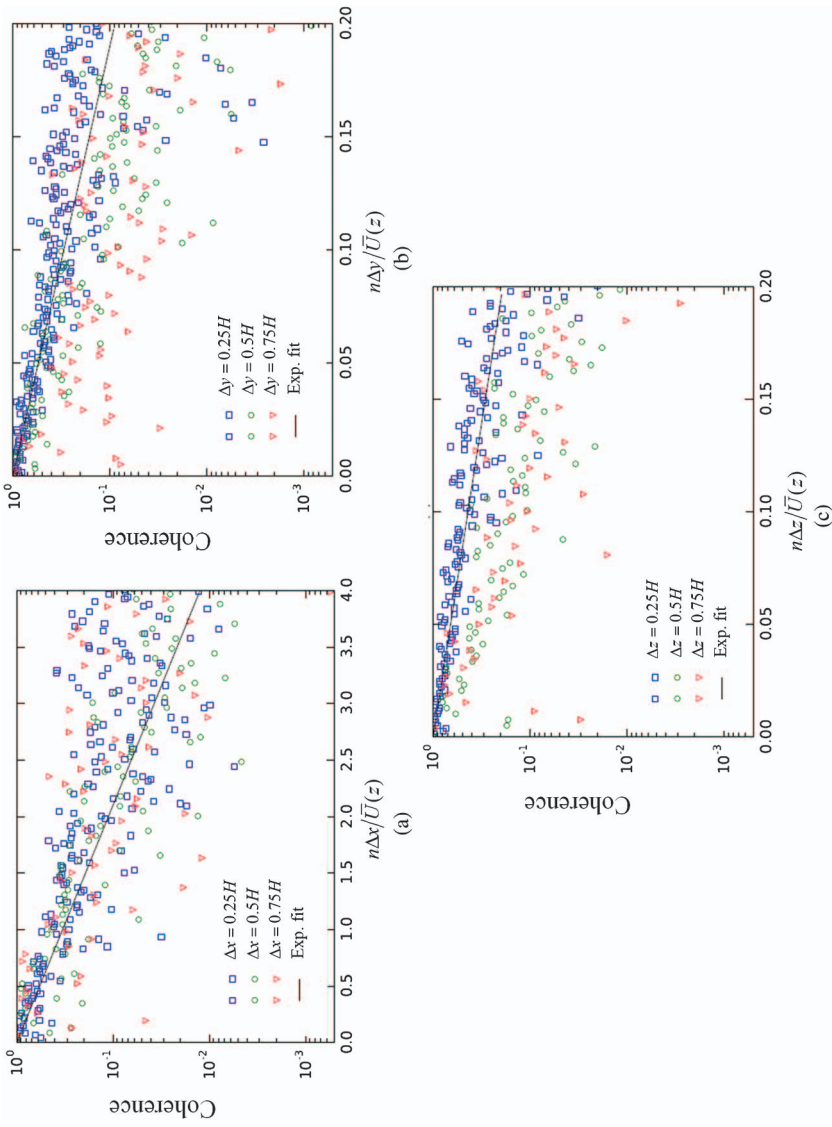


Figure 8. Coherence of wind fluctuations $u(t)$: (a) x direction, (b) y direction, and (c) z direction

Source: Plot (a) from Shi and Yeo 2017.

$u_2 = u(x_1 + x, y_1, z_1, t)$. Alternatively, the length scale can be estimated based on the Taylor's hypothesis of frozen turbulence as follows (Simiu and Scanlan 1996):

$$L_u^x = \frac{U}{\overline{u^2}} \int_0^\infty R_u(\tau) d\tau \quad (23)$$

where $R_u(\tau)$ is the auto-covariance function of the fluctuation $u(t)$ at time lag τ .

The integral length scale L_u^x within the ASL increases with height and decreases over rougher surface terrain (Counihan 1975). The reported values of L_u^x have large variability (ASCE 2012, Simiu and Scanlan 1996). An estimate of L_u^x within the ASL reported in ASCE 49-12 is expressed as

$$L_u^x = \frac{z}{2\pi f_m} \quad (24)$$

where f_m is the Monin reduced frequency at which the spectrum $nS(u)/u_*^2$ reaches the maximum value. The typical value suggested in ASCE 49-12 is $f_m \approx 0.032$, although no validation for this value appears to be available in the literature, which is lower than the counterpart in the simulation ($f_m \approx 0.05$ at $z/H = 0.1$ in Figure 6). However, Pasquill and Butler (1964) state that Eq. (24) can result in the underestimation of L_u^x by a factor of 2 to 3.

An alternative approximate expression of L_u^x was proposed by Counihan (1975):

$$L_u^x \approx Cz^m \quad (L_u^x \text{ and } z \text{ in meters}) \quad (25)$$

where the constant C and m are determined using Figure 13 of Counihan (1975). The proposed estimates L_u^y and L_u^z are

$$L_u^y \approx 0.35L_u^x, \quad L_u^z \approx 0.5L_u^x. \quad (26)$$

Figure 9 shows the integral scales of streamwise wind fluctuations in the x , y , and z directions. The symbols represent simulation results in this study. The curves show Counihan's estimates [Eqs. (25) and (26)]. For $z/H = 0.1$, the estimate of L_u^x/H in ASCE 49-12 [Eq. (24)] is 0.32. As shown in Figure 9, the simulation results are qualitatively consistent with the inequalities $L_u^x > L_u^z > L_u^y$ in the lower ABL height ($z/H \leq 0.3$ in this study). The ratios $L_u^x:L_u^y:L_u^z$ in the simulation are approximately 1:0.25:0.75 for $z/H \leq 0.3$, which is comparable to Eq. (26). While the simulated values of L_u^x and L_u^y are in good agreement with Counihan's estimates [Eqs. (25) and (26)], the simulated values of L_u^z at $z/H = 0.2 \sim 0.3$ are larger by a factor of about 2 than the values proposed in the literature. The peaks of the L_u^x and L_u^z profiles occur at $z/H \approx 0.35$ and 0.55, respectively, and decrease above the elevations of the peaks. L_u^y is almost constant throughout the ABL height. In view of the substantial uncertainties in the estimation of the integral turbulence lengths and of the fact that the latter need not be used in engineering calculations—especially if Eq. (19), rather than the von Kármán spectrum, are used for the spectral densities of the velocity fluctuations—such uncertainties are of limited or no practical significance from a structural engineering viewpoint.

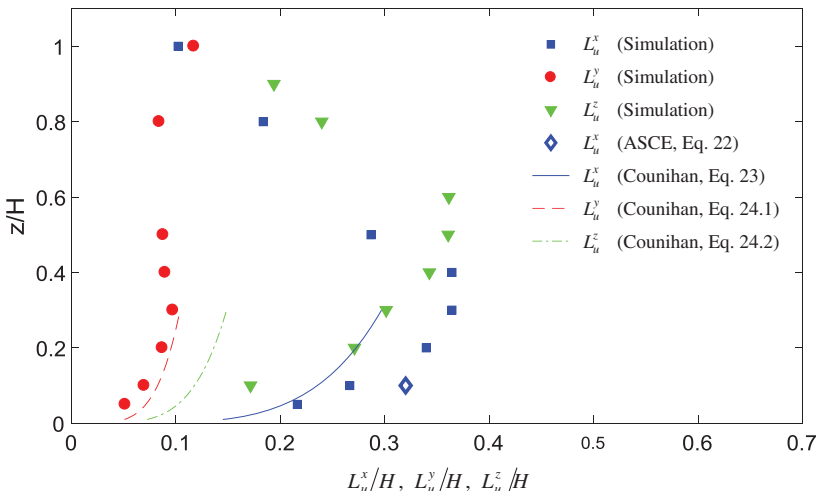


Figure 9. Integral length scales: Numerical simulations

Source: Counihan (1975), ASCE 49-12 (2012).

4 DISCUSSION

4.1 ABL simulation

This LES ABL simulation presented in this paper is based on (i) the use of state-of-the-art ABL research in wind/structural engineering applications, (ii) the balanced-force-driven ABL wind model, (iii) the precursor method, and (iv) a model scale similar to scales used in wind tunnel testing for tall building design applications.

Use of state-of-the-art ABL research in wind/structural engineering applications. Recent meteorological studies in the ABL study show that the ABL wind velocity profile in the mid-latitude region is approximately logarithmic up to elevations of an order of 1 km above the surface and that the veering angle for the elevations is negligible for practical purposes. The state-of-the-art results imply that the governing equations of the ABL flow as used for current structural engineering applications can be simplified by eliminating the Coriolis force terms.

Balanced-force-driven ABL wind model. In CWE applications, ABL simulations typically use “boundary-driven” wind to generate ABL flows by specifying inflow/outflow and top boundary conditions. This approach does not take into account the dynamic equilibrium of the neutrally stratified ABL flow and hence is not optimal for horizontally homogeneous ABL flow simulations. The “balanced-force-driven” approach employs the dynamic equilibrium of the ABL flow using balance of the horizontal pressure gradient force (which drives the wind flow) and the friction force (which retards the wind flow).

Precursor method. The precursor method, in conjunction with the balanced-force-driven mechanism, naturally develops turbulence by shear stress near the

surface, and generates more realistic ABL flows than other methods do. The simulated flow using the precursor method can be stored in databases and be used as incoming flow in a main simulation with objects immersed in the ABL. Though the database of incoming ABL flows from the promising precursor-based simulations requires additional computational time and storage, it allows wind/structural engineering practitioners to perform CFD simulations of ABL flows conveniently and with reduced uncertainties.

The ABL flows simulated by the precursor method are influenced by the periodic boundary condition inherent in the method. The effects of the boundary condition on the simulated flow become weaker as the size of the computational domain increases. Sensitivity studies are recommended to ascertain whether the size of the computational domain is adequate.

Model scale. The LES simulation in this study was performed using scaled length and velocity but employing the viscosity of air, as wind conventional tunnel testing does. One consequence of the reduced model scale—and the consequent violation of the Reynolds number with respect to its prototype counterpart—is that computational costs become affordable for practical wind engineering purposes.

To achieve a ground surface roughness that causes the flow to be independent of viscosity (Isyumov 2014, Sutton 1953), the ASCE 49-12 Standard specifies for the wind-tunnel-scaled flow a surface-roughness Reynolds number $Re_T = u_* z_0 / \nu > 2.5$, where Re_T is in effect the ratio of a turbulent eddy viscosity to the molecular viscosity. This approach is not necessary in CWE precursor method computations, which do not model roughness length but rather shear stresses and a sufficient flow-development length.

This paper examined the case of length scales of the order of 1:1000. This scale is comparable to model scales used for the simulation of wind effects on high-rise buildings. The approach considered in this paper can readily be modified to accommodate simulations of low-rise buildings as well. Typical wind tunnel scales for such buildings are of the order of 1:100 for length and 1:5 for velocity. To achieve CWE simulations comparable to wind tunnel simulations the same scales can be adopted for CWE simulations as well.

4.2 Assessment of simulated ABL flow

As shown in the section, Characteristics of Simulated ABL Flows, the quality of the flow simulated in this study satisfies criteria set forth in the ASCE 49-12 Standard for wind tunnel testing.

The mean wind speed profile follows the logarithmic law with differences of less than 2% at most elevations. The turbulence intensities are in good agreement with the standard values (to within 10% for I_u , 14% for I_w , and 20% for I_v). The predicted coherence and the integral length scales of the ABL flow differ from models typically assumed in engineering calculations by amounts that vary from 15% to more than 100%. However, those models are themselves very uncertain, and differ from reported full-scale measured values by $\pm 100\%$ or even more.

The wind velocity spectra are well reproduced in the non-dimensional frequency range $0.05 \leq f \leq 1$. For example, for a building with height $h = 183$ m under

wind speed of $\bar{U}(10 \text{ m}) = 35 \text{ m/s}$, to $f = 1$ there corresponds a frequency 0.29 Hz, well above the first three lowest natural frequencies of vibration of the building, which were determined to be 0.165 Hz, 0.174 Hz and 0.188 Hz (Park and Yeo 2016). These results show that the simulated ABL flow is capable of producing resonant response in the first three modes for the building considered in this example. More generally, the ASCE 7-16 Standard defines rigid buildings (i.e., buildings not susceptible to experiencing resonant response) as buildings with fundamental natural frequencies in excess of 1 Hz; flexible buildings are therefore buildings with frequencies $n \leq 1 \text{ Hz}$. This can be achieved by using more refined grids or better performed SGS models than those used in this study. Aerodynamic effects of unresolved, small-sized fluctuations are considered in LES by SGS models. For applications in which the simulation of small eddies is important, it is necessary to study the capability of SGS models to produce effects associated with such eddies. This topic should be the object of future research. The effects of missing low-frequency components ($f < 0.05$ in this study) on structural response can be compensated for by using post-processing corrections, as mentioned in Section 3.3.

This study confirms the existence of the well-known logarithmic layer mismatch problem (even worse with buoyancy effects) caused by inaccurate SGS modeling near the ground, where it overestimates the streamwise coherence, a feature that is conservative from a structural engineering viewpoint.

Simulated flow is influenced by the periodic boundary conditions, and the associated along-wind domain length affects coherence of flow. A “wiggled” spectrum in low-frequency component is a consequence of the periodic boundary conditions. As noted by Nozawa and Tamura (2001), this influence is stronger in the upper region of the ABL, owing to the shorter turnover period caused by the higher velocities in that region. Underestimated lateral fluctuations in the y direction are observed as well, which require further investigation.

5 CONCLUDING REMARKS

ABL simulations using LES have been performed to assess the extent to which CWE simulations of ABL flows are comparable to their counterpart conventional wind tunnel simulations. For structural engineering purposes, the governing equations of straight ABL flow were formulated based on state-of-the-art meteorological studies. The balanced forces between horizontal pressure gradient and ground friction were adapted to the CFD solver to achieve dynamic equilibrium throughout ABL. In the simulation using the precursor method, the turbulent ABL flow was naturally developed to achieve horizontally homogenous ABL flow. To reduce computational resource requirements this study employed a model scale approach, similar to the approach used in wind tunnel simulations.

The characteristics of simulated ABL flow were investigated and compared with their counterparts in the literature and the ASCE 49-12 Standard for wind tunnel testing. The mean wind speed profile accurately followed the logarithmic

law to within 2% differences at most elevations. The turbulence intensities were found to be in good agreement with standard values, to within 10% for I_u , 14% for I_w , and 20% for I_v . The wind velocity spectra were correctly simulated in the inertial subrange. The coherence and the integral length scales of the ABL flow were adequately predicted, with differences with respect to models proposed in the literature comparable to differences among most reported prototype measurements. The results also identified issues, mainly due to inaccurate SGS modeling, that need to be addressed in future research. The main conclusion of this study is that LES simulations of the lower 1 km of the turbulent, neutrally stratified ABL can be produced that achieve a level of quality equal to or higher than state-of-the-art, conventional boundary-layer wind tunnel simulations.

This paper examined the case of length scales of the order of 1:1000. This scale is comparable to model scales used for the simulation of wind effects on high-rise buildings. The approach considered in this paper can readily be modified to accommodate simulations of low-rise buildings as well. Typical wind tunnel scales for such buildings are of the order of 1:100 for length and 1:5 for velocity. To achieve CWE simulations comparable to wind tunnel simulations the same scales can be adopted for CWE simulations as well.

Based on the assessment of the simulated results via comparisons with measurements reported in the literature and values recommended in the ASCE 49-12 Standard for wind tunnel testing, the quality of the simulations for structural engineering applications was found to be comparable with the quality of their wind tunnel counterparts. The results also identified issues, mainly due to grid resolution and inaccurate SGS modeling, that need to be addressed by future research.

ACKNOWLEDGMENTS

The authors are indebted to Dr. Tarak Nandi for providing useful inputs regarding estimation of the turbulence intensities and integral length scales of the simulated flow. The contributions to this paper by Dr. Emil Simiu, who served as project leader, are acknowledged with thanks.

References

- Aboshosha, H., A. Elshaer, G. T. Bitsuamlak, and A. El Damatty. 2015. "Consistent inflow turbulence generator for LES evaluation of wind-induced responses for tall buildings." *J. Wind Eng. Ind. Aerodyn.* **142**: 198–216.
- AIJ (Architectural Institute of Japan). 2017. *Guidebook of recommendation for loads on buildings 2: Wind-induced response and load estimation/Practical guides of CFD for wind resistant design*. Tokyo: AIJ.
- ASCE. 2010. *Minimum design loads for buildings and other structures*. ASCE/SEI 7-10. Reston, VA: ASCE.
- ASCE. 2012. *Wind tunnel testing for buildings and other structures*. ASCE/SEI 49-12. Reston, VA: ASCE.

- Asghari Mooneghi, M., P. A. Irwin, and A. Gan Chowdhury. 2016. "Partial turbulence simulation method for predicting peak wind loads on small structures and building appurtenances." *J. Wind Eng. Ind. Aerodyn.* **157**: 47–62.
- Berthaut-Gerentès, J., D. Delaunay, and S. Sanquer. 2014. "Atmospheric turbulent layer simulation providing unsteady inlet conditions for large eddy simulation." In *6th Int. Symp. on Computational Wind Engineering (CWE 2014)*. Hamburg, Germany.
- Blocken, B., T. Stathopoulos, and J. Carmeliet. 2007. "CFD simulation of the atmospheric boundary layer: Wall function problems." *Atmos. Environ.* **41** (2): 238–252.
- Brasseur, J. G., and T. Wei. 2010. "Designing large-eddy simulation of the turbulent boundary layer to capture law-of-the-wall scaling." *Phys. Fluids* **22** (2): 021303.
- Busch, N. E., and H. A. Panofsky. 1968. "Recent spectra of atmospheric turbulence." *Q. J. R. Meteorol. Soc.* **94** (400): 132–148.
- Cai, X., Q. Huo, L. Kang, and Y. Song. 2014. "Equilibrium atmospheric boundary-layer flow: Computational fluid dynamics simulation with balanced forces." *Boundary Layer Meteorol.* **152** (3): 349–366.
- CEN (European Committee for Standardization). 2005. *Actions on structures. Part 1-4: General actions: Wind actions*. Eurocode 1. Brussels, Belgium: CEN.
- Churchfield, M. J., G. Vijayakumar, J. G. Brasseur, and P. J. Moriarty. 2010. "Wind energy-related atmospheric boundary layer large-eddy simulation using OpenFOAM." In *19th Symp. on Boundary Layers and Turbulence*. Keystone, CO.
- Counihan, J. 1975. "Adiabatic atmospheric boundary layers: A review and analysis of data from the period 1880–1972." *Atmos. Environ.* (1967) **9** (10): 871–905.
- Davenport, A. G. 1968. "The dependence of wind loads on meteorological parameters." In *Proc. Int. Research Seminar on Wind Effects on Buildings and Structures*, 19–82. Toronto.
- Drobinski, P., P. Carlotti, R. K. Newsom, R. M. Banta, R. C. Foster, and J.-L. Redelsperger. 2004. "The structure of the near-neutral atmospheric surface layer." *J. Atmos. Sci.* **61** (6): 699–714.
- ESDU (Engineering Sciences Data Unit). 2001. *Characteristics of atmospheric turbulence near the ground. Part II: Single point data for strong winds (neutral atmosphere)*. ESDU 85020. ESDU.
- Fichtl, G. H., and G. E. McVehil. 1970. "Longitudinal and lateral spectra of turbulence in the atmospheric boundary layer at the Kennedy Space Center." *J. Appl. Meteorol.* **9** (1): 51–63.
- Grötzbach, G. 1987. "Direct numerical and large eddy simulation of turbulent channel flows." In *Encyclopaedia of fluid mechanics*, edited by N. P. Cheremisinoff, 6th ed., 1337–1391. Houston, TX: Gulf Publishing Company.
- HE (Highways England). 2001. "Volume I: Highway structures: Approval procedures and general design." In *Design manual for roads and bridges (DMRB)*. HE.
- Hémon, P., and F. Santi. 2007. "Simulation of a spatially correlated turbulent velocity field using biorthogonal decomposition." *J. Wind Eng. Ind. Aerodyn.* **95** (1): 21–29.
- Hess, G. D. 2004. "The neutral, barotropic planetary boundary layer, capped by a low-level inversion." *Boundary Layer Meteorol.* **110** (3): 319–355.
- Huang, S. H., Q. S. Li, and J. R. Wu. 2010. "A general inflow turbulence generator for large eddy simulation." *J. Wind Eng. Ind. Aerodyn.* **98** (10–11): 600–617.
- Kaimal, J. C., J. C. Wyngaard, Y. Izumi, and O. R. Coté. 1972. "Spectral characteristics of surface-layer turbulence." *Q. J. R. Meteorol. Soc.* **98** (417): 563–589.
- Kataoka, H., and M. Mizuno. 2002. "Numerical flow computation around aeroelastic 3D square cylinder using inflow turbulence." *Wind Struct.* **5** (2–4): 379–392.
- Kondo, K., S. Murakami, and A. Mochida. 1997. "Generation of velocity fluctuations for inflow boundary condition of LES." *J. Wind Eng. Ind. Aerodyn.* **67–68**: 51–64.

- Kozmar, H. 2011. "Wind-tunnel simulations of the suburban ABL and comparison with international standards." *Wind Struct.* **14** (1): 15–34.
- Mason, P. J., and D. J. Thomson. 1992. "Stochastic backscatter in large-eddy simulations of boundary layers." *J. Fluid Mech.* **242**: 51–78.
- Munters, W., C. Meneveau, and J. Meyers. 2016. "Turbulent inflow precursor method with time-varying direction for large-eddy simulations and applications to wind farms." *Boundary Layer Meteorol.* **159** (2): 305–328.
- Nozawa, K., and T. Tamura. 2001. "Simulation of rough-wall turbulent boundary layer for LES inflow data." In *Proc., Second Int. Symp. on Turbulence and Shear Flow Phenomena*, 443–448.
- OpenFOAM. 2015. *The open source CFD toolbox: User guide (version 2.4.0)*. OpenFOAM Foundation.
- Park, S., and D. Yeo. 2016. *Database-assisted design and second-order effects on the wind-induced structural behavior of high-rise buildings*. Gaithersburg, MD: NIST.
- Pasquill, F., and H. E. Butler. 1964. "A note on determining the scale of turbulence." *Q. J. R. Meteorol. Soc.* **90** (383): 79–84.
- Porté-Agel, F., C. Meneveau, and M. B. Parlange. 2000. "A scale-dependent dynamic model for large-eddy simulation: Application to a neutral atmospheric boundary layer." *J. Fluid Mech.* **415**: 261–284.
- Richards, P. J., and R. P. Hoxey. 1993. "Appropriate boundary conditions for computational wind engineering models using the k-[epsilon] turbulence model." *J. Wind Eng. Ind. Aerodyn.* **46–47**: 145–153.
- Samali, B., K. C. S. Kwok, G. S. Wood, and J. N. Yang. 2004. "Wind tunnel tests for wind-excited benchmark building." *J. Eng. Mech.* **130** (4): 447–450.
- Schumann, U. 1975. "Subgrid scale model for finite difference simulations of turbulent flows in plane channels and annuli." *J. Comput. Phys.* **18** (4): 376–404.
- Shi, L., and D. Yeo. 2016. *OpenFOAM large-eddy simulations of atmospheric boundary layer turbulence for wind engineering applications: NIST Technical Note 1944*. Gaithersburg, MD: NIST.
- Shi, L., and D. Yeo. 2017. "Large Eddy simulations of model-scale turbulent atmospheric boundary layer flows." *J. Eng. Mech.* **143** (9): 06017011.
- Simiu, E. 2011. *Design of buildings for wind: A guide for ASCE 7-10 Standard users and designers of special structures*. Hoboken, NJ: Wiley.
- Simiu, E., G. T. Bitsuamlak, A. G. Chowdhury, R. Li, A. Tecle, and D. Yeo. 2011. "Testing of residential homes under wind loads." *Nat. Hazard. Rev.* **12** (4): 166–170.
- Simiu, E., and R. H. Scanlan. 1996. *Wind effects on structures*. Hoboken, NJ: Wiley.
- Singer, I. A., N. E. Busch, and J. A. Frizzola. 1968. "The micrometeorology of the turbulent flow field in the atmospheric boundary surface layer." In *Int. Research Seminar on Wind Effects on Buildings and Structures*, 557–594. Ottawa.
- Stull, R. B. 1988. *An introduction to boundary layer meteorology*. Dordrecht, Netherlands: Kluwer Academic Publishers.
- Sutton, O. G. 1953. *Micrometeorology*. New York: McGraw-Hill.
- Tabor, G. R., and M. H. Baba-Ahmadi. 2010. "Inlet conditions for large eddy simulation: A review." *Comput. Fluids* **39** (4): 553–567.
- Tanaka, H., Y. Tamura, K. Ohtake, M. Nakai, Y. C. Kim, and E. K. Bandi. 2013. "Aerodynamic and flow characteristics of tall buildings with various unconventional configurations." *Int. J. High Rise Build.* **2** (3): 213–228.

- Teunissen, H. W. 1970. *Characteristics of the mean wind and turbulence in the planetary boundary layer*. Institute for Aerospace Studies Review No. 32. Toronto: Univ. of Toronto.
- Tominaga, Y. 2015. "Flow around a high-rise building using steady and unsteady RANS CFD: Effect of large-scale fluctuations on the velocity statistics." *J. Wind Eng. Ind. Aerodyn.* **142**: 93–103.
- Vasaturo, R., I. Kalkman, B. Blocken, and P. J. V. van Wesemael. 2018. "Large eddy simulation of the neutral atmospheric boundary layer: Performance evaluation of three inflow methods for terrains with different roughness." *J. Wind Eng. Ind. Aerodyn.* **173**: 241–261.
- Vickery, B. J. 1970. "On the reliability of gust loading factors." In *Proc., Technical Meeting Concerning Wind Loads on Buildings and Structures*. Washington, DC.
- Wu, X. 2017. "Inflow turbulence generation methods." *Ann. Rev. Fluid Mech.* **49** (1): 23–49.
- Xie, Z.-T., and I. P. Castro. 2008. "Efficient generation of inflow conditions for large eddy simulation of street-scale flows." *Flow Turbul. Combust.* **81** (3): 449–470.
- Yang, X. I. A., G. I. Park, and P. Moin. 2017. "Log-layer mismatch and modeling of the fluctuating wall stress in wall-modeled large-eddy simulations." *Phys. Rev. Fluids* **2** (10): 104601.
- Yeo, D., and A. Chowdhury. 2013. "Simplified wind flow model for the estimation of aerodynamic effects on small structures." *J. Eng. Mech.* **139** (3): 367–375.
- Yoshizawa, A., and K. Horiuti. 1985. "A statistically-derived subgrid-scale kinetic energy model for the large-eddy simulation of turbulent flows." *J. Phys. Soc. Jpn.* **54** (8): 2834–2839.
- Zilitinkevich, S. 2012. "The height of the atmospheric planetary boundary layer: State of the art and new development." In *National security and human health implications of climate change*, edited by H. J. S. Fernando, Z. Klaić, and J. L. McCulley, 147–161. Dordrecht, Netherlands: Springer.
- Zilitinkevich, S., I. Esau, and A. Baklanov. 2007. "Further comments on the equilibrium height of neutral and stable planetary boundary layers." *Q. J. R. Meteorol. Soc.* **133** (622): 265–271.
- Zilitinkevich, S. S., and I. N. Esau. 2002. "On integral measures of the neutral barotropic planetary boundary layer." *Boundary Layer Meteorol.* **104** (3): 371–379.

This page intentionally left blank

CHAPTER 10

Application of Wind Fairings for Building Aerodynamic Optimization

Zhendong Xu^{*}
Jiming Xie, Ph.D., P.Eng. M.ASCE[†]

Abstract: Based on principles of wind-adaptable design (WAD), wind fairings can be used as operable flow control devices to optimize building's aerodynamic properties during severe wind storms. With this approach, the common design conflicts between architectural concepts and aerodynamic requirements can be avoided, and wind effects on buildings can therefore be dealt with more smoothly and efficiently during design. This paper lays out the criteria for wind fairing design that meet the requirements for WAD. Two types of fairing, named Scheme A and Scheme B, were studied. Detailed parameter studies using high-frequency force-balance (HFFB) technique are introduced, aiming at optimizing size of the wind fairings to further enhance their effectiveness. It was found that for Scheme A fairings, the optimal configuration has a relative width of about 1/10, a relative height of 1/5 or more and a fairing angle of about 45°. For Scheme B fairings, the optimal configuration has a relative width of about 1/10 and a relative gap of about 1/10. While further optimization is still possible, the current study has validated that a reduction of about 20% on design wind loads is reachable with properly designed wind fairings.

INTRODUCTION

For super-tall buildings of 300 m or taller, across-wind response is one of the major design challenges to which the building designers have to overcome. Compared with along-wind response, across-wind response is more sensitive to building's outer

*Graduate Student, College of Civil Engineering and Architecture, Zhejiang University, Hangzhou, China, email: zhendong_xu@zju.edu.cn

†Professor, College of Civil Engineering and Architecture, Zhejiang University, Hangzhou, China (corresponding author), email: jiming_xie@zju.edu.cn

geometry. A corner shape modification within 10% of building width may result in a reduction of 25% in overturning moments (Irwin 2008). Therefore, aerodynamic optimizations have drawn a great attention in building design community.

Corner chamfering, tapering, twisting, upper portion opening are commonly adapted approaches of building aerodynamic optimizations (Kwok 1988, Dutton and Isyumov 1990, Kareem et al. 1999, Tamura and Miyagi 1999, Tanaka et al. 2012). However, since these approaches, if adapted, will alter a building's geometry and appearance from its original design and may cause inconsistency with the basic architectural concept, their acceptance in design can be a difficult decision (Xie 2014).

The authors have proposed a new design method for aerodynamic optimizations, named wind-adaptable design (WAD), to solve the above described conflicts. WAD method is based on the fact that extreme wind events, such as hurricanes, can be reliably predicted with modern weather forecast technology. As such, aerodynamic optimizations of super-tall buildings are achieved by installing operable flow control devices on the buildings, instead of permanently altering building's exterior geometry. In common wind conditions, which occur most of time, the building remains its originally designed shape (base shape). When a severe storm is forecasted, the building's flow control devices are launched to transform the building from its base shape to an aerodynamically optimized shape to handle additional wind loads imposed on the building by the storm. With WAD approach, the conflicts between architectural design and structural aerodynamic design are basically avoided. The concept of WAD can be illustrated by Figure 1.

The WAD approach brings benefits in two ways: (1) a building is effectively designed to sustain for common wind conditions which occur most of time during the building's life rather than being excessively designed for uncommon severe wind storms, and (2) during uncommon severe wind storms, the building is enhanced by launching specifically designed flow control devices to achieve aerodynamic optimizations. Since the proposed design method is focusing on building's adaptability to wind effects rather than building's resistance to winds, the authors refer the proposed method as "wind-adaptable design (WAD)" to conceptually distinguish it from the conventional wind-resistant design method. Key design parameters of WAD, including design wind speed for common winds, design wind speed for extreme winds, and trigger speed for launching flow control devices, have been established.

The present paper discusses a feasibility study of wind fairing, one of the operable flow control devices, for the application in wind-adaptable design (WAD).

SELECTION OF WIND FAIRINGS FOR BUILDINGS

Although wind fairings are commonly used in bridge aerodynamic design (Yang et al. 2009), these fairings cannot be directly used for buildings. Applicable wind fairings for buildings have to meet the following requirements:

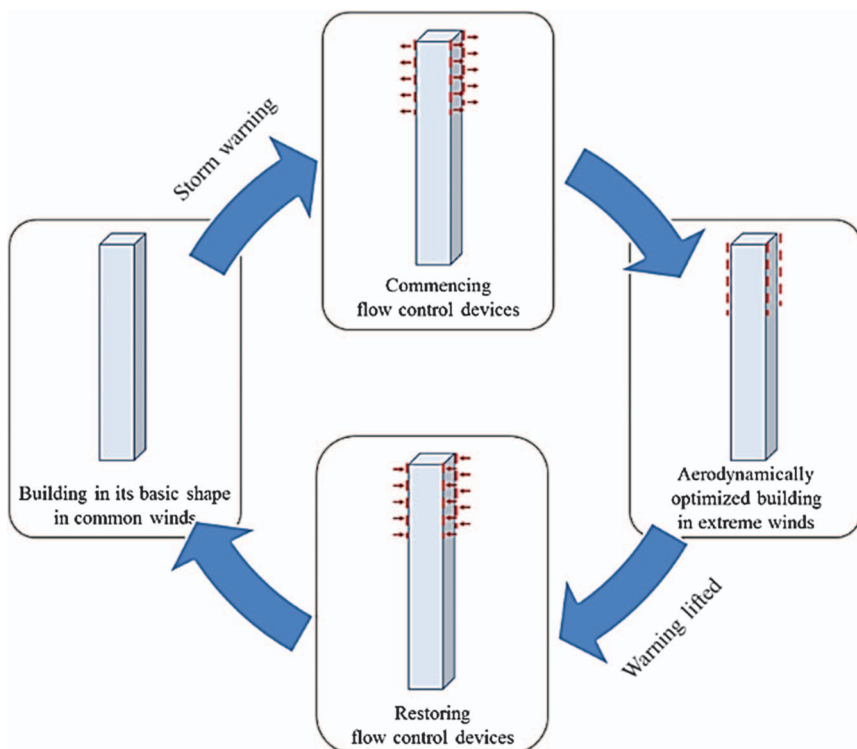


Figure 1. Concept of a WAD building

- **Operable:** With wind-adaptable design, wind fairings installed on a building have to be visually hidden during normal wind conditions and be launched to service position during extreme winds. In comparison, wind fairings for bridges are normally designed as part of deck section
- **Omnidirectional:** While wind fairings of bridges are mainly designed for horizontal winds, the wind fairings of buildings have to be effective for omnidirectional winds.

In this study, a typical square building was examined with five types of wind fairing being chosen as candidates of operable flow control devices, shown in Figure 2.

A first-round selection of fairing types was conducted by using flow visualization tests in wind tunnel. To set a reference, a 10% corner chamfered section was first tested. Favorable aerodynamic effects of chamfering can be clearly observed by comparing the flow patterns between the chamfered section and the original square section. The flow pattern of the chamfered section was then used as the reference to select promising fairings. The fairing types that can generate similar flow patterns as the chamfered section were considered to have high potential to offer effective aerodynamic optimizations.

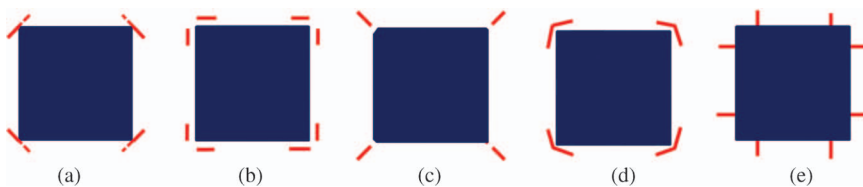


Figure 2. Candidates of wind fairing types

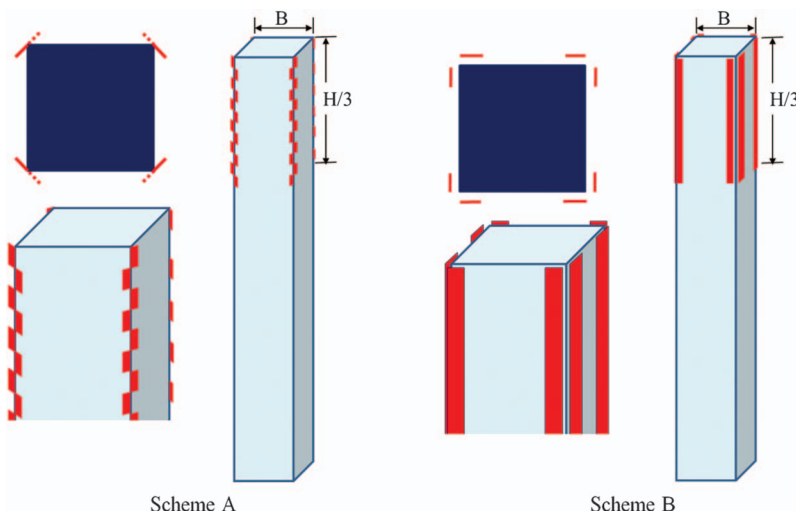


Figure 3. Layout of wind fairing

After the first-round selection, the fairing types shown in Figures 2a and 2b were short listed. These fairing types were then laid out along the building height as shown in Figure 3.

For Scheme A, the fairings were installed alternatively around the building corners. The intention was to suppress the corner vortices as well as to reduce their shedding correlations along the height. For both Scheme A and Scheme B, the fairings were installed only at the top 1/3 height of the building where the wind fairing was considered most effective.

PARAMETER OPTIMIZATION OF WIND FAIRINGS

Test set-up

High-frequency force-balance (HFFB) tests were conducted in the 4 m (width) \times 3 m (height) boundary layer wind tunnel at Zhejiang University, China, to quantify the effectiveness of the selected wind fairings and also to investigate the influence of fairing's shape parameters to their aerodynamic effectiveness.

Table 1. Key Parameters of HFFB Model Tests

Building height	270 m	Building width	45 m × 45 m
Fundamental frequency	0.13 Hz	Mode shape	$(z/H)^{1.5}$
Structural damping ratio	1.5%	Wind exposure	Typical urban ($\alpha = 0.22$)
Reference speed at roof height	65 m/s	Model scale	1:300

The HFFB model represented a typical 60-storey tall building. Table 1 lists the key parameters of the model and the wind tunnel set-up.

The building model was mounted on a six component force balance made by ME-Meßsysteme GmbH of Germany. The fundamental frequency of the assembly was found above 40 Hz which met the high frequency requirement. The wind tunnel reference speed was set at 8.5 m/s. The measurement duration was 90 seconds for each wind direction at a sampling rate of 300 Hz, so that about one-hour time history of wind loading at full scale was recorded for further analysis.

Figure 4a shows one of the tested models in the wind tunnel. Due to geometric symmetry of the building, the wind tunnel tests were conducted for only 7 wind directions, as illustrated in Figure 4b.

For wind fairing of Scheme A, the relative width b/B , the relative height h/B , and the included angle θ between the fairing and the building face were taken as the major shape parameters, as defined in Figure 5a. For wind fairing of Scheme B, the shape parameters include the relative width b/B , and the relative gap d/B , as shown in Figure 5b. Table 2 summarizes the tested model configurations.

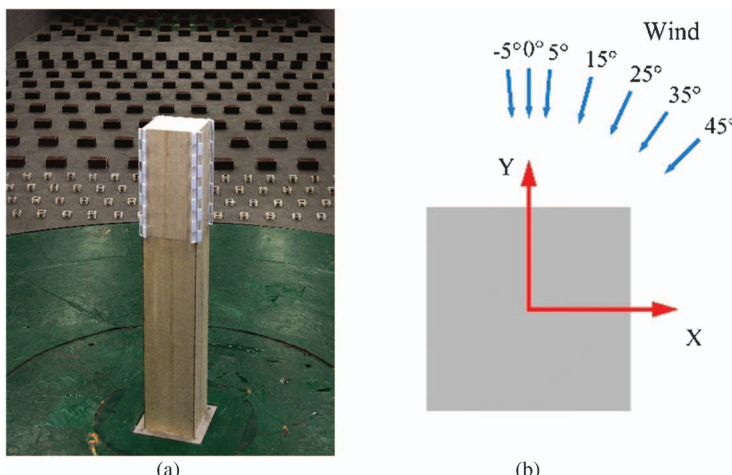


Figure 4. Tested wind directions and definition of coordinate system: (a) Wind tunnel model, and (b) Definition of coordinate system

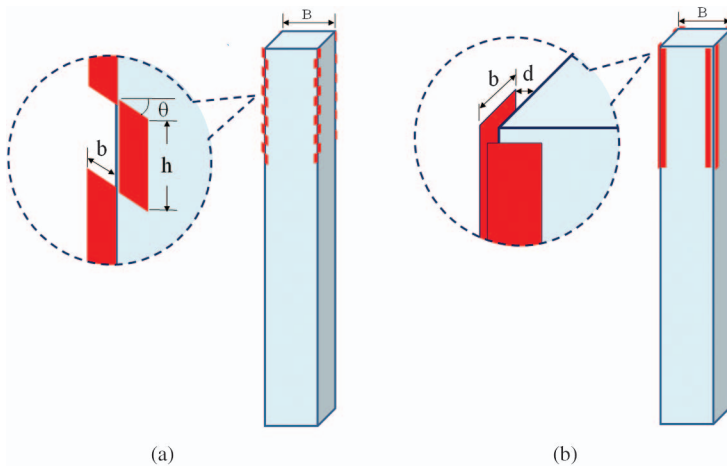


Figure 5. Definition of shape parameters of wind fairings: (a) Scheme A, and (b) Scheme B

Table 2. Wind Tunnel Test Configurations

Symbol	Description			
Base	Square building without wind fairing			
A-30-5-45	Scheme A	$b/B = 1/30$	$h/B = 1/5$	$\theta = 45^\circ$
A-15-5-45	Scheme A	$b/B = 1/15$	$h/B = 1/5$	$\theta = 45^\circ$
A-10-5-45	Scheme A	$b/B = 1/10$	$h/B = 1/5$	$\theta = 45^\circ$
A-10-10-45	Scheme A	$b/B = 1/10$	$h/B = 1/10$	$\theta = 45^\circ$
A-10-3-45	Scheme A	$b/B = 1/10$	$h/B = 1/3$	$\theta = 45^\circ$
A-10-5-30	Scheme A	$b/B = 1/10$	$h/B = 1/5$	$\theta = 30^\circ$
A-10-5-60	Scheme A	$b/B = 1/10$	$h/B = 1/5$	$\theta = 60^\circ$
B-10-30	Scheme B		$b/B = 1/10$	$d/B = 1/30$
B-10-15	Scheme B		$b/B = 1/10$	$d/B = 1/15$
B-10-10	Scheme B		$b/B = 1/10$	$d/B = 1/10$

Analysis method

The generalized force of the j -th mode can be determined from HFFB test by using the following equation to account for nonlinear mode shape effects (Xie and Irwin 1998).

$$\begin{aligned}
 P_j(t) = & (Y_{jFx} + \Lambda_{jFx})S_x(t) + (Y_{jFy} + \Lambda_{jFy})S_y(t) \\
 & + (Y_{jMy} + \Lambda_{jMy})\frac{M_y(t)}{H} + (Y_{jMx} + \Lambda_{jMx})\frac{M_x(t)}{H} + Y_{jMz}\frac{M_z(t)}{R} \quad (1)
 \end{aligned}$$

where

- S_x measured base shear in horizontal x -direction
- S_y measured base shear in horizontal y -direction
- M_y measured base overturning moments about y -axis
- M_x measured base overturning moments about x -axis
- M_z measured base torque about vertical z -axis
- $Y_{jl[\cdot]}$ contribution factors, being functions of mode shapes and building properties
- $\Lambda_{j[\cdot]}$ contribution factors, being functions of mode shapes and building properties
- H building height
- R radius of gyration used for normalizing torsional mode shapes.

With frequency domain analysis, the variance of modal acceleration to wind excitations is given by

$$\sigma_{a_j}^2 \cong \frac{(q_r BH)^2}{M_j^2} \left(\int_0^\infty S_{P_j}^*(f) df + \frac{\pi f_j}{4\zeta_j} S_{P_j}^*(f_j) \right) \quad (2)$$

where

- q_r reference wind pressure
- B typical building width
- M_j generalized mass of the j -th mode
- f_j natural frequency of the j -th mode
- ζ_j structural damping ratio
- $S_{P_j}^*$ generalized force spectrum normalized by $(q_r BH)^2$

The first term in Eq. (2) represents the background contribution while the second term is the resonance. For across-wind response, the background contribution is normally less than 5% (Xu and Xie 2015). Therefore, the dynamic load caused by across-wind response can be written as follows:

$$P_j(z) \cong g_R(q_r BH) \left(\frac{m_z \phi_j(z)}{M_j} \right) \sqrt{\frac{\pi f_j}{4\zeta_j} S_{P_j}^*(f_j)} \quad (3)$$

where

- g_R peak factor of resonant response
- m_z floor mass at elevation z
- ϕ_j mode shape

To assess the effectiveness of wind fairings, we examined the generalized force spectrum and the across-wind loads in comparison with those values of the Base model that has no wind fairing. The comparison of the spectrum reveals the fairing effectiveness as a function of frequency, while the comparison of wind loads represents the effectiveness for the given structural properties.

Results

Scheme A – Sensitivity of fairing width. For Scheme A, we first set the fairing height $h/B = 1/5$, the fairing angle $\theta = 45^\circ$, and took the fairing width as a parameter varying between $b/B = 1/30$ and $b/B = 1/10$. The relative fairing width larger than $1/10$ was not investigated, because oversized fairing was considered difficult for practical implantation. Figure 6a shows the generalized force spectra of Scheme A with three relative fairing widths in comparison with the Base model without wind fairing. In general, the effectiveness of wind fairing tends to increase with the increase of fairing width. For the case of $b/B = 1/10$, the spectrum peak can be reduced by almost $1/3$. It was also observed that if the fairing width is very narrow such as $b/B = 1/30$ or smaller, there will be no aerodynamic benefits or even becoming slightly worsen.

Figure 6b shows the ratio of overturning moment about y -axis between Scheme A and the Base model. The overturning moment about y -axis represents the across-wind loading in wind direction of 0° . About 18% of reduction on the maximum overturning moment was observed for the relative faring width of 10%.

Scheme A – Sensitivity of fairing height. We then set fairing width $b/B = 1/10$ and fairing angle $\theta = 45^\circ$ and investigated the sensitivity of fairing height h/B to aerodynamic behaviors. Figure 7a shows the generalized force spectra of Scheme A with three typical fairing heights in comparison with the Base model without wind fairing. The results indicate that the aerodynamic effectiveness generally increases with the increase of the relative fairing height. However, after the relative height exceeding $1/5$, no significant improvement can be expected by further increase of the relative height. This phenomenon is also evident for the overturning moment as shown in Figure 7b.

Scheme A – Sensitivity of fairing angle. By setting the fairing width $b/B = 1/10$ and the fairing height $h/B = 1/15$, the influence of fairing angles was investigated. It was found that while all the tested fairings provided favorable results in general, the fairing with 30° did not show wind load reductions for wind direction normal to the building surface (wind direction = 0°), as shown in Figure 8. Therefore, we recommend that an optimal fairing angle should be around 45° .

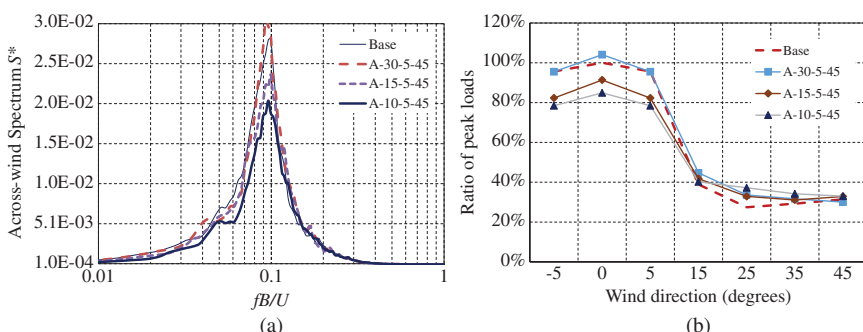


Figure 6. Sensitivity of wind fairing width – Scheme A: (a) Load spectrum, and (b) Overturning moment about y -axis

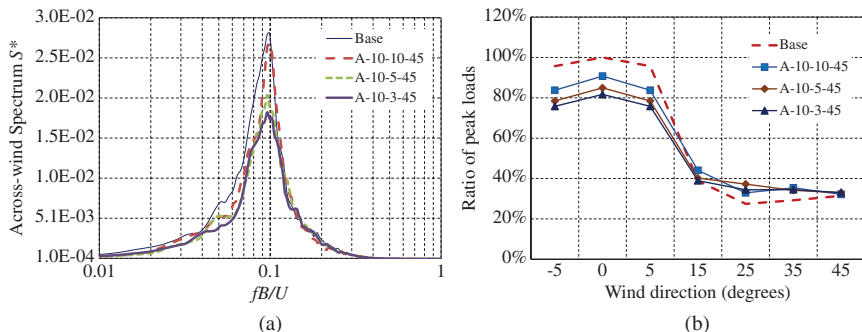


Figure 7. Influence of wind fairing height – Scheme A: (a) Load spectrum, and (b) Overturning moment about y-axis

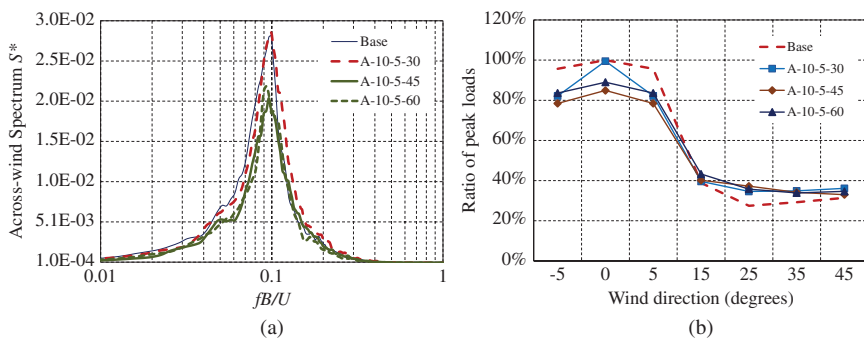


Figure 8. Influence of wind fairing angle – Scheme A: (a) Load spectrum, and (b) Overturning moment about y-axis

Scheme B – Sensitivity of fairing gaps. For Scheme B, by setting the relative fairing width at 1/10, we tested different size of gaps between the fairing and the building exterior wall. While all the tested cases showed considerable aerodynamic improvement with Scheme B fairings, it seems that larger gaps tend to be more effective in favor of aerodynamic responses, as shown in Figure 9. For the study model, the reductions on the overturning moments varied from 10% for the relative gap of 1/30 to 20% for the relative gap of 1/10. In this study we limited the relative gap up to 1/10. The relative gap within 1/10 was considered convenient for practical implantation.

EXAMPLE OF DESIGN APPLICATION

As an example, the application of wind fairings to building aerodynamic design is discussed below. The key parameters of the study building are given in Table 1. The design wind speed of a 100-year return period at building roof height (270 m) was chosen to be 65 m/s, which is typical for typhoon-prone coastal cities in

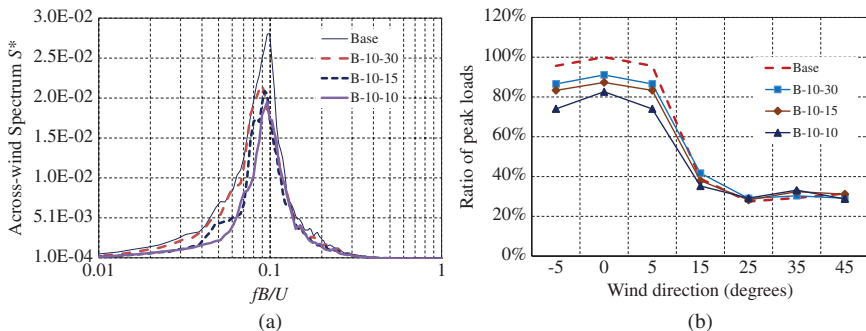


Figure 9. Sensitivity of wind fairing gaps – Scheme B: (a) Load spectrum, and (b) Overturning moment about y-axis

southeast China. The applied wind fairing is Scheme A with typical dimensions of 4.5 m wide ($b = 4.5$ m), 9.0 m height ($h = 9.0$ m) and 45° of included angle ($\theta = 45^\circ$). The wind fairings are installed around each corner of the building within the top 90 m height.

Figure 10 plots the maximum overturning moments as a function of reference wind speed for both the Base building (i.e., without wind fairings) and the flow controlled building (i.e., with Scheme A fairing in place). It is evident that at the 100-year design speed of 65 m/s, the design wind loads for the Base building are about 20% higher than the building with wind fairing launched.

Based on the two-stage method of wind-adaptable design (WAD), the building's main structural system can be designed for the lower wind loads (3.37×10^{10} N·m, about 20% lower than 4.20×10^{10} N·m of the Base building) by

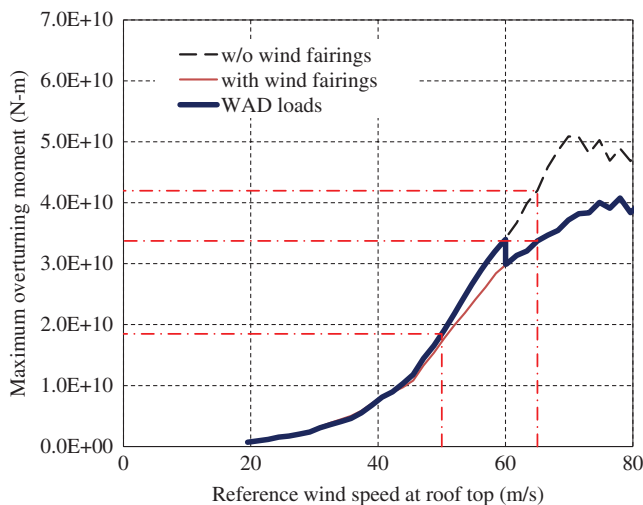


Figure 10. Design wind loads with WAD method

assuming that the wind fairings are launched to service positions during extreme wind storms. Figure 10 indicates that the 100-year wind loads with wind fairings in place are equivalent to wind loads of the Base building at a reference wind speed of 60 m/s. The 60 m/s sets the upper limit of design wind speed for the common wind conditions.

Further reliability analysis suggests that a 20-year return period wind speed can be considered as the trigger speed for the wind fairings to launch. Based on the wind climate data, the 20-year reference wind speed was found to be about 50 m/s. The probability difference of occurrence between the 50 m/s and the upper limit of 60 m/s serves as a safety buffer for the reliability of wind fairing's commencement.

In summary, with WAD, the building structural system is designed for a 100-year return period wind for the aerodynamically optimized building shape, and the wind fairings are designed to be launched when the reference wind speed reaches 50 m/s (a 20-year wind). Since the building without wind fairing is literally safe until 60 m/s (see Figure 10), sufficient margin has been reserved to ensure the structure safety.

In comparison with traditional structural design approach, the application of wind fairings in WAD leads to a considerable cost saving because of the reduction of 20% on design wind loads.

In comparison with traditional aerodynamic optimization approach, the application of wind fairing with WAD does not require alternations of building's original geometry so that the conflicts between the architectural design and the aerodynamic optimization are avoided.

CONCLUSIONS

A feasibility study on the application of wind fairings for building aerodynamic optimizations is presented in this paper.

Based on the principles of wind-adaptable design, wind fairings can be used as operable flow control devices which are literally invisible in normal wind conditions but can be launched to service position during extreme winds, so that the conflicts of traditional building aerodynamic optimization approaches with architectural design are avoided.

Two types of wind fairings were selected from five candidates after qualitative assessments by using flow visualization tests. These two types of wind fairings, named Scheme A and Scheme B, were then undertaken quantitative tests using high-frequency force-balance (HFFB) method to optimize the fairing's shape parameters. The results indicate that properly designed wind fairings have a potential to reduce the design wind loads by about 20%.

For Scheme A fairing, the optimal configuration has a relative width of about 1/10, a relative height of 1/5 or more and a fairing angle of about 45°.

For Scheme B fairing, the optimal configuration has a relative width of about 1/10 and a relative gap of about 1/10.

ACKNOWLEDGMENTS

The research described in this paper was financially supported by the National Natural Science Foundation of China (NSFC), Grant No. 51578505.

References

- Dutton, R., and N. Isyumov. 1990. "Reduction of tall building motion by aerodynamic treatments." *J. Wind Eng. Ind. Aerodyn.* **36**: 739–747.
- Irwin, P. A. 2008. "Bluff body aerodynamics in wind engineering." *J. Wind Eng. Ind. Aerodyn.* **96** (6–7): 701–712.
- Kareem, A., T. Kijewski, and Y. Tamura. 1999. "Mitigation of motion of tall buildings with recent applications." *Wind Struct.* **2** (3): 201–251.
- Kwok, K. C. S. 1988. "Effect of building shape on wind-induced response of tall buildings." *J. Wind Eng. Ind. Aerodyn.* **28** (1–3): 381–390. (88)90134-1.
- Tamura, Y., and T. Muyagi. 1999. "The effects of turbulence on aerodynamic forces on a square cylinder with various corner shapes." *J. Wind Eng. Ind. Aerodyn.* **83** (1–3): 135–145.
- Tanaka, H., Y. Tamura, K. Ohtake, M. Nakai, and Y. C. Kim. 2012. "Experimental investigation of aerodynamic forces and wind pressures acting on tall buildings with various unconventional configurations." *J. Wind Eng. Ind. Aerodyn.* **107–108**: 179–191.
- Xie, J., and P. A. Irwin. 1998. "Application of the force balance technique to a building complex." *J. Wind Eng. Ind. Aerodyn.* **77–78**: 579–590.
- Xie, J. 2014. "Aerodynamic optimization of super-tall buildings and its effectiveness assessment." *J. Wind Eng. Ind. Aerodyn.* **130** (7): 88–98.
- Xu, Z., and J. Xie. 2015. "Assessment of across-wind responses for aerodynamic optimization of tall buildings." *Wind Struct.* **21** (5): 505–521.
- Yang, Y., Y. Ge, and H. Xiang. 2009. "Aerodynamic flutter control for typical girder sections of long-span cable-supported bridges." *Wind Struct.* **12** (3): 205–217.

CHAPTER 11

Bottom Plate Slope Effects on Aerodynamic Behaviour of Hexagonal Cross-Section Bridge Deck

Md. Naimul Haque, D.Eng^{*}

Hiroshi Katsuchi, D.Eng[†]

Hitoshi Yamada, D.Eng, M.ASCE[‡]

Abstract: Long span bridges exhibit various aeroelastic phenomena. The shape of the deck plays an important role to govern the aerodynamic stability against these aeroelastic phenomena. A pentagonal shaped bridge deck has an improved aerodynamic behavior and thus, this has been applied for a number of practical bridges. The advantage of using this type of deck is that this doesn't require additional devices like fairings. Flow on the top deck is controlled by placing a curb on the top deck each side, which is known as Separation Interference Method (SIM), where flow on the bottom deck is controlled by the bottom plate web slope. In the previous researches, detailed investigations have already been carried out on this kind of deck shape, which show their efficiency against aerodynamic instability of the bridge. Recently, a number of constructed bridges have been shaped as hexagon deck instead of pentagon deck. However, the aerodynamic behavior of the hexagonal shaped bridge decks is not well known. In the current study, we carried out a detailed numerical investigation on the bottom plate web slope effect on flow behavior of a hexagonal bridge deck and the results were compared with a pentagonal bridge deck case. Along with the bottom plate web slope, the width of the bottom horizontal flange plate and the side ratio were also altered to observe their influence on the aerodynamic behavior. A two-dimensional finite volume code with RANS turbulence model is utilized in the present study.

*Department of Civil Engineering, East West University, A/2, Jahurul Islam City, Aftabnagar, Dhaka-1212, Bangladesh, email: naimul@ewubd.edu

†Department of Civil Engineering, Yokohama National University, 79-5, Tokiwadai, Hodogaya-ku, Yokohama, 240-8501, Japan, email: katsuchi@ynu.ac.jp

‡Department of Civil Engineering, Yokohama National University, 79-5, Tokiwadai, Hodogaya-ku, Yokohama, 240-8501, Japan, email: y-yamada@ynu.ac.jp

The result revealed that the optimum bottom plate web slope shifts to larger slope when the bridge deck is shaped as hexagon instead of pentagon.

INTRODUCTION

The number and span length of long-span bridges are increasing day by day to connect wider lands apart thus facilitating for the economic development of the region. As the span lengths of the bridges are increasing, their aerodynamic behavior becomes more and more important. Under wind environment, both the static and dynamic behaviors of long-span bridges are of great interest. The shape of the deck is one of the most influential factors that control the aerodynamic behavior of a long-span bridge. If the deck is not well shaped, then it would have poor aerodynamic behaviour and as a consequence the bridge would experience larger drag, lift and moment forces; furthermore, it would not be economical as larger section would be required to withstand larger wind-induced loads. The deck may also vibrate with limited amplitude which is known as vortex shedding behavior and that is not expectable from serviceability and fatigue points of view. The bridge might even collapse due to large divergent vibrations such as flutter instability. Therefore, for an economical, serviceable and sustainable bridge system, the deck should be aerodynamically efficient.

Many researches have already been dedicated to improve the aerodynamic behavior of bridge decks. Normally, bridge decks are bluff in nature and this bluffness deteriorates their aerodynamic behavior. Shirashi and Matsumoto (1983) demonstrated the leading and trailing edge shape modification effects on aerodynamic characteristics of a deck. Conversion of deck shape from rectangular to triangular or circular makes it more streamlined and improves the flow behavior. This additional triangular shaped device is known as a fairing and many investigations (Yamaguchi et al. 1986, Nagao et al. 1993, De Marianda and Bartoli 2001, Sukamto et al. 2008, Han et al. 2016, Haque et al. 2016a) have been dedicated to show the influence and effectiveness of the fairings to improve the aerodynamic responses and explain the flow field around the bridge deck. Some specific shapes of fairings can improve the aerodynamic responses and a wide range of application of fairings can be found in the field of bridge aerodynamics. However, attachment of this additional component requires extra construction and maintenance cost. Considering these issues, Kubo and his research team (Kubo et al. 2007, Noda et al. 2009, Noda 2010) proposed an improved bridge deck shape for long span bridges. The most advantageous point in this type of section was that it doesn't require fairing at the edge of the deck.

The proposed deck is pentagonal in shape and it is shown in Figure 1a. The deck had two important shaping parameters: (i) bottom plate web slope (θ), and (ii) curb on the top surface. The bottom surface flow was controlled by the bottom plate web slope (θ) and the top surface separated flow was controlled by the curb. It was shown that if the curb height (h) and its location are adjusted such that it makes an angle of 30° with the leading edge, then the curb can control the top surface separated flow and improves the flutter wind speed (Kubo et al. 2007,

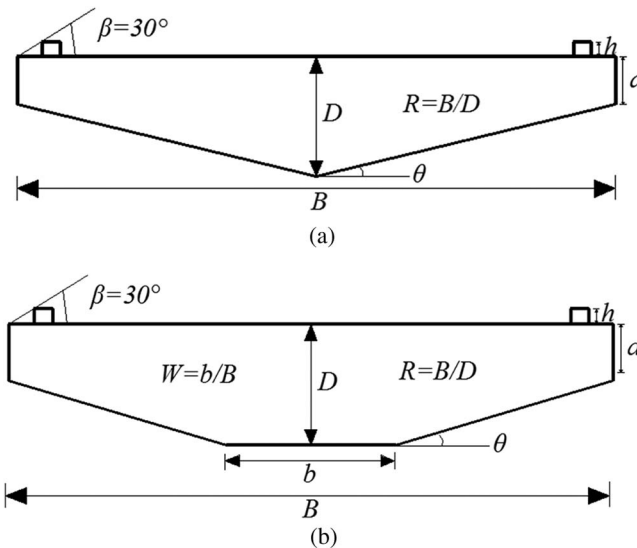


Figure 1. Schematic view of the considered bridge deck section: (a) pentagonal, and (b) hexagonal

Noda et al. 2009, Noda 2010). This technique to control the flow is known as Separation Interference Method (SIM) (Kubo et al. 1993, Kubo et al. 2007, Noda 2009). In previous works the effect of bottom plate web slope (θ) on aeroelastic characteristics of a pentagonal bridge deck was investigated both experimentally (Kubo et al. 2007, Noda et al. 2009) and numerically (Haque et al. 2015a). It was demonstrated that a smaller bottom plate web slope (θ) has better aerodynamic behaviour and the web slope angle of 12° was recommended. It was shown that for the bottom plate web slope of 12° the trailing edge flow separation stops and thus the aerodynamic response of the bridge deck is improved. In Japan, a number of cable-stayed bridges have adopted SIM and placed the bottom plate web slope (θ) of 12° and the curb angle (β) was set to 30° .

However, those bridges had hexagonal deck shape as it is difficult to construct a pentagonal bridge deck. Specially, when the side ratio ($R = B/D$) of the bridge deck increases, the deck cannot be shaped as pentagon and the hexagon shape is adopted, as shown in Figure 1b. The position and orientation of bottom plate web slope (θ) alters due to the appearance of bottom plate horizontal width (b). Haque and Katsuchi (2016b) compared the aerodynamic responses of a pentagonal and a hexagonal bridge deck for a specific value of bottom plate web slope (θ) and found that the aerodynamic responses of the hexagonal bridge deck differ noticeably from the pentagonal bridge deck. Therefore, the bottom plate web slope (θ) is not an independent shaping parameter as its orientation is dependent on the width of the bottom horizontal plate (b). Furthermore, the width of the bottom horizontal plate (b) varies for a range of values as shown in Table 1, which summarizes the sectional properties of a few practical hexagonal bridge deck with the SIM technique. The bottom plate horizontal width (b) was normalized with the

Table 1. Sectional of Properties of a Few Practical Bridges

Name of the Bridge	Span Length (m)	Bottom plate web slope (θ)	Side Ratio ($R = B/D$)	Width Ratio ($W = b/B$)
Takeshima Ohashi	400	15.8°	5.85	0.45
Shintenmom Bridge	264	14.96°	5.20	0.21
Oshima Bridge	226	11.95°	5.50	0.23
Kesennuma Bridge	360	12.18°	7.81	0.47

total width (B) of the bridge deck and was defined as the width ratio ($W = b/B$). As can be seen, the width ratio (W) varies from 0.2 to 0.5 and the side ratio (R) varies between 5 and 8. However, in previous studies the influence of the bottom plate web slope (θ) was investigated without taking into consideration of these important shaping parameters.

Therefore, the present research focused on the aerodynamic characteristics of a hexagonal bridge deck having various width ratios (W) and a relative comparison is made. For each of the width ratios (W), the bottom plate web slope (θ) was varied from 10° to 20° with an increment of 1°. Two-dimensional unsteady RANS simulation was conducted to predict the steady state aerodynamic responses at a Reynolds number of (R_{eB}) of 5.0×10^4 . At first, a relative comparison was made between the aerodynamic responses and flow fields of pentagonal and hexagonal bridge decks. Then, the effect of the side ratio (R) and of the deck attachments such as handrails and a median curb was also investigated. Essentially, the mean and rms values of aerodynamic coefficients, along with the pressure and velocity distributions were considered as parameters of interest to understand the aerodynamic behavior of this type of deck shape.

FORMULATION AND NUMERICAL METHODS

The present study conducted a parametric investigation on various bottom plate web slopes (θ) and bottom horizontal plate widths (b). This kind of parametric study demands massive amount of computational resources. Large Eddy Simulation (LES) and unsteady Reynolds-Averaged Navier-Stokes (RANS) are two common approaches to conduct CFD computation. However, LES requires massive grid system that makes it computationally expensive as compared to the unsteady RANS. Therefore, it was decided to employ unsteady RANS simulation as it is computationally lighter than LES. In the previous work of the authors (Haque et al. 2015a), unsteady RANS was also utilized for simulating aerodynamic behaviour of a pentagonal shaped deck and to compare it with previous experimental work. It was found that unsteady RANS can reproduce the overall trend and the surface pressure distributions, within allowable limit. Moreover, other researchers have already looked into the strength and efficiency of the 2D unsteady RANS in the field of bridge aerodynamics (Mannini et al. 2010, Mannini et al. 2012, Brusiani et al. 2013 Haque et al. 2015b).

The governing equations for two-dimensional incompressible unsteady RANS simulation are as follows:

$$\frac{\partial \bar{U}_i}{\partial x_i} = 0 \quad (1)$$

$$\frac{\partial \bar{U}_i}{\partial t} + \bar{U}_j \frac{\partial \bar{U}_i}{\partial x_j} = -\frac{1}{\rho} \frac{\partial \bar{P}}{\partial x_i} + \frac{\partial}{\partial x_j} \left[\mu \left(\frac{\partial \bar{U}_i}{\partial x_j} + \frac{\partial \bar{U}_j}{\partial x_i} \right) - (\bar{u}'_j \bar{u}'_i) \right] \quad (2)$$

where \bar{U}_i , x_i , t , \bar{P} , ρ , μ represent the time averaged velocity, position vector, time, the time averaged pressure, the air density, and the molecular viscosity, respectively. By solving this equation one can get the time averaged component very easily. However, to solve this equation and to obtain the fluctuating component of velocity, we need the expression of the last term ($\rho \bar{u}'_j \bar{u}'_i$) on the right-hand side of the momentum equation [Eq. (2)]. This term is known as the Reynolds stress and modelling of this term is known as turbulence modelling. There are a number of turbulence models available in the literature. The two most wide used two-equation turbulence models are the $k-\epsilon$ and the $k-\omega$ turbulence model. However, both of these models have their own strong and weak points (Wilcox 1994, Rodi 1997, Lubcke et al. 2001). Therefore, in the present work the turbulence modelling was attained by means of $k-\omega$ -SST (Menter 1994, Menter et al. 2003) turbulence model. This model has combined the best of those previous two turbulence models. The main theme is based on the Boussinesq hypothesis that the Reynolds stress ($\rho \bar{u}'_j \bar{u}'_i$) is proportional to the mean strain rate of tensor (S_{ij}) and can be written in the following way:

$$-\rho \bar{u}'_j \bar{u}'_i = 2\mu_t S_{ij} - \frac{2}{3} \rho k \delta_{ij} \quad (3)$$

where, S_{ij} is the strain rate of tensor and μ_t is the eddy viscosity. The eddy viscosity was modelled based on the equation of two transport variable k and ω (Menter 1994, 2003). Governing equations were discretized by Finite Volume Method (FVM) with the second order accuracy in space and time. A second order accurate backward differentiation formulae method was utilized for time integration. Pressure velocity coupling is attained by PISO (Pressure implicit with splitting of operator) algorithm. An open source code OpenFOAM was used as a solver.

Figure 2 shows the domain size and the meshing pattern. A detail domain sensitivity analysis was carried out before setting the domain size. The computational domain was extended up to 18D in the upstream side and 25D in downstream side of the horizontal direction and 25D in the vertical direction where D is the depth of the bridge deck section. The domain was discretized spatially by a body fitted mesh and the cell size was varied gradually away from the bridge deck in all directions. The first cell height of the mesh was selected based on wall y^+ value and maintained a value of less than 5. The grid resolution was selected based on a detailed mesh dependency test. Total 130,000 elements were

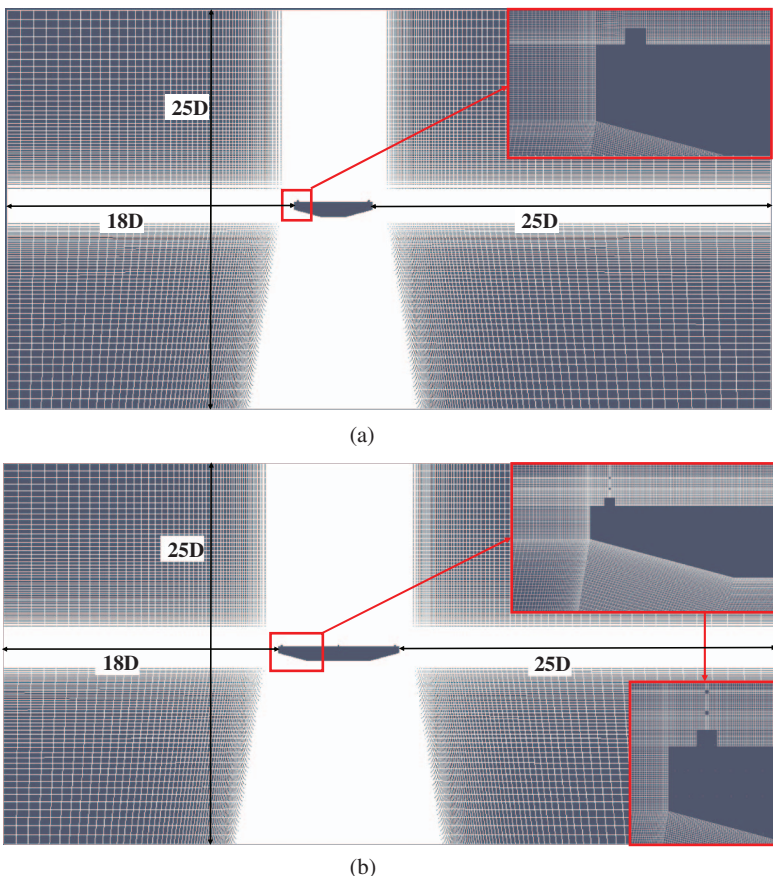


Figure 2. Details of the domain size and meshing: (a) hexagonal bridge deck without handrail and side ratio (R) of 5, and (b) hexagonal bridge deck with handrail and side ratio (R) of 8

used to discretize the flow around the target bridge deck section. A non-slip boundary condition ($\partial u / \partial y \neq 0$ and $v = 0$) was imposed on the bridge deck surface. A Dirichlet type boundary condition for velocity ($u = U$ and $v = 0$) and Neumann type boundary condition for pressure ($\partial p / \partial n = 0$) were implemented at the inlet of the domain, while Neumann type for velocity and Dirichlet type for pressure were applied at the outlet of the domain. A slip boundary condition ($\partial u / \partial y = 0$ and $v = 0$) was imposed at the top and bottom of the domain.

Before utilizing any numerical code and setup, it is important to check the performance and reliability. The present numerical setup has already been validated for a pentagonal bridge deck by comparing the pressure and velocity fields with experimental results in Haque et al. (2015a). Along with that, in the present study we presented one more validation. Simulation was conducted for a square cylinder at Reynolds number (R_e) of 1.0×10^4 and compared the results

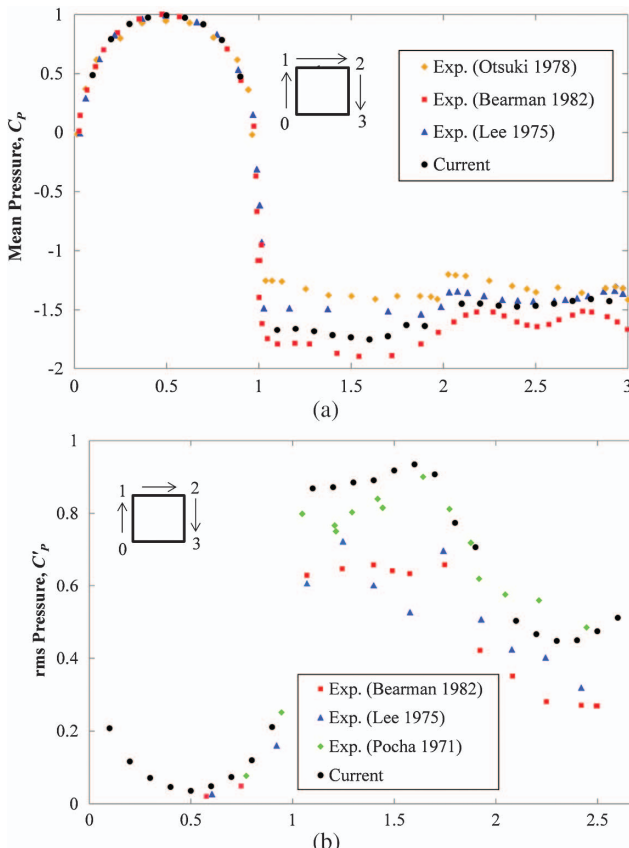


Figure 3. Surface pressure distribution around a square cylinder at $R_e = 1.0 \times 10^4$:
(a) Mean and (b) rms

Source: Experimental results are Otsuki et al. (1978) at $R_e = 6.5 - 7.6 \times 10^4$, Bearman and Obasaju (1982) at $R_e = 2 \times 10^4$, Lee (1975) at $R_e = 1.76 \times 10^4$, Pocha (1971) at $R_e = 9.2 \times 10^4$.

with previous experimental work. Figure 3 compares the mean and rms values of surface pressure around the square cylinder with previous experimental work. For a square cylinder, large flow separation occurs at the trailing edge; however, the current simulation could reproduce the magnitude of pressure and trend of distribution efficiently. The time averaged velocity was plotted along the center line of the domain and compared with the experimental work by Lyn et al. (1995) to check the reliability of flow velocity in Figure 4. The present simulation could grasp the trend of velocity distribution accurately. Finally, the time averaged flow pattern was plotted for the square cylinder in Figure 5 and compared with previous LES simulation, as no experimental data was found. We tried to compare the thickness of cavity zone and vortex core location quantitatively. We found that the current simulation flow pattern matches very well with the LES simulation.

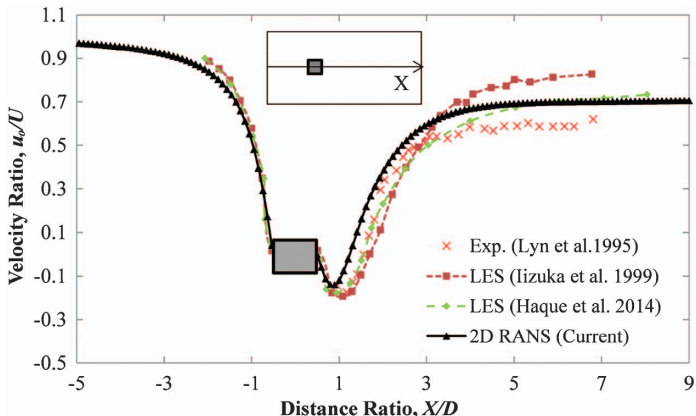


Figure 4. Normalized velocity distributions along the center line of the domain, where, D is the depth of the square cylinder

Source: Experimental and numerical results are [Lyn et al. \(1995\)](#) at $R_e = 2.14 \times 10^4$, [Iizuka et al. \(1999\)](#) at $R_e = 2.2 \times 10^4$, [Haque et al. \(2014\)](#) at $R_e = 2.2 \times 10^4$.

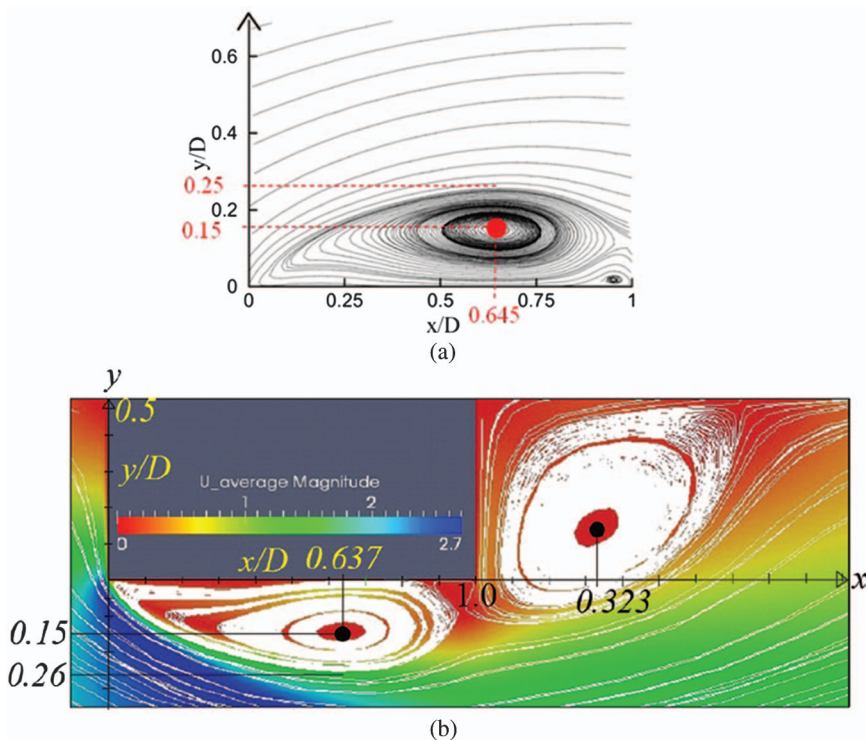


Figure 5. Time averaged flow pattern around the square cylinder: (a) Large Eddy Simulation, (b) current RANS simulation. In the figure, D is the height of the square cylinder

Source: (a) [Kim et al. \(2002\)](#).

EFFECTS OF BOTTOM PLATE WEB SLOPE (θ) AND WIDTH RATIO (W)

Simulations were conducted for bridge decks with width ratios (W): (i) 0, (ii) 0.15 and (iii) 0.3 as shown in Figure 6. The web slope (θ) was altered by changing the height of the side edge (a), without changing the depth of the deck (D) to nullify the effect of the deck side ratio (R). Then, for each of these cases the bottom plate web slope (θ) was varied from 10° to 20° with the increment of 1° . Basically, the length of the bottom plate web slope decreased as the width ratio (W) increased. The mean and rms values of global parameters are plotted in Figure 7 for various bottom plate web slopes (θ). The global parameters such as drag (C_D), lift (C_L) and moment (C_M) coefficients were defined as follows:

$$C_D = \frac{F_D}{\frac{1}{2} \rho U^2 D} \text{ (Downstream positive)} \quad (4)$$

$$C_L = \frac{F_L}{\frac{1}{2} \rho U^2 B} \text{ (Upward positive)} \quad (5)$$

$$C_M = \frac{F_M}{\frac{1}{2} \rho U^2 B^2} \text{ (Counter-clockwise positive)} \quad (6)$$

where F_D , F_L and F_M are the drag, lift and moment force acting on the bridge deck, respectively.

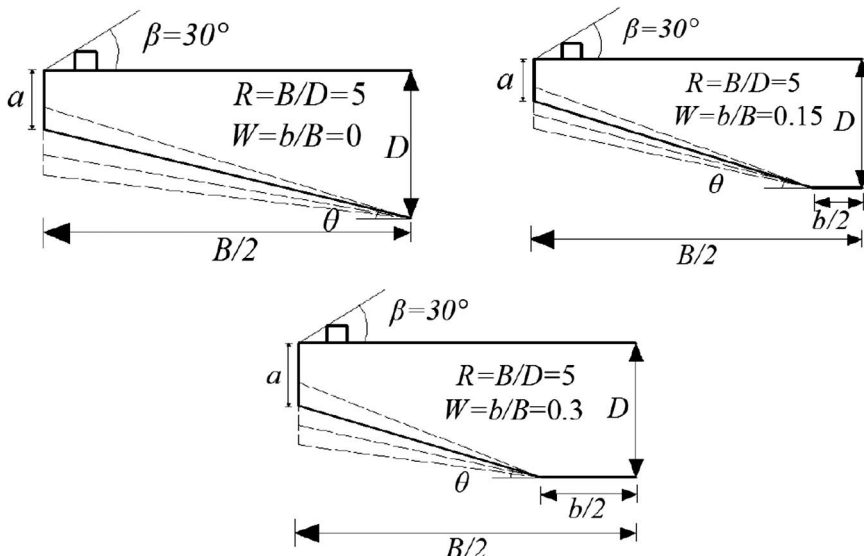


Figure 6. Investigated bridge decks with various width ratios (W)

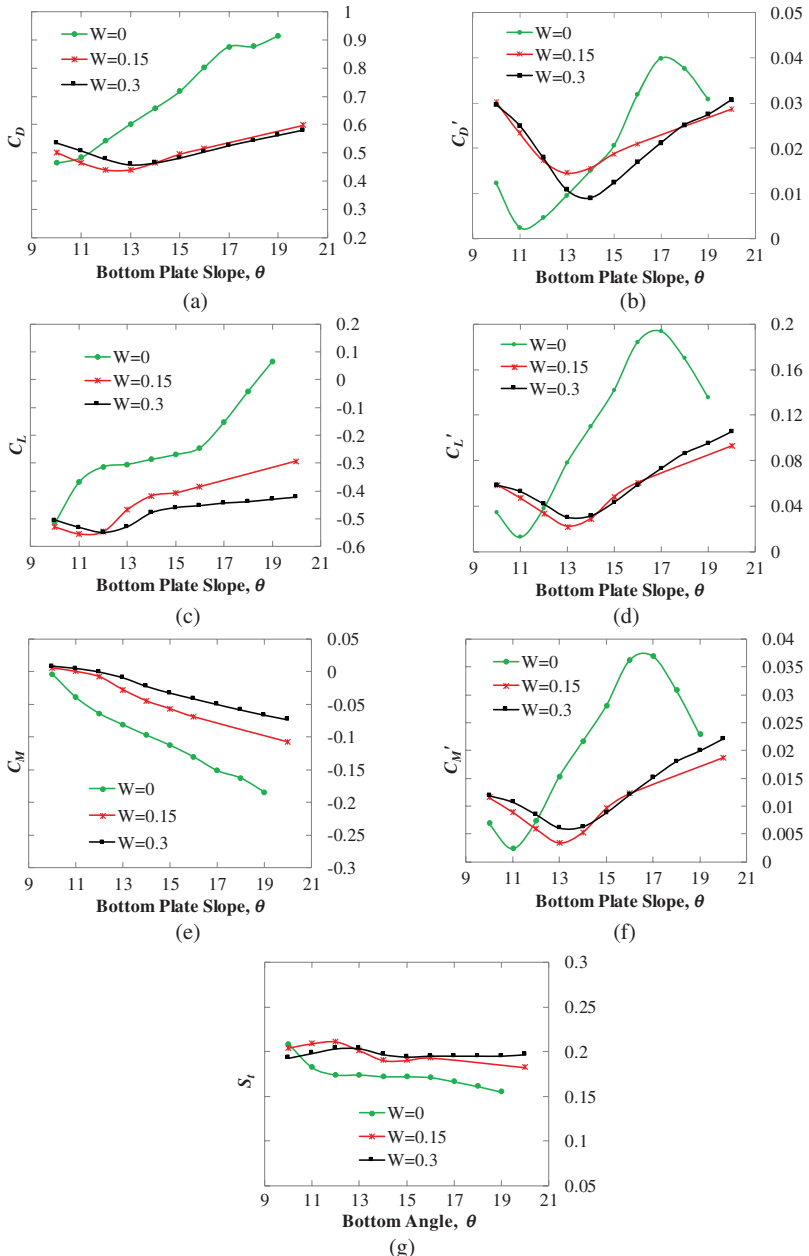


Figure 7. Influence of width ratio (W) and bottom plate web slope (θ) on steady state force coefficients: (a) mean value of drag force coefficients, (b) RMS value of drag force coefficients, (c) mean value of lift force coefficients, (d) RMS value of lift force coefficients, (e) mean value of moment coefficients, (f) RMS value of moment coefficients, and (g) strouhal number

At the first sight, it can be easily noticed that the behaviour of hexagonal decks ($W = 0.15$ and 0.3) is different from the pentagonal shaped deck ($W = 0$). The sensitivity of web slope (θ) decreases significantly as the width ratio (W) increases, that is, it shifts from pentagon to hexagon. This is because as the width ratio (W) increases, the length of the web slope (θ) decreases (Figure 6). As a result, the sensitivity of the web slopes (θ) on steady state force coefficients decreases, as well. Another important trend is that, as the deck changes from pentagonal ($W = 0$) to hexagonal shape ($W = 0.15$ and 0.3), the location of the minimum mean drag and rms values of the force coefficients shifts from small to larger bottom plate web slope (θ) of around 13° as shown in Figure 7a. Further, depending on the width ratio (W), the trend and magnitude doesn't vary noticeably for hexagonal bridge decks ($W = 0.15$ and 0.3). However, for hexagonal bridge decks ($W = 0.15$ and 0.3), the negative lift value (C_L) increases and the negative moment value decreases significantly as compared with the pentagonal bridge decks ($W = 0$).

Figure 8 compares the time averaged velocity distribution for the selected pentagonal and hexagonal bridge decks. As can be seen, a hexagonal bridge deck has larger bottom surface leading-edge separation and smaller trailing-edge separation for a specific bottom plate slope. In our previous work [Haque et al. (2015a)], we have already shown that as the trailing-edge separation decreases the wake size decreases too and aerodynamic response of a pentagonal deck decreases. Therefore, lesser trailing-edge separation would be expectable from aerodynamic stability point of view. On the other hand, bottom surface leading-edge separation (cavity zone) is responsible for Impinging Leading Edge Vortices (ILEV) (Naudascher and Rockwell 1994). Vortices are generated from the bottom surface leading-edge separation zone, which impinges at the side surface of the body and responsible for the global instability (Simpson 1989, Hourigan et al. 2001, Mills et al. 2002, Mills et al. 2003). However, the previous investigations (Simpson 1989, Hourigan et al. 2001, Mills et al. 2002, Mills et al. 2003) were conducted on a rectangular cylinder and very large separation occurred at the leading-edge. From previous works (Kubo et al. 1992, Mills et al. 2003, Tan et al. 2004, Bruno et al. 2010), we can see that this kind of leading-edge separation and vortex size are comparable with the depth of the cylinder. The thickness and length of the leading-edge cavity zone of both pentagonal ($W = 0$) and hexagonal ($W = 0.3$) bridge decks for various bottom plate web slopes (θ) were measured from the vertical plane velocity distribution.

In Figure 9a the thickness (t/D) and length (l/D) of the leading-edge cavity zone for different bottom plate slopes are plotted. For pentagonal deck shape ($W = 0$) with large web slope (θ), the cavity zone disappears completely. For smaller web slope (θ), the size of the cavity zone increased. Hexagonal shapes ($W = 0.3$) have thicker separation length than the pentagonal deck shapes ($W = 0$) as the dimension of the side depth (a/D) increases with the increase of the web slope (θ) for hexagonal shapes. However, the length (l/D) of the separation decreases as compared with the pentagonal bridge deck. For hexagonal shapes, the maximum separation thickness (t/D) of 0.095 was found for the web slope of 10° .

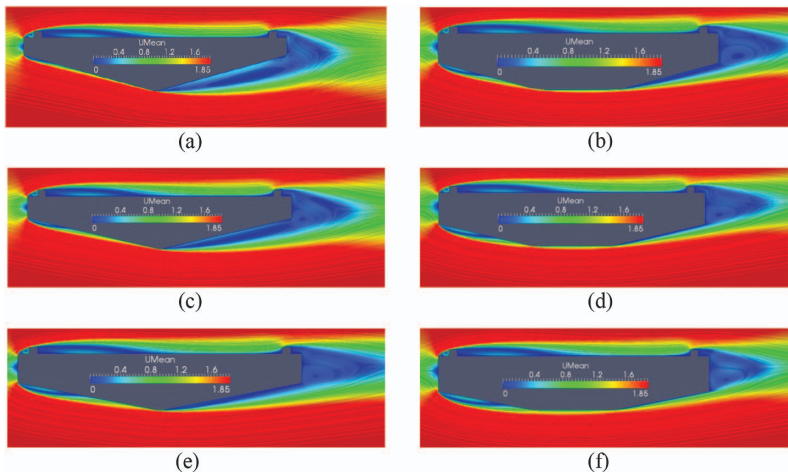


Figure 8. Influence of bottom plate slope (θ) on the flow field for the pentagonal and hexagonal bridge deck: (a) $W = 0$, $\theta = 15^\circ$, $a/D = 0.33$, (b) $W = 0.3$, $\theta = 15^\circ$, $a/D = 0.53$, (c) $W = 0$, $\theta = 13^\circ$, $a/D = 0.42$, (d) $W = 0.3$, $\theta = 13^\circ$, $a/D = 0.59$, (e) $W = 0$, $\theta = 11^\circ$, $a/D = 0.515$, and (f) $W = 0.3$, $\theta = 11^\circ$, $a/D = 0.66$

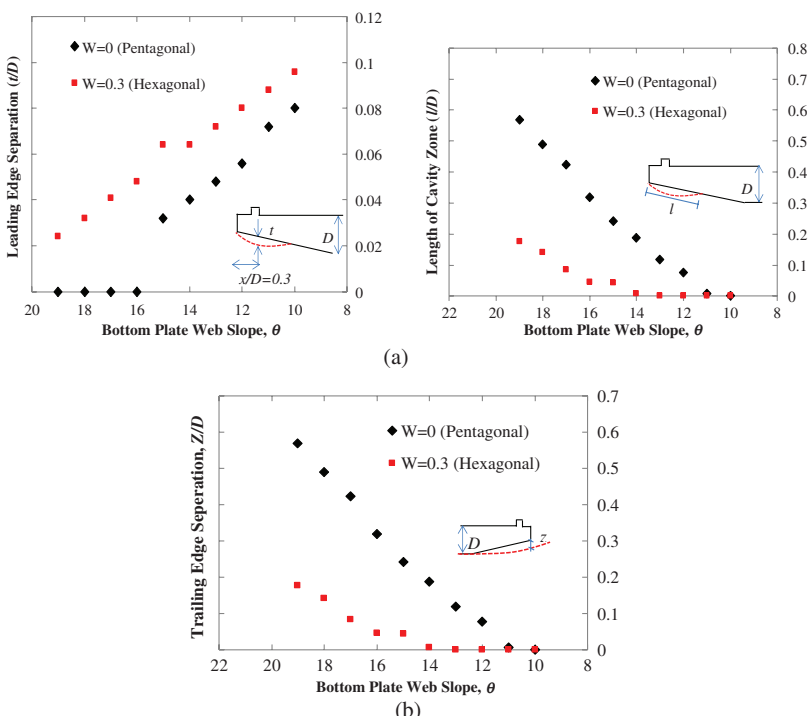


Figure 9. Influence of bottom plate slope (θ) on leading and trailing-edge flow separation: (a) bottom surface leading-edge separation, and (b) bottom surface trailing edge separation

However, this value is very small as compared to a conventional blunt rectangular cylinder. Moreover, a maximum separation length (l/D) of 0.018 was observed for web slopes of 10° to 13° . This is also smaller than the blunt rectangular and triangular edge cylinders as mentioned in previous experimental works. For example, Tylor et al. (2011) reported a cavity length (l/D) of 4.2 and 2.1 for a rectangular cylinder of side ratio (R) of 7 with blunt and triangular leading edges, respectively. Cherry et al. (1984) reported a cavity length (l/D) of 4.4 for an infinite plate while Castro and Epik (1998) mentioned a value of 7.7. Therefore, this kind of leading-edge cavity for a hexagonal shaped deck may not be influential to deteriorate the aerodynamic response. Another important parameter, the trailing-edge separation (z/D) as mentioned in the previous section was also tried to measure quantitatively. Figure 9b shows the boundary layer at the trailing-edge of the decks. The flow separation is very conspicuous in these figures. For the pentagonal shaped deck ($W = 0$) much smaller bottom plate web slope (θ) was required to stop the trailing-edge separation (z/D), while for hexagonal shaped deck ($W = 0.3$) flow serration stopped at much larger bottom plate slope (θ).

Based on this observation, the trend in the steady state force coefficients can be explained. In case of hexagonal bridge deck, it has larger bottom surface leading edge separation, in other word, larger downward force. This leading-edge separation provides extra downward force than pentagonal bridge does and increases the negative lift coefficient values, while the mean drag and rms values of the lift force coefficient depend on the wake size and trailing-edge separation. For the pentagonal bridge, trailing-edge separation stops at a bottom plate web slope (θ) of 11° ; however, for the hexagonal bridge deck the separation stops at much larger bottom plate web slope ($\theta = 13^\circ$). As the trailing-edge separation stops, then the wake size is nothing but the side depth (a/D). For example, in Figure 8b, for bottom plate slope (θ) of 15° , the trailing edge separation is still there. Hence, the total wake size is larger ($z + a$) and the section possesses larger mean drag and rms lift values. If the bottom plate slope is decreased to 13° (Figure 8d), the trailing edge separation stops and the total wake size decreases ($a/D = 0.59$), as a result the mean drag and rms value decreases. However, further decrease in the bottom plate slope to 11° (Figure 8f) increases the wake size ($a/D = 0.66$), as a result the mean drag and rms values increase again.

INFLUENCE OF THE SIDE RATIO (R) AND MEDIAN CURB

This section demonstrates the influence of the side ratio (R) on the aerodynamics of the hexagonal bridge decks. The effects of handrails and a median curb were also investigated by conducting two sets of simulations. The first one was for the bridge deck with side ratio (R) of 8, without handrails and a median curb. For the second set of simulations, both the handrail and the median curb (WHM) were modelled. For both cases, the width ratio (W) of 0.5 was chosen. The bottom plate web slope (θ) was varied from 20° to 10° . The Reynolds number (R_{eB}) was set to 9.7×10^4 for the deck with the side ratio (R) of 8, and the inlet velocity (U) was

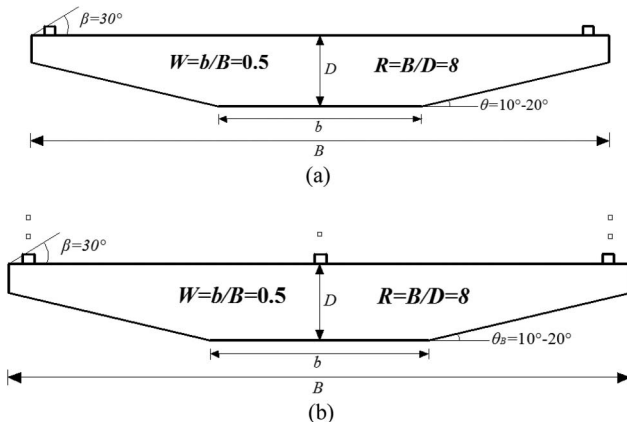


Figure 10. Geometric configuration of the considered bridge deck ($R=8$): (a) hexagonal bridge deck without handrail and median curb, and (b) hexagonal bridge deck with handrail and median curb

maintained constant among all the simulations. Figure 10 shows the geometric configurations of the considered bridge decks. Figure 2b shows the grid system for the bridge deck with handrails and median curb.

The steady state force coefficients for the bridge deck with the side ratios (R) of 5 and 8 are compared in Figure 11. Except the mean value of the moment (C_M), the other responses show quite noticeable sensitivity to the variation of the side ratio (R) and the presence of the median curb. The mean lift (C_L) value does not alter significantly when the side ratio (R) changes, while the negative lift value and the Strouhal number (S_t) decrease significantly due to the addition of handrails and the median curb. On the other hand, the mean drag value and rms of the lift force show sensitivity to the side ratio (R), handrails and a median curb. When the side ratio (R) increases from 5 to 8, the location of optimum aerodynamic coefficient shifts to the larger bottom plate slope ($\theta = 15^\circ$). However, the trend in the results in relation to the bottom plate web slope (θ) does not change a lot due to change in the side ratio (R). With the addition of handrails and a median curb, the bottom plate slope (θ) for optimum response decreases again and shifts to a value close to $14^\circ - 13^\circ$.

The time averaged flow fields are summarized for the particular case of bottom plate slope (θ) of 15° in Figure 12. By observing the flow around the bridge deck, it can be confirmed that the presences of the median curb govern the wind flow on top of the deck, rather than the handrails. Definitely the presence of the handrails increases the drag, however, it doesn't alter the boundary layer flow behaviour. On the other hand, the median curb directly affects the boundary layer flow field. When the side ratio (R) increases from 5 (Figure 8b) to 8, the bottom horizontal plate (b) becomes longer. Hence, the separation tendency of the flow decreases, and the trailing-edge separation stops at a larger bottom plate web slope (θ). Therefore, the

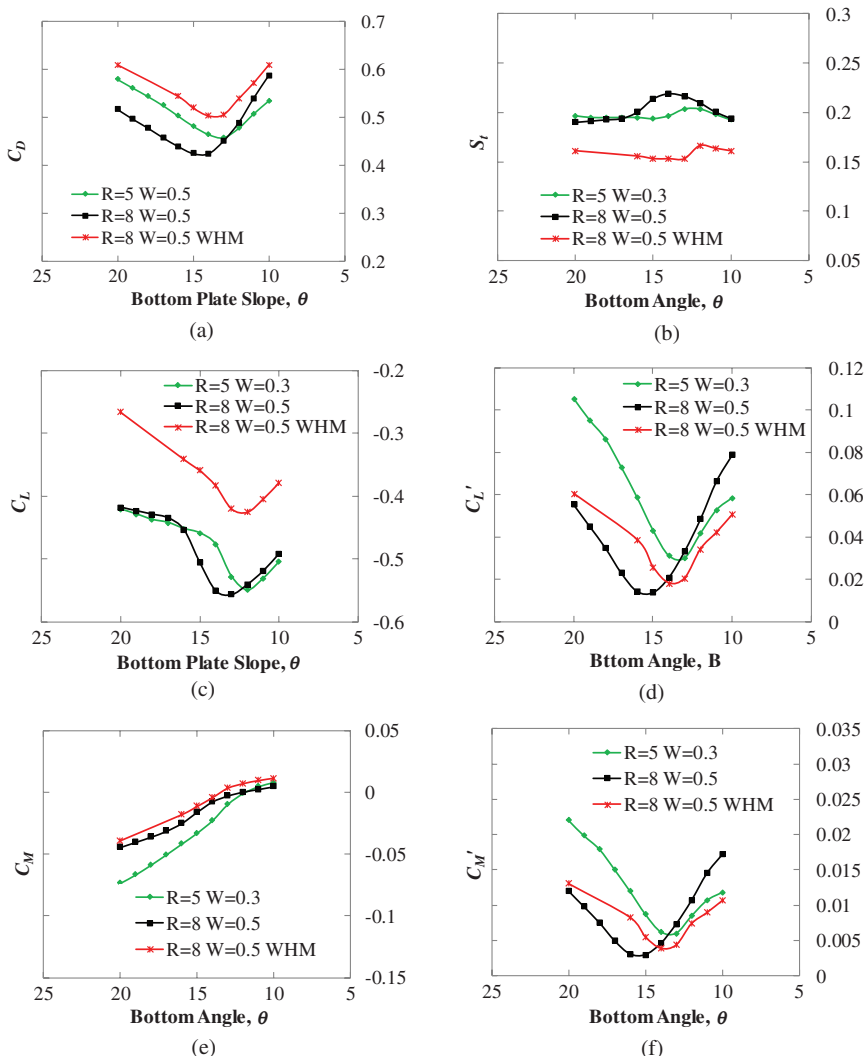


Figure 11. Influence of side ratio (R), handrail and median curb on steady state force coefficients: (a) mean value of drag force coefficients, (b) strouhal number, (c) mean value of lift force coefficients, (d) RMS value of lift force coefficients, (e) mean value of moment coefficients, and (f) RMS value of moment coefficients

optimum location of the bottom plate web slope (θ) increases for larger side ratio (R). When the median curb is attached to the top deck, it makes the flow slower and the trailing-edge flow separation appears again for the same bottom plate slope (Figure 13). Therefore, smaller bottom plate (θ) is required for stopping the trailing edge flow separation and the optimum location shifts.

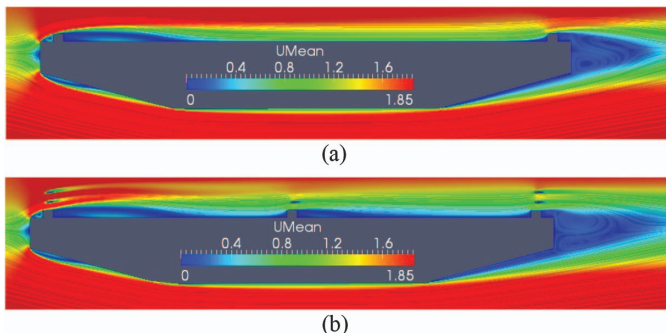


Figure 12. Influence of side ratio (R), handrail and median curb on flow field around the bridg deck: (a) $R = 8$, $W = 0.5$, $\theta = 15^\circ$, and (b) $R = 8$, $W = 0.5$, $\theta = 15^\circ$ (with median curb)

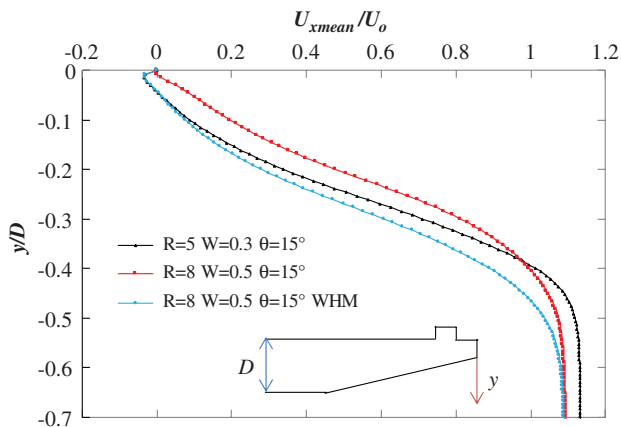


Figure 13. Influence of side ratio (R) and median curb on the trailing edge boundary layer flow separation

CONCLUSIONS

The current mainly focused on the bottom plate web slope (θ) effects on aerodynamic response of a hexagonal bridge deck by employing unsteady RANS simulation. Pentagonal bridge decks ($W = 0$) was compared to the hexagonal decks ($W = 0.15$ and 0.3) with various width ratios. Along with this, the effect of side ratio (R) and other deck attachments such as handrails and a median curb, was also investigated. It was found that aerodynamic coefficients become less sensitive to the bottom plate web slope (θ) when the deck shape is altered from pentagon to hexagonal shape, as the length of the bottom plate web slope decreases. The influence of the bottom plate web slope (θ) decreases even more, with the increase of width ratio (W). Furthermore, depending on the width

ratio (W) and side ratio (R), it was noticed that larger bottom plate slope (θ) is required to obtain the optimum aerodynamic responses. At larger width (W) and side ratio (R), the width of the bottom horizontal plate (b) also increases. Therefore, the flow remains attached to the trailing edge even for large bottom plate slope (θ) of around 15° . However, when a median curb is attached to the deck section, the flow velocity becomes slower, thus requiring smaller bottom plate slopes ($\theta = 14^\circ\text{--}13^\circ$) to stop the trailing edge separation. The flow field of a hexagonal bridge deck is noticeably different from that of a pentagonal deck. Basically, the trailing-edge flow separation stops at larger bottom plate web slope (θ) in case of a hexagonal shaped deck and it possesses thicker leading edge separation. Nevertheless, this leading edge cavity might not be responsible for the Impinging Leading Edge Vortices (IELV), as the size was too small. In future, dynamic simulations can be carried out for some specific parameters of a hexagonal deck, to obtain detailed information regarding the flutter behavior, aerodynamic damping and dynamic flow behavior.

References

- Bearman, P. W., and E. D. Obasaju. 1982. "An experimental study of pressure fluctuations on fixed and oscillating square-section cylinders." *J. Fluid Mech.* **119**: 297–321.
- Bruno, L., D. Fransos, N. Coste, and A. Bosco. 2010. "3D flow around a rectangular cylinder: A computational study." *J. Wind Eng. Ind. Aerodyn.* **98** (6–7): 263–276.
- Brusiani, F., S. De Miranda, L. Patruno, F. Ubertini, and P. Vaona. 2013. "On the evaluation of bridge deck flutter derivatives using RANS turbulence model." *J. Wind Eng. Ind. Aerodyn.* **119**: 39–47.
- Castro, I. P., and E. Epik. 1998. "Boundary development after a separated region." *J. Fluid Mech.* **374**: 91–116.
- Cherry, N., R. Hillier, and M. Latour. 1989. "Unsteady measurement in a separated and reattaching flow." *J. Fluid Mech.* **144**: 13–46.
- De Miranda, M., and G. Bartoli. 2001. "Aerodynamic optimization of decks of cable-stayed bridges." In *IABSE Conf. on Cable-Supported Bridges- Challenging Technical Limits*, 34–41. Seoul.
- Han, Y., H. Chen, C. S. Cai, G. Xu, L. Shen, and P. Hu. 2016. "Numerical analysis on the difference of drag force coefficients of bridge deck sections between the global force and pressure distribution methods." *J. Wind Eng. Ind. Aerodyn.* **159**: 65–79.
- Haque, M. N., H. Katsuchi, H. Yamada, and M. Nishio. 2014. "Investigation of flow field around rectangular cylinder under turbulent flow by LES." *Eng. Appl. Comput. Fluid Mech.* **8** (3): 396–406.
- Haque, M. N., H. Katsuchi, H. Yamada, and M. Nishio. 2015a. "Flow field analysis of a pentagonal-shaped bridge deck by unsteady RANS." *Eng. Appl. Comput. Fluid Mech.* **10** (1): 1–16.
- Haque, M. N., H. Katsuchi, H. Yamada, and M. Nishio. 2015b. "Strategy to develop efficient grid system for flow analysis around two-dimensional bluff bodies." *KSCE J. Civil Eng.* **20** (5): 1913–1924.
- Haque, M. N., H. Katsuchi, H. Yamada, and M. Nishio. 2016a. "Investigation of edge fairing shaping effects on aerodynamic response of long-span bridge deck by unsteady RANS." *Arch. Civil Mech. Eng.* **16** (4): 888–900.

- Haque, M. N., H. Katsuchi, H. Yamada, and M. Nishio. 2016b. "Comparison of aerodynamic characteristics of pentagonal and hexagonal shaped bridge decks." In Vol. 1754 of *AIP Conf. Proc.*, 040017.
- Hourigan, K., M. C. Thompson, and B. T. Tan. 2001. "Self-sustained oscillations in flows around long blunt plates." *J. Fluids Struct.* **15** (3–4): 387–398.
- Iizuka, S., S. Murakami, N. Tsuchiya, and A. Mochida. 1999. "LES of flow past 2D cylinder with imposed inflow turbulence." In *Proc., Wind Engineering Into the 21st Century*, 1291–1298. Rotterdam, Netherland: Balkema.
- Kim, J.-D., B. Havel, H. Hangan, and R. Martinuzzi. 2002. "Numerical and experimental investigation of the near wake dynamics for a square prism." In *AFM2002, Fourth Int. Conf. on Advances in Fluid Mechanics*. Ghent, Belgium.
- Kubo, Y., K. Hirata, and K. Mikawa. 1992. "Mechanism of aerodynamic vibrations of shallow bridges girder sections." *J. Wind Eng. Ind. Aerodyn.* **41–44** (1–3): 1297–1308.
- Kubo, Y., K. Honda, K. Tasaki, and K. Kato. 1993. "Improvement of aerodynamic instability of cable-stayed bridge deck by separated flows mutual interference method." *J. Wind Eng. Ind. Aerodyn.* **49** (1–3): 553–564.
- Kubo, Y., K. Yoshida, E. Tuji, K. Kimura, and K. Kato. 2007. "Development of aerodynamically stable bridge girder cross section for long span bridges." In *Proc., 12th Int. Conf. on Wind Engineering*, 239–246. Cairns, Australia.
- Lee, B. E. 1975. "The effect of turbulence on the surface pressure field of a square prism." *J. Fluid Mech.* **69** (2): 263–282.
- Lubcke, H., S. Schmidt, T. Rung, and F. Thiele. 2001. "Comparison of LES and RANS in bluff-body flows." *J. Wind Eng. Ind. Aerodyn.* **89** (14–15): 1471–51485.
- Lyn, D. A., S. Einav, W. Rodi, and J. H. Park. 1995. "A laser-Doppler Velocimetry study of ensemble-averaged characteristics of the turbulent near wake of a square cylinder." *J. Fluid Mech.* **304**: 285–319.
- Mannini, C., A. Soda, and G. Schewe. 2010. "Unsteady RANS modelling of flow past a rectangular cylinder: Investigation of Reynolds number effects." *Comput. Fluids* **39** (9): 1609–1624.
- Mannini, C., A. Soda, R. Vob, and G. Schewe. 2012. "Unsteady RANS simulations of flow around a bridge deck section." *J. Wind Eng. Ind. Aerodyn.* **98** (12): 742–753.
- Menter, F. R. 1994. "Two-equation eddy-viscosity turbulence models for engineering application." *AIAA J.* **32** (8): 1598–1605.
- Menter, F. R., M. Kuntz, and R. Langtry. 2003. "Ten years of industrial experience with the SST turbulence model." *Turbulence Heat Mass Transfer* **4**: 625–632.
- Mills, R., J. Sheridan, and K. Hourigan. 2002. "Response of base suction and vortex shedding from rectangular prisms transverse forcing." *J. Fluid Mech.* **461**: 25–49.
- Mills, R., J. Sheridan, and K. Hourigan. 2003. "Particle image Velocimetry and visualization of natural and forced flow around rectangular prisms." *J. Fluid Mech.* **478**: 299–323.
- Nagao, F., H. Utsunomiya, T. Oryu, and S. Manabe. 1993. "Aerodynamics efficiency of triangular fairing on box Girder Bridge." *J. Wind Eng. Ind. Aerodyn.* **49** (1–3): 565–574.
- Naudascher, E., and D. Rockwell. 1994. *Flow-induced vibration: An engineering guide*. Rotterdam, Netherlands: A. A. Balkema.
- Noda, T. 2010. "Study on development of narrow width deck section for suspension bridge." [In Japanese] Ph.D. dissertation, Kyushu Institute of Technology.
- Noda, T., Y. Kubo, K. Kimura, K. Kato, K. Okubo, and K. Yoshida. 2009. "The effect of lower flange slope on the aerodynamic stability on a pentagonal cross-section girder." [In Japanese] *J. Civil Eng.* **65** (3): 797–807.

- Ohtsuki, Y. 1978. "Wind tunnel experiments on aerodynamic forces and pressure distributions of rectangular cylinders in a uniform flow." In *Proc. 5th Symp. on Wind Effects on Structures*, 169–175. Tokyo.
- Pocha, J. J. 1971. "On unsteady flow past cylinders of square cross-section." Ph.D. thesis, Queen Mary College.
- Rodi, W. 1997. "Comparison of LES and RANS calculations of the flow around bluff bodies." *J. Wind Eng. Ind. Aerodyn.* **69-71**: 55–75.
- Shirashi, N., and M. Matsumoto. 1983. "On classification of vortex-induced oscillation and its application for bridge structures." *J. Wind Eng. Ind. Aerodyn.* **14** (1–3): 419–430.
- Simpson, R. L. 1989. "Turbulent boundary-layer separation." *Ann. Rev. Fluid Mech.* **21** (1): 205–232.
- Sukamta, N. F., M. Noda, and K. Muneta. 2008. "Aerodynamic stabilizing mechanism of a cable stayed bridge with two edge box girder." In *Proc., 6th Int. Colloquium on Bluff Body Aerodynamics and Applications*, Milano, Italy.
- Tan, N. T., M. C. Thompson, and K. Hourigan. 2004. "Flow past rectangular cylinders: Receptivity of transverse forcing." *J. Fluid Mech.* **515**: 33–62.
- Tylor, Z. J., E. Palombi, R. Gurka, and G. A. Kopp. 2011. "Features of the turbulent flow around symmetric elongated bluff bodies." *J. Fluids Struct.* **27** (2): 250–265.
- Wilcox, D. C. 1994. "Simulation of transition with two-equation turbulence model." *AIAA J.* **32** (2): 247–255.
- Yamaguchi, K., T. Takeuchi, S. Suzuki, M. Miyazaki, T. Kitahara, and K. Kazama. 1986. "Effects of venting and fairing on vortex-induced oscillations and flutter of box bridge deck." In *Proc., 9th National Symp. on Wind Engineering*, 217–222.

This page intentionally left blank

Index

Page numbers followed by *e*, *f*, or *t* indicate equations, figures, or tables, respectively.

- across-wind loads, 81–86, 82*f*, 83*f*
aerodynamics forces, cable-stayed bridges and, 125, 126*f*, 127–128, 127*t*
along-wind loads, 81–86, 82*f*, 83*f*
ANSYS/ICEM, 117
ASCE 7-10 (ASCE 2010): planetary boundary layer (PBL) modeling and provisions on super-tall building design, 12–13; wind speed maps, 3, 21
atmospheric boundary layer (ABL) flow simulation, 169; approaches to determine wind loads and, 170–171; assessment of simulated flow and, 186–187; conclusions related to, 187–188; governing equations, 171–173, 171*e*–173*e*; integral length scales and, 182, 184, 185*f*; mean wind speed profile and, 175–176, 176*f*; methods of, 185–186; numerical simulation, 171–175; turbulence intensity and, 176–179*f*; wind velocity cross-spectra and, 180, 181*f*, 182, 183*f*; wind velocity spectra and, 178–180, 180*f*
balanced-force-driven ABL wind model, 185
basic intervention cost models, tall building performance and, 31–33, 31*e*, 32*f*
bridge decks. *See* long-span bridges
building codes: issues related to, 98; for temporary buildings, 102
CAARC benchmark building, 26, 47; reduced-order model and, 27–31, 27*f*; tall building performance and, 38–39, 38*t*, 44, 45, 45*t*
cable-stayed bridges: aerodynamics forces and, 125, 126*f*, 127–128, 127*t*; background of, 112–115; conclusions related to, 128–129; instantaneous vortex structure and, 120–121, 121*f*, 122*f*; numerical simulation and, 115–120, 117*f*–119*f*; surface pressure distribution and, 121, 123–124, 123*f*, 124*f*; vulnerability of, 128
cladding/components: load levels for main frames and, 98–101, 99*f*–101*f*; overview of, 97, 98; property losses due to damaged, 100–101, 100*f*, 101*f*
Commonwealth Advisory Aeronautical Research Council (CAARC). *See* CAARC benchmark building

- computational fluid dynamics (CFD) simulation: application of, 152; background of, 170; CAD model and mesh and, 156–157, 157*f*; determination of y_+ value and, 158–159; fan and honeycomb section modeling and, 157; initial and boundary conditions and, 157; setup and, 158
- construction work office buildings, design load for, 103–103, 103*f*, 104, 104*f*
- cost probability: power-law cost equation and, 41–44, 41*f*–43*f*; quadratic cost equation and, 39–40, 40*f*
- database-assisted design (DAD), structural engineering application of, 7–8, 9*f*
- design loads: performance-based wind design and, 87, 88*f*–93*f*, 89–94; for temporary-use buildings, 102–104, 103*f*, 104*f*
- design peak wind effect, 4–6, 4*e*–5*e*
- downbursts/downburst loads: background on, 133; downburst windfield and, 136–138, 137*f*, 138*f*; ground axial stiffness and, 141, 142*f*; ground wire properties effecting longitudinal force and, 139–140, 140*t*; ground wire sag and, 141, 142*f*; ground wire spans and, 139; ground wire weight per unit length and, 140, 140*f*; longitudinal force calculation approach and, 142–146, 143*f*, 144*e*–145*e*, 144*f*; procedure validation and, 145, 145*t*; transmission line systems and, 134–136, 135*f*
- dry inclined cable galloping, 112–113, 115
- Galilean-invariant vortex criterion, 120, 120*e*
- gust response concept, 56
- high-frequency force-balance (HFFB) tests, 196–198, 197*t*
- hurricane hazards, design issues and, 18–20, 19*f*, 20*f*
- hybrid LES/RANS simulations, 15–16, 16*e*
- instantaneous vortex structure, cable-stayed bridges and, 120–121, 121*f*, 122*f*
- Itô's differentiation rule, 33, 33*e*
- large-eddy simulation (LES), 169; of atmospheric boundary-layer (ABL) turbulence, 14–15, 15*f*; function of, 173, 173*e*, 185, 187; long-span bridges and, 208, 211, 212*f*; subgrid-scale models for, 13–14
- life cycle cost (LCC) approach: overview of, 97–98; problems related to minimum, 108–109
- local regression, smoothing and, 3
- long-span bridges, 205; background of, 206–208, 207*f*, 208*f*; bottom plate web slope and width ratio and, 213, 214*f*, 215, 216*f*, 217; conclusions related to, 220–221; parametric study of, 208–211, 210*f*–212*f*; side ratio and median curb ratio and, 217–219, 218*f*, 219*f*
- multiple tuned mass dampers (MTMDs): application of, 57; effectiveness of, 57, 58, 62–68, 64*f*–68*f*; overview of, 55
- National Institute of Standards and Technology (NIST) wind engineering research, 1, 20–21, 170;

- codification of pressures on components and cladding, 9–12, 11*f*; computational wind engineering, 13–16, 14*f*–16*f*; database-assisted design, 7–8, 9*f*; joint wind, storm surge, and waves hazards and combined effects, 18–20, 19*f*, 20*f*; planetary boundary layer modeling, 12–13; time series peak estimation, 6–7, 7*f*; tornado hazard mapping and tornado-resistance design, 16–18, 17*f*; wind load factors for use in wind tunnel procedure, 3, 4*f*; wind speed maps for contiguous United States, 3–6
- Navier-Stokes equations, 116
- Newtonian incompressible flow, 116, 116*e*
- peaks-over-threshold (POT) models: classical models vs., 3; two-dimensional Poisson process and, 6–7, 7*f*
- peak wind pressure, for design purposes, 10
- performance-based seismic design (PBSD), function of, 80
- performance-based wind design (PBWD). *See also* tall building design: along-wind and across-wind loading and, 81–86, 82*f*, 83*f*; components of, 80–81; design loads example of, 87, 88*f*–93*f*, 89–94; overview of, 80; wind and seismic intensity and duration and, 81
- planetary boundary layer (PBL) modeling, ASCE 7-10 provisions on super-tall building design and, 12–13
- Port of Tampa, 18, 19*f*, 20*f*
- power-law cost equation, cost probability and, 41–44, 41*f*–43*f*
- power-law cost model: cost variability and, 44–47, 46*f*, 47*f*; intervention cost and, 36–38; parameters, 44
- power spectral density function, wind force simulation and, 61–62
- precursor database method, 171
- pressure codification, on components and cladding, 9–12, 11*f*
- rain-wind-induced vibration (RWIV), 112
- recycling and rescaling method, 170–171
- reduced-order model, 27–31, 27*f*
- Reynolds-averaged Navier-Stokes (RANS) approach, 115, 116, 208, 209, 212*f*, 220
- Reynolds stress, 209, 209*e*
- scaffolding, design load for, 102, 103*f*
- sea, lake, and overland surges from hurricane (SLOSH) model, 18–19, 19*f*
- seismic intensity, probabilistic distribution of, 81, 82*f*
- seismic response, performance-based wind design of tall buildings and, 86–87
- separation interference method (SIM), 207
- simulating waves nearshore (SWAN) third-generation wave model, 18
- single tuned mass dampers (STMDs), effectiveness of, 57, 58, 62–68, 64*f*–68*f*
- soil-structure interaction (SSI): responses, 71*t*–78*t*; tuned mass dampers and, 65–68, 65*f*, 68*f*
- spectral density functions, 178–180, 180*f*
- static wind load effects: damage and, 36–38; extended cost model and, 47–51, 48*f*, 49*t*

- stochastic differential system, 33–34
stochastic linearization, 34–35, 37–38
subgrid-scale (SGS) models, for large-eddy simulations, 13–14
surface pressure distribution, cable-stayed bridges and, 121, 123–124, 123*f*, 124*f*
synthetic turbulence approach, 170
- tall building design. *See also* performance-based wind design (PBWD): planetary boundary layer (PBL) modeling and, 12–13; vulnerabilities of tall buildings and, 79–80; wind loads and, 79–94, 82*f*, 83*f*, 86–87, 88*f*–93*f*
tall building performance. *See also* wind response control: analysis of, 26–27; basic intervention cost models and, 31–33, 32*f*; cost probability results predicted by power-law cost equation and, 41–44, 41*f*–43*f*; cost probability results predicted by quadratic cost equation and, 39–40, 41*f*; cost variability in power-law cost model and, 44–47, 46*f*, 47*f*; extended cost model with static load effect and, 47–51, 48*f*, 49*t*; power-law cost model parameters and, 44; reduced-order model and, 27–31, 27*f*; static wind load effects on damage and power-law model intervention cost and, 36–38; stochastic differential system and, 33–34; stochastic linearization and, 34–35, 37–38
temporary-use buildings, design loads for, 102–108, 103*f*–107*f*
time series peak, estimation of, 6–7, 7*f*
tornadoes, 150, 150*f*, 151*f*
tornado hazard mapping, challenges of, 16–18, 17*f*
- tornado simulators: background of, 149–152; CFD modeling and, 151*f*, 152, 156–159, 156*f*, 156*t*, 157*f*; conclusions related to, 163, 165; general flow field and, 159, 160*f*–162*f*, 163; near-floor wind field and, 160, 161*f*–163*f*, 164; numerically simulated, 153, 154*f*, 155, 155*f*, 156*f*, 156*t*
- tuned mass dampers (TMDs). *See also* multiple tuned mass dampers (MTMDs); single tuned mass dampers (STMDs): application of, 56; effectiveness of, 57
- turbulence: atmospheric boundary layer (ABL) flow simulation and intensity of, 176–178, 178*f*; integral length scales of, 182, 182*e*, 184, 185*f*
- URANS simulations, 15–16
- wind-adaptable design (WAD): background of, 194, 195*f*, 196*f*; design wind loads with, 202, 202*f*, 203
- wind engineering: computational, 13–16, 14*f*–16*f*; research overview on, 2
- wind fairings: background of, 194–196; design application of, 201–203, 202*f*; layout of, 196*f*; parameter optimization of, 196–201, 197*f*, 197*t*, 198*t*, 200*f*
- wind force simulation, power spectral density function and, 61–62
- wind loads: along-wind and across-wind, 81–86, 82*f*, 83*f*; approaches to determine, 170–171; numerical simulation to determine, 171–175; performance-based design and, 79–94, 82*f*, 83*f*, 86–87, 88*f*–93*f*; static wind load effects on damage,

- 36–38; wind tunnel procedure and, 3–6, 4*e*, 4*f*
- wind response control: mathematical modeling and, 57–62, 58*f*; numerical study and, 62–67, 63*t*, 64*f*–68*f*; overview of, 55–57; STMD and MTMD effectiveness and, 64–67, 65*f*–68*f*; uncontrolled vs. controlled responses and, 64; wind force simulation and, 61–62, 62*f*
- wind speed maps, 3, 21
- wind speed profile, atmospheric boundary layer (ABL) flow simulation and, 175–176, 177*f*
- wind velocity spectra: atmospheric boundary layer (ABL) flow simulation and, 178–180, 180*f*; atmospheric boundary layer (ABL) flow simulation and cross-spectra, 180, 181*f*, 182, 183*f*